

WASHINGTON UNIVERSITY IN ST. LOUIS

Department of Chemistry

Dissertation Examination Committee:

Richard A. Loomis, Co-Chair

William E. Buhro, Co-Chair

John R. Bleeke

Bryce Sadtler

Elijah Thimsen

Wave Function Engineering in CdSe/PbS Core/Shell Nanocrystal Heterostructures

by

Brian M. Wieliczka

A dissertation presented to
The Graduate School
of Washington University in
partial fulfillment of the
requirements for the degree
of Doctor of Philosophy

August 2019
St. Louis, Missouri

© 2019, Brian M. Wieliczka

Table of Contents

List of Figures	v
List of Tables	ix
List of Schemes	xi
Acknowledgments	xii
Abstract	xvi
Chapter 1: Introduction	1
1.1 Motivation	1
1.2 Introduction to Semiconductors	2
1.3 Semiconductor Band Structure	4
1.4 Effective Mass Approximation	6
1.5 Excitons	7
1.6 Quantum Confinement	8
1.7 Core/Shell Heterostructures	12
1.8 Wave Function Engineering	15
1.9 k -space Engineering	17
1.10 Absorption and Photoluminescence Spectroscopy	18
1.11 Transition Strengths	20
1.12 Shockley–Queisser Limit	24
1.13 Multiexciton Generation	25
1.14 Luminescent Solar Concentrators	27
1.15 Overview of Dissertation Research	27
1.16 References	29
Chapter 2: Methods	36
2.1 Synthesis	36
2.1.1 Materials	36
2.1.2 Preparation of Lead Oleate	36
2.1.3 Preparation of Cd(myristate) ₂	38
2.1.4 Preparation of Cd(docosanoate) ₂	38
2.1.5 Synthesis of CdSe Core Quantum Dots (QDs)	38

2.1.6	Synthesis of CdSe Core Nanoplatelets (NPLs).....	39
2.1.7	Determination of Shell Precursor Quantities for Core/Shell QDs.....	41
2.1.8	Synthesis of PbS Shells on CdSe QDs.....	41
2.1.9	Determination of Shell Precursor Quantities for Core/Shell NPLs	42
2.1.10	Synthesis of PbS Shells on CdSe NPLs.....	43
2.1.11	CdSe NPL Etching Experiments.....	44
2.2	Optical Spectroscopy	44
2.2.1	Absorption Spectroscopy	44
2.2.2	Photoluminescence Spectroscopy	45
2.2.3	Time-Resolved Photoluminescence Spectroscopy	46
2.3	Physical Characterization.....	47
2.3.1	Transmission Electron Microscopy	47
2.3.2	X-Ray Diffraction	47
2.3.3	Inductively Coupled Plasma Mass Spectrometry	47
2.4	Effective Mass Approximation Calculations.....	48
2.4.1	Calculation Parameters	48
2.4.2	Wave Function Calculations for Spherical CdSe/PbS Core/Shell QDs.....	49
2.4.3	Wave Function Calculations for Core/Shell NPLs	49
2.5	References.....	51
Chapter 3: Wave Function Engineering in CdSe/PbS Core/Shell Quantum Dots.....		54
3.1	Introduction.....	54
3.2	Results and Discussion	55
3.2.1	Synthesis	55
3.2.2	Crystal Structure	60
3.2.3	Spectroscopy	63
3.2.4	Electron and Hole Wave Function Calculations.....	71
3.2.5	Potential Effects of Strain and Crystal Structure	75
3.3	Conclusions.....	76
3.4	References.....	78
Chapter 4: Spectroscopy of CdSe/PbS Core/Shell Nanoplatelets.....		85
4.1	Introduction.....	85

4.2	Results and Discussion	89
4.2.1	Synthesis	89
4.2.2	Morphological Changes	90
4.2.3	Optical Spectroscopy	94
4.2.4	Change in Absorption Transition Strength	98
4.2.5	Wave Function Changes at Different Values of k	103
4.2.6	Other Factors	109
4.2.7	Photoluminescence Lifetimes	111
4.3	Conclusions	118
4.4	References	120
Chapter 5: Facet-Dependent Etching of CdSe Nanoplatelets by Lead Oleate		128
5.1	Introduction	128
5.2	Results	131
5.3	Discussion	140
5.4	Conclusions	144
5.5	References	146
Chapter 6: Conclusions & Future Directions		151
6.1	Summary	151
6.2	Future Directions	154
6.2.1	Synthesis	154
6.2.2	Optical Characterization	156
6.2.3	Calculations of Electronic Structure	157
6.3	Conclusion	157
6.4	References	158
Appendix 1: Wave Function Engineering in CdSe/PbS Core/Shell Quantum Dots		161
Appendix 2: Spectroscopy of CdSe/PbS Core/Shell Nanoplatelets		184
Appendix 3: Facet-Dependent Etching of CdSe Nanoplatelets by Lead Oleate		200
Appendix 4: Maple 2017 Code for Solving 1D Double-Well Particle in a Box Model		207

List of Figures

Figure 1-1: CdSe and PbS band energies.....	5
Figure 1-2: Heterostructure band energy diagrams	13
Figure 1-3: CdSe/PbS core/shell nanocrystal band energies	17
Figure 1-4: Wave function overlap of transitions involving wave functions with varying principal quantum number	20
Figure 1-5: Spectroscopic behavior of type-II and quasi-type-II heterostructures	22
Figure 3-1: TEM image of aggregation of CdSe core quantum dots with overgrown PbS.....	56
Figure 3-2: TEM images of CdSe core and CdSe/PbS core/shell quantum dots using 3 nm diameter cores.....	57
Figure 3-3: TEM images of CdSe core and CdSe/PbS core/shell quantum dots using 4 nm diameter cores.....	58
Figure 3-4: TEM images of 8.3 ML CdSe/PbS core/shell quantum dots with and Without tilting	59
Figure 3-5: X-ray diffraction spectra of CdSe core and CdSe/PbS core/shell quantum dots	61
Figure 3-6: High-resolution TEM image of CdSe/PbS core/shell quantum dots	62
Figure 3-7: Extinction and photoluminescence spectra of CdSe core and CdSe/PbS core/shell quantum dots.....	64
Figure 3-8: Extinction spectra of CdSe core and CdSe/PbS core/shell quantum dots normalized at high energy	69
Figure 3-9: Integrated absorption spectra of CdSe core and CdSe/PbS core/shell quantum dots	70
Figure 3-10: Radial probability densities of CdSe core and CdSe/PbS core/shell quantum dots	72
Figure 3-11: Transition energies of CdSe core and CdSe/PbS core/shell quantum dots.....	74

Figure 4-1: TEM images of CdSe core and CdSe/PbS core/shell nanoplatelets.....	91
Figure 4-2: TEM images of CdSe/PbS core/shell nanoplatelets standing on edge	92
Figure 4-3: Extinction and photoluminescence spectra of CdSe core and CdSe/PbS core/shell nanoplatelets	95
Figure 4-4: Extinction spectra of CdSe core and CdSe/PbS core/shell NPLs plotted with respect to the energy of the first absorption transition	99
Figure 4-5: Extinction spectra of CdSe core and CdSe/PbS core/shell nanoplatelets normalized at high energy.....	103
Figure 4-6: Bulk and quantum confined states at the Γ and L points.....	104
Figure 4-7: Proposed correlation diagram of CdSe and PbS states based on angular momentum quantum number.....	110
Figure 4-8: Photoluminescence lifetimes of CdSe core and CdSe/PbS core/shell NPLs with fitted exponential decay.....	113
Figure 4-9: PLE/1-T spectra of CdSe core and CdSe/PbS core/shell nanoplatelets.....	117
Figure 5-1: TEM images of CdSe nanoplatelets treated with chemical precursors used in PbS shell synthesis.....	133
Figure 5-2: Length distributions of CdSe nanoplatelets etched with lead oleate in octylamine.....	134
Figure 5-3: TEM images of CdSe nanoplatelets treated with lead oleate in octylamine for different periods of time.....	135
Figure 5-4: Extinction spectra of CdSe nanoplatelets etched with lead oleate in octylamine for different periods of time.....	137
Figure A1-1: Size histograms of CdSe core and CdSe/PbS core/shell quantum dots.....	163
Figure A1-2: Identification of first absorption peak of CdSe core and CdSe/PbS core/shell quantum dots by second derivative.....	167
Figure A1-3: Integrated absorption spectra of 4 nm CdSe core and CdSe/PbS core/shell quantum dots.....	170
Figure A1-4: Radial probability distributions for $1S_e$ and $1S_h$ states for CdSe core	

and CdSe/PbS core/shell quantum dots using Haus <i>et. al.</i> method.....	171
Figure A1-5: Radial probability distributions for 2S _e and 2S _h states for CdSe core and CdSe/PbS core/shell quantum dots using Haus <i>et. al.</i> method.....	172
Figure A1-6: Radial probability distributions for 3S _e and 3S _h states for CdSe core and CdSe/PbS core/shell quantum dots using Haus <i>et. al.</i> method.....	173
Figure A1-7: Radial probability distributions for 1S _e and 1S _h states for CdSe core and CdSe/PbS core/shell quantum dots using Kaledin <i>et. al.</i> method using heavy hole.....	174
Figure A1-8: Radial probability distributions for 1S _e and 1S _h states for CdSe core and CdSe/PbS core/shell quantum dots using Kaledin <i>et. al.</i> method using light hole.....	175
Figure A1-9: Radial probability distributions for 1S _e and 1S _h states for CdSe core and CdSe/PbS core/shell quantum dots using Poulsen <i>et. al.</i> method.....	176
Figure A1-10: Radial probability distributions for 2S _e and 2S _h states for CdSe core and CdSe/PbS core/shell quantum dots using Poulsen <i>et. al.</i> method.....	177
Figure A1-11: Radial probability distributions for 3S _e and 3S _h states for CdSe core and CdSe/PbS core/shell quantum dots using Poulsen <i>et. al.</i> method.....	178
Figure A1-12: Calculated eigenstate energies <i>versus</i> radius for CdSe core and CdSe/PbS core/shell quantum dots.....	179
Figure A1-13: Calculated band gap energies <i>versus</i> d ² for CdSe core and CdSe/PbS core/shell quantum dots.....	180
Figure A2-1: Size histograms of CdSe core and CdSe/PbS core/shell nanoplatelets.....	187
Figure A2-2: TEM image of CdSe core nanoplatelets standing on edge.....	188
Figure A2-3: Peak identification of extinction spectra of CdSe core and CdSe core/shell nanoplatelets by second derivative.....	191
Figure A2-4: Trap emission from CdSe core nanoplatelets.....	194
Figure A2-5: Fitting of first two absorption transitions of CdSe core and CdSe/PbS core/shell nanoplatelets.....	195
Figure A2-6: Extinction and photoluminescence spectra of CdSe core and CdSe/PbS	

core/shell nanoplatelets used in photoluminescence lifetime studies.....	197
Figure A2-7: Instrument response function for photoluminescence lifetime studies.....	198
Figure A3-1: Size histograms of CdSe core nanoplatelets before and after etching with lead oleate.....	200
Figure A3-2: Size histograms of nanodots produced by etching CdSe nanoplatelets.....	201
Figure A3-3: Size histograms of nanoplatelets etched with lead oleate in octylamine with varying etching times.....	202
Figure A3-4: Identification of first absorption feature of etched CdSe nanoplatelets by second derivative without baseline subtraction.....	203
Figure A3-5: Identification of first absorption feature of etched CdSe nanoplatelets by second derivative with baseline subtraction.....	205

List of Tables

Table 4-1: Results of fitting the 1_e-1_{hh} transitions to the sum of two Gaussians....	99
Table 4-2: Results of fitting the photoluminescence decay of CdSe core and CdSe/PbS core/shell to the sum of three exponentials....	114
Table 5-1: Elemental composition of NPLs after etching with lead oleate....	139
Table A1-1: Calculation of shell precursor quantities for CdSe/PbS core/shell quantum dot synthesis....	162
Table A1-2: Diameter statistics of CdSe core and CdSe/PbS core/shell quantum dots....	164
Table A1-3: List of other CdSe/PbS core/shell quantum dot synthetic attempts....	165
Table A1-4: Table of spectroscopic data for CdSe core and CdSe/PbS core/shell quantum dots....	168
Table A1-5: Photoluminescence quantum yield values of CdSe core and CdSe/PbS core/shell quantum dots....	169
Table A1-6: Calculated eigenstate and transition energies for CdSe core and CdSe/PbS core/shell quantum dots....	181
Table A2-1: Calculation of shell precursor quantities for CdSe/PbS core/shell nanoplatelet synthesis....	185
Table A2-2: Size statistics of CdSe core and CdSe/PbS core/shell nanoplatelets....	186
Table A2-3: Size statistics of CdSe core and CdSe/PbS core/shell nanoplatelets used in ICP-MS experiments....	189
Table A2-4: ICP-MS data of CdSe/PbS core/shell nanoplatelets....	190
Table A2-5: Spectroscopic details of CdSe core and CdSe/PbS core/shell nanoplatelets....	192
Table A2-6: Photoluminescence quantum yield values for CdSe core and CdSe/PbS core/shell nanoplatelets....	193
Table A2-7: Calculated difference between light hole and heavy hole effective masses in CdSe core and CdSe/PbS core/shell nanoplatelets....	196

Table A2-8: Fitting parameters for photoluminescence lifetimes of CdSe core and CdSe/PbS core/shell nanoplatelets.....	199
Table A3-1: Fitting parameters of curved extinction spectra baseline of CdSe nanoplatelets etched with lead oleate.....	204
Table A3-2: Example calculation of surface and interior cadmium atoms in CdSe core nanoplatelet.....	206

List of Schemes

Scheme 5-1: CdSe nanoplatelet facets and proposed schematic of etching during treatment with lead oleate in octylamine.....	141
Scheme 5-2: Proposed schematic of etching during PbS shell synthesis....	143

Acknowledgments

First, I would like to thank my advisors, Rich Loomis and Bill Buhro. Thank you for giving me the freedom to pursue my own interests, a strong set of ideals, and a spirit of curious questioning. This dissertation would not have been possible without your advice and support in the experiments I conducted and my development as a scientist.

I would also like to thank Bryce Sadtler, who served as a valuable member of my committee these past six years. His knowledge, insights, and questions – not to mention his seemingly eidetic memory – have been extremely valuable in developing this thesis. I also have particularly appreciated his mentorship as I look towards my next steps in my career.

This work was supported by the National Science Foundation under award number DMR-1611149 and CHE-1607862. This research used resources of the Institute of Materials Science and Engineering at Washington University in St. Louis and the X-ray diffractometer in the Department of Earth and Planetary Sciences at Washington University in St. Louis, which is supported by the National Science Foundation under award number EAR-1161543. The authors gratefully acknowledge D. Gamelin and V. Vlaskin (U. Washington) and L. Yang and W. Song (Washington U. – Physics) for helpful discussions and use of their codes for calculating the eigenstates and wavefunctions in the CdSe/PbS QDs. We also gratefully acknowledge the use of resources at the Cherry Emerson Center for Scientific Computation.

I would like to thank the many members of the Buhro and Loomis laboratories, including Fudong Wang, Camille Makarem Yang Zhou, Linjia Mu, Jie Chen, PJ Morrison, Yuewei Yao, Calynn Morrison, Haochen Sun, and Hailey Meiers. I would especially like to thank Matt Sanderson for the many times we worked on instruments or the glovebox together, making those frustrating times a little more bearable.

My first experience of academic research started as an undergraduate student in the lab of Gary Miessler at St. Olaf college. While I learned so much new chemistry from him through his textbook, classes, and lab, I will most especially always remember and be grateful for his extraordinary kindness. He and his wife, Becky Benedict, and their two daughters, Rachel and Naomi, welcomed me into their home for fun, games, laughter, and support since I first met them some eight years ago – and they haven't stopped since.

A tremendous number of friends were a source of joy, support, and – when I needed it – distraction, including the entire Lomneth family, Kelsey Lied, and Charles Nye.

Graduate school can sometimes be lonely or isolating, but living at the Catholic Student Center has meant that community has been at the forefront for the last six year. I would first like to thank Cathy Denault, Cynthia Enghauser, and Linda Straub, who first pulled me into the fold. I would especially like to thank my many fellow residents, including Sean O'Rourke, Austin Wesevich, Gary Braun, Chris Place, Duncan Fischley, Brice Albert, and Adam Becker. Many staff and interns I have become close friends with as well, including Anna Cychowski, Susan Quinn, Anna Mazur, Lisa Bachmann, Jackie Kading, Linda Domeyer, Lynn Duffield, Troy Woytek, and Mark Zaegel. These people, and so many more, formed the backbone for this amazingly supportive community. The Catholic Student Center was also how I was first connected with Rachel Drotar. Without Rachel's love and support, these last few years would not have been possible.

Lastly, I would like to thank my family. My fascination with photovoltaics and semiconductors started when I was 9, working with my dad on a grade school science fair project. It was because of the value my mom and dad placed in my education and personal development that I could dream about who I wanted to be when I "grew up." And it was because

of all the time, support, sacrifice, and love that they put into the day-to-day process of putting those values into practice that I am where I am today.

Brian M. Wieliczka

Washington University in St. Louis

August 2019

Dedicated to my parents.

ABSTRACT OF THE DISSERTATION

Wave Function Engineering in CdSe/PbS Core/Shell Nanocrystal Heterostructures

by

Brian M. Wieliczka

Doctor of Philosophy in Chemistry

Washington University in St. Louis, 2019

Professor Richard A. Loomis, Co-Chair

Professor William E. Buhro, Co-Chair

Colloidal semiconducting nanocrystals hold significant potential for third generation photovoltaics as solution processable materials that can surpass the Shockley-Queisser limit through multiexciton generation. In pursuit of this goal, the synthesis and optical characterization of CdSe/PbS core/shell quantum dots is reported. The spectroscopic behavior of these particles demonstrates their potential for use in optoelectronic devices, taking advantage of wave function engineering of the electron and hole. The rock salt PbS shell grows on all sides of the underlying zinc blende CdSe quantum dot, creating a core/shell structure. With increasing shell thickness, the band edge absorption and photoluminescence transitions decrease in energy as a result of reduced quantum confinement. At the same time, the strength of the first absorption transition decreases by over an order of magnitude relative to the higher energy transitions due to reduced electron—hole wavefunction overlap in the core/shell quantum dots. This leads to a tunable energetic shift of up to 550 meV between the onset of strong absorption and photoluminescence. These proposed changes in wave function overlap are further corroborated by effective mass approximation wave function calculations, which indicate a transition between quasi-type-I and quasi-type-II behavior. These results demonstrate the prospects for this system as luminescent

solar concentrators with a tunable emission energy with prospects for multiexciton generation in third generation photovoltaics.

The same synthetic scheme can be used to synthesize CdSe/PbS core/shell nanoplatelets, allowing for applications requiring directional charge transport. The PbS shell growth results in a change of morphology of the nanoplatelets from rectangular to oval shaped with increasing thickness. The distinct heavy hole, light hole, and split off hole transitions in CdSe nanoplatelets make this system a useful tool for further probing the effects of the changing wave functions on the spectroscopy and dynamics. The changes to the spectral properties of the nanoplatelets were rationalized using a model of the differing band structures of CdSe and PbS. The band gap of CdSe occurs at the Γ point, where the gap between the conduction and valence bands of PbS is large, while the band gap of PbS is at the L point, where the gap between the conduction and valence bands of CdSe is large. This leads to differing absorption transition energies and strengths with increasing PbS shell thickness. The charge carrier wave function overlap is further studied by measuring the photoluminescence lifetimes, which increase with increasing shell thickness, suggesting the wave function overlap between the electron and hole at the band gap decreases.

The shape changes induced during PbS shell deposition on CdSe nanoplatelets is also investigated by treating the nanoplatelets with a variety of chemical precursors used in the PbS shell synthesis. The lead precursor, lead oleate, is found to etch the CdSe nanoplatelets. Transmission electron microscopy images show that both the size and shape of the nanoplatelets change with etching, but the morphology of the product nanocrystals varies depending on the

lead oleate solvent. Etching in the presence of non-coordinating solvents causes the formation of nanodots separate from the CdSe nanoplatelets, while etching in the presence of a coordinating solvent, octylamine, causes the formation of nanodots attached to the CdSe nanoplatelets. Absorption spectroscopy of the nanoplatelets with varying etching times shows a modest shift of the absorption features to higher energy. With increased etching, the nanoplatelet width decreases, causing the quantum confinement to increase, and resulting in the observed spectral shift. Elemental analysis of the product nanocrystals indicates that the newly formed nanodots contain lead. Together, these results suggest that the etching begins from the smallest {110} edges of the nanoplatelets, which also explains the observed shape changes to the nanoplatelets during the CdSe/PbS core/shell nanoplatelet synthesis.

Chapter 1: Introduction

Parts of this chapter were reproduced with permission from: Wieliczka, B. M.; Kaledin, A. L.; Buhro, W. E.; Loomis, R. A., Wave Function Engineering in CdSe/PbS Core/Shell Quantum Dots. *ACS Nano*. **2018**, *12*, 5539-5550. Copyright 2018 by the American Chemical Society.

1.1 Motivation

Climate change caused by anthropogenic greenhouse gas (GHG) emissions, or those originating from human activity, is a significant threat to humanity. Agricultural costs due to reduced crop yield have been estimated to be \$8.5 per ton CO₂ emissions.¹ With climate change, storms will not only increase in power, but more powerful storms will occur more frequently.² These storms are responsible for destruction of property, death, and displacing people. While the effects of these storms will only increase, we already experience the effects of extreme weather; since 2008, 21.5 million people have been displaced every year as a result of extreme weather.³ Agriculture will also be disrupted, putting particular strain on the poorest in developing countries.⁴

Anthropogenic GHG emissions come from a variety of sources, but a major component of these emissions is from fossil fuels used for power.⁵ Despite recent advances in the deployment of renewable energy, these advances will not be sufficient to achieve the GHG emissions targets set by the Paris climate accords. The economically-motivated Bloomberg New Energy Outlook (NEO) projects carbon emissions to drop by only 37% in a most likely scenario and by 59% in the event of a forced phase out of coal.⁶ Both of these paths fall far short of the emissions reductions required to avert a +2 °C change in global temperatures. In the NEO 2018 projection, GHG emissions are projected to drop by approximately 37% of their current levels, whereas a path to the +2° C target requires GHG emissions to drop by almost 93% by 2050.⁶

The development of new technology aimed at accelerating the transition from fossil fuels to renewable energy is imperative. The work on semiconducting nanoparticles presented here is primarily motivated by this need. This dissertation is focused on developing and characterizing new, solution-processable materials that could enable the production of highly efficient solar cells at a much lower cost. The average cost of solar power is measured in dollars per Watt of solar capacity. This means that the average cost of installing solar power systems can be decreased in one of two ways. First, the cost to produce the same capacity of solar power can be reduced through incremental technological advancements and economies of scale, which has already occurred dramatically over the past seven years.⁵ Second, by increasing the total wattage (the total efficiency) from each panel, the overall cost per watt can also be reduced. Increasing the efficiency of these panels is extremely important because the costs of the panel hardware, including the glass, AC/DC converter, and circuitry, are significant and will not change much.⁵ New semiconductor systems have the potential to dramatically increase the efficiency of the solar cells, thereby reducing the total cost of solar power.

1.2 Introduction to Semiconductors

Shared electrons serve as the bases for covalent bonding. In the simplest molecule, H_2 , each hydrogen atom in its ground state contributes a single electron occupying its $1s$ atomic orbital. These two $1s$ atomic wave functions can constructively interfere to create a bonding molecular orbital (σ_{1s}) or destructively interfere to form an antibonding molecular orbital (σ_{1s}^*). The bonding σ_{1s} molecular orbital, which has a lower energy than the $1s$ atomic orbitals, is occupied by two electrons in the ground state of molecular hydrogen. The antibonding σ_{1s}^* molecular orbital, meanwhile, is empty in the ground state.

This simplistic example of diatomic molecular orbital theory serves as an example for how electron orbitals interact in molecules to form occupied or unoccupied states. In bulk materials, there are many interacting atoms, each with many electrons, that interact to form states grouped into bands. The highest-energy, occupied states of the unexcited material form the valence band (VB), while the lowest-energy, unoccupied states form the conduction band (CB). The difference in energy between the VB maximum (VBM) and the CB minimum (CBM) dictate whether the material behaves as an insulator, a metal, or a semiconductor.

In insulators, the energetic gap between the VBM and CBM is very large. Electrons are stationary in the VB and require a very large amount of energy to access the CB, where they can be mobile. On the other hand, metals require a very small amount of energy to excite an electron since the VB is only partially filled. As a result, electrons in metals can be mobile in the VB without the large energetic transition required to access a higher energy band.

Semiconductors represent a middle ground between insulators and metals. Like insulators, there is an energetic gap between the VBM and CBM (the band gap), but unlike insulators, this gap is relatively small. The band gap varies significantly depending on the semiconductor material, ranging approximately from 0.3 to 4 eV.⁷ This dissertation focuses on two semiconductors, CdSe and PbS, that have band gaps of 1.74 eV and 0.37 eV, respectively.⁷⁻⁹ Of particular interest is the effects of these materials' structure on their optoelectronic properties.

CdSe and PbS are crystalline materials, and therefore the atoms are arranged in a periodic, repeating lattice. CdSe nanoparticles can be synthesized in either the wurtzite (WZ) or zinc blende (ZB) crystal structures.^{10,11} WZ is a close-packed structure forming a hexagonal unit cell. ZB, on the other hand, is a face-centered cubic crystal structure in which the Se atoms form a cubic anionic sublattice and the Cd atoms occupy half of the available tetrahedral interstitial

sites in the anionic sublattice.¹² PbS crystalizes in the rock salt (RS) structure. RS is also a face-centered cubic structure, similar to the ZB structure, in which the chalcogen atoms (S atoms) form a cubic anionic sublattice. In RS, however, the Pb atoms occupy octahedral interstitial sites in the sublattice.¹² Due to the similarity in the ZB and RS crystal structures, particularly the common cubic anionic sublattice, this work focuses on CdSe in the ZB crystal structure and heterostructures of CdSe(ZB)/PbS(RS).

1.3 Semiconductor Band Structure

When an electron is promoted from the VB to the CB in a semiconductor, a region of electron deficiency is created in the VB, called a hole, which behaves as a positively charged particle. An electron's or hole's movement through the periodic potential of a semiconductor crystal can be described by the electron or hole momentum, represented by the wave vector k . This leads to the classification of semiconductors as one of two types, direct and indirect, based on the relationship between k and the band gap. In direct band gap semiconductors, the CBM and VBM are at the same value of k .¹³ In an indirect band gap semiconductor, the CBM and VBM have different values of k .¹³ Therefore, exciting an electron from the VBM to the CBM in an indirect gap semiconductor requires a change in the value of k or the momentum of at least one of the charge carriers. This can be done by coupling the electronic excitation with crystal lattice vibrations that carry momentum (phonons). Since the optical transitions (absorption or emission) must be accompanied by a coupling to phonons, these transitions are typically less intense and the transition probability is typically lower than the corresponding band edge transitions in direct band gap semiconductors. CdSe and PbS are direct band gap semiconductors.

Since a crystal structure has well-defined atomic positions and potential energy landscapes that are dictated by the bonding orbitals and elements comprising the crystal, the

energetics of a charge carrier moving through a crystal depend uniquely on the direction of motion. The wave vector k describing the charge carrier momentum along these different crystallographic directions is affected by the atomic positions, the orientation of orbitals, and the electron density. Consequently, the energies of the electronic states of a crystalline semiconductor material depend on the value of k , leading to a band diagram, or a map that indicates the possible electronic energies for all directions and values of k .¹⁴ The direction of k can be described in the Brillouin zone, which is the equivalent of the unit cell in momentum space rather than in real space. The Brillouin zone differs for different types of atomic packing in the crystal structure. Since CdSe and PbS are both face-centered cubic, they share a common Brillouin zone.¹⁴ In each different Brillouin zone, different crystallographic directions correspond to different named points. In the face-centered cubic Brillouin zone, the (0,0,0) point is the Γ point, and (1/2,1/2,1/2) is the L point. The VB and CB energies of CdSe and PbS at the Γ and L points are shown in Figure 1-1 with the continuum of states in the VB and CB associated with translational kinetic energy of charge carriers within each band (shaded boxes).^{15,16} The

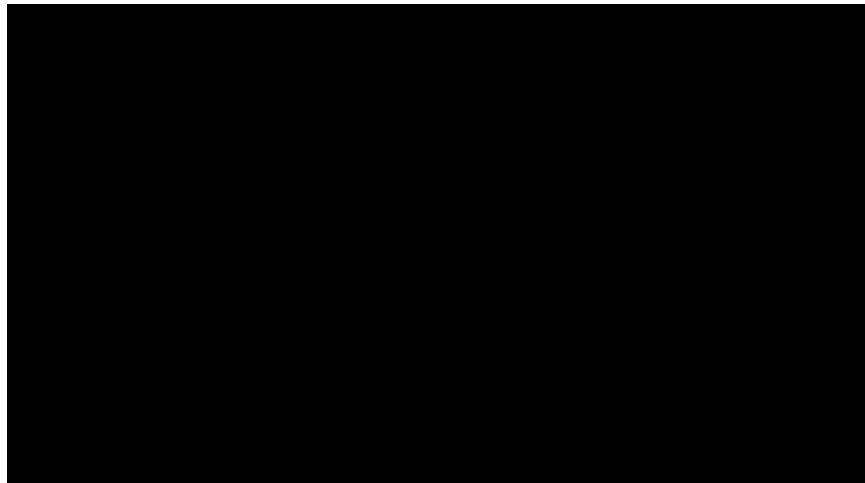


Figure 1-1. Schematic of band energies of CdSe and PbS at the Γ and L points. The shaded boxes represent the continuum of states in the conduction (top) and valence (bottom) bands of the semiconductor. The energies of the band edges are relative to the PbS valence band maximum set at 0 eV.^{7-9,15,16}

band gap of CdSe (1.74 eV) occurs at the Γ point, where the gap between the VB and CB of PbS is significantly larger (8.05 eV) than its band gap.^{7,9,15} The band gap of PbS (0.37 eV) occurs at the L point, where the gap between the VB and CB of CdSe is also significantly larger (4.40 eV) than its band gap.^{7,8,16} These band energies are important to consider in the understanding of the optoelectronic properties of these crystalline semiconductors (discussion continued below).

1.4 Effective Mass Approximation

The periodicity of the crystal structure also changes the effective mass of the charge carriers. In vacuum, the electron mass is a well-known constant: 9.11×10^{-31} kg. Within a semiconductor crystal structure, however, an electron behaves as if its mass is different, giving it an effective mass, m_e^* . This effective mass, which is a fitted parameter based on the curvature of the electronic energy plotted versus k near the CBM, is a function of the interactions between the excited electron (in the CB), nuclei and VB electron density in the crystal.^{13,17,18} The electron effective mass is calculated by fitting the CB energy to a parabola, Eq. (1.1) $E = \frac{\hbar^2 k^2}{8\pi^2 m_e^*}$, where \hbar is Planck's constant and k is the wave vector. As a result of the dissimilar electronic permittivity, bonding, and lattice parameters of different crystalline materials, electrons in different materials have different effective masses. Similarly, since holes behave as positively charged particles, the holes also exhibit an effective mass, m_h^* , based on the curvature of the electronic energy plotted versus k near the VBM. These electron and hole effective masses are commonly expressed in fractions of the bare electron mass (the mass of the electron in a vacuum, 9.11×10^{-31} kg). The temperature can also change the electron effective mass since the crystal structure and carrier interactions within a material depend on temperature.

1.5 Excitons

After excitation, the electron and hole experience a mutual Coulombic attraction. If the Coulombic attraction is large enough, the electron and hole can be bound together with an equilibrium distance, termed the Bohr radius, r_B , forming an exciton. Since the Coulombic attraction between the electron and hole is determined by the permittivity of the semiconductor, r_B varies for different materials.^{13,17} Some materials exhibit a high dielectric constant, and there is significant screening of the electrons within the material. As a result, there is weak Coulombic attraction between the electron and hole and a large Bohr radius in these materials. On the other hand, in a material with a low dielectric constant there is little screening, and a strong Coulombic attraction and a small Bohr radius results.

The Coulombic attraction between the bound electron and hole is analogous to that in a hydrogen atom. Like the electron and proton in a hydrogen atom, the electron, hole, and exciton in a semiconductor behave quantum mechanically with discrete energies and quantum mechanical wave functions. The discrete energy levels of an exciton can be approximated by the

equation Eq. (1.2) $E_n = \frac{\mu e^4}{6h^2 n^2 \epsilon_0^2 \epsilon_{semi}^2}$, where μ is the reduced mass of the electron and hole ($\mu = \frac{m_e^* m_h^*}{m_e^* + m_h^*}$), e is the charge of the electron ($1.602 \times 10^{-19} C$), h is Planck's constant

($6.626 \times 10^{-34} J \cdot s$), n is a quantum number associated with the exciton state, ϵ_0 is the vacuum permittivity ($8.854 \times 10^{-12} F \cdot m^{-1}$), and ϵ_{semi} is the dielectric constant of the semiconductor

($\epsilon_{CdSe} = 9.4$, $\epsilon_{PbS} = 17$).^{17,18} The binding energy, which is the energy of the $n = 1$ excitonic level ($E_b = |E_1|$), is typically very weak in bulk semiconductors as a result of screening of the electric field by the semiconductor crystal lattice: ~ 5 meV in CdSe and 3.968 meV in PbS.^{8,9,14} In comparison, the electric field is significantly less screened in vacuum, and as a result, the binding

energy of the electron in the H atom (13.6 eV) is ~3000 times stronger. This binding energy and the wave function nature of the electron and hole result in an equilibrium distance between the electron and hole that is analogous to the equilibrium distance between the nucleus and electron in the hydrogen atom. The exciton Bohr radius can be approximated by the equation Eq. (1.3)

$$r_B = \frac{\epsilon_{semi}\epsilon_0\hbar^2}{\mu e^2}, \text{ where } \hbar \text{ is Planck's constant } h \text{ divided by } 2\pi.^{19}$$

The exciton Bohr radius is 5.6 nm in CdSe and 18 nm in PbS.^{20,21} The stronger the Coulombic interaction, the shorter the exciton Bohr radius. Note, the dielectric constant is known for CdSe in the WZ structure but has not been reported for ZB. The exciton binding energy and Bohr radius are therefore calculated for the WZ phase. The difference in the crystal structure may change the exciton binding energy and Bohr radius, but these values are expected to be close to the values for the ZB phase of CdSe.

1.6 Quantum Confinement

When a sample of semiconductor material is significantly larger than the exciton Bohr radius, an equilibrium distance between the bound electron and hole, r_B , is established. As the crystal size of a semiconductor is decreased, approaching r_B , the equilibrium distance between the electron and hole is reduced, and the wave functions of the exciton, electron, and hole become perturbed. The resulting energies and wave functions of the electrons and holes in these semiconductor nanocrystals are similar to the simplistic quantum mechanical particle in a box (PIB) model for size ranges in the quantum confinement regime.¹⁸

The PIB model is easiest described for the one-dimensional (1D) case. In a 1D PIB, a quantum-mechanical particle is confined to a region of space by an infinite potential. The total energy of the quantum-mechanical particle is given by Eq. (1.4) $E_{tot} = V_{box} + E_n$, where V_{box} is a constant potential energy inside the box, and E_n is the kinetic energy of the quantum-confined

state, given by Eq. (1.5) $E_n = \frac{n^2 h^2}{8mL^2}$. n is a positive integer used to identify the eigenstates (discrete wave functions) and their energies. m is the mass of the particle, and L is the length of the box.¹³ Eq. (1.5) reveals three important relationships. First, with increasing n , the energy of these kinetic energy states increases quadratically. Second, the smaller the mass of the quantum-mechanical particle, the larger the kinetic energy of each state n . Lastly, the energies of the quantum-confined states are inversely proportional to the length of the box; with decreasing length, the energies of the states increase.

Quantum confinement can occur in each of the three spatial dimensions with the contribution from each to the kinetic energy being additive, given by Eq. (1.6) $E_{n_x, n_y, n_z} = \frac{n_x^2 h^2}{8mL_x^2} + \frac{n_y^2 h^2}{8mL_y^2} + \frac{n_z^2 h^2}{8mL_z^2}$ or more simply Eq. (1.7) $E_{n_x, n_y, n_z} = \frac{h^2}{8m} \left(\frac{n_x^2}{L_x^2} + \frac{n_y^2}{L_y^2} + \frac{n_z^2}{L_z^2} \right)$ for the directions x , y , and z in a simple three-dimensional cuboid PIB model. In semiconductor nanoparticles, this model is directly applied to the electron and holes. The mass of the particle is the effective mass of either the electron or hole, the length corresponds to the dimensions of the nanoparticle, and the potential inside the box is determined by the CBM (VBM) for the electron (hole). While in a bulk semiconductor, the electrons and holes occupy bands, in semiconductor nanoparticles, the electrons and holes occupy discrete kinetic energy states shifted to higher energies due to quantum confinement. The band gap of quantum confined nanoparticles is therefore greater than the bulk band gap by an amount approximated by $E_{1,1,1} =$

$$\frac{h^2}{8} \left(\frac{1}{m_e^*} + \frac{1}{m_h^*} \right) \left(\frac{1}{L_x^2} + \frac{1}{L_y^2} + \frac{1}{L_z^2} \right).$$

Different shapes of particles can result in varying quantum confinement in different dimensions. In semiconductor quantum dots (QDs), which are small, approximately spherical nanoparticles, the electron and hole are confined in the radial dimension.²² The wave functions

and energy levels for this spherical quantum-confinement system are determined by solutions of the spherical Bessel functions and depend on two quantum numbers, n and l . The energies, $E_{n,l}^e$, of the quantum confined states of the electron can be approximated by Eq. (1.8) $E_{n,l}^e = \frac{\hbar^2 \phi_{n,l}^2}{2\pi^2 d^2 m_e^*}$, where $\phi_{n,l}$ is the value of the n^{th} root of the spherical Bessel function, and d is the diameter of the QD. Similarly, the quantum confined states of the hole ($E_{n,l}^h$) can be approximated using the hole effective mass Eq. (1.9) $E_{n,l}^h = \frac{\hbar^2 \phi_{n,l}^2}{2\pi^2 d^2 m_h^*}$. The transition energy, $E_{transition}$, between a particular electron and hole state can be approximated by Eq. (1.10) $E_{transition} = E_g^{bulk} + E_{n,l}^h + E_{n',l'}^e$ where E_g^{bulk} is the bulk band gap. Since the transition energy can be calculated between electron and hole states with dissimilar n and l quantum numbers, n' and l' are used to describe the quantum numbers n and l associated with the electron state. The band gap energy of the QDs, E_g is equal to the transition energy for $n = 1$ and $l = 0$ for both the electron and hole, $E_g = E_g^{bulk} + E_{1,0}^h + E_{1,0}^e$. The order of the spherical Bessel functions (0, 1, 2... or S, P, D...) corresponds to the angular momentum quantum number, l , of the wave function. The indexed number of the root of the wave function gives the principal quantum number, n . For example, the 0th order spherical Bessel function, Eq. (1.11) $j_0(x) = \frac{\sin(x)}{x}$, is used for the energies of the S wave functions.^{23,24} The value of the first root of this function, $\phi_{1,0} = 3.14$, is used for the $n = 1$ state, or the 1S wave function, and the value of the second root, $\phi_{2,0} = 6.28$, is the solution for the $n = 2$ state, or the 2S wave function. The spherical Bessel functions corresponding to $l = 1$ and $l = 2$ are Eq. (1.12) $j_1(x) = \frac{\sin(x)}{x^2} - \frac{\cos(x)}{x}$ and Eq. (1.13) $j_2(x) = \left(\frac{3}{x^3} - \frac{1}{x}\right) \sin(x) - \frac{3}{x^2} \cos(x)$, and the n^{th} roots are precisely known.²⁴ The different $\phi_{n,l}$ can be used to estimate $E_{n,l}$ for a QD with a given composition and size.

In semiconductor quantum wires, which have cylindrical shapes with a single, long dimension (much longer than the Bohr radius), but have a small diameter, the electron and hole experience 2D confinement.²⁵ These wave functions and energies are determined by solutions to the cylindrical Bessel functions, which are also dependent on two quantum numbers n and l that similarly correspond to the n^{th} root of the l^{th} order of the cylindrical Bessel function.²⁶ Similar to the QDs, the energy of the quantum confined states for each charge carrier in QWs can be estimated with Eq. (1.14) $E_{n,l}^e = \frac{\hbar^2 \phi_{n,l}^2}{2\pi^2 d^2 m_e^*}$ for the electron or Eq. (1.15) $E_{n,l}^h = \frac{\hbar^2 \phi_{n,l}^2}{2\pi^2 d^2 m_h^*}$ for the hole except the $\phi_{n,l}$ term here is the value of the n^{th} root of the cylindrical Bessel function, not the spherical Bessel function, and d is the nanowire diameter.

Lastly, 1D confinement can occur in semiconductor nanoplatelets (NPLs) with large lateral sizes (lengths and widths) and very small thicknesses. These thicknesses can be as small as 3.5 monolayers of the semiconductor and can be controlled with high precision for cadmium chalcogenide NPLs.²⁷⁻³⁰ The very small thickness of the NPLs gives rise to quantum confinement, while the two lateral dimensions of the NPLs, length and width, are large enough that they do not significantly contribute to the confinement energies. As a result, the quantum confinement in NPLs is best described using the 1D PIB model, Eq. (1.5).^{27,31} If the length and width of the nanoplatelet approach the size of the exciton Bohr radius, the charge carriers can be weakly confined in these dimensions, but the energies of the NPLs tend to be dominated by the thickness, especially for very thin nanoplatelets.

With decreasing sizes, the carriers in the semiconductor nanoparticles experience increasing quantum confinement, and the energy of the electron (hole) in an excited system increases (decreases) relative to the bulk CBM (VBM). This directly affects the energy of the first absorption transition. In bulk materials, absorption transitions access a continuum of states

at or above the bulk band gap. The band gap absorption transition in semiconductor nanocrystals must access quantized or discrete states corresponding to the lowest energy quantum numbers for both charge carriers ($n = 1, l = 0$ for QDs, $n = 1, l = 0$ for QWs, and $n = 1$ for NPLs) that are shifted to higher energy than the bulk due to quantum confinement. Above the band gap, absorption transitions in semiconductor QDs must access discrete states (corresponding to larger quantum numbers) while absorption transitions in NPLs or QWs must access states with a discrete onset and a continuum above. For example, the bulk band gap of zinc blende CdSe is 1.74 eV, but the lowest energy absorption transition in a zinc blende CdSe QDs can be tuned from 2.6 to 2.0 eV for 2 to 5 nm diameter particles, respectively.^{9,32,33} Controlling the sizes of nanomaterials and thus the degree of quantum confinement is therefore a powerful method for tuning the absorption and emission energies of a semiconductor.

1.7 Core/Shell Heterostructures

While tuning of the band gap energy of a semiconductor is possible through varying the degree of quantum confinement by changing the particle's size, these changes are relatively limited. A heterostructure, or the combination of at least two different semiconductors with at least one interface, is a potent method of tuning both the optical properties, such as the band gap energy, and the excitonic properties, such as the excitonic binding energy and r_B .³⁴

Nanoparticle heterostructures can occur in one of several physical conformations, but this dissertation will focus on core/shell semiconductor heterostructures (Figure 1-2). A core/shell heterostructure is one in which a semiconductor nanocrystal (the core) is overcoated with a different semiconductor (shell). In Figure 1-2, the possible energies of the VB and CB of the core (red) and shell (black) are represented by shaded boxes.

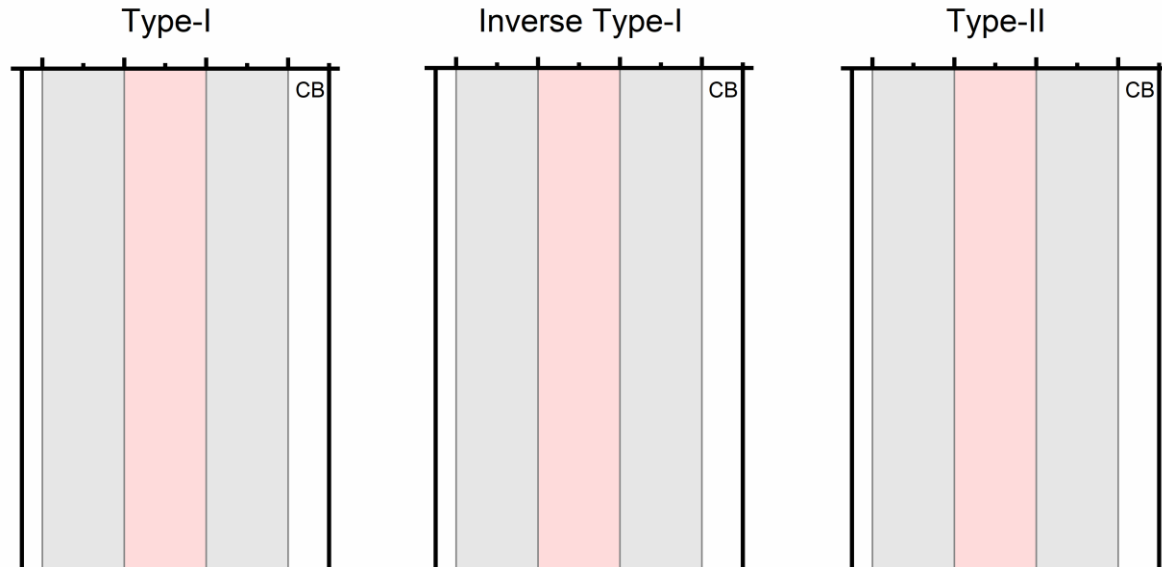


Figure 1-2. Schematic of band energies in core/shell heterostructure types. The bulk continuum of states are represented by shaded red (core) and black (shell) boxes. The higher (lower) energy band states correspond to the conduction (valence) bands.

The band alignment of the core and shell CBM and VBM changes the overall electronic and optical properties of the heterostructure. The electron and hole can be treated as point charges that, upon excitation, must be at the same point in real space for a strong absorption transition. Additionally, since momentum must be conserved, the absorption transition must occur between charge carriers with the same value of k . After excitation, the electron and hole quickly relax to the lowest energy states *via* phonon coupling. Radiative recombination from the lowest energy electron and hole states can then lead to photoluminescence (PL). As a result of these limitations, the strongest absorption transitions in a heterostructure are vertical while the PL transitions can be either vertical or diagonal in a band energy diagram, as in Figure 1-2. For charge carriers to be at the same point in real space, the absorption transition must occur between the VB of the shell and the CB of the shell or the VB of the core and the CB of the core (so-called “vertical” transitions) and cannot occur between the VB of the shell and the CB of the core (a “diagonal” transition).

The bulk band alignments of the core and shell can be classified as different types, three of which are important for this work: type-I, inverse type-I, and type-II.

Type-I. In type-I heterostructures, the VBM of the core is higher in energy than the VBM of the shell, while the CBM of the core is lower in energy than the CBM of the shell. Vertical absorption transitions at high energy can occur in either the core or shell, but absorption at lower energy (near the core bulk band gap) can only occur in the core. The electron (hole) in type-I heterostructures usually relax to the lowest (highest) energy state in the CB (VB). PL is therefore typically only the result of radiative recombination between the core CB and VB states.

Inverse Type-I. In inverse type-I heterostructures, the VBM of the shell is higher in energy than the VBM of the core, and the energy of the CBM of the shell is lower than the CBM of the core. Similar to type-I heterostructures, high energy absorption events can occur between the VB and CB of either the core or the shell. Absorption at low energy, however, can only occur between VB and CB states in the shell. Relaxation of the charge carriers into their lowest energy states results in emission from the shell. Additionally, since charge carriers typically relax to states in the shell, they are available for extraction in an electronic device.

Type-II. In type-II heterostructures, the band gaps of the core and shell materials are offset. In this type-II example, the lowest energy CBM is in the core region while the highest energy VBM is in the shell, as shown in Figure 1-2. In type-II heterostructures, the absorption transition must occur either in the core or shell, but in the example shown, the electron relaxes into the core while the hole relaxes into the shell. Emission can occur between the core CB and the shell VB states, which is significantly lower in energy than the first strong absorption transition.

Careful design of a heterostructure can be used to leverage the energetic differences between the CBM and VBM of two different materials to drive efficient charge separation or combination. Type-II heterostructures can spatially separate electron and hole wavefunctions so that the charge carriers can be separately steered towards different spatial regions, such as the anode and cathode in a device.^{34,35} The opposite scenario, in which the semiconductor band potentials lead to the electron and hole occupying the same region in a heterostructure (type-I) leads to charge combination, which is particularly useful for the efficient emission of light.^{36,37} While the tuning of band gap energies in QDs through size and quantum-confinement effects is now common, a core/shell heterostructure provides two additional degrees of freedom for tuning the energetics of the nanoparticle: the shell material and thickness.

1.8 Wave Function Engineering

To a first approximation, the behavior of the charge carriers in a heterostructure can be predicted by treating them as point charges, but like core nanocrystals, the electron and hole states are quantized with discrete energies and wave functions that are more complex than the VBM and CBM energies. In nanocrystals with a single composition, the PIB model can be used to estimate the quantum confinement energies and wave functions of electrons and holes. The states in a core/shell heterostructure can be calculated using a perturbed PIB model that depend on (1) the dimensions of the core and shell, (2) the effective masses, and (3) the VBM and CBM in the different regions.

These perturbations to the simple PIB model in heterostructures can be used to control the localization of the charge carrier wave functions, called wave function engineering. Apart from changing the wave function behavior by selecting two semiconductors with desired CBM and VBM offsets, the electron and hole localization can be tuned by changing the core size or

shell thickness. While the ZnSe/CdSe bulk band alignment is classified as inverse type-I, the charge carrier localization ranges from type-I (thin shell) to type-II (moderate shell thickness) to inverse type-I (thick shell) with a fixed core size.³⁸

It is tempting to view the bulk CBM and VBM potentials as strict indicators of electron and hole localization in core/shell heterostructures. For example, an electron in the CB of a type-I core/shell bulk heterostructure would have the lowest potential in the core and would therefore be expected to be localized in the core. In a quantum-confined semiconductor nanoparticle, however, the electrons and holes behave quantum mechanically, and where they are likely to be found in the nanoparticle is dictated by the probability density, or Ψ^2 of the state. The potential energy mismatch plays a role in determining the wave function and associated eigenstate energy, but it is not always a straightforward predictor.

Heterostructures comprised of CdSe and CdS serve as a good example of this complexity. CdSe/CdS core/shell QDs are formally a type-I system based on the bulk band edges, and both the electron and hole might be expected to be localized in the core region of the QDs.⁷ Consider a heterostructure with a 3.0 nm thick CdS shell grown on a 3.8 nm diameter CdSe core.³⁹ For these QDs, the energy of the lowest quantum-confinement state in the CB is above the CBM of the CdS shell, and the electron wave function can sample the entire QD. The energy of the lowest quantum-confinement state in the VB is above the VBM of the CdS shell, and the hole wave function remains localized in the core region of the QD. Due to quantum confinement, the electron has significant wave function amplitude (and therefore radial probability density) in the shell.³⁹ Since the lowest state of the electron in these CdSe/CdS core/shell QDs is delocalized and that of the hole is localized, the general type-I and type-II classification breaks down, and this type of heterostructure is commonly referred to as quasi-type-II. Like type-II

heterostructures, the wave function overlap of the electron and hole in a quasi-type-II system is reduced, despite the type-I alignment based on the bulk CBM and VBM energies, but the separation of the carriers is incomplete.

1.9 *k*-space Engineering

Core/shell heterostructures comprised of semiconductors with CBM and VBM at different points in *k* space offer another opportunity for tuning the optoelectronic properties of nanoparticles. As mentioned in Section 1.3, CdSe and PbS are both direct band gap materials, but the band gaps occur at different points in *k* space, illustrated in Figure 1-1. The bulk band energies for a CdSe/PbS core/shell heterostructure are shown in Figure 1-3. The bulk band alignment of CdSe/PbS core/shell nanocrystals is type-I at the Γ point,¹⁴ but at the L point, the alignment is inverse type-I.¹⁴ Thus, if a photon is absorbed at low photon energies near the Γ point both the electron and hole will be confined to the core. At higher excitation energies, the electron or hole states accessed could be delocalized over the entire nanoparticle. The carriers would relax down to the lowest states within the core region and may radiatively recombine. In

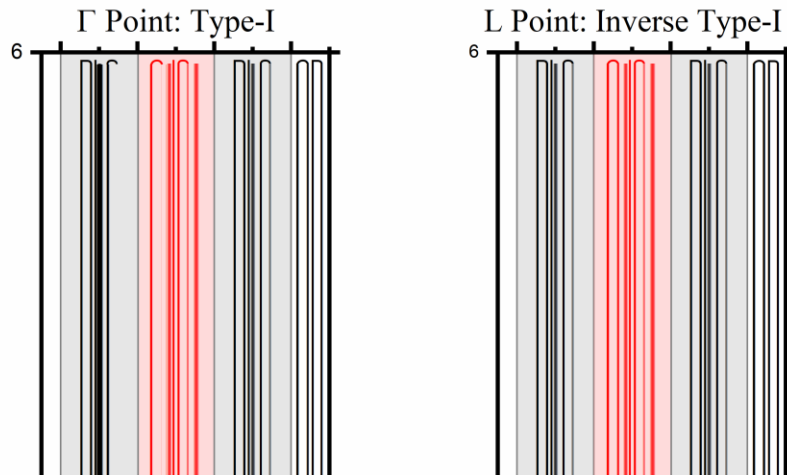


Figure 1-3. Schematic of band energies of CdSe/PbS core/shell nanocrystals at the Γ and L points showing type-I and inverse type-I heterostructure behavior, respectively, based on the bulk band energies. The bulk continua of states of CdSe (red) and PbS (black) are represented by shaded boxes.^{7-9,15,16}

contrast, an electron photoexcited from the VB to the CB at the L point could remain localized in the shell region at lower excitation energies as a result of the inverse type-I band alignment. At higher excitation energies, the electron and hole states accessed could be delocalized, but the carriers would promptly relax to the CBM and VBM of the PbS shell before radiatively recombining. In principle, it is possible for the highly excited charge carriers to evolve from the Γ point to the L point, or vice versa, but in order to do so there must be efficient coupling with phonons to conserve momentum (or wave vector) while doing so.

This picture of two contrasting band alignments for CdSe/PbS heterostructures becomes more complicated when quantum-confinement of either the electron or hole in either the core or shell region of a nanoparticle. The size of the core and the thickness of the shell combined with the effective masses of the charge carriers in the different regions of the heterostructure will play roles in dictating the quantum-confinement energies and the properties of the wave functions. Ultimately, the electron and hole wave functions will dictate the strengths of the transitions between the different quantum-confinement states.

1.10 Absorption and Photoluminescence Spectroscopy

Throughout this dissertation, I use absorption and PL spectroscopy to probe and characterize the energies and properties of the wave functions in CdSe/PbS core/shell nanocrystals. For core-only nanocrystals, quantum confinement dictates the absorption and photoluminescence (PL) transition energies. As stated in Section 1.6, reducing the size of the nanocrystal more strongly confines the charge carriers, leading to higher transition energies through increased quantum confinement. The first absorption transition energy in type-I semiconductors can be measured by absorption spectroscopy and its optical band gap energy can be used to approximate the average size of semiconductor nanocrystals.^{33,40,41} Like the first

absorption peak, the PL peak energy of core nanocrystals increases with reduced nanocrystal size, but the PL energy is shifted to lower energy relative to the first absorption peak energy. This shift to lower energy is called the Stokes shift, which can be the result of factors including the coupling of electronic transitions with phonons or inhomogeneous nanocrystal size distributions.⁴²

The absorption and PL transition energies can change differently with shell deposition and can be indicative of the heterostructure band alignment (type-I, type-II, *etc.*). In ZnSe/CdSe core/shell QDs, the absorption and PL were used to identify different heterostructure type regimes corresponding to different CdSe shell thicknesses.³⁸ Thus, these optical techniques are powerful tools to probe wave function engineering. In thin-shell ZnSe/CdSe core/shell QDs, the electron and hole remain localized in the core, leading to type-I behavior evidenced by a small Stokes shift between the first absorption peak and the PL peak. The band edge absorption and PL peaks also shift slightly to lower energy with shell growth as a result of reduced confinement. In the type-II regime (moderate CdSe shell thickness), the Stokes shift increases dramatically since the charge carriers relax to different band edges. The electron relaxes to a quantum confined state in the shell while the hole relaxes to a quantum confined state in the core. Both the absorption and PL transitions between these two states are relatively weak due to the reduced wave function overlap. Furthermore, the PL associated with the diagonal transition across the core/shell interface is observed at significantly lower energies than the first strong absorption transition, resulting in a large Stokes shift.⁴³ Lastly, for the thick CdSe shell ZnSe/CdSe QDs, both the electron and hole are localized in the shell, causing inverse type-I behavior. In this regime, since the PL and lowest-energy absorption transitions involve states in the same spatial region, the Stokes shift is small (like in the type-I regime) and the band edge absorption and PL peaks shift

together to lower energies with increasing shell thickness as a result of reduced quantum confinement. These optical transitions are therefore a powerful method for probing both the degree of quantum confinement and the charge carrier behavior in heterostructures.

1.11 Transition Strengths

The optical spectroscopy measurements used to probe the quantum confinement states and heterostructure type rely on allowed electronic transitions that must adhere to a series of quantum mechanical selection rules. The first selection rule for an optical transition in a PIB is if the change in the principal quantum number (Δn) is zero. Several hole (n_h , black) and electron (n_e , red) wave functions are plotted in Figure 1-4, labeled with the principal quantum number n , ranging from 1 to 3. Transitions between these states, $n_e - n_h$ ($1_e - 1_h$, $1_e - 2_h$, $1_e - 3_h$ and $2_e - 2_h$ in panels a-d) demonstrate the $\Delta n = 0$ selection rule. These wave functions can be complex with real and imaginary components, and so the transition strength is dependent on the integrated area

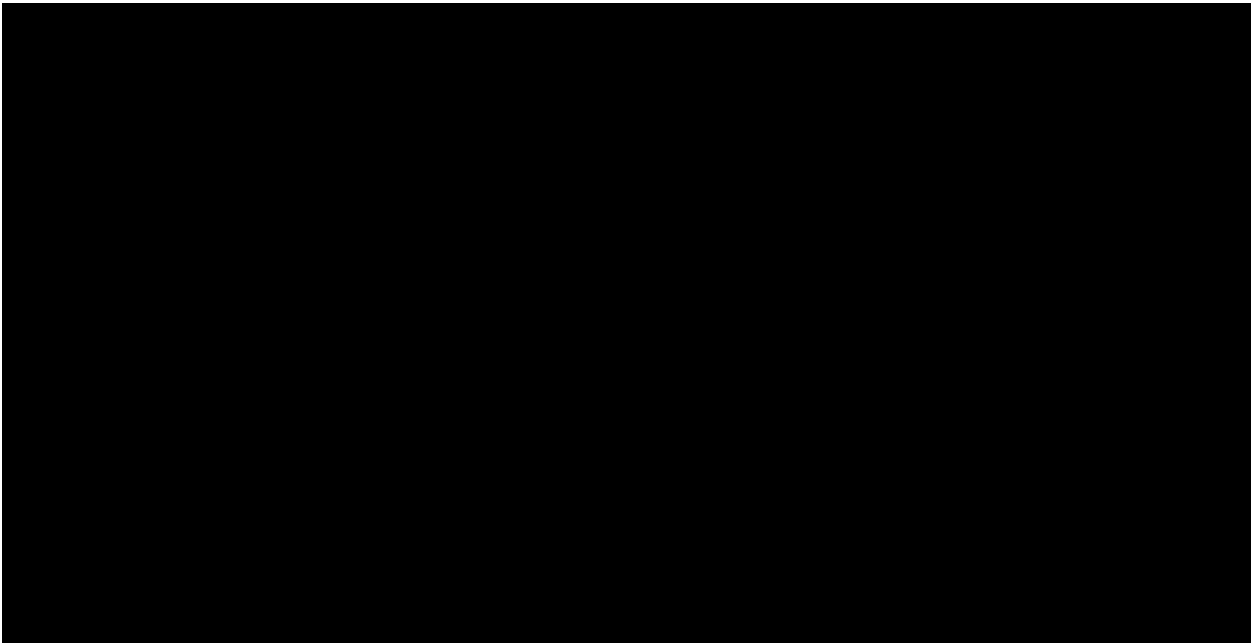


Figure 1-4. One dimensional particle in a box wave functions for hole (black) and electron (red) with varying principal quantum number, n . The product of the electron and hole wave functions is in blue.

of the complex conjugate of the hole times the electron wave functions. In a simplistic view of these wave functions, the transition strength can be approximated as being proportional to the square of the integrated area of the product of the hole and electron wave functions, $|\int \Psi_h \Psi_e|^2$. This product of the hole and electron wave functions is plotted in blue in Figure 1-4. When $\Delta n = 0$ (1_e-1_h , Figure 1-4a and 2_e-2_h , Figure 1-4d), the symmetry of the two wave functions match, and the integrated area of the product is one, resulting in a strongly allowed transition. On the other hand, for $\Delta n = 1$ or $\Delta n = 2$ (Figure 1-4b, 1-4c), the hole and electron wave functions do not have the same symmetry (i.e. they are not both symmetric or both antisymmetric around the center point). Therefore, the integrated area under the product of the wave functions is zero, resulting in a forbidden transition. The $\Delta n = 0$ selection rule is not strictly observed for optical transitions in semiconductor nanocrystals due to the fact that nanocrystals are not strictly PIB systems. Ekimov *et. al.* found that several $\Delta n \neq 0$ transitions had significant probability and contributed to the overall absorption spectrum of CdSe QDs.⁴⁴ This is the result of the non-infinite walls at the edges of the QDs.

A second selection rule for PIB systems is the $\Delta l = 0$ rule.⁴⁴ Again, since the transition probability is proportional to $|\int \Psi_h \Psi_e|^2$, the symmetry of the angular component of the wave functions is important to the transition strength. The $1S_e-1S_h$ transition ($\Delta l = 0$) is allowed because the spherical wave functions of the hole and electron have the same symmetry around the center of the QD. On the other hand, the $1S_e-1P_h$ transition is forbidden since the two wave functions have differing symmetry around the center point. The $1S_e$ wave function is symmetric around the center point, having a positive phase on both sides, but the $1P_h$ wave function is antisymmetric around the central point, having a positive phase on one side and a negative phase on the other. After multiplying these two angular wave functions together, the integrated area is

zero since the positive and negative areas cancel, resulting in no transition probability for the $1S_e-1P_h$ transition.

As stated above, core/shell heterostructures impact the wave function amplitude in different regions, changing the absorption transition strength and energies. For example, the charge carrier behavior can be similar to that predicted for point charges in a type-II potential energy landscape, such as in the type-II heterostructure in Figure 1-5a. The separation of the lowest energy electron and hole wave functions causes significant changes to the spectroscopic properties of these nanocrystals, demonstrated by the sketched wave functions in Figure 1-5a. As before, the range of bulk CB and VB energies of the core (red) and shell (black) are plotted. Sketched $n = 1$ (blue) and $n = 2$ (purple) wave functions are plotted at their eigenstate energies (dashed lines). For simplicity, only the first two electron and hole wave functions are illustrated, but there are other states at energies above (below) these electron (hole) states.

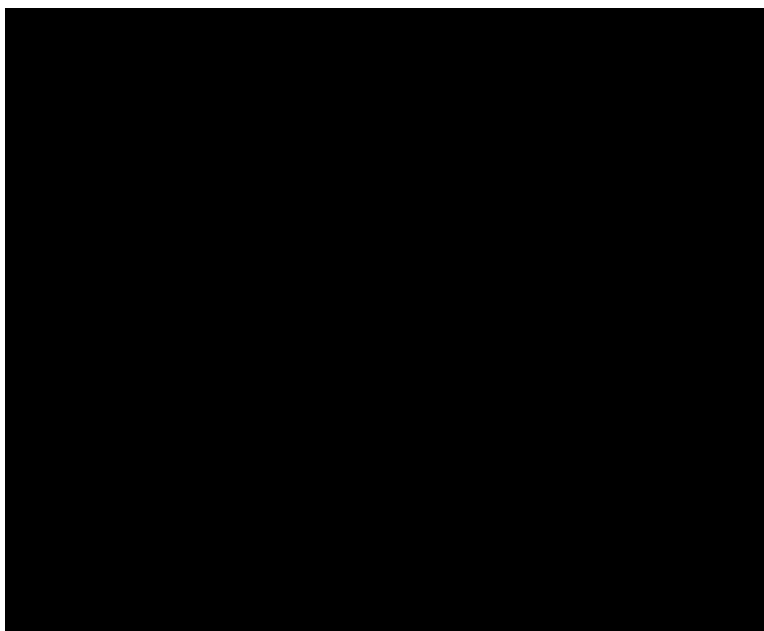


Figure 1-5. Spectroscopic behavior of type-II (a) and quasi type-II (b) core/shell heterostructure assuming a 1D PIB model. Bulk continuum of valence and conduction band states (shaded boxes) of core (red) and shell (black). The eigenstate energies (dashed lines) and wave functions (solid lines) for the 1_e and 1_h states (blue) and 2_e and 2_h (purple) are sketched. The lowest energy observed absorption and PL transitions are labeled as arrows.

In this type-II example, the 1_e and 1_h wave functions are strongly influenced by the VBM and CBM, and the electron is primarily localized in the core while the hole is primarily localized in the shell. Since the absorption transition strength is dependent on the wave function overlap, the absorption transition between the lowest energy electron and hole quantum confinement states, 1_e-1_h , is very weak. The first strong absorption transition energy is therefore a higher energy transition, such as the 2_e-2_h (maroon arrow), in which both the electron and hole wave functions have significant amplitude in both the core and shell. After excitation, the charge carriers relax to the lowest energy states, 1_e and 1_h , before they radiatively recombine. The PL energy in this type-II heterostructure is determined by the difference in energy between the 1_e and 1_h quantum confinement states (black arrow). The Stokes shift between the strong absorption and the PL is therefore large in type-II heterostructures due to the difference in transition energy between the two lowest energy states (PL) and the lowest energy transition with strong wave function overlap (strong absorption).

Quantum confinement effects can also give rise to quasi-type-II behavior even with type-I or inverse-type-I bulk band alignments. Sketched $n = 1$ (blue) and $n = 2$ (purple) wave functions for a type-I core/shell QD based on the bulk VBM and CBM alignment are plotted in Figure 1-5b. In this case, the 1_h wave function amplitude is primarily located in the core due to the large difference in the VBM energies of the core and shell. On the other hand, the 1_e wave function has significant amplitude in both the core and the shell due to the relatively small difference in the CBM energies of the core and shell. The 1_e-1_h absorption transition strength is weaker compared to the same transition in the core QDs due to the reduced wave function overlap, and is therefore classified as a quasi-type-II heterostructure due to the partial charge separation. Unlike type-II behavior (Figure 1-5a), there is significant band edge wave function

overlap, and so the 1_e-1_h transition dictates both the first observed absorption transition and PL transition energies, leading to a relatively small Stokes shift. Like in core nanocrystals, both inhomogeneous size distributions and coupling of electronic transitions to phonons can result in a Stokes shift in these core/shell QDs.

1.12 Shockley–Queisser Limit

Many solar cell architectures rely on semiconductors to absorb sunlight and convert that energy to electricity in the form of an excited electron and hole. In these solar cells, an active semiconductor layer absorbs sunlight and generates excited charge carriers, which are collected at electrodes. When the energy of an incident photon is lower than the semiconductor band gap, the light cannot excite an electron, and so light is not absorbed. When an incident photon has an energy equal to that of the band gap, the light is absorbed and the solar energy is used to create electronic energy by exciting an electron and hole, which are subsequently collected at the anode and cathode, respectively (barring any losses). Lastly, when an incident photon has an energy greater than that of the band gap, an excited electron and hole are generated with excess kinetic energy. That is, the electron and hole are prepared above or below the CBM and VBM, respectively. These charge carriers typically relax to the band edge before collection at the electrodes, releasing the excess energy as heat by coupling to the phonon modes of the semiconductor.

This method of collecting solar energy in a single junction solar cell presents a compromise in the choice of the semiconductor band gap energy. If the band gap is very small, then a very high fraction of the incident photons is collected, but a significant portion of the energy of each photon is lost as heat as the charge carriers relax to the band edge. On the other hand, if the band gap is very large, each photon absorbed imparts significant energy, but

relatively few photons are absorbed because a greater fraction of the solar spectrum has an energy less than the band gap.

Given the energy dependence of the intensity of sunlight reaching the surface of the Earth, an optimal band gap can be calculated, which limits the total efficiency of a single junction solar cell. This limitation is called the Shockley-Queisser limit after the two authors who described the limit in the 1960s.⁴⁵ For Earth, this optimal band gap is 1.1 eV and the maximum efficiency of a solar cell using this band gap is 33%.⁴⁵ The Shockley-Queisser limit of 33% efficiency can be overcome through advanced architectures of solar cells, for example, through the use of multiple layers of semiconductors with varying band gap energies. These strategies, however, typically lead to more complex engineering and higher costs.⁴⁶

1.13 Multiexciton Generation

One mechanism for surpassing the 33% Shockley-Queisser limit is multiexciton generation (MEG). The MEG mechanism requires an incident photon to have an energy of at least twice the band gap of the semiconductor of the solar cell.⁴⁷ After this highly energetic photon is absorbed, hot-carrier relaxation can lead to the generation of additional charge carriers, improving the overall efficiency. This can only occur if the hot charge carrier's excess energy is at least equal to the band gap. In order to generate two excitons with a single photon, the energy of the absorbed photon must be greater than or equal to the energy of the band gap, $E_{ph} \geq 2E_g$. To generate three excitons, $E_{ph} \geq 3E_g$. MEG can increase the maximum efficiency of a solar cell from 33% to 66% by eliminating thermal energy losses of the photogenerated carriers.⁴⁸

Semiconducting nanoheterostructures could allow for greater solar cell efficiency through MEG^{47,49} and wavefunction engineering^{35,50-53} with the manufacturing ease and cost savings of a simple device architecture. These materials also benefit from their solution processability. The

different spatial regions and energetics in heterostructures can provide a medium for MEG. Here, photons can be absorbed in one material within a heterostructure that has a high-energy band gap, for example in the core of a core/shell QD, and the generated charge carriers can be transferred to the spatial region of the second material that has a low-energy band gap, the shell. It is the coupling of the high-energy absorption material with the low-energy material and the efficient transfer of the charge carriers between them that can lead to MEG. Cirloganu *et al.* demonstrated the viability of this strategy in quasi-type-II PbSe/CdSe core/shell QDs;⁵² a narrow band gap PbSe core is coated with a wider band gap CdSe shell. Ultimately, the holes are localized in the cores of these PbSe/CdSe heterostructures, and they would not be easily extracted into the circuit of a solar cell. In contrast, an inverse type-I heterostructure would be better suited for MEG and the subsequent extraction and collection of both electrons and holes in a device. While inverse type-I core/shell heterostructures have been made,^{38,54} they have not yet been synthesized with a narrow band gap semiconductor shell, such as PbSe or PbS, on a high-energy core material that would be conducive for MEG, such as CdSe or CdS. In order to achieve efficient transfer of the photogenerated charge carriers from the high band gap core to the low band gap shell the heterostructures should have a defect-free, epitaxial interface. The electron and hole should also transfer quickly from the core to the shell with minimal non-radiative pathways, such as Auger relaxation and phonon coupling, that would compete with the efficiency of MEG.⁴⁸ Though CdSe/PbS core/shell heterostructures are candidates for enhanced MEG as compared with PbS nanocrystals alone, the fact that the VBM and CBM are at different k points in CdSe and PbS could complicate the MEG process. In order for excited charge carriers to transfer energy from a Γ point state to the L point in order to conduct MEG, the charge

carriers must couple with phonons. The efficiency of this coupling and the transfer of energy from states at the Γ point to states at the L point is unknown and could prevent efficient MEG.

1.14 Luminescent Solar Concentrators

Wavefunction engineering in core/shell QDs also enables their use as luminescent solar concentrators (LSCs). In LSCs, relatively diffuse sunlight is collected over a large area by absorption and subsequent directed reemission onto a relatively small area containing a solar cell or other optoelectronic device.⁵⁵⁻⁵⁷ A major key to an efficient LSC is the ability to absorb light over a broad frequency range and to emit light in a narrow frequency range at lower photon energies. These lower-energy photons are then absorbed by another medium and converted to electricity. The narrower the frequency range of the emission and the more it is energetically separated from the absorption frequencies the better the efficiency of the entire photovoltaic device. Core/shell heterostructures have been proposed for this use.^{37,58} The growth of a CdS shell on CdSe QDs reduces the band edge absorption-emission overlap due to increased absorption at energies greater than the bulk CdS band gap.⁵⁸ This strategy, however, limits the energies of strong absorption in the core/shell QDs. Specifically, CdSe/CdS core/shell QDs strongly absorb only at energies greater than the bulk CdS band gap, 2.42 eV, and the energy of this strong absorption is not tunable by shell thickness.¹⁴ Type-II systems would be excellent candidates for LSCs since they have no absorption-emission overlap due to their large Stokes shift. These materials, however, often suffer from reduced emission intensity as a result of the separation of the electron and hole wavefunctions.^{43,54}

1.15 Overview of Dissertation Research

During my dissertation research, I have synthesized CdSe/PbS core/shell QDs and NPLs and studied their optical properties to probe the energies and wave functions of the quantum

confinement states. The bulk band alignment of CdSe/PbS is an inverse type-I heterostructure, which has potential for use in solar cell designs aimed at exceeding the Shockley-Queisser limit. Despite this predicted behavior, I will show that the CdSe/PbS core/shell nanocrystal samples I synthesized do not behave as an inverse type-I heterostructures using optical spectroscopy. Instead, the optical properties change with the PbS shell thickness; with increasing shell thickness, the strength of the band edge absorption transition decreases relative to the high energy transitions. Effective mass approximation calculations of CdSe/PbS core/shell QDs indicate the importance of the difference in the hole effective masses in CdSe and PbS to the optoelectronic properties. These calculations did not consider the different band structures of CdSe and PbS, which complicates the interpretation of the optical spectra. CdSe/PbS core/shell NPLs are potentially a simpler system, following the simpler pseudo-1D quantum confinement. The spectra of these NPLs collected as a function of shell thickness suggest the band gaps being at different points in k space may have impacts on their utility in solar cell designs.

I also investigated differences in the PbS shell synthesis on CdSe QD and NPL cores. The PbS shell growth is isotropic on CdSe core QDs, with shell growth on all sides of the QDs, whereas the PbS shell growth is not isotropic on CdSe core NPLs. I will show that lead oleate (the lead precursor used in the PbS shell synthesis) causes facet-dependent chemical etching of the CdSe NPLs, causing these differences in the PbS shell synthesis on CdSe QDs and NPLs. This is inferred from the transmission electron microscope images of the NPLs as the overall shape of the NPLs changes from the characteristic rectangular form. While this work did not ultimately test the CdSe/PbS core/shell nanocrystals for MEG, it is an important step towards this type of solar cell. Nevertheless, the wave function tunability could be useful in a variety of optoelectronic applications, particularly in LSCs.

1.16 References

- (1) Moore, F. C.; Baldos, U.; Hertel, T.; Diaz, D., New Science of Climate Change Impacts on Agriculture Implies Higher Social Cost of Carbon. *Nat. Commun.* **2017**, *8*, 1607.
- (2) Coumou, D.; Rahmstorf, S., A Decade of Weather Extremes. *Nat. Clim. Change* **2012**, *2*, 491.
- (3) *Global Report on Internal Displacement*; Norwegian Refugee Council: 2016.
- (4) Rosenzweig, C.; Parry, M. L., Potential Impact of Climate Change on World Food Supply. *Nature* **1994**, *367*, 133.
- (5) Fu, R.; Feldman, D.; Margolis, R.; Woodhouse, M.; Ardani, K., U.S. Solar Photovoltaic System Cost Benchmark: Q1 2017. Energy, Ed. 2017.
- (6) Henbest, S.; Giannakopoulou, E.; Kimmel, M.; Grace, A.; Rooze, J.; Lu, S.; Harries, T.; Chase, J.; Goldie-Scot, L.; Chatterton, R.; Turner, A., Bloomberg New Energy Outlook 2018. 2018.
- (7) Reiss, P.; Couderc, E.; De Girolamo, J.; Pron, A., Conjugated Polymers/Semiconductor Nanocrystals Hybrid Materials—Preparation, Electrical Transport Properties and Applications. *Nanoscale* **2011**, *3*, 446-489.
- (8) Springholz, G.; Bauer, G., 9.1 IV-VI Semiconductors: General Properties. In *Landolt-Börnstein - Group III Condensed Matter 34A*, Springer-Verlag Berlin Heidelberg: Berlin, Heidelberg, 2013; Vol. 16, pp 415-421.
- (9) Cadmium Selenide (CdSe) Electronic Properties, Cubic Modification. In *Landolt-Börnstein - Group III Condensed Matter 41B (II-VI and I-VII Compounds; Semimagnetic Compounds)*, Madelung, O.; Rössler, U.; Schulz, M., Eds. Springer-Verlag: Berlin/Heidelberg, 1999; pp 1-6.

- (10) Chen, O.; Chen, X.; Yang, Y.; Lynch, J.; Wu, H.; Zhuang, J.; Cao, Y. C., Synthesis of Metal-Selenide Nanocrystals Using Selenium Dioxide as the Selenium Precursor. *Angew. Chem. Int. Ed.* **2008**, *47*, 8638-8641.
- (11) Peng, X.; Manna, L.; Yang, W.; Wickham, J.; Scher, E.; Kadavanich, A.; Alivisatos, A. P., Shape Control of CdSe Nanocrystals. *Nature* **2000**, *404*, 59-61.
- (12) West, A. R., *Basic Solid State Chemistry*. 2, illustrated ed.; John Wiley & Sons: 1999.
- (13) Efros, A. L.; Rosen, M., The Electronic Structure of Semiconductor Nanocrystals. *Annu. Rev. Mater. Sci.* **2000**, *30*, 475-521.
- (14) Madelung, O., *Semiconductors - Basic Data*. Springer-Verlag: 1996.
- (15) Elfurawi, U. Optical and Electronic Properties of PbS Colloidal Nanocrystals. 2012.
- (16) Szemjonov, A.; Pauporté, T.; Ciofini, I.; Labat, F., Investigation of the Bulk and Surface Properties of CdSe: Insights from Theory. *Phys. Chem. Chem. Phys.* **2014**, *16*, 23251-23259.
- (17) Scholes, G. D.; Rumbles, G., Excitons in Nanoscale Systems. In *Materials for Sustainable Energy*, Co-Published with Macmillan Publishers Ltd, UK: 2010; pp 12-25.
- (18) Yoffe, A. D., Low-Dimensional Systems: Quantum Size Effects and Electronic Properties of Semiconductor Microcrystallites (Zero-Dimensional Systems) and Some Quasi-Two-Dimensional Systems. *Adv. Phys.* **1993**, *42*, 173-262.
- (19) Schmidt, H. M.; Weller, H., Quantum Size Effects in Semiconductor Crystallites: Calculation of the Energy Spectrum for the Confined Exciton. *Chemical Physics Letters* **1986**, *129*, 615-618.
- (20) Machol, J. L.; Wise, F. W.; Patel, R. C.; Tanner, D. B., Vibronic Quantum Beats in PbS Microcrystallites. *Phys. Rev. B: Condens. Matter Mater. Phys* **1993**, *48*, 2819-2822.

- (21) Morrison, P. J.; Loomis, R. A.; Buhro, W. E., Synthesis and Growth Mechanism of Lead Sulfide Quantum Platelets in Lamellar Mesophase Templates. *Chem. Mater.* **2014**, *26*, 5012-5019.
- (22) Murray, C. B.; Norris, D. J.; Bawendi, M. G., Synthesis and Characterization of Nearly Monodisperse CdE (E = Sulfur, Selenium, Tellurium) Semiconductor Nanocrystallites. *J. Am. Chem. Soc.* **1993**, *115*, 8706-8715.
- (23) Prosperetti, A., *Advanced Mathematics for Applications*. 2011.
- (24) Weisstein, E. W. Spherical Bessel Function of the First Kind.
<http://mathworld.wolfram.com/SphericalBesselFunctionoftheFirstKind.html>.
- (25) Sun, J.; Buhro, W. E.; Wang, L.-W.; Schrier, J., Electronic Structure and Spectroscopy of Cadmium Telluride Quantum Wires. *Nano Lett.* **2008**, *8*, 2913-2919.
- (26) Hill, D. A., *Electromagnetic Fields in Cavities*. IEEE Press: 2009.
- (27) Ithurria, S.; Tessier, M. D.; Mahler, B.; S M Lobo, R. P.; Dubertret, B.; Efron, A. L., Colloidal Nanoplatelets with Two-Dimensional Electronic Structure. *Nat. Mater.* **2011**, *10*, 936-941.
- (28) Schliehe, C.; Juarez, B. H.; Pelletier, M.; Jander, S.; Greshnykh, D.; Nagel, M.; Meyer, A.; Foerster, S.; Kornowski, A.; Klinke, C.; Weller, H., Ultrathin PbS Sheets by Two-Dimensional Oriented Attachment. *Science* **2010**, *329*, 550.
- (29) Aerts, M.; Bielewicz, T.; Klinke, C.; Grozema, F. C.; Houtepen, A. J.; Schins, J. M.; Siebbeles, L. D. A., Highly Efficient Carrier Multiplication in PbS Nanosheets. *Nat. Commun.* **2014**, *5*, 3789.

- (30) Cho, W.; Kim, S.; Coropceanu, I.; Srivastava, V.; Diroll, B. T.; Hazarika, A.; Fedin, I.; Galli, G.; Schaller, R. D.; Talapin, D. V., Direct Synthesis of Six-Monolayer (1.9 nm) Thick Zinc-Blende CdSe Nanoplatelets Emitting at 585 nm. *Chem. Mater.* **2018**, *30*, 6957-6960.
- (31) Wang, F.; Wang, Y.; Liu, Y.-H.; Morrison, P. J.; Loomis, R. A.; Buhro, W. E., Two-Dimensional Semiconductor Nanocrystals: Properties, Templated Formation, and Magic-Size Nanocluster Intermediates. *Acc. Chem. Res.* **2015**, *48*, 13-21.
- (32) Kim, Y. D.; Klein, M. V.; Ren, S. F.; Chang, Y. C.; Luo, H.; Samarth, N.; Furdyna, J. K., Optical Properties of Zinc-Blende CdSe and $Zn_xCd_{1-x}Se$ Films Grown on GaAs. *Phys. Rev. B: Condens. Matter Mater. Phys* **1994**, *49*, 7262-7270.
- (33) Karel Čapek, R.; Moreels, I.; Lambert, K.; De Muynck, D.; Zhao, Q.; Van Tomme, A. A.; Vanhaecke, F.; Hens, Z., Optical Properties of Zincblende Cadmium Selenide Quantum Dots. *J. Phys. Chem. C* **2010**, *114*, 6371-6376.
- (34) Reiss, P.; Protière, M.; Li, L., Core/Shell Semiconductor Nanocrystals. *Small* **2009**, *5*, 154-168.
- (35) Piryatinski, A.; Ivanov, S. A.; Tretiak, S.; Klimov, V. I., Effect of Quantum and Dielectric Confinement on the Exciton-Exciton Interaction Energy in Type II Core/Shell Semiconductor Nanocrystals. *Nano Lett.* **2007**, *7*, 108-115.
- (36) Greytak, A. B.; Allen, P. M.; Liu, W.; Zhao, J.; Young, E. R.; Popović, Z.; Walker, B. J.; Nocera, D. G.; Bawendi, M. G., Alternating Layer Addition Approach to CdSe/CdS Core/Shell Quantum Dots with Near-Unity Quantum Yield and High On-Time Fractions. *Chemical Science* **2012**, *3*, 2028-2034.
- (37) Guk Jeong, B.; Park, Y.-S.; Hyuk Chang, J.; Cho, I.; Kyeong Kim, J.; Kim, H.; Char, K.; Cho, J.; Klimov, V. I.; Park, P.; Lee, D. C.; Ki Bae, W., Colloidal Spherical Quantum Wells with

Near-Unity Photoluminescence Quantum Yield and Suppressed Blinking. *ACS Nano* **2016**, *10*, 9297-9305.

(38) Ivanov, S. A.; Nanda, J.; Piryatinski, A.; Achermann, M.; Balet, L. P.; Bezel, I. V.; Anikeeva, P. O.; Tretiak, S.; Klimov, V. I., Light Amplification Using Inverted Core/Shell Nanocrystals: Towards Lasing in the Single-Exciton Regime. *J. Phys. Chem. B* **2004**, *108*, 10625-10630.

(39) Ithurria, S.; Talapin, D. V., Colloidal Atomic Layer Deposition (c-ALD) using Self-Limiting Reactions at Nanocrystal Surface Coupled to Phase Transfer Between Polar and Nonpolar Media. *J. Am. Chem. Soc.* **2012**, *134*, 18585-18590.

(40) Moreels, I.; Lambert, K.; Muynck, D. D.; Vanhaecke, F.; Poelman, D.; Martins, J. C.; Allan, G.; Hens, Z., Size-Dependent Optical Properties of Colloidal PbS Quantum Dots. *ACS Nano* **2009**, *3*, 3023-3030.

(41) Moreels, I.; Lambert, K.; De Muynck, D.; Vanhaecke, F.; Poelman, D.; Martins, J. C.; Allan, G.; Hens, Z., Composition and Size-Dependent Extinction Coefficient of Colloidal PbSe Quantum Dots. *Chem. Mater.* **2007**, *19*, 6101-6106.

(42) Salvador, M. R.; Graham, M. W.; Scholes, G. D., Exciton-Phonon Coupling and Disorder in the Excited States of CdSe Colloidal Quantum Dots. *J. Chem. Phys.* **2006**, *125*, 184709.

(43) Kim, S.; Fisher, B.; Eisler, H. J.; Bawendi, M., Type-II Quantum Dots: CdTe/CdSe(Core/Shell) and CdSe/ZnTe(Core/Shell) Heterostructures. *J. Am. Chem. Soc.* **2003**, *125*, 11466-11467.

(44) Ekimov, A. I.; Hache, F.; Schanne-Klein, M. C.; Ricard, D.; Flytzanis, C.; Kudryavtsev, I. A.; Yazeva, T. V.; Rodina, A. V.; Efros, A. L., Absorption and Intensity-Dependent

Photoluminescence Measurements on CdSe Quantum Dots: Assignment of the First Electronic Transitions. *J. Opt. Soc. Am. B* **1993**, *10*, 100-107.

(45) Shockley, W.; Queisser, H. J., Detailed Balance Limit of Efficiency of p-n Junction Solar Cells. *J. Appl. Phys.* **1961**, *32*, 510-519.

(46) Polman, A.; Atwater, H. A., Photonic Design Principles for Ultrahigh-Efficiency Photovoltaics. *Nat. Mater.* **2012**, *11*, 174-177.

(47) Beard, M. C.; Luther, J. M.; Semonin, O. E.; Nozik, A. J., Third Generation Photovoltaics Based on Multiple Exciton Generation in Quantum Confined Semiconductors. *Acc. Chem. Res.* **2013**, *46*, 1252-1260.

(48) Beard, M. C., Multiple Exciton Generation in Semiconductor Quantum Dots. *J. Phys. Chem. Lett.* **2011**, *2*, 1282-1288.

(49) Kovalenko, M. V.; Manna, L.; Cabot, A.; Hens, Z.; Talapin, D. V.; Kagan, C. R.; Klimov, V. I.; Rogach, A. L.; Reiss, P.; Milliron, D. J.; Guyot-Sionnest, P.; Konstantatos, G.; Parak, W. J.; Hyeon, T.; Korgel, B. A.; Murray, C. B.; Heiss, W., Prospects of Nanoscience with Nanocrystals. *ACS Nano* **2015**, *9*, 1012-1057.

(50) Zhang, J.; Chernomordik, B. D.; Crisp, R. W.; Kroupa, D. M.; Luther, J. M.; Miller, E. M.; Gao, J.; Beard, M. C., Preparation of Cd/Pb Chalcogenide Heterostructured Janus Particles via Controllable Cation Exchange. *ACS Nano* **2015**, *9*, 7151-7163.

(51) Smith, A. M.; Lane, L. A.; Nie, S., Mapping the Spatial Distribution of Charge Carriers in Quantum-Confined Heterostructures. *Nat. Commun.* **2014**, *5*, 4506.

(52) Cirloganu, C. M.; Padilha, L. A.; Lin, Q.; Makarov, N. S.; Velizhanin, K. A.; Luo, H.; Robel, I.; Pietryga, J. M.; Klimov, V. I., Enhanced Carrier Multiplication in Engineered Quasi-Type-II Quantum Dots. *Nat. Commun.* **2014**, *5*, 4148.

- (53) Granados del Águila, A.; Groeneveld, E.; Maan, J. C.; de Mello Donegá, C.; Christianen, P. C. M., Effect of Electron–Hole Overlap and Exchange Interaction on Exciton Radiative Lifetimes of CdTe/CdSe Heteronanocrystals. *ACS Nano* **2016**, *10*, 4102-4110.
- (54) Balet, L. P.; Ivanov, S. A.; Piryatinski, A.; Achermann, M.; Klimov, V. I., Inverted Core/Shell Nanocrystals Continuously Tunable between Type-I and Type-II Localization Regimes. *Nano Lett.* **2004**, *4*, 1485-1488.
- (55) Bradshaw, L. R.; Knowles, K. E.; McDowall, S.; Gamelin, D. R., Nanocrystals for Luminescent Solar Concentrators. *Nano Lett.* **2015**, *15*, 1315-1323.
- (56) Erickson, C. S.; Bradshaw, L. R.; McDowall, S.; Gilbertson, J. D.; Gamelin, D. R.; Patrick, D. L., Zero-Reabsorption Doped-Nanocrystal Luminescent Solar Concentrators. *ACS Nano* **2014**, *8*, 3461-3467.
- (57) Meinardi, F.; Colombo, A.; Velizhanin, K. A.; Simonutti, R.; Lorenzon, M.; Beverina, L.; Viswanatha, R.; Klimov, V. I.; Brovelli, S., Large-Area Luminescent Solar Concentrators Based on ‘Stokes-Shift-Engineered’ Nanocrystals in a Mass-Polymerized PMMA Matrix. *Nat. Photonics* **2014**, *8*, 392-399.
- (58) Coropceanu, I.; Bawendi, M. G., Core/shell Quantum Dot Based Luminescent Solar Concentrators with Reduced Reabsorption and Enhanced Efficiency. *Nano Lett.* **2014**, *14*, 4097-4101.

Chapter 2: Methods

Parts of this chapter were reproduced with permission from: Wieliczka, B. M.; Kaledin, A. L.; Buhro, W. E.; Loomis, R. A., Wave Function Engineering in CdSe/PbS Core/Shell Quantum Dots. *ACS Nano*. **2018**, *12*, 5539-5550. Copyright 2018 by the American Chemical Society.

2.1 Synthesis

2.1.1 Materials

The following chemicals were purchased from commercial sources and used without further purification: $\text{Pb}(\text{Ac})_2 \cdot 3\text{H}_2\text{O}$ (99.999%), oleic acid (90%, technical grade), octadecene (90% technical grade), methanol (99.9% HPLC grade), toluene (99.9% HPLC grade), thioacetamide (ACS reagent grade, 99%), octylamine (99%), chloroform (ACS reagent grade), $\text{Cd}(\text{NO}_3)_2 \cdot 4\text{H}_2\text{O}$ (98%), methanol (anhydrous), 40% tetrabutylammonium hydroxide in water, docosanoic acid (99%), sodium hydroxide (ACS reagent grade, $\geq 97.0\%$), myristic acid (99.5%), selenium dioxide ($\geq 99.9\%$, trace metals basis), 1,2-hexadecanediol (90%, technical grade), $\text{Cd}(\text{Ac})_2 \cdot 2\text{H}_2\text{O}$ (99.99%), Se (99.99%, trace metals basis), methylcyclohexane ($\geq 99\%$, anhydrous), Lead(II) oxide (99.999%), acetonitrile (99.5%), trifluoroacetic acid (99%), trifluoroacetic anhydride ($\geq 99\%$), triethylamine ($\geq 99\%$), isopropanol ($\geq 99.5\%$), CdCl_2 (99.99%, trace metals basis), ZnCl_2 (99.99%, trace metals basis), sodium oleate ($\geq 99\%$), nitric acid (concentrated, trace metals grade).

2.1.2 Preparation of Lead Oleate

Lead oleate was prepared using two previously published procedures.^{1,2} There was no discernable difference in the results using the differently prepared lead oleate.

Preparation from $\text{Pb}(\text{Ac})_2$ Lead Oleate ($\text{Pb}(\text{oleate})_2$) was prepared based on the synthesis published by Chang *et al.*¹ 1.138 g $\text{Pb}(\text{Ac})_2 \cdot 3\text{H}_2\text{O}$ (3 mmol) and 1.188 g oleic Acid (6.66 mmol)

were dissolved in 23.67 g octadecene (30 mL) to prepare a solution of 0.1 M Pb(oleate)₂. The solution was heated under vacuum at 100°C overnight with stirring, and formed a white solid. This 0.1 M solution was diluted with octylamine to form the 0.01 M Pb(oleate)₂ in octylamine solution that was used for the PbS shell precursor.

Preparation from Lead Trifluoroacetate Lead oleate was also prepared according to the method published by Hendricks *et. al.*² Lead (II) oxide (5.0 g, 22.4 mmol) and acetonitrile (10 mL) were loaded in a 100 mL round bottom flask. The mixture was chilled on an ice bath for about 10 minutes with stirring. Trifluoroacetic acid (0.35 mL, 4.57 mmol, 0.2 equiv.) and trifluoroacetic anhydride (3.1 mL, 22.0 mmol, 0.98 equiv.) were injected into the solution. On injection, the color was reduced immediately, and after 10 minutes the solution was clear and colorless. The solution was warmed to room temperature. To a 500 mL flask, oleic acid (12.7185 g, 45 mmol, 2.01 equiv.) triethylamine (5.123 g, 50.6 mmol, 2.26 equiv.), and isopropanol (90 mL) were added. The lead trifluoroacetate solution was added to the oleic acid solution (1 mL at a time), and a white solid was immediately formed. The flask was heated to reflux, which caused the dissolution of the solid. The solution was allowed to slowly cool to room temperature (≥ 2 hours) in the warm heating mantle used for refluxing before it was stored overnight in a -20 °C. As the solution cooled to room temperature, large quantities of white, fluffy solid formed. The solid was isolated from the solution by filtration over a 250 mL glass frit, and a spatula and mortar and pestle were used to break up the largest chunks. This solid was washed with 5-150 mL aliquots of methanol. The first two aliquots of methanol were used to transfer residual solid from the flask into the glass frit. The solid was then dried under vacuum for 6.25 hours. The yield was 13.240 g (78.1% yield, 16.943 g theoretical yield).

2.1.3 Preparation of Cd(myristate)₂

In a 100 mL Erlenmeyer flask, 1.5424 g Cd(NO₃)₂ · 4H₂O (5 mmol) were dissolved in 50 mL anhydrous methanol. In a 1 L Erlenmeyer flask, 599.97 mg NaOH (15 mmol) and 3.425 g myristic acid (15 mmol) were dissolved in 500 mL anhydrous methanol. The solution of cadmium nitrate was added dropwise to the myristate solution, 1 drop/sec, with very vigorous stirring, and a significant amount of white precipitate formed. The solid was collected by vacuum filtration, and the white solid was washed using cold anhydrous methanol. The white solid was dried overnight under vacuum at 60 °C.

2.1.4 Preparation of Cd(docosanoate)₂

1.5424 g Cd(NO₃)₂ · 4H₂O (5 mmol) were dissolved in 50 mL of anhydrous methanol. In a 5 mL volumetric flask, 3.2435 g tetrabutylammonium hydroxide solution (40% by wt. in water) were diluted to 5 mL in methanol to prepare a 1 M solution. 5.1087 g docosanoic acid (15 mmol) were dissolved in 500 mL anhydrous methanol. The solution of tetrabutylammonium hydroxide was added over the course of ~5 minutes to the solution of docosanoic acid. The solution of cadmium nitrate was added dropwise to the docosanoate solution, 1 drop/sec, with very vigorous stirring, and a significant amount of white precipitate formed. The solid was collected by vacuum filtration, and the white solid was washed using cold anhydrous methanol. The white solid was dried overnight under vacuum at 60 °C.

2.1.5 Synthesis of CdSe Core Quantum Dots (QDs)

The zinc blende CdSe core QDs were synthesized using the method of Cao *et al.*³ After synthesis, the QDs were washed three times by precipitation with methanol, centrifugation, and redispersion in toluene. After the third washing procedure, the QDs were resuspended in a quantitative amount of toluene.

Synthesis of 3 nm ZB CdSe Cores. 79.2 mg Cd(docosanoate)₂, 11.1 mg SeO₂, 25.8 mg 1,2-hexadecanediol, and 4.9707 g (6.3 mL) octadecene were loaded into a Schlenk flask. The flask was degassed by alternately reducing the pressure to 300 mtorr under vacuum and filling with nitrogen three times. The flask was heated to 240 °C in a heating mantle at a rate of 24 °C/minute under 300 RPM stirring. At 240 °C, the solution was very pale yellow. 0.1 mL oleic acid were delivered dropwise starting 4 minutes after the solution reached 240 °C (pale yellow solution), and the oleic acid addition was finished 5.5 minutes after reaching 240 °C (yellow-gold solution). The solution continued to change color to gold-orange, orange, and orange-red before it was removed from the heat 10 minutes after the solution reached 240 °C. The solution was then allowed to cool to room temperature.

Synthesis of 4 nm ZB CdSe Cores. 56.7 mg Cd(myristate)₂, 11.1 mg SeO₂, and 4.9707 g (6.3 mL) octadecene were loaded into a Schlenk flask. The flask was degassed by alternately reducing the pressure to 300 mtorr under vacuum and filling with nitrogen three times to atmospheric pressure. The flask was immersed in a salt bath at 256 °C (which corresponds to an internal temperature of the reaction solution of 240 °C) under 300 RPM stirring. The solution reached 240 °C in 6 minutes, and the color of the solution progressed from pale yellow to bright yellow, gold, orange, and red. 10 minutes after reaching 240 °C, when the reaction solution appeared red, 0.1 mL oleic acid were injected at a rate of 1 drop/10 sec. The reaction was allowed to proceed another 5 minutes during which time the solution turned much darker red, after which the reaction solution was removed and allowed to cool.

2.1.6 Synthesis of CdSe Core Nanoplatelets (NPLs)

170 mg Cd(myristate)₂ and 11.836 g ODE (15 mL) were loaded into a three-neck round bottom flask with a stir bar. The flask was connected to a Schlenk line by a side arm adapter

and a water-cooled condenser with mineral oil bubbler. A septum fitted with a thermocouple was used on the third neck of the flask for addition of reagents and monitoring the temperature. The mixture was degassed under vacuum at 100 °C with 200 RPM stirring for 30 minutes before 12 mg Se were added. Nitrogen was flowed from the Schlenk line through the flask and condenser and out through the bubbler. The temperature was increased at an average rate of 15 °C per minute to 240 °C. In a typical synthesis, at approximately 195 °C, the reaction solution began to change color from clear and colorless to very pale yellow. As the temperature continued to increase, the solution became increasingly intense yellow before becoming golden yellow, typically around 205-210 °C. At this time, 40 mg of freshly ground $\text{Cd}(\text{Ac})_2 \cdot 2\text{H}_2\text{O}$ were swiftly added, and the color changed to red. Once the reaction reached 240 °C, the temperature was held constant for 5 minutes. After 5 minutes at 240 °C, the reaction flask was removed from the heat and quenched to 150 °C in cold tap water. The product solution was cooled in air to 70 °C, at which point a solution of 2 mL oleic acid in 10 mL methylcyclohexane was added. The reaction was cooled to room temperature before purification.

The desired 4.5 ML CdSe NPLs were purified from 3.5 ML CdSe NPLs and CdSe QDs through centrifugation and filtration. First, the as-synthesized reaction solution was centrifuged at 4500 RPM for 10 minutes. The red-orange supernatant, rich in CdSe QDs, was decanted from the yellow solid (NPL enriched). This solid was redispersed in 5 mL methylcyclohexane and filtered through a 200 micron syringe filter before the absorption spectra was checked for product purity. In rare circumstances, this purification was sufficient to obtain a sample of pure 4.5 ML CdSe NPLs. More often, additional purification was required to remove 3.5 ML CdSe NPLs and CdSe QDs. The removal of 3.5 ML CdSe NPLs was accomplished by centrifuging the solution at 3000 RPM in 10-minute increments. This caused the 3.5 ML NPLs to come out of

solution as a solid and permitted the supernatant (containing the desired 4.5 ML NPLs) to be decanted. The removal of QDs was achieved through successive washing by precipitation, centrifugation, and redispersion. A single washing cycle consists of adding 1 mL methanol, centrifuging at 1500 RPM, decanting the supernatant (enriched in CdSe QDs), and redispersing the solid (enriched in CdSe NPLs) in 5 mL methylcyclohexane. After each cycle, the purity of the CdSe NPLs was checked using absorption and photoluminescence spectroscopy, and the washing process was continued until the spectra contained only features associated with the 4.5 ML NPLs without contributions of QDs or 3.5 ML NPLs.

2.1.7 Determination of Shell Precursor Quantities for Core/Shell QDs

The sizes and concentrations of the CdSe QDs suspended in the stock solutions were determined by optical spectroscopy.⁴ For each ML of PbS desired, the QDs were estimated to increase in radius by 0.343 nm, which is the distance between two layers of close packed sulfur atoms in the PbS cubic unit cell. The volumes of the shell were calculated assuming the core and core/shell QDs adopt a spherical morphology and the number of lead and sulfur atoms were calculated using the unit cell volume (209.16 \AA^3). The amounts of TAA and Pb(oleate)₂ were calculated with lead as the limiting reactant and a 130:1 TAA:Pb(Oleate)₂ ratio. See Table A1-1 (Appendix 1), for an example set of reagents for a series of core/shell QDs.

2.1.8 Synthesis of PbS Shells on CdSe QDs

The quantities used in this synthetic procedure are for the deposition of 3 ML PbS on 3 nm CdSe cores, but in general the desired amount of TAA and Pb(oleate)₂ is dependent on the total PbS desired. 200 μL of the stock solution of CdSe QDs in toluene were added to a vial. 15 mg TAA (amount dependent on desired shell thickness), octylamine (50 μL), and chloroform (2 mL) were added. The solution was sonicated for 5 minutes, or until all of the TAA dissolved,

sometimes taking as long as 8-10 minutes when larger amounts of TAA were used. After sonication, 20 μL of 0.01 M $\text{Pb}(\text{oleate})_2$ in octylamine solution were added every 5 minutes with vigorous stirring after each addition until 150 μL of 0.01 M $\text{Pb}(\text{oleate})_2$ were added. Over the course of adding the $\text{Pb}(\text{oleate})_2$, the solution changed from bright orange to a darker orange, and then to a brown solution, depending on the final thickness of the shell. In addition, a black precipitate was observed. The vial was then allowed to sit for 3 hours before isolating the product.

After three hours, the vial was centrifuged at 4500 RPM for 5 minutes to fully separate the black precipitate to the bottom of the vial. The colored supernatant was carefully decanted by pipette before the solvent was reduced to approximately one quarter of its original volume under a stream of dry nitrogen gas. The core/shell QDs were then precipitated by adding methanol and isolated by centrifuging at 1500 RPM for 5 minutes. The supernatant, which contains excess TAA, was decanted and discarded before the precipitated core/shell QDs were redispersed in toluene. This purified product was used for characterization.

2.1.9 Determination of Shell Precursor Quantities for Core/Shell NPLs

The average lateral size (LS) of the CdSe NPLs was determined from TEM images. The concentration of the CdSe NPL stock solution was determined by optical spectroscopy by measuring the absorbance of the solution and using the previously published molar extinction coefficient.⁵ For each ML of PbS desired, the size of the NPL was estimated to increase in each dimension by 0.343 nm, the distance between two layers of close packed sulfur atoms in the PbS cubic unit cell. The volume of the shell was calculated assuming the shell was deposited isotropically on all sides of the core NPL, and the number of lead and sulfur atoms were calculated using the unit cell volume (209.16 \AA^3). The amounts of TAA and $\text{Pb}(\text{oleate})_2$ were

calculated with lead as the limiting reactant and a 130:1 TAA:Pb(Oleate)₂ ratio. See Table A2-1 (Appendix 2), for example set of reagents for a series of core/shell QDs.

2.1.10 Synthesis of PbS Shells on CdSe NPLs

The quantities used in this synthetic procedure are for the deposition of 4 ML PbS on 31.5 nm × 8.3 nm 4.5 ML CdSe core NPLs, but in general the desired amount of TAA and Pb(oleate)₂ were dependent on the total thickness of the PbS desired. 200 μL of the stock solution of CdSe NPLs in methylcyclohexanes were added to a vial. 5.3 mg TAA (amount dependent on desired shell thickness), octylamine (100 μL), and chloroform (2 mL) were added. The solution was sonicated for 5 minutes, or until all of the TAA had dissolved, sometimes taking as long as 10-15 minutes when larger amounts of TAA were used. After sonication, 20 μL of 0.01 M Pb(oleate)₂ in octylamine solution were added every 5 minutes with vigorous stirring after each addition until 53 μL of 0.01 M Pb(oleate)₂ was added. Over the course of adding the Pb(oleate)₂, the solution changed from bright yellow to a darker orange, and then to a brown solution, depending on the final thickness of the shell. In addition, a black precipitate was observed. The vial was then allowed to sit for 3 hours before isolating the product.

After three hours, the vial was centrifuged at 4500 RPM for 5 minutes to fully separate the black precipitate to the bottom of the vial. The clear, colored supernatant was carefully decanted by pipette before the solvent was reduced to approximately one quarter of its original volume under a stream of dry nitrogen gas. The core/shell NPLs were then precipitated by adding methanol and isolated by centrifuging at 1500 RPM for 5 minutes. The supernatant, which contains excess TAA, was decanted and discarded before the precipitated core/shell QDs were redispersed in toluene. This purified product was used for characterization.

2.1.11 CdSe NPL Etching Experiments

A series of precursor solutions were prepared: 0.01 M sodium oleate in methanol, 0.01 M oleic acid in toluene, 0.01 M lead oleate in *n*-octylamine, and 0.1 M lead oleate in octadecene. 30 μ L aliquots of CdSe NPLs in methylcyclohexane were added to each of seven vials with 2 mL toluene. The CdSe NPLs in the first control vial were not treated with any chemical or physical process other than dilution and subsequent isolation. The CdSe NPLs in the other vials were treated with one of the following: 100 μ L of the 0.01 M sodium oleate in methanol, 100 μ L 0.01 M oleic acid in toluene, 100 μ L 0.01 M lead oleate in *n*-octylamine, 100 μ L *n*-octylamine or 10 μ L 0.1 M lead oleate in octadecene, or 10 minutes of sonication. After 3 hours, the nanoparticles were isolated from the solution. 1 mL methanol was added to each vial, and the nanoparticles were isolated by centrifuging at 4500 RPM for 5 minutes. The product was redispersed in approximately 0.5 mL toluene.

2.2 Optical Spectroscopy

2.2.1 Absorption Spectroscopy

Samples for optical characterization were prepared by taking a small amount of the reaction product in solution and diluting it in toluene. Extinction spectra were recorded using a commercial spectrometer with an integration sphere to minimize scattering. The energies of the absorption features in the spectra were identified by taking the second derivative of each extinction spectrum.

Calibration check of absorption spectrometer. Before data were collected on the absorption spectrometer, a holmium oxide standard was used to verify the wavelength calibration.

Correction of extinction spectra for scattering. Extinction spectra were collected using a forward-facing integration sphere, but some scattering of light was still present in the spectra. To correct for this scattering, the low-energy region of each extinction spectrum, below the QD or NPL band edge, was fitted to the equation $A = m\lambda^{-4} + b$, where λ is the wavelength. This correction was applied to all extinction spectra except for the CdSe/PbS core/shell QD sample with 8.1ML PbS on 3nm CdSe core and the sample with 7.3ML PbS on 4nm CdSe core.

2.2.2 Photoluminescence Spectroscopy

PL spectra were collected using a commercial fluorimeter using a xenon arc lamp for excitation and a PMT or a CCD for emission collection. For PLQY measurements, the sample was placed in the center of an integration sphere, allowing the collection of all light, including scattering and emission. The intensity of the first absorption peak was kept between 0.05 and 0.1 absorbance units for optimal signal and to prevent reabsorption of emitted light. The intensity profiles of the emission spectra were corrected using an instrument response function created using standard reference materials.⁶⁻¹⁰

Calibration of fluorimeter. The abbreviated procedure for wavelength and instrument calibration and creation of instrument response function is as follows. The emission monochromators were calibrated for wavelength using a mercury pen lamp. The excitation monochromator was then calibrated using scattered light measured by the calibrated emission monochromator. Once all emission and excitation monochromators were calibrated based fundamentally on the narrow mercury pen lamp emission lines, emission spectra of the SRMs were collected and used to create an instrument response function over the full spectral range (320-830 nm) using previously published procedures.⁶⁻¹⁰

2.2.3 Time-Resolved Photoluminescence Spectroscopy

PL lifetimes were collected using the doubled output of a Ti:Sapphire laser (200 fs pulse duration) for excitation at 450 nm (2.755 eV) and a time-correlated single-photon photomultiplier tube detector and electronics. A monochromator was used to collect the light emitted at the sample's peak emission energy. The fluence of the excitation was $1.55 \text{ nJ cm}^{-2} \text{ pulse}^{-1}$. Using the reported absorption cross section of $1.2 \times 10^{-13} \text{ cm}^{-2}$ to $8.0 \times 10^{-14} \text{ cm}^{-2}$ for CdSe NPLs with a lateral size of 230 nm^2 , the expected number of excitons per pulse per NPL was estimated to be 2.81×10^{-4} to 4.21×10^{-4} , respectively. In order to ensure that multiexcitons were not generated with the same pulse, the repetition rate of the excitation laser was varied between 1.61×10^5 and 8.06×10^4 pulses per second, and the highest repetition rate that gave the same PL decay trace was used in order to minimize the collection of stray light.

Each PL intensity decay profile was fitted to a multiexponential curve. No wrap-around was observed in the PL intensity decay data, but some noise (for example, counts from stray light sources) was observed. This noise was subtracted with a baseline offset equal to the average number of counts before the excitation pulse arrived. The average PL lifetime was calculated using Equation 2.1 where A_n is the amplitude of each exponential decay component and τ_n is the lifetime of that component. The percent contribution f_i of each lifetime component to the total PL counts was then calculated using Equation 2.2.

$$\tau_{ave} = \frac{\sum_n A_n \tau_n^2}{\sum_n A_n \tau_n} \quad \text{Eq. 2.1}$$

$$f_i = \frac{A_i \tau_i}{\sum_n A_n \tau_n} * 100\% \quad \text{Eq. 2.2}$$

2.3 Physical Characterization

2.3.1 Transmission Electron Microscopy

Samples for TEM analysis were washed a total of two times by precipitation with methanol, centrifugation at 4500 RPM for 5 minutes, and redispersion in toluene before a TEM grid with carbon film was dipped in the lightly colored solution. TEM images were collected on commercial instruments operating at 200 keV in the Institute of Materials Science & Engineering at Washington University in St. Louis.

2.3.2 X-Ray Diffraction

Samples for TEM analysis were washed a total of two times by precipitation with methanol, centrifugation at 4500 RPM for 5 minutes, and redispersion in toluene. Powder x-ray diffraction patterns were collected on a commercial instrument in the Department of Earth and Planetary Sciences at Washington University in St. Louis using Cu K_α radiation (1.5418 Å) and a low background silicon holder. The samples were drop cast from a concentrated solution of the purified CdSe/PbS QDs onto a silicon low background holder, and the solvent was allowed to evaporate.

2.3.3 Inductively Coupled Plasma Mass Spectrometry

Nanocrystal samples for ICP-MS elemental analysis were prepared by washing a total of two times by precipitation with methanol, centrifugation at 4500 RPM for 5 minutes, and redispersion in toluene. On the final washing cycle, the particles were not resuspended and instead were dried under vacuum. For samples that were already washed twice and redispersed, the solvent was reduced under vacuum.

The samples were then digested in acid using a microwave digester. First, the microwave vessels were cleaned by adding 2 mL nitric acid to each vessel. The vessels were then heated in

the microwave to 180 °C over the course of 20 minutes, held at 180 °C for 20 minutes, and allowed to cool to room temperature over 20 minutes. The nitric acid was poured out and the vessels were thoroughly rinsed with Millipore water. Each sample was dissolved in 1 mL nitric acid and transferred to a clean microwave vessel. The same digestion program was run (20 minute ramp to 180 °C, 20 minute hold at 180 °C, and 20 minute cooling to room temperature), and the sample was diluted in 5% nitric acid in Millipore water to a concentration range of approximately 1-200 ppb. This dilution factor varied depending on the sample but was commonly achieved by diluting the digested nitric acid by a factor of 100.

The ICP-MS data were collected using a commercial spectrometer in the Nano Research Facility in the Department of Energy, Environmental & Chemical Engineering at Washington University in St. Louis using 3 replicates for each sample or standard measured. A blank consisting of the same 5% nitric acid solution used for sample preparation was collected at least after every 4 samples to ensure appropriate background subtraction. The instrument response was calibrated using a series of standards made at 1, 10, 100, and 200 ppb concentrations in the relevant metal ions.

2.4 Effective Mass Approximation Calculations

2.4.1 Calculation Parameters

Effective mass approximation calculations simulating a spherical core/shell heterostructure were performed using bulk conduction band (CB) and valence band (VB) potentials of -3.865 eV and -5.541 eV in the CdSe core and -4.35 eV and -4.72 eV in the PbS shell, respectively.^{11,12} The effective masses utilized in the calculations are $m_e^*(\text{CdSe}) = 0.12m_e$, $m_e^*(\text{PbS}) = 0.105m_e$, $m_{hh}^*(\text{CdSe}) = 2.14m_e$, and $m_h^*(\text{PbS}) = 0.108m_e$.¹³⁻¹⁵ The spin-orbit splitting was 420 meV.¹⁶

2.4.2 Wave Function Calculations for Spherical CdSe/PbS Core/Shell QDs

Calculations using the method described by Haus *et al.*^{17,18} were performed in Maple 2017 using an infinite wall at the overall surface of the QDs and Coulombic interactions were calculated using dielectric constants of 10.2 and 17.2 in CdSe and PbS, respectively.^{14,19}

Calculations using the method described by Kaledin *et al.*²⁰ were performed using a soft wall at the overall surface of the QDs, using the ionization potential of octylamine (−8.5 eV) to approximate the energy of the highest occupied molecular orbital while the energy of the lowest unoccupied molecular orbital was approximated to be 0 eV.²¹ The bare electron mass was used as the effective mass of the electron and hole outside the QD. Coulombic interactions were calculated using dielectric constants of 10.2, 17.2, and 2.4 in CdSe, PbS, and toluene (the surrounding solvent), respectively.^{14,19,22} Calculations using this method were solved using Fortran.

Calculations using the method by Poulsen *et al.*²³ were performed in Maple 2017 using a soft wall at the edge of the QDs and the ionization potential of octylamine (−8.5 eV) to approximate the energy of the highest occupied molecular orbital while the energy of the lowest unoccupied molecular orbital was approximated to be 0 eV.²¹ The bare electron mass was used as the effective mass of the electron and hole outside the QD. Coulombic interactions were not incorporated in this model.

2.4.3 Wave Function Calculations for Core/Shell NPLs

Calculations for modeling a core/shell NPL were based on a one-dimensional double-well particle in a box model with infinite potentials at the boundaries of the box. The wave functions for the first shell region (the first well), the core region, and the second shell region (the second well) were Equations 2.3, 2.4, and 2.5, respectively, where d_{tot} is the total thickness of the core/shell NPL.

$$\Psi_s(x) = A * \sin(k_s x) \quad \text{Eq. 2.3}$$

$$\Psi_c(x) = B * \cosh(k_c(x - \frac{d_{tot}}{2})) \quad \text{Eq. 2.4}$$

$$\Psi_s(x) = B * \sin(k_s(d_{tot} - x)) \quad \text{Eq. 2.5}$$

The coefficients A and B were solved using the transcendental equation obtained from the boundary conditions. The values of the solved wave functions must be equal at each interface, Equations 2.6 and 2.7. The slopes of the wave functions divided by the effective mass (m^*) in each region must also be equal to each other at each interface, Equations 2.8 and 2.9. The solvable transcendental equations at each interface were found by dividing Equation 2.6 by Equation 2.8 (for the first interface) and dividing Equation 2.7 by Equation 2.9 (for the second interface).

$$\Psi_c(x_{int,1}) = \Psi_s(x_{int,1}) \quad \text{Eq. 2.6}$$

$$\Psi_c(x_{int,2}) = \Psi_s(x_{int,2}) \quad \text{Eq. 2.7}$$

$$\frac{1}{m_c^*} \frac{d\Psi_c(x_{int,1})}{dx} = \frac{1}{m_s^*} \frac{d\Psi_s(x_{int,1})}{dx} \quad \text{Eq. 2.8}$$

$$\frac{1}{m_c^*} \frac{d\Psi_c(x_{int,2})}{dx} = \frac{1}{m_s^*} \frac{d\Psi_s(x_{int,2})}{dx} \quad \text{Eq. 2.9}$$

The Maple 2017 code used to solve the 1D double-well particle in a box model is included in Appendix 4.

2.5 References

- (1) Chang, L.-Y.; Lunt, R. R.; Brown, P. R.; Bulović, V.; Bawendi, M. G., Low-Temperature Solution-Processed Solar Cells Based on PbS Colloidal Quantum Dot/CdS Heterojunctions. *Nano Lett.* **2013**, *13*, 994-999.
- (2) Hendricks, M. P.; Campos, M. P.; Cleveland, G. T.; Jen-La Plante, I.; Owen, J. S., A Tunable Library of Substituted Thiourea Precursors to Metal Sulfide Nanocrystals. *Science* **2015**, *348*, 1226.
- (3) Chen, O.; Chen, X.; Yang, Y.; Lynch, J.; Wu, H.; Zhuang, J.; Cao, Y. C., Synthesis of Metal-Selenide Nanocrystals Using Selenium Dioxide as the Selenium Precursor. *Angew. Chem. Int. Ed.* **2008**, *47*, 8638-8641.
- (4) Karel Čapek, R.; Moreels, I.; Lambert, K.; De Muynck, D.; Zhao, Q.; Van Tomme, A. A.; Vanhaecke, F.; Hens, Z., Optical Properties of Zincblende Cadmium Selenide Quantum Dots. *J. Phys. Chem. C* **2010**, *114*, 6371-6376.
- (5) Yeltik, A.; Delikanli, S.; Olutas, M.; Kelestemur, Y.; Guzelturk, B.; Demir, H. V., Experimental Determination of the Absorption Cross-Section and Molar Extinction Coefficient of Colloidal CdSe Nanoplatelets. *J. Phys. Chem. C* **2015**, *119*, 26768-26775.
- (6) DeRose, P. C.; Smith, M. V.; Anderson, J. R.; Kramer, G. W., Characterization of Standard Reference Material 2944, Bi-Ion-Doped Glass, Spectral Correction Standard for Red Fluorescence. *J. Lumin.* **2013**, *141*, 9-14.
- (7) DeRose, P. C.; Smith, M. V.; Mielenz, K. D.; Anderson, J. R.; Kramer, G. W., Characterization of Standard Reference Material 2943, Cu-Ion-Doped Glass, Spectral Correction Standard for Blue Fluorescence. *J. Lumin.* **2011**, *131*, 2509-2514.

- (8) DeRose, P. C.; Smith, M. V.; Mielenz, K. D.; Anderson, J. R.; Kramer, G. W.,
Characterization of Standard Reference Material 2942, Ce-Ion-Doped Glass, Spectral Correction
Standard for UV Fluorescence. *J. Lumin.* **2011**, *131*, 1294-1299.
- (9) DeRose, P. C.; Smith, M. V.; Mielenz, K. D.; Blackburn, D. H.; Kramer, G. W.,
Characterization of Standard Reference Material 2940, Mn-Ion-Doped Glass, Spectral
Correction Standard for Fluorescence. *J. Lumin.* **2009**, *129*, 349-355.
- (10) DeRose, P. C.; Smith, M. V.; Mielenz, K. D.; Blackburn, D. H.; Kramer, G. W.,
Characterization of Standard Reference Material 2941, Uranyl-Ion-Doped Glass, Spectral
Correction Standard for Fluorescence. *J. Lumin.* **2008**, *128*, 257-266.
- (11) Reiss, P.; Couderc, E.; De Girolamo, J.; Pron, A., Conjugated Polymers/Semiconductor
Nanocrystals Hybrid Materials—Preparation, Electrical Transport Properties and Applications.
Nanoscale **2011**, *3*, 446-489.
- (12) Li, J.; Wang, Shape Effects on Electronic States of Nanocrystals. *Nano Lett.* **2003**, *3*, 1357-
1363.
- (13) Cadmium Selenide (CdSe) Electronic Properties, Cubic Modification. In *Landolt-Börnstein
- Group III Condensed Matter 41B (II-VI and I-VII Compounds; Semimagnetic Compounds)*,
Madelung, O.; Rössler, U.; Schulz, M., Eds. Springer-Verlag: Berlin/Heidelberg, 1999; pp 1-6.
- (14) Springholz, G.; Bauer, G., 9.1 IV-VI Semiconductors: General Properties. In *Landolt-
Börnstein - Group III Condensed Matter 34A*, Springer-Verlag Berlin Heidelberg: Berlin,
Heidelberg, 2013; Vol. 16, pp 415-421.
- (15) Kim, Y. D.; Klein, M. V.; Ren, S. F.; Chang, Y. C.; Luo, H.; Samarth, N.; Furdyna, J. K.,
Optical Properties of Zinc-Blende CdSe and $Zn_xCd_{1-x}Se$ Films Grown on GaAs. *Phys. Rev. B:
Condens. Matter Mater. Phys* **1994**, *49*, 7262-7270.

- (16) Naeem, A.; Masia, F.; Christodoulou, S.; Moreels, I.; Borri, P.; Langbein, W., Giant Exciton Oscillator Strength and Radiatively Limited Dephasing in Two-Dimensional Platelets. *Phys. Rev. B: Condens. Matter Mater. Phys* **2015**, *91*, 121302.
- (17) Haus, J. W.; Zhou, H. S.; Honma, I.; Komiyama, H., Quantum Confinement in Semiconductor Heterostructure Nanometer-Size Particles. *Phys. Rev. B: Condens. Matter Mater. Phys* **1993**, *47*, 1359-1365.
- (18) Vlaskin, V. A.; Beaulac, R.; Gamelin, D. R., Dopant—Carrier Magnetic Exchange Coupling in Colloidal Inverted Core/Shell Semiconductor Nanocrystals. *Nano Lett.* **2009**, *9*, 4376-4382.
- (19) Madelung, O., *Semiconductors - Basic Data*. Springer-Verlag: 1996.
- (20) Kaledin, A. L.; Lian, T.; Hill, C. L.; Musaev, D. G., An Infinite Order Discrete Variable Representation of an Effective Mass Hamiltonian: Application to Exciton Wave Functions in Quantum Confined Nanostructures. *J. Chem. Theory Comput.* **2014**, *10*, 3409-3416.
- (21) Aue, D. H.; Bowers, M. T., In *Gas-Phase Ion Chemistry*, Bowers, M. T., Ed. Academic Press: 1979.
- (22) Boles, M. A.; Ling, D.; Hyeon, T.; Talapin, D. V., The Surface Science of Nanocrystals. *Nat. Mater.* **2016**, *15*, 141-153.
- (23) Poulsen, F.; Hansen, T., Band Gap Energy of Gradient Core—Shell Quantum Dots. *J. Phys. Chem. C* **2017**, *121*, 13655-13659.

Chapter 3: Wave Function Engineering in CdSe/PbS Core/Shell Quantum Dots

Reproduced with permission from: Wieliczka, B. M.; Kaledin, A. L.; Buhro, W. E.; Loomis, R. A., Wave Function Engineering in CdSe/PbS Core/Shell Quantum Dots. *ACS Nano*. **2018**, *12*, 5539-5550. Copyright 2018 by the American Chemical Society.

3.1 Introduction

In the efforts we report here, we have focused on synthesizing and characterizing CdSe/PbS core/shell QDs that have an inverse type-I heterostructure based on bulk band energies.^{1,2} As such, the CdSe/PbS QDs could be capable of MEG, could behave as an LSC, and could permit the efficient separation and extraction of photogenerated charge carriers. The efficiencies of these dynamics will depend on the relative energies of the conduction and valence band states as dictated by both the diameter of the core and thickness of the shell. With small dimensions of the core and shell, the effective masses of the charge carriers in the different regimes of the heterostructure will also impact the properties of the wave functions and the energetics of the states. The effective masses of the electrons in CdSe, $m_e^*(\text{CdSe}) = 0.12m_e$, and PbS, $m_e^*(\text{PbS}) = 0.105m_e$, are quite similar, but there is a notable difference in the effective masses of the holes in CdSe, $m_{hh}^*(\text{CdSe}) = 2.14m_e$ for the heavy hole, and PbS, $m_h^*(\text{PbS}) = 0.108m_e$.³⁻⁵ The large difference between $m_{hh}^*(\text{CdSe})$ and $m_h^*(\text{PbS})$ could likely lead to significant changes in the energies and spatial regions spanned by the wave functions of the quantum-confined states in the valence band of the CdSe/PbS QDs as the diameter of the CdSe core and the thickness of the PbS shell is varied.

We synthesized CdSe/PbS core/shell QDs with two different CdSe core diameters, 3.0 and 4.2 nm, referred to as 3 and 4 nm, and varying shell thicknesses to study the effects of the degree of quantum confinement on the energetics of the charge-carrier states and the spatial

regions sampled by the electron and hole wave functions. These properties were probed for each sample by recording traditional extinction and photoluminescence (PL) spectra of ensembles of the QDs suspended in solution. The spectra indicate the CdSe/PbS QDs with PbS shell thicknesses of several monolayers or more have promise for LSC applications. The interpretation of the spectral data is bolstered using three different models to estimate the properties of the lowest-energy quantum-confined electron and hole wave functions for the CdSe/PbS QDs with different shell thicknesses.

3.2 Results and Discussion

3.2.1 Synthesis

Numerous PbE/CdE (E = S, Se, Te) heterostructures have been previously synthesized through cation exchange resulting in PbE/CdE core/shell QDs,^{6,7} PbSe/CdSe axially heterostructured nanorods,⁸ and CdE/PbE Janus particles – particles where one half of the QD is CdE with the other half PbE made through cation exchange with additive growth.⁹ Since Cd-for-Pb cation exchange complicates the additive growth of a Pb chalcogenide shell at elevated temperatures,^{8,9} we chose to base our CdSe/PbS core/shell QD syntheses on a previously reported room-temperature shell synthesis. Due to the rock salt (RS) crystal structure of PbS, the synthesis was attempted using zinc blende (ZB) CdSe core QDs to minimize the strain and lattice mismatch at the core/shell interface; the RS and ZB structures share a similarly structured chalcogenide sublattice, and the lattice constant of ZB CdSe is 6.050 Å, while the lattice constant of RS PbS is 5.936 Å, only a 1.9% difference.¹⁰ The CdSe core QDs having diameters of 3 and 4 nm were synthesized using the method of Cao *et al.*¹¹ (details provided in Chapter 2.1).

The PbS shell-growth scheme used here is a derivative of the room-temperature method reported by Mahler *et al.* for making CdSe/CdS core/shell nanoplatelets.¹² In adapting this

synthesis for the formation of PbS on CdSe QDs, thioacetamide (TAA) and lead oleate ($\text{Pb}(\text{oleate})_2$) were used as the PbS shell precursors. The approximate increase in volume of the final core/shell QDs was used to calculate the number of unit cells, and therefore the number of sulfur and lead atoms, required for each shell thickness (Table A1-1 in Appendix 1). The $\text{Pb}(\text{oleate})_2$ was the limiting reagent, and the TAA was used in large excess. When the TAA was not in excess, very large PbS crystals nucleated. Black precipitate formed immediately after the lead precursor was added, and we found this to be an aggregate of CdSe QDs overcoated by a matrix of PbS (Figure 3-1). A yellow, clear solution of core/shell CdSe/PbS QDs was isolated from the black precipitate by centrifugation. By slowly adding the $\text{Pb}(\text{oleate})_2$, 20 μL every 5 min, the amount of PbS precipitate was reduced or virtually eliminated in the synthesis of the thinnest PbS shells. Ultimately, the shell-growth synthesis was conducted using varied quantities of shell precursors to control the final thickness up to a maximum of ~ 8 monolayers (ML).

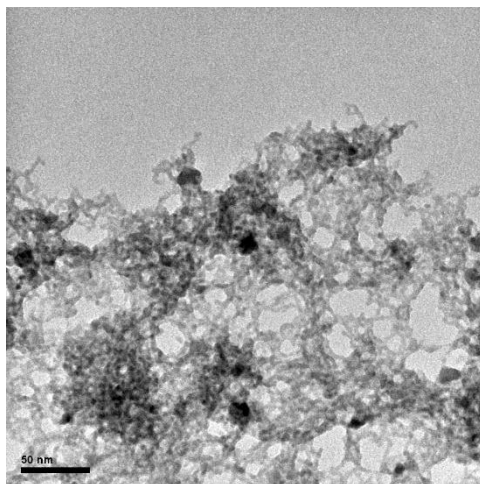


Figure 3-1. Representative TEM image of aggregation of CdSe QDs with overgrown PbS.

After treatment with lead and sulfur precursors, the particles adopt a core/shell structure under these synthetic conditions, in contrast to previous syntheses of CdSe/PbS heterostructures, which have resulted in anisotropic Janus particles or cation exchange.⁶⁻⁹ A representative series

of CdSe core, 3 nm diameter, and CdSe/PbS core/shell QDs are shown in Figure 3-2 with the number of monolayers indicated on the top right of each image. The relationship between the amount of shell precursors used and the resulting shell thicknesses was verified by measuring the diameters of the CdSe/PbS core/shell QDs observed in TEM images. Consistent with a RS

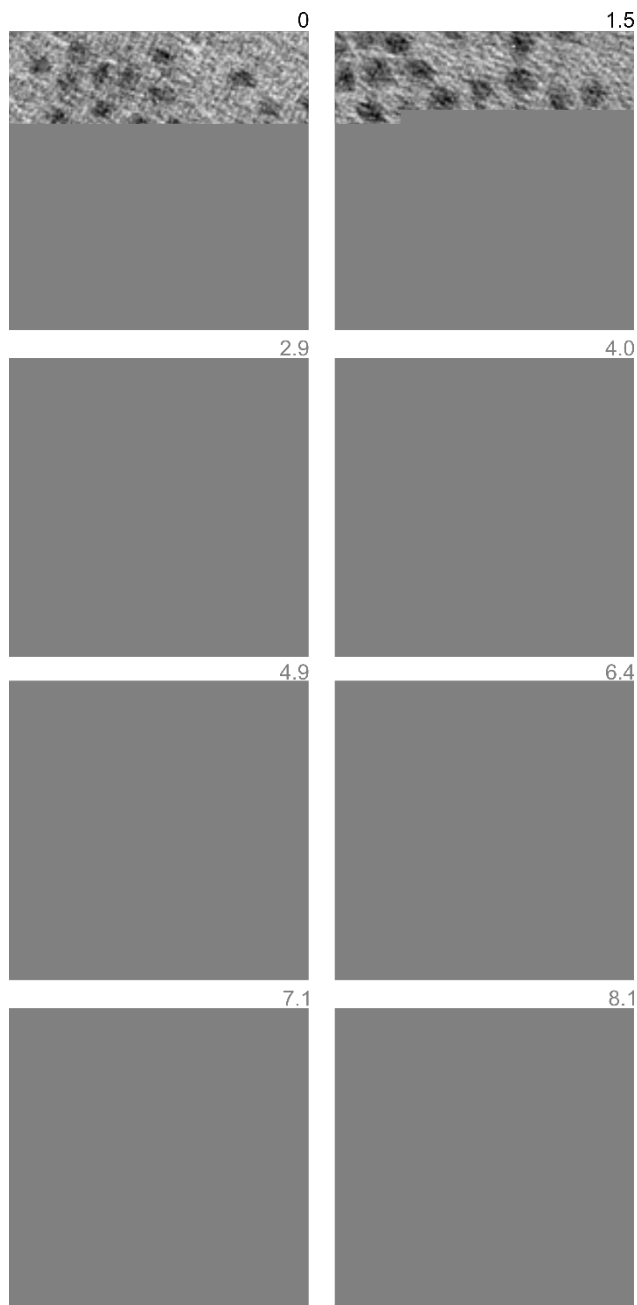


Figure 3-2. Representative TEM images of CdSe/PbS core/shell QDs with 3 nm cores labeled with the number of PbS monolayers. Each image is 50 nm × 50 nm.

crystal shell structure, the particles became increasingly cubic as the shell thickness increased. Similar TEM images of the QDs synthesized using the 4 nm diameter cores are included in Figure 3-3. The size dispersions as a percentage of the average diameter remain the same with increasing size, 9.5-13%, for both the 3 nm and 4 nm core samples (see Figure A1-1 and Table A1-2 in Appendix 1).

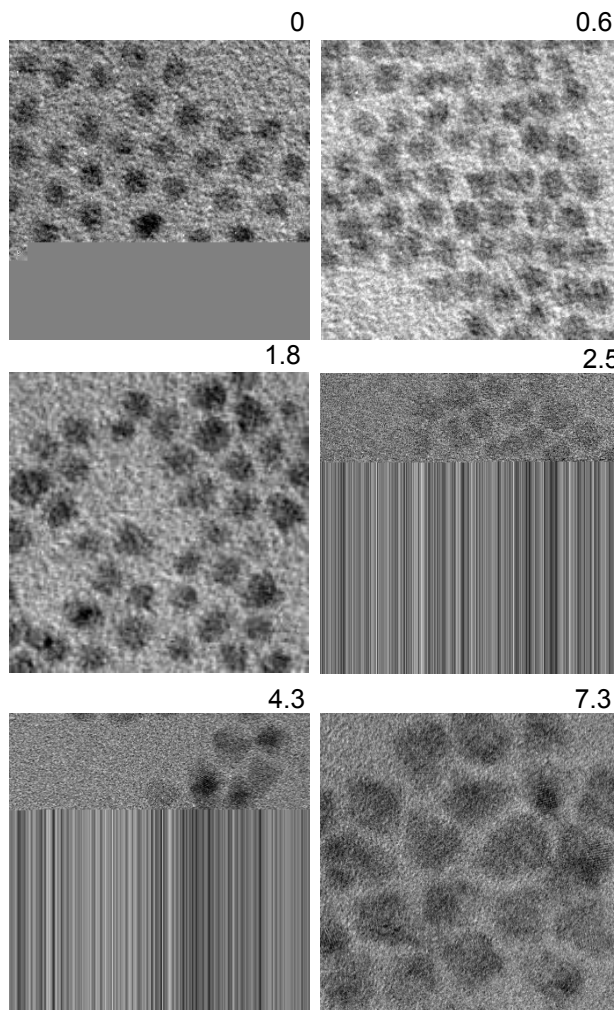


Figure 3-3. Representative TEM images of CdSe core and CdSe/PbS core/shell QDs with 4 nm cores labeled with the number of PbS monolayers. Each image is 50 nm × 50 nm.

The core/shell structure of these CdSe/PbS QDs is not always noticeable in the TEM images since the QDs are randomly oriented on the TEM grid. We collected multiple TEM images as a function of tilting angle to bring the crystal lattice of some of the QDs into better

alignment to strongly diffract electrons and verify the core/shell structure of the QDs. At particular angles, the crystal lattice of the CdSe core, strongly diffracts the electron beam while the PbS shell does not diffract as strongly, allowing a contrast between the core and shell to be observed in the TEM images. With increasing shell thickness, the contrast between the CdSe core and PbS shell materials becomes increasingly pronounced as illustrated in Figure 3-4, which contains TEM images of QDs with 8.3 ML (2.85 nm) thick PbS shells grown on the 3 nm CdSe cores. The images indicate these CdSe/PbS QDs are core/shell structures and the PbS does not grow anisotropically on the CdSe QDs, as would be observed for Janus particles or dot-in-rod structures. Direct Cd-to-Pb cation exchange previously relied on high temperatures and preferential hard soft acid base theory to explain why cation exchange occurs in certain circumstances.⁸ Notably, despite the presence of both hard and soft bases in this synthesis (octylamine and oleate), the reaction results in shell growth rather than cation exchange, which we hypothesize is a result of the room-temperature synthesis. To test this hypothesis, the core CdSe QDs were treated with octylamine and Pb(oleate)₂ without TAA. Neither the morphology

Figure 3-4. TEM images of CdSe/PbS 8.3 ML core/shell QDs (3 nm core and overall diameter = 8.5 nm) without tilting (top row) and with 10° tilting (bottom row), revealing the contrast between the CdSe cores and PbS shells. Each image is 20 nm × 20 nm.

nor the spectral features of the QDs changed, indicating that the Cd-to-Pb cation exchange does not occur under these conditions.

We found the adopted approach for synthesizing CdSe/PbS core/shell QDs is limited in the range of shell thicknesses that can be grown on the CdSe cores. While the resulting shell thickness is closely related to the quantities of precursors added for synthesizing thin PbS shells, 1-4 ML, the final PbS shell thickness is less reliable for syntheses attempting to grow more than 4 ML. Attempts at growing shells thicker than 4 ML resulted in a significant amount of the aggregated CdSe/PbS product, which likely complicates the ratio of CdSe QDs to PbS shell precursors. Several other methods to synthesize CdSe/PbS core/shell QDs were attempted, including the use of different lead and sulfur precursors, different ratios of lead and sulfur precursors, and using CdSe wurtzite (WZ) core QDs. These efforts were unsuccessful and the precipitation of black CdSe/PbS aggregates was typically observed (see Table A1-3 in Appendix 1 for details).

3.2.2 Crystal Structure

The powder XRD patterns of the different samples of the CdSe/PbS core/shell QDs were compared to identify the crystal structures of the cores and shells. The XRD spectra of the QDs made with 4 nm diameter CdSe cores are included in Figure 3-5. The gray (bottom) and magenta (top) XRD patterns are the simulated spectra for ZB CdSe and RS PbS structures, respectively. The 111 reflection at $2\theta = 25.4^\circ$ is the most intense peak in the ZB CdSe structure, while the most intense peak of the RS PbS structure is the 200 reflection at $2\theta = 30.1^\circ$. The 200 reflection is systematically absent in the ZB pattern, making it an excellent indicator of the crystal structure of the PbS shell. Both ZB and RS patterns exhibit moderate 220 and 311 reflections, but are at slightly different angles due to the differing CdSe and PbS lattice parameters.

Figure 3-5. XRD spectra of CdSe/PbS QDs (4 nm CdSe cores) and varying shell thicknesses (labeled on the right in #ML). Simulated stick patterns for bulk CdSe ZB and PbS RS structures are included at the bottom and top, respectively.

The CdSe core QDs were confirmed to be ZB – 0 ML pattern (black). If the PbS shell adopted the underlying ZB structure, it would exhibit a pattern similar to the CdSe core, but slightly shifted to higher 2θ values due to the smaller lattice parameter of PbS. Immediately after adding a PbS shell, the 200 reflection ($2\theta = 30.1^\circ$) is present at relatively low intensity in the XRD pattern for 0.6 ML CdSe/PbS QDs (red). It is possible that the PbS adopts a ZB structure and the 200 reflection is only present due to a break in symmetry at the core/shell interface. In this scenario, the 200 diffraction peak would remain very weak relative to the other diffraction peaks, since it would only result from reflections at the interface. Instead, the intensity of the 200 reflection increased relative to the other peaks in the XRD spectra recorded for the thicker shells, and we concluded that the PbS shell adopted the RS crystal structure. As the PbS shell became the dominant component in the core/shell QDs based on volume, the ratios of the peak intensities approached the PbS RS simulated pattern. In the XRD pattern for the thickest shell, the QD was

approximately 89% PbS by volume, and the 111 and 200 peaks were nearly equal in intensity. The 220 and 311 XRD peaks shifted to slightly higher angles with the addition of the shell. This suggests the lattice constant of the CdSe/PbS QDs was intermediate between the CdSe ZB and the PbS RS values for thin shells. The 220 and 311 peaks only reached the PbS RS 2θ angles at the thickest shell, 7.3 ML, at which point we presume the XRD signal was dominated by the large volume of the PbS RS shell.

In principle, the CdSe ZB cores could change to a RS structure during shell growth, but this conversion occurs under very high pressures, between 6.6 and 7.1 GPa.¹³ In contrast, the CdSe QDs experience only 0.95 GPa of compressive pressure exerted by the PbS shell, assuming bulk lattice parameters, and up to 1.8 GPa of pressure using the calculated lattice parameters.¹⁴⁻¹⁸ Furthermore, in the RS structure, the 200 peak is more intense than the 111 peak. This is not observed in the XRD data with the 111 peak remaining dominant, even up to a shell thickness of 7.3 ML (blue). While the 111 and 200 XRD peak intensities suggest this conversion does not occur, the XRD peak breadths complicates this conclusion. Finally, the extinction spectra presented below are indicative of the CdSe ZB phase and not the RS phase. Despite the RS phase of the PbS shell, we conclude that the shell grows epitaxially from the CdSe core and the core maintains its ZB crystal structure. High-resolution TEM images confirm the preferential

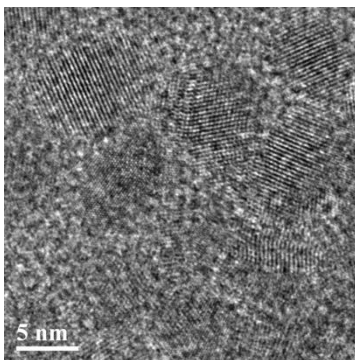


Figure 3-6. High-resolution TEM image of CdSe/PbS core/shell QDs showing continuous atomic lattice throughout the CdSe/PbS QDs.

crystallographic alignment of the core and shell, demonstrating epitaxial growth in these CdSe/PbS QDs (Figure 3-6).

Strain arising from the smaller lattice parameter of the PbS RS shell than the CdSe ZB core could play a role in the electronic and energetic properties of the CdSe/PbS core/shell QDs. The CdSe ZB core-only QDs have a lattice constant of 6.144 Å calculated from the 111 reflection, which is slightly larger than the bulk value of 6.050 Å.¹⁰ This 1.6% tensile strain indicates 0.8 GPa of stress based on the calculated Young's modulus for CdSe, which is consistent with previously reported strain values for this size of QD.^{14,19,20} This lattice spacing decreases with the addition of the PbS shell, down to 5.927 Å for the thickest shell, which is only 0.15% smaller than the PbS bulk value of 5.936 Å.¹⁰ This reduction in lattice parameter indicates a compressive strain of 3.6% compared to the CdSe ZB core-only QDs. This compressive strain in the CdSe/PbS core/shell QDs will likely give rise to a shifting of the conduction and valence bands to higher energies and a larger band gap than there would be with only quantum confinement.²¹

3.2.3 Spectroscopy

Characterization of Band Gap Energies. Extinction and PL spectra of the CdSe/PbS core/shell QDs were recorded to probe the energetics of the quantum-confined states and to identify changes in the spatial overlap of the electron and hole wave functions as the shell thickness was varied. All spectral data were collected with samples having absorbance values between 0.05 and 0.1 at the first absorption peak. The extinction spectra for CdSe/PbS core/shell QDs are plotted as solid lines in Figure 3-7, normalized to the same extinction at the energy of the lowest feature, the $1S_e-1S_h$ absorption band. The spectra are labeled with the number of PbS MLs for that sample, lower left in each panel, and are offset for clarity. The extinction spectra of

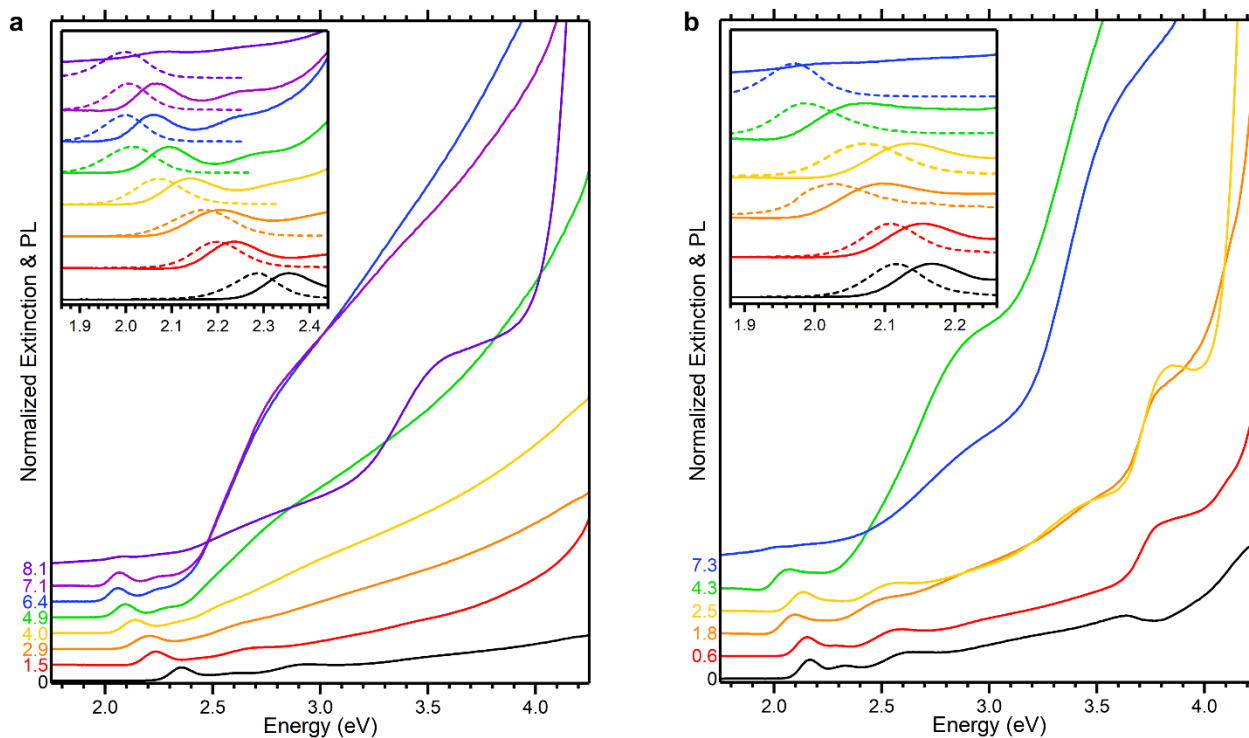


Figure 3-7. Extinction spectra (solid lines) and PL spectra (dashed lines in the insets) of CdSe QDs and CdSe/PbS core/shell QDs with core diameters of 3 nm (a) and 4 nm (b) labeled with the number of monolayers (lower left in each panel). The extinction spectra are normalized at the lowest-energy, $1S_e-1S_h$ absorption feature, and the PL spectra are normalized at their peaks.

the 3 and 4 nm CdSe core-only QDs, black, exhibit at least three distinct absorption features resulting from quantum confined states at lower energies, and there is a gentle rise in the absorbance with increasing photon energy.

In general, the absorption and PL spectra are observed to shift to lower energies with increasing PbS shell thickness (Figure 3-7, red through purple spectra). Specifically, the $1S_e-1S_h$ absorbance features shift by a total of 280 meV for the 3 nm core/8.1 ML sample and 155 meV for the larger 4 nm core/7.3 ML sample. These $1S_e-1S_h$ features remain above 1.74 eV, the CdSe ZB bulk band gap,⁴ and they do not approach the band gap of bulk PbS, 0.37 eV.³ See Figure A1-2 in Appendix 1 for details of accurately identifying the lowest-energy, $1S_e-1S_h$ transition energies. These band edge transition energies suggest that one or both of the charge carrier wave functions delocalize into the shell region of the QD, causing the shift to lower energy, but the

energies are still dominated by the CdSe core. There is a repeatable, abrupt shift of the $1S_e-1S_h$ feature to 40(10) meV higher energy observed between the spectra recorded for the samples with 1.8 ML (orange) and 2.5 ML (yellow) shells and 4 nm diameter cores. The $1S_e-1S_h$ feature then continues to lower energies with increasing shell thickness. For the 3 nm diameter samples, the first absorbance spectral features stop shifting to lower energies between the 6.4 ML (blue) and 7.1 ML (light purple) spectra and remain at the same energy within the noise of the absorption spectra. These features that contrast the general trend of shifting to lower energies both occur at energies just below 2.1 eV in the extinction spectra.

The PL spectra recorded for the 3 and 4 nm core diameter CdSe/PbS QD samples, Figure 3-7 (inset, dashed lines), are dominated by single features associated with radiative recombination of the electrons and holes *via* the $1S_e-1S_h$ transitions that are Stokes shifted just slightly from the lowest-energy absorption feature by 31-90 meV. The energies of the PL features recorded for the different CdSe/PbS QD samples mimic the trends of the first absorption peaks with shifts to lower energies with increasing shell thickness; total shifts of 304 and 148 meV for the 3 and 4 nm core samples, respectively, were measured (Table A1-4 in Appendix 1). Consistent with the absorption data collected for the 4 nm diameter CdSe cores, the PL peak in the spectrum recorded for the 2.5 ML thick PbS shell sample (yellow) is observed 34(8) meV to higher energy than the PL peak in the 1.8 ML thick shell sample (orange). The PL peak in the spectrum of the 7.1 ML PbS thick shell, 3 nm diameter CdSe core sample is also observed to shift to just slightly higher transition energies than the peak in the 6.4 ML sample, 9(7) meV, but this very small shift is reversed by a subsequent 10(8) meV shift to lower energy for the 8.1 ML sample.

The PL spectrum of the 3 nm CdSe core-only QDs (black) contains some very broad low-energy trap emission centered ~ 600 meV below the band edge PL peak,²² and a PL quantum yield (PLQY) of just 3.50(9)% was measured when exciting at 2.61 eV for these CdSe QDs. This trap PL was greatly diminished with the addition of a thin, 1.5 ML shell (red), and was eliminated for the QDs with thicker shells, 2.9 ML and greater. Despite the ZB/RS crystal structure mismatch at the core/shell interface, the PbS shell passivates the surface of the CdSe core and minimizes the density of low-energy surface trap states that are associated with the sub-bandgap emission. Though these loss mechanisms are reduced, the PLQY values decrease with the addition of the PbS shell; the PLQYs range from 0.10(1) to 1.37(7)% for the 3 nm core diameter CdSe/PbS core/shell QDs with a dependence on excitation energy.^{23,24} The PL spectra of the 4 nm CdSe QDs do not contain trap emission, and the PLQY is higher, 12.9(4)%, when exciting at 2.76 eV. The addition of the PbS shell on these larger core CdSe QDs lowers the PLQY values to 0.21(2) to 10.2(3)% with a dependence on excitation energy. A summary of the PLQY data is included in Table A1-5 in Appendix 1.

The $1S_e-1S_h$ transition energies also support the conclusion from the XRD data that the CdSe core remains in the ZB phase. The bulk band gap of RS CdSe is 0.67 eV, but that value can increase for quantum confined nanostructures; a band gap of 1.5 eV was reported for 2 nm diameter CdSe RS QDs.¹³ If the strain exerted by the PbS RS shell caused the CdSe core crystal to transform from ZB to RS, the energies of the $1S_e-1S_h$ absorption and PL features would dramatically decrease, likely down to ~ 1 eV.^{13,25} A dramatic shift of the spectral features to lower energies with shell growth is not observed.

Characterization of Wave Function Overlap. The bulk band alignment of CdSe ZB and PbS RS indicate an inverse type-I band alignment.¹ Even though quantum-confinement effects

would alter the energetics of the core and shell differently with varying core diameter and shell thickness, the inverse type-I band alignment would be achieved with very thick shells. At this extreme, the electrons and holes would both become localized in the shell region of the QDs, and the band gap would approach the PbS value, 0.37 eV. This is not observed. Instead, the energies of the $1S_e-1S_h$ absorption and PL features follow a general trend of shifting to lower energies with increasing shell thickness, but the energies remain greater than the bulk CdSe ZB band gap energy. There is no evidence of absorption or emission to lower energies. This suggests the electron and hole wave functions are not becoming localized in the PbS shells, even with the thickest shells synthesized.

In previous experiments performed on ZnSe/CdSe QDs, there was clear evidence in the extinction spectra for an inverse type-I heterostructure.^{26,27} Specifically, the extinction spectra contained absorption features at lower energies that were associated with transitions of electrons and holes both confined within the shell region, and other absorption features at higher energies that were associated with transitions of electrons and holes that are localized preferentially within the core region of the QDs. Similar features are not observed in the extinction spectra of the CdSe/PbS core/shell QDs; no low-energy absorption features are observed to grow in with shell thickness.

Evidence for distinct core and shell transitions were previously reported in type-I heterostructures. Specifically, the spectra contain one absorption and one PL feature associated with the core and one absorption and one PL feature associated with the shell.²⁸⁻³⁰ This dual emission can only occur if a) there is a large potential barrier at the core/shell interface that results in two separate quantum-confined regions or b) the intraband relaxation is slow compared to the radiative lifetime so that there is a probability for emission from the excited states prior to

relaxation to the band edge. For the CdSe/PbS core/shell QDs, the lack of absorption below the CdSe bulk band gap energy suggests that there is not a separate lower-energy band edge associated with only the PbS shell region even though the volume of the PbS shell becomes dominant. This also excludes the possibility of a second emission feature associated with the PbS shell. As mentioned, the observed PL feature smoothly shifts with the first absorption feature to lower energies, maintaining a Stokes shift of 20-70 meV (Appendix 1, Table A1-4), with shell growth. All of the spectroscopic evidence indicates these materials do not have an inverse-type-I band alignment.

Significant changes in the shapes of the CdSe/PbS QD extinction spectra are noticeable with increasing shell thickness, Figure 3-7. Most notably, the absorbance of the lowest-energy, $1S_e-1S_h$ feature decreases relative to the absorbance at higher transition energies with increasing shell thickness for both the 3 and the 4 nm core-diameter samples. Quantitative changes in the absorbance values are difficult to determine as the concentrations of the CdSe/PbS QDs in solution and the absorption coefficients are not accurately known. In order to emphasize the relative changes of the absorption at lower *versus* higher excitation energies, the spectra of the core-only and 7.1 ML CdSe/PbS QDs with 3 nm core diameters are plotted in Figure 3-8a with the spectra normalized to the same extinction at an energy of 1.5 eV above the $1S_e-1S_h$ feature in each spectrum. For the core-only sample (black), the extinction at the peak of the $1S_e-1S_h$ feature is 40.8% of that measured 1.5 eV to higher energy, at 3.862 eV. This percentage decreases with shell thickness as the absorbance of the $1S_e-1S_h$ feature continues to decrease relative to the absorbance at higher excitation energies. By a PbS shell thickness of 7.1 ML (purple) the absorbance at the $1S_e-1S_h$ feature is only 3.4% of the absorbance measured 1.5 eV higher in energy, 3.563 eV. Similar absorbance decreases are observed in the 4 nm extinction spectra,

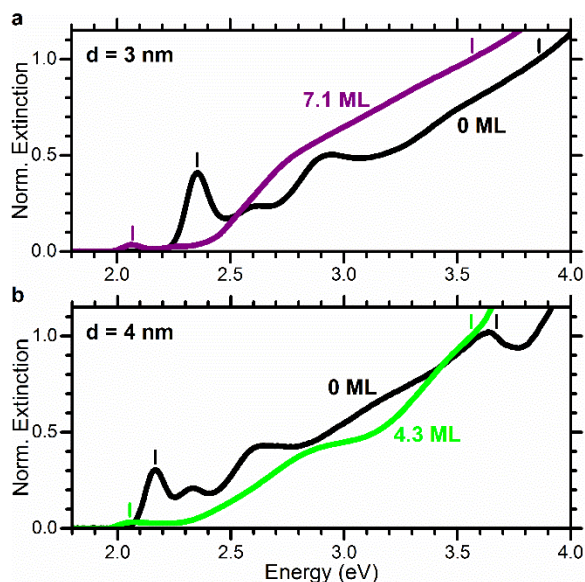


Figure 3-8. Normalized extinction spectra of (a) 3 nm CdSe core QDs (black) and 7.1 ML CdSe/PbS core/shell QDs (purple) and (b) 4 nm CdSe core QDs (black) and 4.3 ML CdSe/PbS core/shell QDs (green). The spectra are normalized to the same value at 1.5 eV above each $1S_e-1S_h$ absorption peak, indicated by tics.

Figure 3-8b. Here, the absorbance at the peak of the $1S_e-1S_h$ feature for the core-only sample (black) is 30.5% of the absorbance measured 1.5 eV to higher energy, at 3.668 eV. This percentage decreases by an order of magnitude, down to 3.1%, for a 4.3 ML PbS shell grown on the 4 nm CdSe core (green) at 3.563 eV. Since these spectra are collected using a forward-collecting scattering sphere and back scattering was corrected after data acquisition, the scattering in these spectra is negligible and thus the differences in extinction represent differences in absorption.

The energetic shift between the strong absorption and band-edge PL can also be quantified by integrating the extinction spectrum rather than relying on an arbitrary normalization point. The absorption spectra were integrated starting from high energy, 4.2 eV, just below the onset of absorption by ligands, down through the absorption of the QDs. The extinction spectra for the samples with the thickest PbS shells were not integrated since the scattering for those spectra could not be corrected. Since the shift between strong absorption and

PL is important for use as LSC, these integral curves are plotted *versus* the difference between the absorbance energy and the PL peak. These curves are plotted for QDs with 3 nm CdSe cores, Figure 3-9. For the 3 nm CdSe cores, the integrated absorption signal reaches 98% of the total integrated signal just 65 meV above the peak of the PL spectrum. The energetic shift between this 98%-level and the PL peak increases with shell growth, reaching 550 meV above the PL peak for the CdSe/PbS QDs with a shell thickness of 7.1 ML. Similar data were calculated for the 4 nm CdSe cores (see Figure A1-3 in Appendix 1), and the 98% level increased from 71 eV to 516 eV above the PL peak with the growth of a 4.3 ML PbS shell. These differences could simply result from differing levels of quantum confinement rather than changes in absorption spectral shape since a larger spectral region is integrated for the CdSe/PbS QDs. When comparing the two core-only samples, however, there is only a 6 meV difference between the 98%-level absorbance for the two samples resulting from the 193(6) meV difference in spectral window. Therefore, we conclude that the increased strength of absorption transitions at high energies in the CdSe/PbS core/shell QDs causes these large energetic shifts, offering promise for their use in LSCs. These properties can also be exploited for biological imaging by matching the

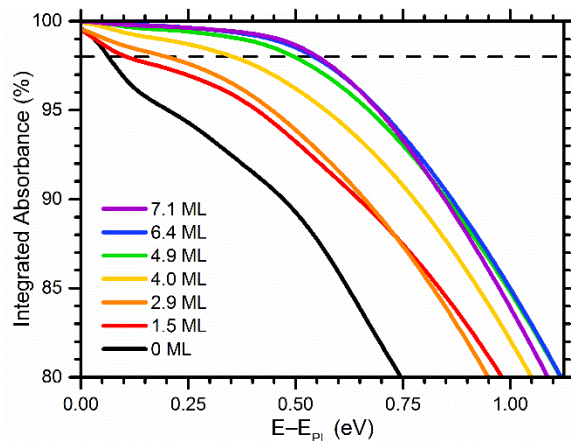


Figure 3-9. Normalized integral curves of absorption spectra for CdSe and CdSe/PbS QDs with 3 nm diameter cores versus shift between absorption and PL energy. The spectra are normalized to a total of 100%, and the 98% level is indicated with a dashed line.

broad, strong absorption to one biological window for excitation while the QD emission is tuned to a second, significantly lower-energy spectral window.^{6,31-33}

We propose these significant changes in the ratios of the absorbance values measured near band gap *versus* higher excitation energies with PbS shell growth are a direct result of dissimilar modifications of the electron and hole wave functions. Consider the CdSe/PbS QDs with the thickest shells. The lowest-energy quantum-confined state of the electron, $1S_e$, samples both the core and shell regions, and the lowest-energy state of the hole, $1S_h$, largely remains in the core region, a significant decrease in the overlap of the ground state electron and hole wave functions would result. With a decrease in wave function overlap, the absorption coefficient for this low-energy transition would decrease. This partial separation of band edge charge carrier wave functions is classified as a quasi-type-II heterostructure.³⁴⁻³⁶ In contrast, the absorption coefficients for transitions between higher energy states that remain delocalized over the entire region of the QDs, *e.g.*, $3S_e-3S_h$, may remain high. The modification of the electron and hole wave functions with shell growth may also enhance the oscillator strengths of higher-energy transitions with $\Delta n \neq 0$ that are typically weak or forbidden in spherical, core-only QDs, *e.g.*, $1S_e-3S_h$.

3.2.4 Electron and Hole Wave Function Calculations

The electron and hole wave functions of the low-lying quantum-confined states in the CdSe/PbS core/shell QDs were calculated to probe how they may be changing with PbS shell growth and to verify the proposed quasi-type-II behavior of these QDs. Specifically, calculations using three different single-band effective-mass approximation (EMA) models were performed.³⁷⁻⁴⁰ The full set of energies and radial probability density (RPD) functions for all three methods are included in Appendix 1, and the results from the three models are consistent

with each other with only subtle differences. Some of the results obtained using the analytical method developed by Haus *et al.* and implemented by Vlaskin *et al.* are presented to summarize how the RPD functions change with shell thickness.^{37,38}

The radial particle-in-a-box potentials representing the 3 nm core CdSe/PbS core/shell QDs with PbS shell thicknesses of 0, 1.5, and 2.9 ML are plotted in Figure 3-10a-c (black).^{1,2,41-}
⁴³ The calculated quantum-confined energies (red dashed) and RPD functions (red solid) for the $1S_e$ and $1S_h$ states are superimposed on the minimum conduction band and maximum valence band potentials. The electron and hole RPD functions change dissimilarly in part because of the effective masses of the charge carriers in the core and shell regions of the QDs. The electron has a very similar effective mass in the CdSe core, $m_e^* = 0.12m_e$, as it does in the PbS shell, $m_e^* = 0.105m_e$,³⁻⁵ and the small values result in a delocalization of the $1S_e$ RPD function over the entire

Figure 3-10. Radial probability densities calculated using the method by Haus *et al.*^{37,38} of the $1S_e$ (red) state in the conduction band (CB) and the $1S_h$ (red) and $3S_h$ (blue) states in the valence band (VB) superimposed on the potentials (black) and state energies (dashed) for the 3 nm core CdSe/PbS core/shell QDs. The panels are for shell thicknesses of (a) 0 ML, (b) 1.5 ML, and (c) 2.9 ML.

QD, even for the samples with the thickest shells. In contrast, there is a large difference between the effective masses of the hole in the CdSe core, $m_{hh}^* = 2.14m_e$ for the heavy hole, and in the PbS shell, $m_h^* = 0.108m_e$.³⁻⁵ This significant difference results in the localization of the $1S_h$ RPD function in the core region CdSe/PbS QDs, where the effective mass is much larger, with little probability density found in the shell region as long as the energy of the hole state lies above the energy of bulk CdSe. The resultant character of the CdSe/PbS QDs with thin shells, ≤ 1.5 ML, is quasi-type-I with only a small delocalization of the $1S_e$ RPD into the shell and the localization of the $1S_h$ RPD function in the core region, Figure 3-10a,b. The calculations suggest this system evolves into a quasi-type-II band alignment with increasing shell thickness. By a shell thickness of 2.9 ML, Figure 3-10c, there is a significant reduction in the overlap of the $1S_e$ and $1S_h$ wave functions, as only 62% of the $1S_e$ RPD is in the core region while 99% of the $1S_h$ RPD remains in the core region of the QD. This reduction in overlap results in a notable reduction in oscillator strength of the near band gap $1S_e-1S_h$ transition, which would lead to the significant decrease in absorbance observed experimentally for the lowest-energy transitions.

The calculations indicate the different effective masses in the valence band also influence the nature of the higher-lying hole quantum-confined states. The calculated energies and RPD functions of the $n = 3$ heavy hole state, $3S_h$, are also included in Figure 3-10 (blue). This state initially remains confined in the core region of the CdSe/PbS QD, but then spreads over the entire QD by a shell thickness of 2.9 ML for the 3 nm core sample. Absorptive transitions with $\Delta n > 1$ within a spherical QD with infinite potential walls are not allowed due to symmetry constraints, but they have been observed in the spectra of QDs.^{44,45} The dissimilar effective masses and band alignments in the CdSe/PbS core/shell QDs can further reduce the influence of the particle-in-a-sphere $\Delta n = 0$ selection rule. As a result, the oscillator strength for the $1S_e-3S_h$

transition and other $\Delta n \neq 0$ transitions will likely increase in comparison to that of the $1S_e-1S_h$ transition with increasing shell thickness. Based on these simple EMA calculations, we propose that indeed the low-lying transitions in the CdSe/PbS absorption spectra, such as the $1S_e-1S_h$ transition, become weaker and the higher-energy transitions, such as the $1S_e-3S_h$ transition, become stronger with shell growth. This scenario would still result in radiative recombination of the electrons and holes being observed near the band gap with only a small Stokes shift of the PL emission from the $1S_e-1S_h$ absorptive transition, as is observed experimentally.

The observed energies of the $1S_e-1S_h$ transitions can also be used to identify the point at which the QD heterostructure changes from quasi-type-I to quasi-type-II.²¹ The $1S_e-1S_h$ absorption peak (solid) and PL peak (open) energies are plotted *versus* the number of monolayers for samples with 3 (squares) and 4 nm (circles) diameter CdSe cores in Figure 3-11. Initially, small increases in shell thickness dramatically reduces the $1S_e-1S_h$ transition energy as the degree of quantum confinement of the electron changes. For QDs with thicker shells, however, there are only small changes to the $1S_e-1S_h$ transition energies with additional PbS MLs. The transition from quasi-type-I to quasi-type-II behavior is most obvious for samples with 3 nm

Figure 3-11. Transition energies of the $1S_e-1S_h$ absorption peaks (solid symbols) and PL peaks (open symbols) for CdSe QDs and CdSe/PbS core/shell QDs versus number of shell monolayers. The data for the 3 and 4 nm diameter CdSe cores are black squares and red circles, respectively. The error bars, based on spectral noise and feature curvature, are smaller than the data points. The bulk CdSe ZB band gap is 1.74 eV.⁴

CdSe cores, occurring at ~5 ML, while the shift to higher energy complicates the identification of this transition in the series with 4 nm CdSe cores. Nevertheless, the energetic difference between samples with 4 nm cores with 4.3 ML and 7.3 ML is only 50 meV, despite the 1.9 nm increase in diameter.

It is important to note that these calculations are not quantitative, nor do they reveal the full picture of the behavior of the electron and hole states in these CdSe/PbS QDs. The band gaps predicted by the calculations do not match the experimentally determined values. With increasing PbS shell thickness, ≥ 4.0 ML, the calculated $1S_h$ state becomes localized in the shell region, and a notable shift of the band gap to lower energies, approaching the PbS bulk band gap, is predicted. Since the experimentally observed band gap remains just above the bulk CdSe band gap for the CdSe/PbS QDs synthesized, it appears other factors not included in these simple EMA models are also influencing the energetics and properties of the quantum-confined states (see Figures A1-12 and A1-13 in Appendix 1). Incorrect alignment of the bulk CdSe and PbS bands could also play a factor in predicting the energetics and wave functions of the electrons and holes.^{46,47}

3.2.5 Potential Effects of Strain and Crystal Structure

We propose one of the deviations between the measured and calculated ΔE values results from lattice strain, which was not modeled in the simple EMA calculations performed. Strain caused by lattice mismatch in core/shell heterostructures can be significant and cause deviations from expected trends solely based on quantum confinement.²¹ In this system, the smaller RS PbS (5.936 Å lattice constant) experiences tensile strain while the ZB CdSe core (6.050 Å lattice constant) experiences compressive strain.¹⁰ Since the $1S_h-1S_e$ transitions are dominated by the CdSe core, the compressive strain on the core would impact the observed spectral features.

Compressive strain shifts the $1S_h-1S_e$ transition to higher energies, countering the expected shifts to lower energies due to decreasing quantum confinement. Based on the difference between the bulk lattice constants of CdSe and PbS (1.9% strain), the maximum calculated shift to higher energy of the CdSe band gap is ~ 41 meV (see Appendix 1 for more details). Since the as-synthesized CdSe QD lattice parameter is larger than the bulk value, however, this strain-induced change could be as great as ~ 75 meV.

This strain-induced change in band gap is likely significantly more important for the core/shell QDs with 4 nm cores. First, the magnitude of strain is larger for a larger core and second, the quantum confinement is weaker in a larger core, reducing the degree to which the electron reduces its energy through reduced quantum confinement in the core/shell QDs. Strain could be the source of the unusual, abrupt shift to higher energy seen in the CdSe/PbS QDs with 4 nm CdSe cores. Without being able to measure the lattice parameters of the CdSe and PbS phases separately, it is unclear precisely how much strain contributes to the trends in band gaps. Additionally, since strain shifts the valence and conduction band edge energies, these strain effects could impact the band offsets between the core and shell, and therefore impact the electron and hole radial probability density calculations.

3.3 Conclusions

We have synthesized CdSe/PbS core/shell QDs with varying shell thicknesses that are dictated by the quantities of shell precursors. XRD data confirm that the PbS shell adopts the RS structure despite a mismatch with the CdSe ZB core lattice. The growth of the PbS shell on the CdSe core results in a significant reduction of the absorbance near the band gap relative to higher energies. We propose the absorbance changes result from changes in the spatial overlap of the electrons and holes, and this rationale is supported by EMA calculations. The wave functions of

the lowest energy electron and hole states in QDs with shell thicknesses of a few MLs become partially separated, and these absorptive transitions become weaker. In contrast, the wave functions of higher energy states maintain significant overlap and maintain significant oscillator strength. These large differences in oscillator strength result in the energetic separation, up to 550 meV shift based on the 98% integrated absorption, between the absorption and PL spectral windows that is essential for use in luminescent solar concentrators as well as biological imaging.^{31,32,48,49} Compared to other LSC candidates, the range over which this energetic separation can be tuned is larger for the CdSe/PbS QDs due to the ability to change both the diameter of the CdSe core and the thickness of the PbS shell. Ultimately, the large differences between the bulk band gap energies of the core *versus* the shell indicate their potential for improved efficiencies in solar cells through MEG if these core and band gap energies can be achieved on the nanoscale. The synthesis of CdSe/PbS core/shell QDs demonstrates the first step towards MEG in an inverse-type-I core/shell QD system.

3.4 References

- (1) Reiss, P.; Couderc, E.; De Girolamo, J.; Pron, A., Conjugated Polymers/Semiconductor Nanocrystals Hybrid Materials—Preparation, Electrical Transport Properties and Applications. *Nanoscale* **2011**, *3*, 446-489.
- (2) Li, J.; Wang, Shape Effects on Electronic States of Nanocrystals. *Nano Lett.* **2003**, *3*, 1357-1363.
- (3) Springholz, G.; Bauer, G., 9.1 IV-VI Semiconductors: General Properties. In *Landolt-Börnstein - Group III Condensed Matter 34A*, Springer-Verlag Berlin Heidelberg: Berlin, Heidelberg, 2013; Vol. 16, pp 415-421.
- (4) Cadmium Selenide (CdSe) Electronic Properties, Cubic Modification. In *Landolt-Börnstein - Group III Condensed Matter 41B (II-VI and I-VII Compounds; Semimagnetic Compounds)*, Madelung, O.; Rössler, U.; Schulz, M., Eds. Springer-Verlag: Berlin/Heidelberg, 1999; pp 1-6.
- (5) Kim, Y. D.; Klein, M. V.; Ren, S. F.; Chang, Y. C.; Luo, H.; Samarth, N.; Furdyna, J. K., Optical Properties of Zinc-Blende CdSe and $Zn_xCd_{1-x}Se$ Films Grown on GaAs. *Phys. Rev. B: Condens. Matter Mater. Phys* **1994**, *49*, 7262-7270.
- (6) Pietryga, J. M.; Werder, D. J.; Williams, D. J.; Casson, J. L.; Schaller, R. D.; Klimov, V. I.; Hollingsworth, J. A., Utilizing the Lability of Lead Selenide to Produce Heterostructured Nanocrystals with Bright, Stable Infrared emission. *J. Am. Chem. Soc.* **2008**, *130*, 4879-4885.
- (7) Lambert, K.; De Geyter, B.; Moreels, I.; Hens, Z., PbTe|CdTe Core|Shell Particles by Cation Exchange, a HR-TEM Study. *Chem. Mater.* **2009**, *21*, 778-780.
- (8) Lee, D.; Kim, W. D.; Lee, S.; Bae, W. K.; Lee, S.; Lee, D. C., Direct Cd-to-Pb Exchange of CdSe Nanorods into PbSe/CdSe Axial Heterojunction Nanorods. *Chem. Mater.* **2015**, *27*, 5295-5304.

- (9) Zhang, J.; Chernomordik, B. D.; Crisp, R. W.; Kroupa, D. M.; Luther, J. M.; Miller, E. M.; Gao, J.; Beard, M. C., Preparation of Cd/Pb Chalcogenide Heterostructured Janus Particles *via* Controllable Cation Exchange. *ACS Nano* **2015**, *9*, 7151-7163.
- (10) Madelung, O., *Semiconductors - Basic Data*. Springer-Verlag: 1996.
- (11) Chen, O.; Chen, X.; Yang, Y.; Lynch, J.; Wu, H.; Zhuang, J.; Cao, Y. C., Synthesis of Metal-Selenide Nanocrystals Using Selenium Dioxide as the Selenium Precursor. *Angew. Chem. Int. Ed.* **2008**, *47*, 8638-8641.
- (12) Mahler, B.; Nadal, B.; Bouet, C.; Patriarche, G.; Dubertret, B., Core/Shell Colloidal Semiconductor Nanoplatelets. *J. Am. Chem. Soc.* **2012**, *134*, 18591-18598.
- (13) Martin, T. P., *Large Clusters of Atoms and Molecules*. Springer Netherlands: Dordrecht, 1996.
- (14) Zhou, Y.; Wang, F.; Buhro, W. E., Large Exciton Energy Shifts by Reversible Surface Exchange in 2D II-VI Nanocrystals. *J. Am. Chem. Soc.* **2015**, *137*, 15198-15208.
- (15) Shan, W.; Walukiewicz, W.; Ager, J. W.; Yu, K. M.; Wu, J.; Haller, E. E., Pressure Dependence of the Fundamental Band-Gap Energy of CdSe. *Appl. Phys. Lett.* **2004**, *84*, 67-69.
- (16) Yang, J. W.; Hou, H. J., A First-Principles Study on the Structural and Elastic Properties and the Equation of State of Wurtzite-Type Cadmium Selenide under Pressure. *High Pressure Res.* **2012**, *32*, 376-384.
- (17) Jastrzebski, Z. D., In *The Nature and Properties of Engineering Materials*, 2nd ed.; Jon Wiley & Sons: New York, 1977; pp 202-203.
- (18) Deligoz, E.; Colakoglu, K.; Ciftci, Y., Elastic, Electronic, and Lattice Dynamical Properties of CdS, CdSe, and CdTe. *Phys. B.* **2006**, *373*, 124-130.

- (19) Wang, F.; Wang, Y.; Liu, Y.-H.; Morrison, P. J.; Loomis, R. A.; Buhro, W. E., Two-Dimensional Semiconductor Nanocrystals: Properties, Templated Formation, and Magic-Size Nanocluster Intermediates. *Acc. Chem. Res.* **2015**, *48*, 13-21.
- (20) Meulenbergh, R. W.; Jennings, T.; Strouse, G. F., Compressive and Tensile Stress in Colloidal CdSe Semiconductor Quantum Dots. *Phys. Rev. B: Condens. Matter Mater. Phys.* **2004**, *70*, 235311.
- (21) Smith, A. M.; Mohs, A. M.; Nie, S., Tuning the Optical and Electronic Properties of Colloidal Nanocrystals by Lattice Strain. *Nat. Nanotechnol.* **2009**, *4*, 56-63.
- (22) Houtepen, A. J.; Hens, Z.; Owen, J. S.; Infante, I., On the Origin of Surface Traps in Colloidal II–VI Semiconductor Nanocrystals. *Chem. Mater.* **2017**, *29*, 752-761.
- (23) Hoy, J.; Morrison, P. J.; Steinberg, L. K.; Buhro, W. E.; Loomis, R. A., Excitation Energy Dependence of the Photoluminescence Quantum Yields of Core and Core/Shell Quantum Dots. *J. Phys. Chem. Lett.* **2013**, *4*, 2053-2060.
- (24) Martynenko, I. V.; Baimuratov, A. S.; Osipova, V.; Kuznetsova, V. A.; Purcell-Milton, F.; Rukhlenko, I. D.; Fedorov, A. V.; Gun'ko, Y. K.; Resch-Genger, U.; Baranov, A. V., Excitation Energy Dependence of the Photoluminescence Quantum Yield of Core/Shell CdSe/CdS Quantum Dots and Correlation with Circular Dichroism. *Chem. Mater.* **2018**, *30*, 465-471.
- (25) Tolbert, S.; Herhold, A.; Johnson, C.; Alivisatos, A. P., Comparison of Quantum Confinement Effects on the Electronic Absorption Spectra of Direct and Indirect Gap Semiconductor Nanocrystals. *Phys. Rev. Lett.* **1994**, *73*, 3266-3269.
- (26) Ivanov, S. A.; Nanda, J.; Piryatinski, A.; Achermann, M.; Balet, L. P.; Bezel, I. V.; Anikeeva, P. O.; Tretiak, S.; Klimov, V. I., Light Amplification Using Inverted Core/Shell

Nanocrystals: Towards Lasing in the Single-Exciton Regime. *J. Phys. Chem. B* **2004**, *108*, 10625-10630.

(27) Battaglia, D.; Li, J. J.; Wang, Y.; Peng, X., Colloidal Two-Dimensional Systems: CdSe Quantum Shells and Wells. *Angew. Chem. Int. Ed.* **2003**, *42*, 5035-5039.

(28) Lin, Q.; Makarov, N. S.; Koh, W.-k.; Velizhanin, K. A.; Cirloganu, C. M.; Luo, H.; Klimov, V. I.; Pietryga, J. M., Design and Synthesis of Heterostructured Quantum Dots with Dual Emission in the Visible and Infrared. *ACS Nano* **2015**, *9*, 539-547.

(29) Pinchetti, V.; Meinardi, F.; Camellini, A.; Sirigu, G.; Christodoulou, S.; Bae, W. K.; De Donato, F.; Manna, L.; Zavelani-Rossi, M.; Moreels, I.; Klimov, V. I.; Brovelli, S., Effect of Core/Shell Interface on Carrier Dynamics and Optical Gain Properties of Dual-Color Emitting CdSe/CdS Nanocrystals. *ACS Nano* **2016**, *10*, 6877-6887.

(30) Razgoniaeva, N.; Yang, M.; Colegrove, C.; Kholmicheva, N.; Moroz, P.; Eckard, H.; Vore, A.; Zamkov, M., Double-Well Colloidal Nanocrystals Featuring Two-Color Photoluminescence. *Chem. Mater.* **2017**, *29*, 7852-7858.

(31) Kovalenko, M. V.; Manna, L.; Cabot, A.; Hens, Z.; Talapin, D. V.; Kagan, C. R.; Klimov, V. I.; Rogach, A. L.; Reiss, P.; Milliron, D. J.; Guyot-Sionnest, P.; Konstantatos, G.; Parak, W. J.; Hyeon, T.; Korgel, B. A.; Murray, C. B.; Heiss, W., Prospects of Nanoscience with Nanocrystals. *ACS Nano* **2015**, *9*, 1012-1057.

(32) Derfus, A. M.; Chan, W. C. W.; Bhatia, S. N., Probing the Cytotoxicity of Semiconductor Quantum Dots. *Nano Lett.* **2004**, *4*, 11-18.

(33) Kirchner, C.; Liedl, T.; Kudera, S.; Pellegrino, T.; Javier, A. M.; Gaub, H. E.; Stölzle, S.; Fertig, N.; Parak, W. J., Cytotoxicity of Colloidal CdSe and CdSe/ZnS Nanoparticles. *Nano Lett.* **2005**, *5*, 331-338.

- (34) Cirloganu, C. M.; Padilha, L. A.; Lin, Q.; Makarov, N. S.; Velizhanin, K. A.; Luo, H.; Robel, I.; Pietryga, J. M.; Klimov, V. I., Enhanced Carrier Multiplication in Engineered Quasi-Type-II Quantum Dots. *Nat. Commun.* **2014**, *5*, 4148.
- (35) De Geyter, B.; Justo, Y.; Moreels, I.; Lambert, K.; Smet, P. F.; Van Thourhout, D.; Houtepen, A. J.; Grodzinska, D.; De Mello Donega, C.; Meijerink, A.; Vanmaekelbergh, D.; Hens, Z., The Different Nature of Band Edge Absorption and Emission in Colloidal PbSe/CdSe Core/Shell Quantum Dots. *ACS Nano* **2011**, *5*, 58-66.
- (36) Maiti, S.; Debnath, T.; Ghosh, H. N., Elucidating the Electronic Cross-Talk Dynamics across the Heterointerface of Janus CdSe/PbSe Nanocrystals. *J. Phys. Chem. C* **2016**, *120*, 29054-29061.
- (37) Haus, J. W.; Zhou, H. S.; Honma, I.; Komiyama, H., Quantum Confinement in Semiconductor Heterostructure Nanometer-Size Particles. *Phys. Rev. B: Condens. Matter Mater. Phys* **1993**, *47*, 1359-1365.
- (38) Vlaskin, V. A.; Beaulac, R.; Gamelin, D. R., Dopant—Carrier Magnetic Exchange Coupling in Colloidal Inverted Core/Shell Semiconductor Nanocrystals. *Nano Lett.* **2009**, *9*, 4376-4382.
- (39) Kaledin, A. L.; Lian, T.; Hill, C. L.; Musaev, D. G., An Infinite Order Discrete Variable Representation of an Effective Mass Hamiltonian: Application to Exciton Wave Functions in Quantum Confined Nanostructures. *J. Chem. Theory Comput.* **2014**, *10*, 3409-3416.
- (40) Poulsen, F.; Hansen, T., Band Gap Energy of Gradient Core—Shell Quantum Dots. *J. Phys. Chem. C* **2017**, *121*, 13655-13659.
- (41) Li, Y.-H.; Walsh, A.; Chen, S.; Yin, W.-J.; Yang, J.-H.; Li, J.; Silva, J. L. F. D.; Gong, X. G.; Wei, S.-H., Revised *ab initio* Natural Band Offsets of All Group IV, II-VI, and III-V Semiconductors. *Appl. Phys. Lett.* **2009**, *94*, 212109.

- (42) Wei, S. H.; Zhang, S. B., Structure Stability and Carrier Localization in CdX (X = S, Se, Te) Semiconductors. *Phys. Rev. B: Condens. Matter Mater. Phys* **2000**, *62*, 6944-6947.
- (43) Murayama, M.; Nakayama, T., Chemical Trend of Band Offsets at Wurtzite/Zinc-Blende Heterocrystalline Semiconductor Interfaces. *Phys. Rev. B: Condens. Matter Mater. Phys* **1994**, *49*, 4710-4724.
- (44) Ekimov, A. I.; Hache, F.; Schanne-Klein, M. C.; Ricard, D.; Flytzanis, C.; Kudryavtsev, I. A.; Yazeva, T. V.; Rodina, A. V.; Efros, A. L., Absorption and Intensity-Dependent Photoluminescence Measurements on CdSe Quantum Dots: Assignment of the First Electronic Transitions. *J. Opt. Soc. Am. B* **1993**, *10*, 100-107.
- (45) Norris, D. J.; Bawendi, M. G., Measurement and Assignment of the Size-Dependent Optical Spectrum in CdSe Quantum Dots. *Phys. Rev. B: Condens. Matter Mater. Phys* **1996**, *53*, 16338-16346.
- (46) Miller, E. M.; Kroupa, D. M.; Zhang, J.; Schulz, P.; Marshall, A. R.; Kahn, A.; Lany, S.; Luther, J. M.; Beard, M. C.; Perkins, C. L.; van de Lagemaat, J., Revisiting the Valence and Conduction Band Size Dependence of PbS Quantum Dot Thin Films. *ACS Nano* **2016**, *10*, 3302-3311.
- (47) Oh, S. J.; Berry, N. E.; Choi, J. H.; Gauldin, E. A.; Lin, H.; Paik, T.; Diroll, B. T.; Muramoto, S.; Murray, C. B.; Kagan, C. R., Designing High-Performance PbS and PbSe Nanocrystal Electronic Devices through Stepwise, Post-Synthesis, Colloidal Atomic Layer Deposition. *Nano Lett.* **2014**, *14*, 1559-1566.
- (48) Erickson, C. S.; Bradshaw, L. R.; McDowall, S.; Gilbertson, J. D.; Gamelin, D. R.; Patrick, D. L., Zero-Reabsorption Doped-Nanocrystal Luminescent Solar Concentrators. *ACS Nano* **2014**, *8*, 3461-3467.

(49) Bradshaw, L. R.; Knowles, K. E.; McDowall, S.; Gamelin, D. R., Nanocrystals for Luminescent Solar Concentrators. *Nano Lett.* **2015**, *15*, 1315-1323.

Chapter 4: Spectroscopy of CdSe/PbS Core/Shell Nanoplatelets

4.1 Introduction

As stated in Chapter 1, semiconductor nanocrystals (NCs) can be synthesized in a variety of shapes and sizes in each dimension, changing the energies and densities of the quantum confinement states. Shape modification of NCs can also tailor properties such as light absorption and emission, charge transport, and charge separation.¹ Quantum dots (QDs), such as those studied in Chapter 3, are confined in all three dimensions.^{2,3} Increasing the NC length in one dimension results in quantum wires (QWs) with confinement in two dimensions.⁴ Carriers in zinc blende (ZB) CdSe nanoplatelets (NPLs) are strongly confined in one dimension with thicknesses varying for 3.5 up to 8.5 monolayers (ML), but are (at most) weakly confined in the length and width dimensions.⁵⁻⁷ Zinc blende (ZB) CdSe NPLs have generated significant interest because their shape results in unique optical and assembly properties.⁸⁻¹⁰

Optically, the energies of absorption and photoluminescence (PL) features are primarily dictated by the thickness of the CdSe NPLs. These NPLs have atomically flat top and bottom surfaces, which lead to strong, uniform quantum confinement of the charge carriers in the thickness dimension of the NPLs. Since the large lateral dimensions of the NPLs only weakly confine the charge carriers (at most), the band edge optical features are extremely sharp with minimal inhomogeneous broadening. Due to the quasi 1D quantum confinement in CdSe NPLs, absorption transitions involving different hole states and the same electron state are observed. The bulk ZB CdSe valence band (VB) has three low-lying states, the heavy hole (hh), light hole (lh), and split off hole (soh) with different curvatures and effective masses.¹⁰ While the hh and lh

bulk band edge potentials are degenerate at the gamma point, the soh band is separated by 0.42 eV.¹¹ Transitions from each of these different hole states access the same electron state in the CB, including the transition between the lowest energy electron state and the lowest energy hh state (1_e-1_{hh}), the lowest energy lh state (1_e-1_{lh}), and the lowest energy soh state (1_e-1_{soh}). After electronic excitation, the photo-generated electron-hole pair forms an exciton since the binding energy of ~165 meV (calculated for 4.5 ML CdSe NPLs) is significantly larger than the thermal energy at room temperature ($kT = 25.7$ meV).^{11,12} Additionally, the NPL shape and electronic structure cause unique optical polarization of the absorption and PL transitions, leading to circularly polarized emission from the face of the NPL and linearly polarized emission from the edges of the NPL.^{9,13,14}

Similarly, the NPL shape results in unique assembly abilities. The flat NPL faces, aligned ligands, and strong van der Waals interaction between the large NPL faces can be exploited to stack and self-assemble the NPLs in devices. Since the NPL geometry causes directional, polarized light emission, self-assembled NPLs also exhibit directional, polarized emission in devices.⁹ Compared to QDs, the NPL's longer dimensions could be used for charge transport, but the dimensionality and high level of quantum confinement in as-synthesized CdSe NPLs leads to extremely large exciton binding energies, hindering charge separation and conduction.¹⁰⁻¹²

Post-synthetic modification of semiconductor NPLs can help tailor the properties of these particles while retaining the advantages of “two-dimensional” crystals over “zero-dimensional” QDs, such as charge transport. The NC properties and charge carrier dynamics can be tuned through ligand exchange^{15,16} and heterostructure growth.¹⁷⁻²¹ Ligand exchange can passivate trap sites on the semiconductor surface,^{22,23} shift the NC band edge energies,²⁴ modify the band gap energy,^{15,16,25} and induce charge transfer and/or separation.²⁶ Semiconductor NPL

heterostructures can be synthesized to exhibit either type-I^{17,18} or type-II²¹ behavior in either a core/shell or core/crown heterostructure morphology. In a core/crown NPL, the thickness of the NPL does not change, and the lateral dimensions of the NPL are extended by the addition of a second semiconductor material. For example, in 4.5 ML CdSe/CdTe core/crown NPLs, the 4.5 ML CdSe NPLs are extended in length and width by the addition of a 4.5 ML thick CdTe crown surrounding the core on the four small sides without changing the thickness.²¹ While crown growth is anisotropic, shell growth is isotropic, resulting in crystal growth on all facets of the core NPL. For example, CdS growth occurs on all facets of the core CdSe NPL, creating a CdSe/CdS core/shell NPL.^{17,18}

These two heterostructure types, type-II CdSe/CdTe core/crown NPLs and type-I CdSe/CdS core/shell NPLs, tune the optoelectronic properties of the NCs. In the type-II CdSe/CdTe core/crown NPL, the electron and hole are spatially separated, resulting in a significantly longer PL lifetime and a large Stokes shift between the first absorption feature and the PL.²¹ Despite the separation of the electron and hole wave functions in these type-II CdSe/CdTe core/crown NPLs, the photoluminescence quantum yield (PLQY) was as high as 46%.²¹ Alloying the core/crown to form a CdSe/CdSe_xTe_{1-x}/CdTe core/alloy/crown structure improves the PLQY to as high as 70% by reducing interfacial strain.²¹ The CdS shell in the type-I CdSe/CdS core/shell NPLs effectively passivates the CdSe core, increasing the PLQY from 20 to 40%.^{17,18} A type-I heterostructure with a larger potential barrier between the NPL surface and core, as in CdSe/CdZnS core/shell NPLs, can raise the PLQY to as high as 60%.¹⁷ These heterostructures provide an opportunity to tune the NC properties for a wide range of applications, including incorporation in light emitting diodes, photocatalysis, imaging, and photovoltaic devices.

In Chapter 3, the CdSe/PbS core shell QD system was analyzed using the inverse-type-I band alignment of the CdSe and PbS bulk band gaps, which was understood to cause heterostructure tunability from quasi-type-I to quasi-type-II depending on the PbS shell thickness.²⁷ Effective mass approximation calculations indicated that the electron and hole wave function localization is not simply the result of differing conduction and valence band energies, but also the result of the charge carriers' effective masses. The study in Chapter 3 did not consider the effect of differing band structures for the CdSe and PbS semiconductors. This difference makes the CdSe/PbS core/shell system particularly attractive for tuning the optoelectronic properties. The differences in the band structure at different values of the wave vector k could allow additional tuning of the absorption transition energies and strengths. As stated in Chapter 1, the band alignment of the CdSe/PbS core/shell heterostructure NCs at the Γ point is a type-I configuration, while the band alignment at the L point is an inverse-type-I alignment. The band edge wave functions can therefore change between states dominated by CdSe (Γ point) or PbS (L point) depending on shell thickness.

We report here the synthesis of CdSe/PbS core/shell NPLs based on the previously reported synthesis of CdSe/PbS core/shell QDs.²⁷ Transmission electron microscopy (TEM) and inductively coupled plasma mass spectrometry (ICP-MS) were used to monitor morphological and compositional changes to the NPLs. Optical characterization through steady-state absorption and PL spectroscopies was used to probe the quantum confinement of the charge carrier states. Fitting of the absorption features close to the band edge was used to study changes to the hh and lh wave functions. The spectroscopic changes were understood using a model of quantum confinement at the Γ and L points in CdSe/PbS core/shell NPLs. Time-resolved PL was used to further examine the effective heterostructure type with changing shell thickness.

4.2 Results and Discussion

4.2.1 Synthesis.

The CdSe core NPLs were synthesized with a length of 30(3) nm, width of 8(1) nm, and thickness of 4.5 ML (1.22 nm) with Cd-terminated top and bottom facets using a slightly modified procedure as reported previously.²⁸ The 4.5 ML NPLs were purified from 3.5 ML NPL and QD byproducts through a modified precipitation and filtration process. See Chapter 2 for full details on the synthesis and purification of the CdSe NPLs.⁹ The PbS shell synthesis used to make the CdSe/PbS core/shell NPLs is similar to the procedure for making CdSe/PbS core/shell QDs.²⁷ This room-temperature synthesis uses ZB CdSe core NPLs in order to reduce structural mismatch between the CdSe core and the PbS shell since the ZB and rock salt (RS) structures share a common cubic anionic sublattice.

After synthesis and purification, the absorbance of the CdSe NPL stock solution was measured quantitatively and the lateral sizes of the NPLs were measured from transmission electron microscopy (TEM) images in order to calculate the concentration of NPLs in the stock solution.²⁹ See Figure A2-1 for histograms of the length, width, and thickness of these CdSe core NPLs. These NPL concentration and size data were used to calculate the quantities of shell precursors required for a desired shell thickness, assuming isotropic growth on all sides (see Table A2-1 in Appendix 2 for more details). A 200 μL aliquot of the CdSe NPLs in methylcyclohexane was added to a vial containing 50 μL octylamine. This dispersion of NPLs was diluted with 2 mL chloroform, and the desired quantity of thioacetamide (TAA, S precursor) was added. This solution was sonicated for 5-10 minutes, until all TAA dissolved, which was indicated by the solution changing from bright yellow to orange, indicative of sulfide deposition.¹⁷ A 0.01 M solution of lead oleate ($\text{Pb}(\text{oleate})_2$, lead precursor) in octylamine was

added over time at a rate of 20 μL every 5 min until the desired quantity of $\text{Pb}(\text{oleate})_2$ was added. After the reaction proceeded for three hours, the product CdSe/PbS core/shell NPLs were isolated from remaining shell precursors and homogeneously nucleated PbS (black solid). This black solid, which we showed to be homogeneously nucleated PbS in the CdSe/PbS core/shell QD synthesis,²⁷ was first removed by centrifuging at 4500 RPM (3260 g) for 5 min. The clear solution, containing the desired product, was decanted from the black precipitate (homogeneously nucleated PbS). The solution was reduced to about 25% its original volume under a stream of dry nitrogen gas, 1 mL methanol was added to induce flocculation, and the vial was centrifuged for 5 min at 4500 RPM (3260 g). The pale yellow solution, which contains excess shell precursors, was decanted, using excess methanol to carefully wash away the supernatant. The solid CdSe/PbS core/shell NPLs were redispersed in 1 mL toluene.

4.2.2 Morphological Changes.

Unlike the synthesis of CdSe/PbS core/shell QDs, which results in growth of PbS on all surfaces of the CdSe QD, the growth of a PbS shell on CdSe NPLs results in anisotropic changes in the morphology of the CdSe/PbS core/shell NPLs. Starting with CdSe NPLs with a relatively large aspect ratio (i.e. 30(3) L \times 8(1) W nm NPLs that are more rectangular than square in shape), the NPLs increase in thickness, decrease in length, and increase in width (Figure 4-1). See Figure A2-1 for histograms of the length, width, and thickness of these CdSe/PbS core/shell NPLs.

Clustering results in some of the NPLs being positioned on their sides in the TEM images, permitting the thickness of the NPLs to be measured. This is very common in the CdSe core-only NPLs (see Figure A2-2 in Appendix 2), but the CdSe/PbS core/shell NPLs do not appear to cluster as readily. Still, a few CdSe/PbS core/shell NPLs stand on end, allowing for the

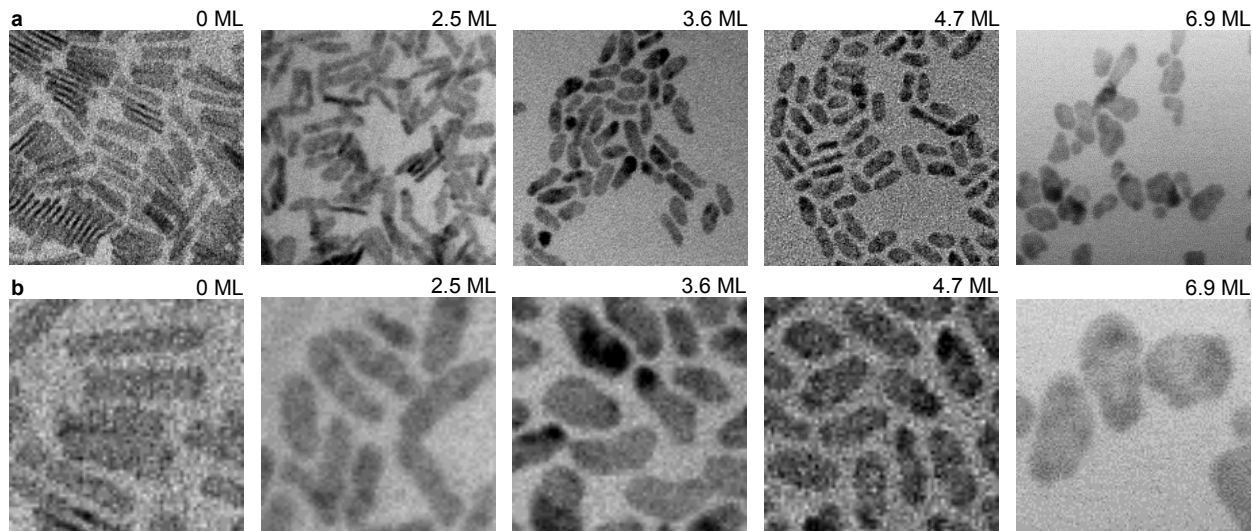


Figure 4-1. Representative TEM images of CdSe/PbS core/shell NPLs labeled with the number of PbS monolayers. (a) Each image is 125 nm × 125 nm. (b) Each image is 50 nm × 50 nm, highlighting changes in shape of the NPL face with increasing shell thickness.

thickness of the NPLs to be measured, confirming the direct relationship between increasing PbS shell reagents and thickness. Representative TEM images of the CdSe/PbS core/shell NPLs standing on end are shown in Figure 4-2. A change in the uniformity of thickness along the length of the NPLs is observed with increasing shell thickness, and the NPL thickness variation increases. While the profiles of 2.7 and 3.4 ML CdSe/PbS core/shell NPLs appear to be relatively smooth, the profiles of the 4.7 and 6.9 ML CdSe/PbS core/shell NPLs are more varied along the length of the NPLs. Slight variations in the angle of the crystal lattice and the NPL's alignment with the electron beams cause some difference in contrast along the length of the NPLs, which is also observed in CdSe core NPLs (Figure A2-2). In the high-resolution scanning transmission electron microscope (STEM) image of 6.9 ML CdSe/PbS core/shell NPLs, the shell growth appears to be particularly uneven, with a “dog-bone”-like profile, i.e. the ends are thicker than the middle. Furthermore, in this STEM image, the contrast between the core and shell can be observed, confirming the core/shell morphology. Optical spectroscopy measurements further confirm the increase in shell thickness observed in these TEM images (discussion below).

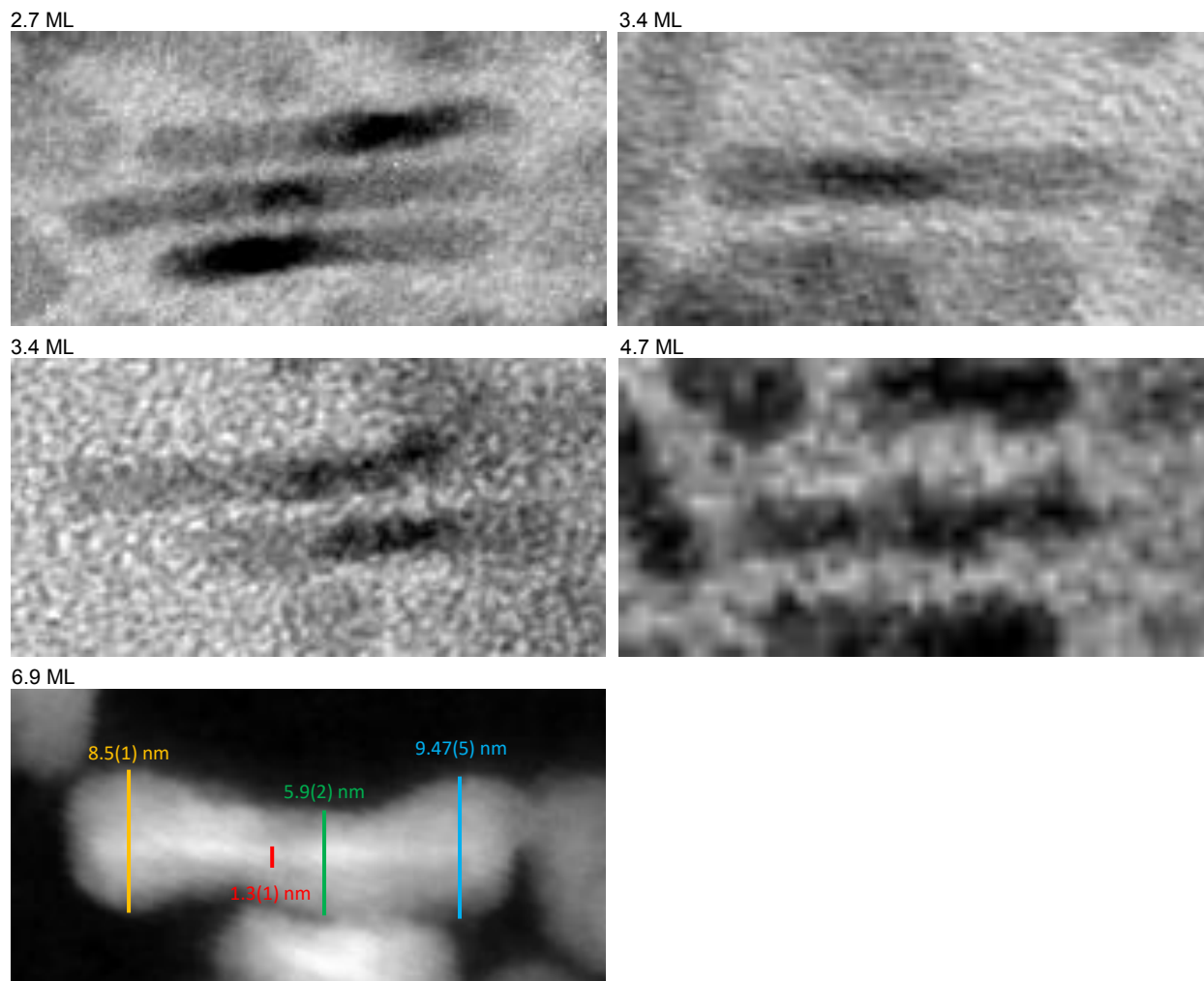


Figure 4-2. Edge view of CdSe/PbS core/shell NPLs with the average PbS shell thickness in number of monolayers labeled in the upper left of each image. The high resolution STEM image of a single 6.9 ML CdSe/PbS core/shell NPL demonstrates contrast between core and shell as well as thickness variation along the length of the NPL.

TEM images indicate the lateral size and shape of the NPLs change dramatically with shell growth. Instead of isotropic growth of a shell in all directions, as observed in the CdSe/PbS core/shell QDs,²⁷ or in CdSe/CdS core/shell NPLs,^{17,18} the length decreases from 30(3) nm for the CdSe core NPLs to 20(3) nm for the 4.5 ML CdSe/PbS core/shell NPLs, and the width increases from 7(1) nm to 9(1) nm for the growth of the 4.5 ML shell. In addition, the shape changes dramatically, from the starting rectangular shape to more oval-type shapes (Figure 4-1b).

Though the shape of the NPL faces changes with increasing shell thickness, the shape is relatively smooth and does not show the same signs of islanding as other core/shell NPLs. Both CdSe/CdS core/shell NPLs, synthesized by a similar method, and CdSe/CdS core/shell quantum belts have distorted shapes with the CdS shell appearing to grow in separate crystal domains similar to Stranski-Krastanov growth.^{17,30} This may arise from the large lattice mismatch between the CdSe core and CdS shell (4%).^{17,30} While the PbS shell growth is uneven in thickness, as seen in Figure 4-2, the NPL shape is not distorted in the same way, presumably due to the significantly smaller 1.9% difference in the bulk lattice constants (6.050 Å in ZB CdSe and 5.936 Å RS PbS).³¹ Due to this low lattice mismatch and the presence of an epitaxial interface in the CdSe/PbS core/shell quantum dots,²⁷ we hypothesize that the interface in the CdSe/PbS core/shell NPLs is also epitaxial. This is supported by the synthesis of some CdSe/PbS core/shell NPL samples with high quantum yield (see below).

With the loss of CdSe from the four corners of the CdSe NPL in the transition from rectangular CdSe core NPLs to the oval CdSe/PbS core/shell NPLs, it is possible that the increasing thickness is not the result of PbS deposition, but from the re-deposition of etched Cd and Se. In order to determine if this is occurring, we analyzed the Pb:Cd ratio of the CdSe/PbS core/shell NPLs using inductively coupled plasma mass spectroscopy (ICP-MS). The Pb:Cd ratio increases with increasing shell thickness in accord with the measured shell thickness from 0.7 (1.4 ML) to 1.5 (2.7 ML) to 3.9 (4.8 ML) (see Table A2-3 in Appendix 2 for full results). We therefore conclude that Cd etched from the CdSe NPL during shell deposition is not redeposited as the shell in either an alloy or as a pure cadmium chalcogenide shell.

4.2.3 Optical Spectroscopy.

Extinction and PL spectra were recorded to investigate the effects of the PbS shell on the energetics of the quantum-confinement states and the wave function overlap of the 1_e-1_{hh} and 1_e-1_{lh} transitions. See Tables S4 and S5 in Appendix 2 for details of the spectroscopic methods and results, including measured Stokes shifts, PL full width at half maximum (FWHM) values, PL excitation energies and PLQYs of each sample. All spectra were collected with an absorbance of between 0.05 and 0.1 at the lowest energy absorption peak (1_e-1_{hh}). The baseline of the extinction spectra were corrected for scattering, except for the CdSe/PbS 3.4 ML sample, which could not be corrected. The extinction spectra are plotted as solid lines in Figure 4-3, normalized to the same extinction at the energy of the lowest energy feature, the 1_e-1_{hh} absorption peak. The PL spectra, plotted as dashed lines in Figure 4-3b, are also normalized to a maximum of unity at the PL peak near the band gap. The spectra are offset for clarity. The PL spectra were collected at multiple excitation energies to ensure that there were no other PL features other than those identified in Figure 4-2. The CdSe NPL cores (black) exhibit characteristic, well-defined absorption transitions corresponding to the 1_e-1_{hh} , 1_e-1_{lh} , and 1_e-1_{soh} transitions. The transition energies were identified by taking the second derivative of the extinction spectra (see Figure A2-3 in Appendix 2) and are labeled in Figure 4-3 using tick marks. The CdSe core NPLs (PLQY of 4.8% and 7.9% for different batches) exhibit narrow, band edge PL (FWHM of 43 meV fitted to a single Gaussian peak) and broad, low-energy trap PL centered at approximately 1.75 eV. See Figure A2-4 for emission profile of CdSe core NPLs demonstrating trap emission. The band edge NPL emission is Stokes shifted by only 9 meV from the 1_e-1_{hh} absorption peak.

In the PbS shell deposition reaction, the CdSe core NPLs are first treated with TAA, which caps the NPLs with a layer of sulfide. This process results in the shifting of the first absorption and PL peaks to significantly lower energy (by ~ 100 meV) and a quenching of the

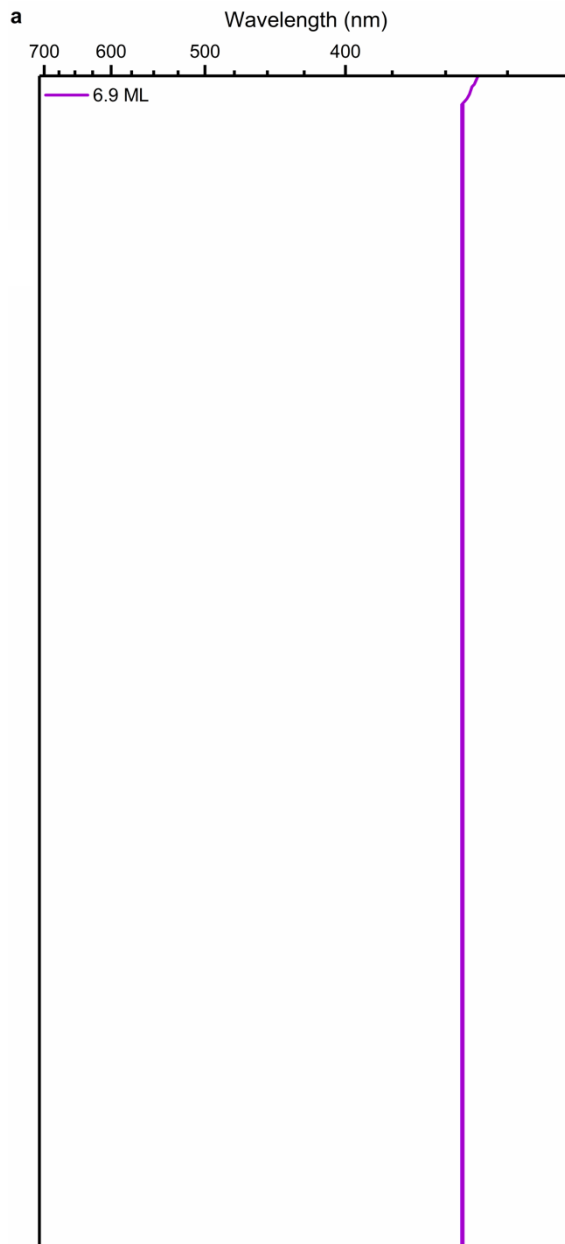


Figure 4-3. Extinction spectra (solid lines) and PL spectra (dashed lines) of CdSe NPLs and CdSe/PbS core/shell NPLs showing full UV-Vis absorption (a) and band edge region (b). The energies of the first three absorption transitions, identified from the second derivative, are labeled as tick marks for each spectrum. Spectra are offset for clarity.

PL; the PLQY drops from 7.9% for CdSe core NPLs to <0.01% for CdSe core NPLs treated with TAA.

With PbS shell deposition, the absorption and PL peaks of the CdSe/PbS core/shell NPLs shift to lower energy with increasing shell thickness by up to 480 meV. We attribute the

monotonic shift of the absorption and PL band edge transitions to lower energy to reduced quantum confinement of the electron and hole. Quantum confinement in the as-synthesized 30(3) $L \times 8(1) W \times 1.22 T$ nm CdSe NPLs is dominated by confinement in the thickness dimension. Using a simple 3D particle in a box model, as described in Chapter 1, the effective masses of the electron and hh in CdSe ($m_e^* = 0.12m_e$, $m_{hh}^* = 2.14m_e$),^{32,33} and the dimensions of the NPLs, the contribution of confinement in each dimension to the to the 1_e-1_{hh} transition energy can be estimated. Quantum confinement in the length, width, and thickness of the NPL increases the optical band gap by approximately 0.004, 0.052, and 2.223 eV, respectively. This simple 3D PIB model significantly overestimates the band gap, but demonstrates that confinement of charge carriers in the thickness of the NPL is significantly stronger than confinement in the length or width. We conclude that the shift of the band gap transition to lower energy with increasing PbS shell thickness is principally the result of reduced quantum confinement in the NPL thickness. Reduced confinement in the width of the NPL could have a small contribution to this trend. Additionally, the charge carriers could sample both the large band gap core and small band gap shell, reducing the optical band gap. Since the band gap of these particles does not approach the bulk PbS band gap, however, we believe that reduced quantum confinement dominates these band edge optical trends.

Although the PL is quenched with TAA treatment, the PL recovers for the CdSe/PbS core/shell samples. Table A2-5 details the values of the PLQY for the core and core/shell samples synthesized, with a maximum PLQY ranging from 17–21%, which is significantly greater than the value for the CdSe core NPLs used for those samples (4.8%). The shell growth in the 2.5, 3.4, and 4.7 ML samples eliminates the trap emission present in the CdSe core NPL sample, suggesting the core/shell interface is relatively free of defects (see Figure A2-4 for

emission spectrum of trap emission in CdSe core NPLs). The 6.9 ML CdSe/PbS core/shell NPL sample, however, does show significant trap emission below the absorption transition edge. This could be the result of poor surface passivation, demonstrating the presence of surface traps and population or occupation of these traps.

With PbS deposition, the widths of the PL and absorption features increase. Since the top and bottom facets of the as-synthesized CdSe core NPLs are atomically flat and the NPLs are all 4.5 MLs in thickness, there is little inhomogeneous broadening of the absorption and photoluminescence features associated with variations of the thickness within and between the core-only-NPLs. This uniformity in quantum confinement results in a narrow PL FWHM of 43 meV for the CdSe core NPLs. The breadth increases to a PL FWHM as large as 100 meV for the CdSe/PbS core/shell NPLs (see Table A2-4).¹⁰ This is likely because the PbS shell is not atomically smooth, and the width of the absorption and PL features increases due to the reduced homogeneity. The changes in the lateral size and shape of the NPLs could also contribute to this inhomogeneity, since the length, width, and shape of the CdSe/PbS core/shell NPLs have larger variations than the starting CdSe core NPLs. Similar broadening was also observed in CdSe/CdS core/shell NPLs in which the thickness inhomogeneity increases noticeably in high-resolution STEM images.¹⁷ With increasing shell thickness, the Stokes shift modestly increases from 10 meV (CdSe core NPLs) to as large as 33 meV (CdSe/PbS core/shell NPLs). Though the Stokes shift value increases by a factor of three, this is consistent with uneven PbS shell growth, similar to the CdSe/CdS core/shell NPLs.¹⁷ The modest Stokes shift is not consistent with a type-II heterostructure, which would cause a dramatic increase in the Stokes shift.²¹

4.2.4 Change in Absorption Transition Strength.

With increasing PbS shell thickness, the strength of the absorption transitions near the band edge and at high energies are observed to change relative to each other. In the case of the CdSe/PbS core/shell QDs (Chapter 3), we reasoned that the electron and hole wave functions are strongly affected by the electron and hole effective masses in the core and shell, but the effective mass approximation (EMA) calculations did not take into account the differences in band structure of CdSe and PbS. To help elucidate how the changing wave functions may contribute to the strengths of different excitation transitions, we studied the first two absorption transitions in CdSe core and CdSe/PbS core/shell NPLs ($1_{e-1_{hh}}$ and $1_{e-1_{lh}}$) as an indicator for the wave function overlap of the same electron wave function with different hole wave functions.

Since the area of the peak is proportional to $|\int \psi_e \psi_h|^2$ (where ψ_e is the electron wave function and ψ_h is the hole wave function), the relative area of the absorption transitions should provide a direct probe of the wave function overlap. The lowest-energy region of the absorption spectra, including only the first two features, were fitted to the sum of two Gaussians. The two fitted Gaussians are plotted in Figure A2-5 (red and blue) and the sum of these two Gaussians (black) is plotted for reference compared to the extinction data (gray squares). The fitting parameters and errors of the fitting are summarized in Table 4-1. Based on the centroid and curvature of the spectra, the error in the peak identification is 5-10 meV (see Table A2-4 in Appendix 2), which is approximately an order of magnitude greater than the error in the fit. With increasing shell thickness, the FWHM of the $1_{e-1_{hh}}$ feature increases from 39.4(6) meV (CdSe core NPLs) to 61.3(5)–75.2(9) meV (CdSe NPLs with TAA and CdSe/PbS core/shell NPLs). The FWHM of the fitted $1_{e-1_{lh}}$ feature, on the other hand, does not change monotonically, starting at 174(4) meV for the CdSe core NPLs and ranging from 157(2)–217(1) meV for CdSe

Table 4-1. Results of fitting the $1_{e-1_{hh}}$ and $1_{e-1_{lh}}$ transitions to the sum of two Gaussians. The energy (eV), full width at half maximum (FWHM, eV), and integrated area of each Gaussian are included. The ratio of areas is the ratio of the area of the light hole peak to the heavy hole peak. ΔE_{lh-hh} is the difference in energy between the light hole and heavy hole absorption transitions (eV). The fitting error (for the Energy, FWHM, and Area) and the propagated error (for Ratio of Areas and ΔE_{lh-hh}) are denoted in parentheses.

		0 ML	0 ML with S	2.5 ML	3.4 ML	4.7 ML	6.9 ML
Heavy Hole	Energy	2.4305(3)	2.3107(2)	2.1114(3)	2.0555(3)	2.0026(5)	1.9668(7)
	FWHM	0.0394(6)	0.0613(5)	0.0752(9)	0.0646(7)	0.063(1)	0.073(2)
	Area	0.0410(8)	0.0385(5)	0.061(2)	0.068(1)	0.068(2)	0.070(3)
Light Hole	Energy	2.589(2)	2.4646(4)	2.2786(5)	2.2131(6)	2.1678(9)	2.1472(9)
	FWHM	0.174(4)	0.217(1)	0.201(2)	0.157(2)	0.157(3)	0.184(3)
	Area	0.161(3)	0.349(1)	0.336(3)	0.256(3)	0.273(4)	0.416(7)
Ratio of Areas		3.9(1)	9.1(1)	2.2(2)	3.76(7)	4.0(1)	5.9(3)
ΔE_{lh-hh}		0.159(2)	0.1539(4)	0.1672(6)	0.1576(7)	0.165(1)	0.180(1)

NPLs with TAA and CdSe/PbS core/shell NPLs. The trend in the FWHM of the $1_{e-1_{hh}}$ Gaussian is clearly visible when plotting the truncated extinction spectra with the first absorption transition at the same energy (Figure 4-4); the onsets of the first absorption feature for the CdSe/PbS core/shell NPLs (orange, yellow, green, and purple) are clearly different than that of the CdSe

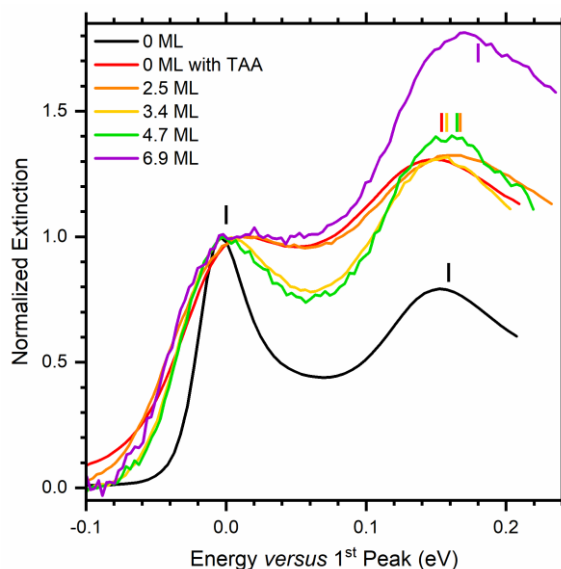


Figure 4-4. Extinction spectra of CdSe core and CdSe/PbS core/shell NPLs normalized to the first absorption peak and plotted with respect to the energy of the first fitted Gaussians. The energies of the first and second fitted Gaussians are labeled with ticks. See Table 4-1 for energies of $1_{e-1_{hh}}$ and $1_{e-1_{lh}}$ transitions.

core NPLs (black) or the CdSe NPLs with TAA (red). The ratio of the 1_e-1_{lh} to the 1_e-1_{hh} Gaussian areas generally increases with increasing thickness, indicating that the overlap between the 1_e and 1_{lh} wave functions increases relative to the overlap of the 1_e and 1_{hh} wave functions. This ratio does not increase monotonically, suggesting that other factors could also be at play that are affecting the absorption transition strengths.

Plotting the first two absorption transitions at the same energy (as in Figure 4-4) also reveals an important trend in the hole effective mass with increasing shell thickness. While in CdSe NPLs, the splitting between the 1_e-1_{hh} and 1_e-1_{lh} features decreases with increasing NPL thickness,³⁴ the splitting energy remains approximately constant in CdSe/PbS core/shell NPLs (see values in Table 4-1). Since the transitions associated with these features are between two different hole states with the same electron state, the relative difference in light hole and heavy hole effective mass can be inferred with changing shell thickness by using a simple one-dimensional effective mass approximation calculation. The difference in energy between the two features (ΔE_{lh-hh} , Eq. 4.1) can be rewritten using the 1D PIB model to include terms for the bulk transition energy and quantum confinement of the electron, light hole, and heavy hole (Eq. 4.2). This simplifies to the terms for the quantum confinement of the light hole and heavy hole (Eq. 4.3), which can be further simplified to Eq. 4.4. The difference in energy between the light hole and heavy hole features is therefore proportional to $1/m_{lh} - 1/m_{hh}$ (Eq. 4.4). Therefore, as the difference in the mass of the hh and lh increases or as the mass of both the hh and lh decrease, ΔE_{lh-hh} increases. In the case of the CdSe/PbS core/shell NPLs, ΔE_{lh-hh} remains relatively constant with increasing shell thickness. ΔE_{lh-hh} of the CdSe core NPLs is 157(2) meV while ΔE_{lh-hh} of the CdSe/PbS core/shell NPLs ranges from 141(2) to 179(1) meV (see Table 4-1). Since the size of the box (L) increases with increasing shell thickness, the difference in m_{lh} and

m_{hh} must be increasing with increasing shell thickness or the masses of both charge carriers must be decreasing with increasing shell thickness. See Table A2-6 in Appendix 2 for full details.

It is also possible that, instead of the relative masses changing, the effective length of the box is changing differently for the lh and hh. For example, if the hh tunnels into the shell more than the lh, the quantum confinement energy of the hh would decrease more quickly than the lh. Since the quantum confinement energy of the lh, having a smaller effective mass, is expected to decrease more quickly with increasing shell thickness, this difference in the effective length of the box could allow the splitting between the hh and lh features to remain constant with increasing shell thickness. Since the quantum confinement of the hh is so small (~ 0.118 eV) compared to the lh (~ 2.105 eV) in the CdSe core NPL assuming a simple 1D PIB model, it is unlikely that a difference in the effective box length is sufficient to offset the difference in effective mass. Furthermore, since the lh is at a higher energy due to the increased quantum confinement and smaller mass, we expect the lh to tunnel into the shell more than the hh. In this case, the energetic splitting between the 1_{e-1lh} and 1_{e-1hh} features is expected to decrease with increasing shell thickness.

$$\Delta E_{lh-hh} = E_{lh} - E_{hh} \quad \text{Eq. 4.1}$$

$$\Delta E_{lh-hh} = \left(E_{bulk} + \frac{\hbar^2}{8m_{lh}L^2} + \frac{\hbar^2}{8m_eL^2} \right) - \left(E_{bulk} + \frac{\hbar^2}{8m_{hh}L^2} + \frac{\hbar^2}{8m_eL^2} \right) \quad \text{Eq. 4.2}$$

$$\Delta E_{lh-hh} = \frac{\hbar^2}{8m_{lh}L^2} - \frac{\hbar^2}{8m_{hh}L^2} \quad \text{Eq. 4.3}$$

$$\Delta E_{lh-hh} = \frac{\hbar^2}{8L^2} \left(\frac{1}{m_{lh}} - \frac{1}{m_{hh}} \right) \quad \text{Eq. 4.4}$$

Since the hh and lh absorption features shift together, it could be reasoned that the overall shift is solely due to changing of quantum confinement of the electron state in the CB. This rationalization is likely not correct. If the PbS shell only decreases the quantum confinement

energy of the electron state, then the difference in energy between the hh and lh features would remain constant. It is unclear why this would be the case. The large effective mass of the hh, $m_{hh}^* = 2.14m_e$, could cause the hh to primarily be localized in the CdSe core.^{32,33} With increasing PbS shell thickness, therefore, the hh localization would prevent the quantum confinement energy from decreasing with increasing PbS shell thickness. The lh and electron in CdSe, however, have very similar effective masses, $m_e^* = 0.12m_e$ and $m_{lh}^* = 0.16m_e$.^{32,33} Any difference in the hh and electron behavior on the basis of a difference in effective mass would not apply to the lh state. Therefore, the localization of the hole states in the CdSe core on the basis of effective mass cannot explain the constant splitting between the hh and lh absorption features. Without another plausible reason for the hole eigenstate energies to remain constant, it is unlikely this is the case.

As the strength of the 1_e-1_{hh} and 1_e-1_{lh} transitions change with increasing shell thickness, the absorption profile also changes at much higher energy. Above the $n = 1$ transitions, the absorptivity of the CdSe core NPLs does not increase dramatically until approximately 3.8 eV, where the absorbance is twice that of the band edge feature. The absorption of the CdSe/PbS NPLs at higher energies, however, increases dramatically with increasing shell thickness relative to that of the 1_e-1_{hh} feature. The change in transition strength was approximated by normalizing the extinction spectra at 1.5 eV above the band edge 1_e-1_{hh} transition (see Figure 4-5). The CdSe core NPLs have a band edge transition that is 66.6% the intensity of the transition at 1.5 eV higher energy. The band edge 1_e-1_{hh} transition of the 6.9 ML CdSe/PbS core/shell NPLs, however, is just 7.1% the intensity compared to the higher energy absorption. Since the peak widths change, likely due to the loss of the atomic smoothness of the top and bottom facets, this renormalization of the extinction spectra does not allow the direct comparison of absorption

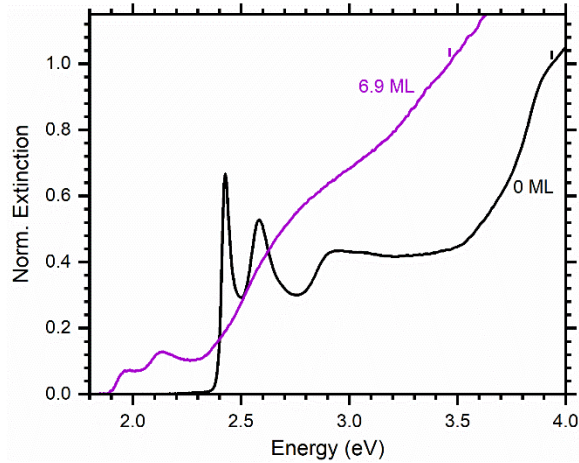


Figure 4-5. Extinction spectra of CdSe core NPLs and 6.9 ML CdSe/PbS core/shell NPLs normalized to the same extinction 1.5 eV above the first absorption peak (tic marks).

transition strength, but the change in transition intensity is significantly greater than the change in the peak area. Normalized at high energy, the 1_e-1_{hh} transition decreases in intensity by almost an order of magnitude (9.4 times) between the CdSe core and the 6.9 ML CdSe/PbS core/shell NPLs. This change is significantly greater than expected due to broadening of the spectral lines, which would only decrease the 1_e-1_{hh} intensity by a factor of 0.59 based on the fitting of the 1_e-1_{hh} transitions.

4.2.5 Wave Function Changes at Different Values of k .

Differences in CdSe and PbS Band Structure. The optical spectra and carrier relaxation dynamics in a core/shell NPL heterostructure depend on the alignment of the VB & CB, the dimensionality of the core and shell, the effective masses of the electrons and holes in the core and shell regions, and the wave functions of the quantum confinement states in these perturbed particle-in-a-box systems. As stated in Chapter 1, CdSe and PbS have different band structures with their band gaps at different values of k , shown schematically in Figure 4-6 for the Γ point (panels a-d) and L point (panels e-h). The bulk continuum of VB and CB states are represented by shaded boxes. The VB and CB energies at different points in k were found by comparing the

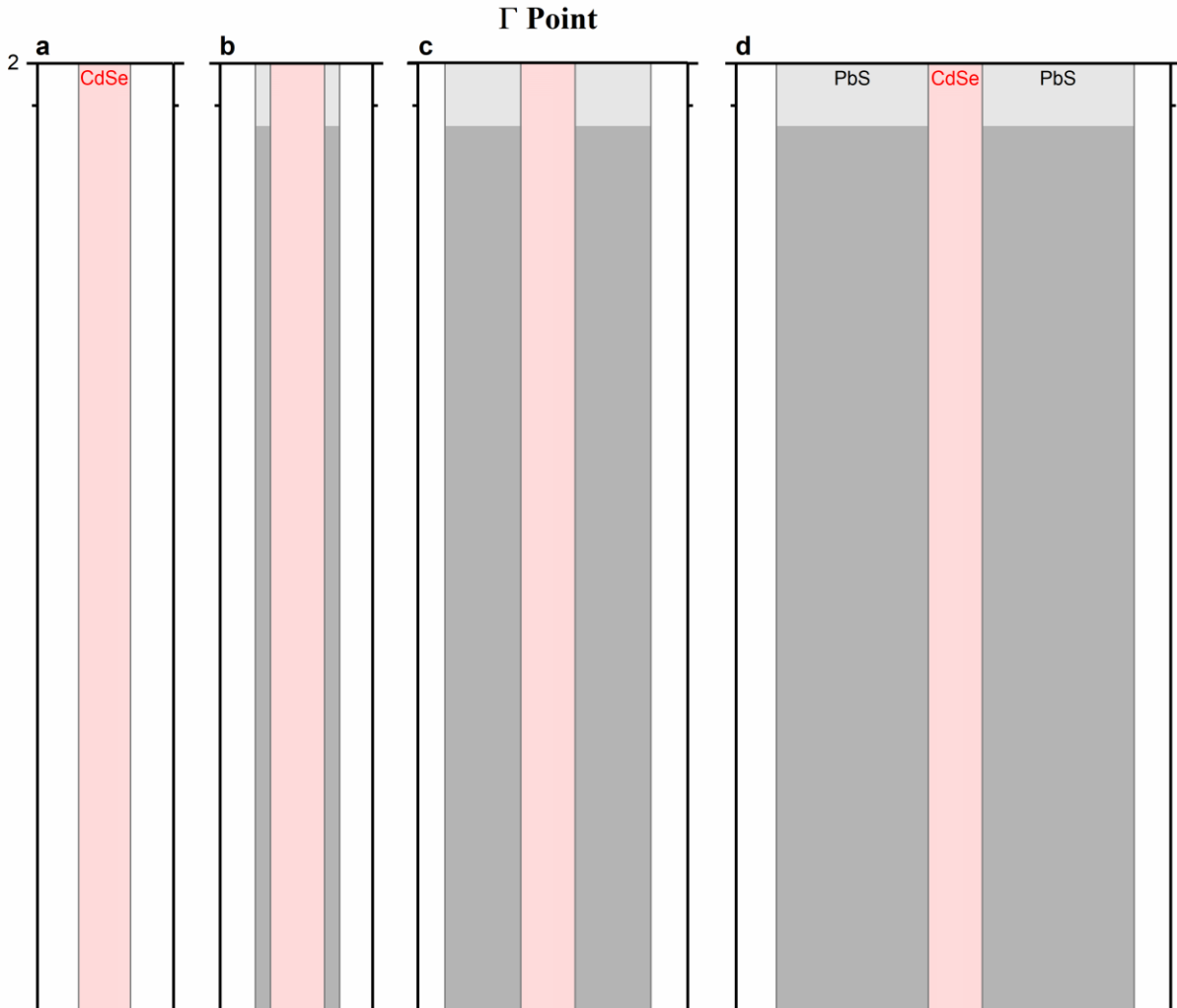


Figure 4-6. Bulk continuum of valence and conduction band states (shaded boxes) of CdSe (red) and PbS (black) at the Γ point (a-d) and L point (e-h) plotted as a function of position in CdSe core (a, e) and CdSe/PbS core/shell nanoplatelets with thin shell (b, f), moderately thick shell (c, g), and very thick shell (d, h). Hypothetical eigenstate energies of the least quantum confined conduction and valence band states for the core and core/shell nanoplatelets are plotted as solid blue lines.

relative changes in band structure diagrams to the reported valence band maximum (VBM) and conduction band minimum (CBM) at the band gap. For example, the absolute energies of the VBM and CBM of CdSe at the Γ point (its band gap), are at -5.541 and -3.865 eV with respect to vacuum (0 eV), respectively.³³ According to the CdSe band structure diagram, which was digitized from Szemjonov *et. al.*,³⁵ the VB and CB states at the L point are shifted by -0.711 and $+2.01$ eV compared to the band edge positions at the Γ point, for an absolute band energy of

−6.252 and −1.855 eV at the L point, respectively. At the PbS band gap at the L point, the VBM and CBM are at −4.72 and −4.35 eV, respectively, while at the Γ point, the VB and CB are at −7.564 and 0.486 eV.^{36,37} These band energies lead to a type-I band alignment at the Γ point and an inverse type-I band alignment at the L point (Figure 4-6b-d, 4-6f-h).

Effective mass approximation calculations at these two points in k would be beneficial in understanding the optoelectronic properties of the CdSe/PbS core/shell NPLs. Unfortunately, this is not possible since the effective mass approximation breaks down for CdSe at the L point and for PbS at the Γ point. The effective masses of the charge carriers in CdSe and PbS are well known since the band energies close to the band gap can be approximated to be parabolic with respect to k . The CdSe core has a single CB at the band gap with $m_e^* = 0.12m_e$.^{32,33} In the CdSe VB at the Γ point, there are two degenerate hole states with dissimilar effective masses, $m_{hh}^* = 2.14m_e$ and $m_{lh}^* = 0.16m_e$.^{32,33} At the band gap (L point) in PbS, the charge carriers have very small effective masses, $m_e^* = 0.105m_e$ and $m_h^* = 0.108m_e$.³⁸ Away from the band gap, the CdSe CB and VB edges at the L point go through an inflection point and are not parabolic. The CB (VB) state of PbS at the Γ point is at a local energetic maximum (minimum) and is therefore not parabolic. As a result, the effective mass approximation is not valid for these scenarios. We can, however, speculate how the charge carrier behavior is affected by the band alignment when an electron is excited at each point in k (Γ and L). The suggested eigenstate energies depicted in Figure 4-6 are strictly representations of how the eigenstate energies at the Γ and L points could change with increasing shell thickness and should not be considered a prediction of the eigenstate energy for a particular shell thickness.

At the Γ point, we expect the type-I band alignment to confine the charge carriers to the CdSe core, though the charge carrier wave functions can tunnel into the PbS shell, reducing the Γ

point transition energy. The energies of the band edge electron, hh, and lh states are schematically represented by solid blue lines in Figures 4-6a, 4-6b, 4-6c, and 4-6d in order of increasing PbS shell thickness. The electron and hole are strongly confined in the CdSe core (Figure 4-6a). After adding a thin PbS shell (Figure 4-6b), the quantum confinement is reduced as the charge carriers tunnel into the PbS shell. We expect this tunneling to continue with increasing shell thickness (Figure 4-6c), but the Γ point transition energy should not reach the bulk CdSe band gap even for a very thick shell (Figure 4-6d) since the charge carriers will always be confined by the relatively large gap between the CB and VB in the PbS shell.

At the L point, the charge carrier behavior is expected to be slightly more complicated, potentially transitioning from type-I to inverse type-I behavior, Figure 4-6e, 4-6f, 4-6g, and 4-6h. The gap between the quantum confinement electron and hole states in the CdSe core is very large (Figure 4-6g). After adding a thin PbS shell, the lowest energy L point transition could still be extremely large (larger than the gap between the VB and CB of CdSe at the L point, Figure 4-6f) due to the very small electron and hole effective masses in PbS. If this is the case, the electron and hole wave function amplitude could be greatest in the CdSe core and have strong overlap, indicative of type-I behavior. With increasing PbS shell thickness, as the strength of the quantum confinement decreases, the eigenstate energy of the electron would drop below the CdSe CB energy (Figure 4-6g). Likewise, the eigenstate energy of the hole would rise above the CdSe VB energy. For these eigenstate energies in a CdSe/PbS core/shell NPL with a moderately thick PbS shell, the electron and hole could be primarily localized in the PbS shell due to the potential barrier between the eigenstate energy and core band edges. On the other hand, since the charge carriers' localization is also based on their effective masses, which is unknown for CdSe at the L point, they could have varying degrees of localization in the core and shell. As a result, one of

the wave functions (or both) could significantly tunnel into the core while the other charge carrier is localized in the shell, resulting in varying wave function overlap and absorption transition strength. Tunneling of the wave function into the core is also dependent on the difference between the core band edge and the charge carrier's eigenstate energy; a small difference results in more tunneling of the wave function while a larger difference in energy results in less tunneling. For a thick PbS shell (Figure 4-6h), the charge carrier eigenstate energies are expected to approach the PbS bulk band gap with increasingly exclusive localization in the PbS shell. This inverse type-I heterostructure behavior would be characterized by strong wave function overlap. These charge carriers would also be available for extraction from the NPL into a device, such as a solar cell.

In this model, the lowest energy absorption transition could occur at different values of k depending on the PbS shell thickness. For CdSe core NPLs, the lowest energy absorption transition is at the Γ point. The lowest energy Γ point absorption transition is expected to be the smallest energy transition even for a thin PbS shell. For some PbS shell thickness, however, the absorption transition energy at the L point must be smaller than the Γ point band edge transition.

Application of the Γ and L Point Model to CdSe/PbS Core/Shell NPLs. This model could help explain two key trends in the absorption spectra of the CdSe/PbS core/shell NPLs. First, the 1_e-1_{hh} feature energy decreases with increasing PbS shell thickness. Second, the absorption transition strength at high energies dramatically increases *versus* the 1_e-1_{hh} transition.

The absorption spectra of the synthesized CdSe/PbS core/shell NPLs are consistent with this model. With increasing PbS shell thickness, the lowest energy absorption feature (1_e-1_{hh}) decreases in energy, but does not reach the bulk CdSe band gap. This matches the expected

trends depicted in Figure 4-6b, 4-6c, and 4-6d since the charge carriers in the CdSe core will always be confined by the large energetic gap between the VB and CB in PbS at the Γ point.

At the same time, the dramatic changes in the absorption transition strength could be the result of separate absorption transitions at the Γ and L points. As stated above, the absorption transition strength is proportional to the electron and hole wave function overlap, $|\int \psi_e \psi_h|^2$, but it is also affected by the total volume of the NPLs. To a first approximation, the low energy absorption at the Γ point must occur within the CdSe core (though the PbS shell can contribute due to tunneling of the charge carrier wave functions), and so the absorptivity at the Γ point would remain relatively constant with increasing shell thickness since the volume of the core remains relatively constant. On the other hand, the absorptivity at the L point would change significantly with increasing PbS shell thickness. The bulk L point absorption transition in the CdSe core is so large (4.397 eV) that absorption into these states was not measured (0 ML, Figure 4-3a). With increasing PbS shell thickness, the L point transition energy is expected to decrease. Since these states are primarily derived from the PbS shell, which increases in volume with increasing shell thickness, the L point absorptivity is also expected to increase. Tunneling of the charge carriers into the CdSe band could also increase the total volume of the NPL that can contribute to the lowest energy L point transition.

This difference in the absorptivity at the Γ and L points with increasing PbS shell thickness could be the cause of the large changes in the absorption transition strength above the band gap. The L point absorption transition may occur at too large an energy to observe in the extinction spectra of the 2.5 ML sample. The growth in absorptivity at high energy in the 3.4, 4.7, and 6.9 ML samples could be the L point band edge transition, which simultaneously decreases in energy with reduced quantum confinement and increases in strength with increasing

shell thickness (increasing PbS shell volume). The changing extinction spectra are therefore a result of differing absorption transitions that are accessed by either relatively low energy excitation into the CdSe dominated state at the Γ point or relatively high energy excitation in the PbS dominated state at the L point.

4.2.6 Other Factors.

While changes in the energetics and spatial sampling of the charge carriers are significantly impacted by changes in quantum confinement, the optoelectronic properties of CdSe/PbS core/shell NPLs may also be affected by a variety of other factors that complicate the wave function behavior. Furthermore, these factors complicate the fitting of the absorption spectra and are not considered in the Γ and L point model.

Phonon modes may couple to the quantum confinement transitions, such as the band-edge 1_e-1_{hh} transitions, which inhomogeneously broadens these spectral features.^{39,40} Dissimilar phonon modes of CdSe (ZB) NCs occur from surface and internal vibrations at 22.3 and 26.0 meV, respectively.³⁹ The phonon modes from RS PbS, meanwhile, are at 8.1 and 26 meV, corresponding to acoustic and optical phonons, respectively.⁴¹⁻⁴³ With increasing shell thickness, the energies of the phonon modes and the propensity for exciting phonon modes are expected to change, complicating the fitting of the absorption spectra. Additionally, with increasing PbS shell thickness, the excitonic fine structure could be shifting, changing the breadth of the absorption transitions.^{40,44-47} In CdSe, this excitonic fine structure leads to an energetic splitting between optically bright and dark states, which could change with increasing PbS shell thickness and the shape of the core/shell NPL.^{40,44-47}

The angular momentum of the valence bands could be integral in the mixing of electronic states between the CdSe core and PbS shell. The valence band states of CdSe and PbS are

represented in Figure 4-7, and are labeled with the total angular momentum quantum number (J) of each state.^{10,43,48} The CdSe heavy hole has $J = 3/2$ while the light hole and split off hole have $J = 1/2$.⁴⁰ The PbS valence band is split into five different states at three different energy levels with J values of $1/2$, $3/2$, and $5/2$.^{43,48} The two lower energy levels of PbS are doubly degenerate, where each state has a different J value. The coupling of the CdSe and PbS states in the core/shell structures could be limited to matching angular momentum quantum numbers. For example, the CdSe heavy hole ($3/2$) could only couple with the second and third PbS valence band states (also corresponding to $3/2$). This limitation in coupling is underdeveloped in the literature and could lead to significant changes in the optoelectronic properties of core/shell NCs. Since this coupling is expected to affect the hh and lh states differently, this will affect the energies and strengths of the $1e-1_{hh}$ and $1e-1_{lh}$ transitions. High level calculations are necessary to further probe the effect of this coupling. The coupling will change the energies, wave functions, and oscillator strengths of the transitions accessing these states.

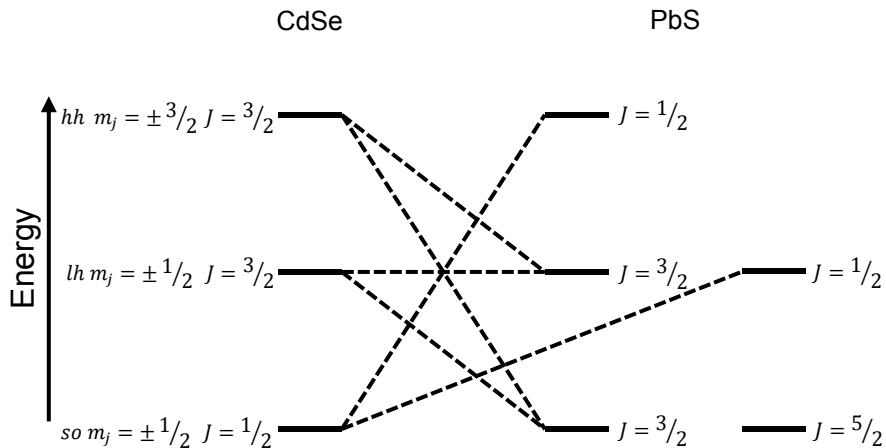


Figure 4-7. Proposed correlation diagram of valence band states in CdSe and PbS based on the total angular momentum quantum number (J) at the Γ and L points. Valence band states are in order of energy but are not to scale.

Lastly, while this work hypothesizes how the eigenstate energies and wave functions could change with varying PbS shell thickness for absorption transitions at different values of k , this work does not report calculations for these core/shell NPLs. Since the EMA model breaks

down for CdSe at the L point and PbS at the Γ point, higher level calculations are necessary to determine how the band structure of the CdSe/PbS core/shell heterostructure is affected by the combination of these two materials, as well as the size and shape of the NPLs, particularly focusing on the wave functions and eigenstate energies at the Γ and L points.

4.2.7 Photoluminescence Lifetimes.

The energetics of the CdSe/PbS core/shell NPL absorption and emission spectra suggest the charge carrier behavior, particularly the wave function localization, is impacted by the differences in band structure between the CdSe core and PbS shell. The quantum confinement states and wave function overlap can also be probed by measuring the PL lifetimes of core and core/shell NPLs. Reduced wave function overlap in heterostructures increases the photoluminescence lifetimes in core/shell QDs and NPLs^{20,21,49-51} while increased wave function overlap reduces the photoluminescence lifetimes in core/shell QDs⁵². Since the comparison of the core and core/shell PL lifetimes is so important, it is vital to understand how the charge carriers behave in the core CdSe NPLs.

The PL lifetime in CdSe core NPLs is dictated by two major components: (1) prompt emission and (2) delayed emission.⁵³ After a NPL is optically excited, the ground state exciton can radiatively recombine on a relatively fast timescale with a lifetime of only a few nanoseconds. Recombination on this fast timescale occurs for less than 50% of the excited charge carriers that eventually radiatively recombine⁵³ and has been attributed to the giant oscillator strength transition.^{10,53} In the samples studied by Rabouw *et. al.*, which were excited using a long exposure time and high fluences, more than 50% of the charge carriers that eventually radiatively recombine are trapped in the NPL.⁵³ These trapped charge carriers can undergo a de-trapping process, restoring the original excitonic state from which the charge

carriers can radiatively recombine on the same lifetime as the non-trapped excitonic radiative recombination.

Further studies in QDs have revealed that the excitation pulse width strongly influences the proportion of excitons that undergo delayed luminescence; a larger excitation pulse width results in increased delayed luminescence.⁵⁴ Since the effect of the excitation pulse width has not been studied for CdSe NPLs, and the delayed luminescence in CdSe NPLs was studied using a relatively large pulse width, it is likely that the proportion of excitons that undergo delayed emission for a very short excitation pulse duration is significantly smaller than reported. Nevertheless, this trapping and de-trapping mechanism may significantly influence the exciton lifetimes.

Shell deposition can change both the excitonic PL lifetime (the prompt emission) and the trapping. Rabouw *et. al.* also studied CdSe/CdS core/shell NPLs, in which the short PL decay kinetics are significantly slower than the CdSe core NPLs.⁵³ CdSe/CdS core/shell NPLs are formally a type-I heterostructure, which would suggest a high degree of wave function overlap and therefore a short PL lifetime, but the differing behavior of the electron and hole reduces the electron–hole overlap. The difference in energies between the CBM of the core and shell is very small, allowing the electron to delocalize across the entire thickness of the core/shell NPL while the hole is confined by the relatively large energetic difference between the core and shell VBM. This reduced wave function overlap slows the radiative recombination and reduces the trapping processes, resulting in significantly different prompt emission behavior. By reducing the trapping probability, the CdS shell deposition changes the proportion of charge carriers that are trapped and de-trapped. In the CdSe core NPLs, 56% of the excitons that radiatively recombine are trapped and de-trapped before emitting at the band edge. In CdSe/CdS core/shell NPLs, only

16% of the excitons undergo the trapping/de-trapping process before radiative recombination. Though the number of excitons that go through trapping and de-trapping is different in the CdSe core and CdSe/CdS core/shell NPLs, the resultant long PL lifetime is almost the same, suggesting that the reversible trapping could occur at sites that are intrinsic to CdSe or that are present at the CdSe/CdS core/shell interface. Again, the proportion of excitons that undergo prompt *versus* delayed radiative recombination is dependent on the excitation conditions,⁵⁴ which was not tested for the CdSe core and CdSe/CdS core/shell NPLs, but these studies demonstrate the effect that a shell can have on PL lifetimes of core/shell NPLs.

In order to probe the relative overlap of the charge carriers' wave functions, we studied the time-resolved PL of CdSe core and CdSe/PbS core/shell NPLs, plotted in Figure 4-8 (scatter plot) with the decay fit (solid line). All samples were excited at 2.755 eV (450 nm) for PL decay measurements. The thickness of these samples could not be measured directly, as TEM images did not show any NPLs standing on edge, and so the thickness was estimated from the energy of

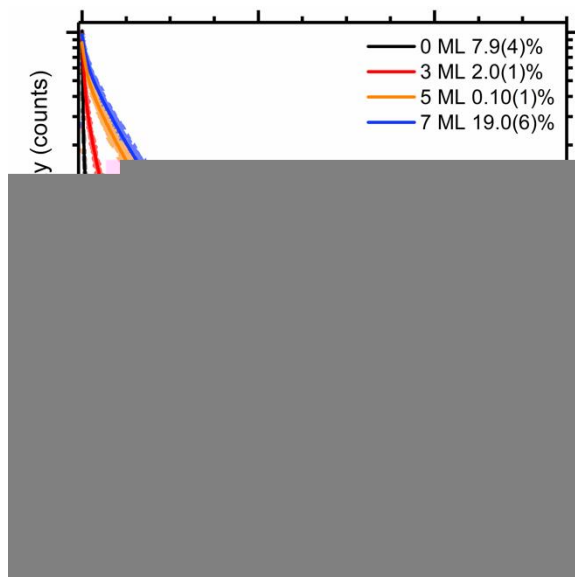


Figure 4-8. Measured photoluminescence lifetimes of CdSe core NPLs and CdSe/PbS core/shell NPLs (data points) with the fitted exponential decay (line) labeled with the photoluminescence quantum yield.

the first absorption peak by comparing it to samples for which the thickness could be measured. Extinction and PL spectra of the CdSe core and CdSe/PbS core/shell NPLs used to study the PL lifetimes are plotted in Figure A2-6 in Appendix 2. The PLQY when excited at 3.1 eV (400 nm), average lifetime, lifetime of each exponential component, and the percent contribution of each component (organized by short, medium and long lifetimes) can be found in Table 4-2.

Additionally, the time for the PL intensity to reach half its original value, $\tau_{1/2}$, is included in Table 4-2 for comparison to other studies that report $\tau_{1/2}$. The PL intensity decay data were fit to the sum of three exponentials, but a full Bayesian analysis is necessary to determine the most probable number of exponential decay functions. The fitting error for each lifetime and percent contribution is noted in parentheses. The amplitude for each exponential decay and methods for calculating the percent contribution of each component and the average lifetime can be found in Table A2-7 in Appendix 2. The instrument response function is plotted in Figure A2-7 in Appendix 2.

Table 4-2. Results of fitting time-correlated single-photon counting data for CdSe core and CdSe/PbS core/shell nanoplatelets with the percent contribution (% Cont.) and lifetime of each component. The PLQY was collected by exciting the samples at 3.1 eV. The time-resolved PL data was collected exciting the samples at 2.755 eV.

#ML	PLQY (%)	Short		Medium		Long		Average Lifetime (ns)	$\tau_{1/2}$ (ns)
		% Cont.	Lifetime (ns)	% Cont.	Lifetime (ns)	% Cont.	Lifetime (ns)		
0	7.9(4)	18(2)	0.384(2)	30(3)	3.36(5)	52(6)	37.1(7)	20(2)	0.35
3	2.0(1)	8(1)	0.90(1)	42(3)	5.55(7)	51(4)	35.5(6)	20(1)	1.39
5	0.10(1)	4.2(2)	2.08(6)	52(2)	15.5(2)	43(3)	64(1)	36(2)	3.99
7	19.0(6)	3.3(2)	2.05(6)	54(2)	16.6(2)	43(3)	61(1)	35(1)	6.59

The observed PL decay of the CdSe core NPLs (black in Figure 4-8) is very short and roughly matches the lifetimes measured in other studies. The average lifetime of the core NPLs was 20(2) ns, which is similar to the average lifetime of 24 ns reported by Kelestemur *et. al.* for CdSe NPLs of the same thickness.²⁰ The $\tau_{1/2}$ for differing thicknesses of CdSe NPLs was

reported by Ithurria *et. al.* as 0.4 ns (3.5 ML, 1% PLQY), 3.5 ns (4.5 ML, ~30% PLQY), and 3.99 ns (5.5 ML, ~30% PLQY).¹⁰ $\tau_{1/2}$ for the 4.5 ML CdSe cores studied here is 0.35 ns, which is shorter than the $\tau_{1/2}$ lifetime reported for the same thickness, though the PLQY of the CdSe cores studied here is lower (7.9(4)%) than those synthesized by Ithurria *et. al.* This could be indicative of a higher density of traps, leading to the shorter PL lifetime. Nevertheless, the PL lifetime in the short time window is similar to the lifetimes reported previously.

After PbS shell deposition, both the percent contribution and the lifetime of each component changes. Generally, the contribution of the short component decreases while the contribution of the medium component increases. The lifetimes of each exponential component increases with increasing shell thickness. With increasing shell thickness, the contribution of the short lifetime component reduces from 18(2)% to 3.3(2)% and the lifetime also increases from 0.384(2) ns to 2.05(6) ns. While the percent contribution of the longest lifetime component decreases slightly from 52(6)% to 43(3)%, it represents the contribution from a longer lifetime, increasing from 37.1(7) ns (core) to a maximum of 64(1) ns (core/shell). Lastly, the medium lifetime increases dramatically from 3.36(5) ns to 16.6(2) ns and its contribution increases from 30(3)% to 54(2)%.

The overall increased lifetime in the CdSe/PbS core/shell NPLs could be the result of two major effects of the different band structures of CdSe and PbS. First, changes to the band edge wave functions could increase the lifetime of the prompt excitonic emission. Since the 1_e-1_{hh} transition shifts to lower energy, one or both of the band edge wave functions must delocalize into the PbS shell, reducing the total wave function overlap, thereby increasing the PL lifetime. Similar behavior was observed in CdSe/CdS core/shell NPLs, in which the electron delocalized into the shell more than the hole, reducing the wave function overlap.⁵³ Second, the relaxation

pathway for excited charge carriers could change significantly as a result of the CdSe/PbS core/shell heterostructure. The PL lifetimes were measured with an excitation energy of 2.755 eV, which could be large enough to excite above the lowest energy L point quantum confinement states. If the exciton is generated at the L point, then it must couple to phonons in order to change k to reach the Γ point before relaxing to the band edge at the Γ point. This relaxation pathway could take a longer amount of time than relaxation from an excited state at the Γ point to the lowest energy quantum confinement state at the Γ point, thereby increasing the observed PL lifetime.

It is also possible that the PbS shell deposition changes the PL dynamics by changing the number of charge carriers that are trapped, as in CdSe/CdS core/shell NPLs.⁵³ In order to quantify these changes, further studies of the long PL lifetimes (up to 20 μ s) of CdSe/PbS core/shell NPLs are necessary using a short excitation pulse and low photon fluence.

The increase in lifetime is also consistent despite the changes in PLQY. The 5 ML and 7 ML samples, despite having PLQY that differ by over two orders of magnitude (0.10(1) *versus* 19.0(6)%) have almost identical average photoluminescence lifetimes. Since the PLQY and PL lifetimes were measured at two different excitation energies, it is possible that the apparent lack of correlation between PL lifetimes and PLQY is simply the result of the differing excitation energies. This could arise from the different states or relaxation pathways available when charge carriers are excited with different excitation energies, which has been shown to cause an excitation energy dependence to the PLQY.⁵⁵⁻⁵⁷ In this situation, the samples would have a strong excitation energy dependence, indicating different PL lifetimes at excitation energies with different PLQYs.

The samples do not have a strong excitation energy dependence between the excitation energies used for measuring the PLQY and PL lifetimes. This is demonstrated by the $PLE/1 - T$ spectra (Figure 4-9), which gives the relative PLQY at different excitation energies.⁵⁵ If the behavior was significantly different, the values of the $PLE/1 - T$ spectra would be significantly different between the energy at which the PL lifetime was collected (2.755 eV) and the PLQY was collected (3.1 eV). Instead, the $PLE/1 - T$ value is lower at the excitation energy used for the PLQY measurement by 9.6% for the 5 ML sample and 7.4% for the 7 ML sample. Since the PLQYs of these two samples are different by over two orders of magnitude, this <10% difference cannot explain the similar behavior in the PL lifetimes.

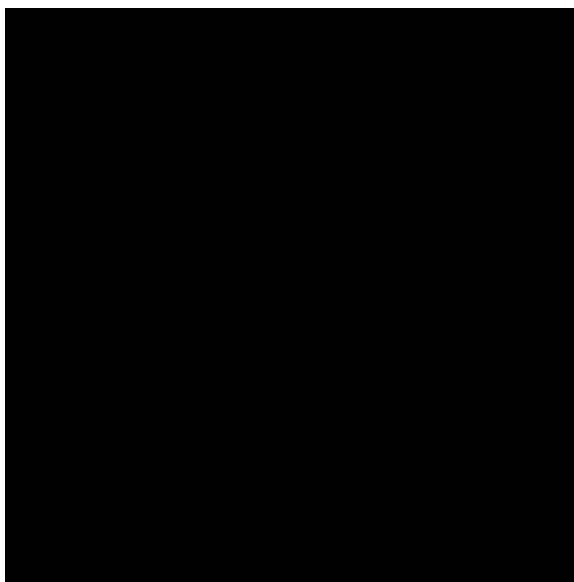


Figure 4-9. PLE/1-T spectra of CdSe core and CdSe/PbS core/shell NPLs normalized to the first data point used for the measurement of the photoluminescence lifetimes. The energies as which the photoluminescence quantum yields (3.1 eV) and the PL lifetimes (2.7 eV) are labeled as dotted lines.

The apparently contradictory response of the ensemble PLQY and PL lifetime could be the result of a mixture of “bright” and “dark” NPLs that, in a simplistic interpretation, have 100% and 0% PLQY, respectively.⁵³ PL lifetime measurements only measure the PL from the “bright” NPLs, while the PLQY measures the relative population of the “bright” and “dark”

NPLs. With changing NPL composition, morphology, and surface passivation, the shell synthesis could either eliminate trap sites or cause the formation of trap sites, changing the fraction of “bright” and “dark” NPLs, thereby changing the ensemble PLQY. Changing wave functions and quantum confinement states with PbS shell synthesis change the PL lifetimes in the “bright” NPLs. Therefore, the PL lifetimes of the “bright” NPLs could be similar due to the similar effect the PbS shell has on the electron and hole wave functions.

4.3 Conclusions

We have developed a synthetic scheme for making CdSe/PbS core/shell NPLs. Unlike the synthesis of CdSe/PbS core/shell QDs, PbS shell growth on CdSe NPL cores is not isotropic. Instead, the thickness and width increase and the length decreases with shell growth. The first absorption and PL peaks shift to lower energy with increasing shell thickness, indicating a decrease in quantum confinement and a delocalization of the electron and hole wave functions over the entire NPL. Similar to the CdSe/PbS core/shell QDs, the high energy absorption transitions increase in strength relative to the lower energy absorption feature. These changes to the energies and strength of the absorption transitions could be the result of the difference in the band structure at the Γ and L points, which could separate absorption into the CdSe core and PbS shell dominated states, respectively. The optoelectronic properties of the CdSe/PbS core/shell NPLs were further studied using PL lifetimes, which increase with increasing PbS shell thickness. Changes to the PL lifetimes also indicate the delocalization and reduced overlap of the electron and hole wave functions.

Charge carrier separation in CdSe/PbS core/shell NPLs could allow for improved selective charge transport as a result of the partial charge separation and long NPL lateral dimensions. NCs with different band structures could also be used as luminescent solar

concentrators (LSCs) due to the large difference between the strong absorption and photoluminescence transitions as a result of the different volume of core and shell materials that allow absorption at different points in k . These properties, coupled with the directional light emission of self-assembled NPLs, make this system even more attractive for use in LSCs than CdSe/PbS core/shell QDs. Lastly, multiexciton generation (MEG) in PbS nanosheets is significantly enhanced compared to NCs with higher degrees of quantum confinement because of the much higher density of states in nanosheets.⁵⁸ CdSe/PbS core/shell NPLs could combine the advantages of the increased density of states in NPLs with the enhanced MEG as a result of the interaction between the high band gap core with a low band gap shell.

4.4 References

- (1) Buhro, W. E.; Colvin, V. L., Shape Matters. *Nat. Mater.* **2003**, *2*, 138.
- (2) Murray, C. B.; Norris, D. J.; Bawendi, M. G., Synthesis and Characterization of Nearly Monodisperse CdE (E = Sulfur, Selenium, Tellurium) Semiconductor Nanocrystallites. *J. Am. Chem. Soc.* **1993**, *115*, 8706-8715.
- (3) Peng, X.; Manna, L.; Yang, W.; Wickham, J.; Scher, E.; Kadavanich, A.; Alivisatos, A. P., Shape Control of CdSe Nanocrystals. *Nature* **2000**, *404*, 59-61.
- (4) Wang, F.; Dong, A.; Buhro, W. E., Solution–Liquid–Solid Synthesis, Properties, and Applications of One-Dimensional Colloidal Semiconductor Nanorods and Nanowires. *Chem. Rev.* **2016**, *116*, 10888-10933.
- (5) Lhuillier, E.; Pedetti, S.; Ithurria, S.; Nadal, B.; Heuclin, H.; Dubertret, B., Two-Dimensional Colloidal Metal Chalcogenides Semiconductors: Synthesis, Spectroscopy, and Applications. *Acc. Chem. Res.* **2015**, *48*, 22-30.
- (6) Wang, F.; Wang, Y.; Liu, Y.-H.; Morrison, P. J.; Loomis, R. A.; Buhro, W. E., Two-Dimensional Semiconductor Nanocrystals: Properties, Templated Formation, and Magic-Size Nanocluster Intermediates. *Acc. Chem. Res.* **2015**, *48*, 13-21.
- (7) Nasilowski, M.; Mahler, B.; Lhuillier, E.; Ithurria, S.; Dubertret, B., Two-Dimensional Colloidal Nanocrystals. *Chem. Rev.* **2016**, *116*, 10934-10982.
- (8) Jana, S.; Phan, T. N. T.; Bouet, C.; Tessier, M. D.; Davidson, P.; Dubertret, B.; Abécassis, B., Stacking and Colloidal Stability of CdSe Nanoplatelets. *Langmuir* **2015**, *31*, 10532-10539.
- (9) Abécassis, B.; Tessier, M. D.; Davidson, P.; Dubertret, B., Self-Assembly of CdSe Nanoplatelets into Giant Micrometer-Scale Needles Emitting Polarized Light. *Nano Lett.* **2014**, *14*, 710-715.

- (10) Ithurria, S.; Tessier, M. D.; Mahler, B.; S M Lobo, R. P.; Dubertret, B.; Efros, A. L., Colloidal Nanoplatelets with Two-Dimensional Electronic Structure. *Nat. Mater.* **2011**, *10*, 936-941.
- (11) Naeem, A.; Masia, F.; Christodoulou, S.; Moreels, I.; Borri, P.; Langbein, W., Giant Exciton Oscillator Strength and Radiatively Limited Dephasing in Two-Dimensional Platelets. *Phys. Rev. B: Condens. Matter Mater. Phys* **2015**, *91*, 121302.
- (12) Achtstein, A. W.; Schliwa, A.; Prudnikau, A.; Hardzei, M.; Artemyev, M. V.; Thomsen, C.; Woggon, U., Electronic Structure and Exciton–Phonon Interaction in Two-Dimensional Colloidal CdSe Nanosheets. *Nano Lett.* **2012**, *12*, 3151-3157.
- (13) Yoon, D.-E.; Kim, W. D.; Kim, D.; Lee, D.; Koh, S.; Bae, W. K.; Lee, D. C., Origin of Shape-Dependent Fluorescence Polarization from CdSe Nanoplatelets. *J. Phys. Chem. C* **2017**, *121*, 24837-24844.
- (14) Gao, Y.; Weidman, M. C.; Tisdale, W. A., CdSe Nanoplatelet Films with Controlled Orientation of their Transition Dipole Moment. *Nano Lett.* **2017**, *17*, 3837-3843.
- (15) Zhou, Y.; Buhro, W. E., Reversible Exchange of L-Type and Bound-Ion-Pair X-Type Ligation on Cadmium Selenide Quantum Belts. *J. Am. Chem. Soc.* **2017**, *139*, 12887-12890.
- (16) Zhou, Y.; Wang, F.; Buhro, W. E., Large Exciton Energy Shifts by Reversible Surface Exchange in 2D II-VI Nanocrystals. *J. Am. Chem. Soc.* **2015**, *137*, 15198-15208.
- (17) Mahler, B.; Nadal, B.; Bouet, C.; Patriarche, G.; Dubertret, B., Core/Shell Colloidal Semiconductor Nanoplatelets. *J. Am. Chem. Soc.* **2012**, *134*, 18591-18598.
- (18) Ithurria, S.; Talapin, D. V., Colloidal Atomic Layer Deposition (c-ALD) using Self-Limiting Reactions at Nanocrystal Surface Coupled to Phase Transfer Between Polar and Nonpolar Media. *J. Am. Chem. Soc.* **2012**, *134*, 18585-18590.

- (19) Bouet, C.; Laufer, D.; Mahler, B.; Nadal, B.; Heuclin, H.; Pedetti, S.; Patriarche, G.; Dubertret, B., Synthesis of Zinc and Lead Chalcogenide Core and Core/Shell Nanoplatelets Using Sequential Cation Exchange Reactions. *Chem. Mater.* **2014**, *26*, 3002-3008.
- (20) Kelestemur, Y.; Guzelurk, B.; Erdem, O.; Olutas, M.; Gungor, K.; Demir, H. V., Platelet-in-Box Colloidal Quantum Wells: CdSe/CdS@CdS Core/Crown@Shell Heteronanoplatelets. *Adv. Func. Mat.* **2016**, *26*, 3570-3579.
- (21) Pedetti, S.; Ithurria, S.; Heuclin, H.; Patriarche, G.; Dubertret, B., Type-II CdSe/CdTe Core/Crown Semiconductor Nanoplatelets. *J. Am. Chem. Soc.* **2014**, *136*, 16430-16438.
- (22) Anderson, N. C.; Hendricks, M. P.; Choi, J. J.; Owen, J. S., Ligand Exchange and the Stoichiometry of Metal Chalcogenide Nanocrystals: Spectroscopic Observation of Facile Metal-Carboxylate Displacement and Binding. *J. Am. Chem. Soc.* **2013**, *135*, 18536-18548.
- (23) Houtepen, A. J.; Hens, Z.; Owen, J. S.; Infante, I., On the Origin of Surface Traps in Colloidal II–VI Semiconductor Nanocrystals. *Chem. Mater.* **2017**, *29*, 752-761.
- (24) Kroupa, D. M.; Vörös, M.; Brawand, N. P.; McNichols, B. W.; Miller, E. M.; Gu, J.; Nozik, A. J.; Sellinger, A.; Galli, G.; Beard, M. C., Tuning Colloidal Quantum Dot Band Edge Positions Through Solution-Phase Surface Chemistry Modification. *Nat. Commun.* **2017**, *8*, 15257.
- (25) Yao, Y.; Zhou, Y.; Sanderson, W. M.; Loomis, R. A.; Buhro, W. E., Metal-Halide-Ligated Cadmium Selenide Quantum Belts by Facile Surface Exchange. *Chem. Mater.* **2018**, *30*, 2848-2857.
- (26) Harris, R. D.; Bettis Homan, S.; Kodaimati, M.; He, C.; Nepomnyashchii, A. B.; Swenson, N. K.; Lian, S.; Calzada, R.; Weiss, E. A., Electronic Processes within Quantum Dot-Molecule Complexes. *Chem. Rev.* **2016**, *116*, 12865-12919.

- (27) Wieliczka, B. M.; Kaledin, A. L.; Buhro, W. E.; Loomis, R. A., Wave Function Engineering in CdSe/PbS Core/Shell Quantum Dots. *ACS Nano* **2018**, *12*, 5539-5550.
- (28) Pelton, M.; Andrews, J. J.; Fedin, I.; Talapin, D. V.; Leng, H.; O'Leary, S. K., Nonmonotonic Dependence of Auger Recombination Rate on Shell Thickness for CdSe/CdS Core/Shell Nanoplatelets. *Nano Lett.* **2017**, *17*, 6900-6906.
- (29) Yeltik, A.; Delikanli, S.; Olutas, M.; Kelestemur, Y.; Guzelurk, B.; Demir, H. V., Experimental Determination of the Absorption Cross-Section and Molar Extinction Coefficient of Colloidal CdSe Nanoplatelets. *J. Phys. Chem. C* **2015**, *119*, 26768-26775.
- (30) Morrison, C. E.; Wang, F.; Rath, N. P.; Wieliczka, B. M.; Loomis, R. A.; Buhro, W. E., Cadmium Bis(phenyldithiocarbamate) as a Nanocrystal Shell-Growth Precursor. *Inorg. Chem.* **2017**, acs.inorgchem.7b01711-acs.inorgchem.7b01711.
- (31) Madelung, O., *Semiconductors - Basic Data*. Springer-Verlag: 1996.
- (32) Kim, Y. D.; Klein, M. V.; Ren, S. F.; Chang, Y. C.; Luo, H.; Samarth, N.; Furdyna, J. K., Optical Properties of Zinc-Blende CdSe and $Zn_xCd_{1-x}Se$ Films Grown on GaAs. *Phys. Rev. B: Condens. Matter Mater. Phys* **1994**, *49*, 7262-7270.
- (33) Cadmium Selenide (CdSe) Electronic Properties, Cubic Modification. In *Landolt-Börnstein - Group III Condensed Matter 41B (II-VI and I-VII Compounds; Semimagnetic Compounds)*, Madelung, O.; Rössler, U.; Schulz, M., Eds. Springer-Verlag: Berlin/Heidelberg, 1999; pp 1-6.
- (34) Christodoulou, S.; Climente, J. I.; Planelles, J.; Brescia, R.; Prato, M.; Martín-García, B.; Khan, A. H.; Moreels, I., Chloride-Induced Thickness Control in CdSe Nanoplatelets. *Nano Lett.* **2018**, *18*, 6248-6254.
- (35) Szemjonov, A.; Pauporté, T.; Ciofini, I.; Labat, F., Investigation of the Bulk and Surface Properties of CdSe: Insights from Theory. *Phys. Chem. Chem. Phys.* **2014**, *16*, 23251-23259.

- (36) Reiss, P.; Couderc, E.; De Girolamo, J.; Pron, A., Conjugated Polymers/Semiconductor Nanocrystals Hybrid Materials—Preparation, Electrical Transport Properties and Applications. *Nanoscale* **2011**, *3*, 446-489.
- (37) Elfurawi, U. Optical and Electronic Properties of PbS Colloidal Nanocrystals. 2012.
- (38) Springholz, G.; Bauer, G., 9.1 IV-VI Semiconductors: General Properties. In *Landolt-Börnstein - Group III Condensed Matter 34A*, Springer-Verlag Berlin Heidelberg: Berlin, Heidelberg, 2013; Vol. 16, pp 415-421.
- (39) Beecher, A. N.; Dziatko, R. A.; Steigerwald, M. L.; Owen, J. S.; Crowther, A. C., Transition from Molecular Vibrations to Phonons in Atomically Precise Cadmium Selenide Quantum Dots. *J. Am. Chem. Soc.* **2016**, *138*, 16754-16763.
- (40) Shornikova, E. V.; Biadala, L.; Yakovlev, D. R.; Sapega, V. F.; Kusrayev, Y. G.; Mitioglu, A. A.; Ballottin, M. V.; Christianen, P. C. M.; Belykh, V. V.; Kochiev, M. V.; Sibeldin, N. N.; Golovatenko, A. A.; Rodina, A. V.; Gippius, N. A.; Kuntzmann, A.; Jiang, Y.; Nasilowski, M.; Dubertret, B.; Bayer, M., Addressing the Exciton Fine Structure in Colloidal Nanocrystals: the Case of CdSe Nanoplatelets. *Nanoscale* **2018**, *10*, 646-656.
- (41) Geiregat, P.; Delerue, C.; Justo, Y.; Aerts, M.; Spoor, F.; Van Thourhout, D.; Siebbeles, L. D. A.; Allan, G.; Houtepen, A. J.; Hens, Z., A Phonon Scattering Bottleneck for Carrier Cooling in Lead Chalcogenide Nanocrystals. *ACS Nano* **2015**, *9*, 778-788.
- (42) Hall, R. N.; Racette, J. H., Band Structure Parameters Deduced from Tunneling Experiments. *J. Appl. Phys.* **1961**, *32*, 2078-2081.
- (43) Wise, F. W., Lead Salt Quantum Dots: The Limit of Strong Quantum Confinement. *Acc. Chem. Res.* **2000**, *33*, 773-780.

- (44) Vezzoli, S.; Manceau, M.; Leménager, G.; Glorieux, Q.; Giacobino, E.; Carbone, L.; De Vittorio, M.; Bramati, A., Exciton Fine Structure of CdSe/CdS Nanocrystals Determined by Polarization Microscopy at Room Temperature. *ACS Nano* **2015**, *9*, 7992-8003.
- (45) Zhao, Q.; Graf, P. A.; Jones, W. B.; Franceschetti, A.; Li, J.; Wang; Kim, K., Shape Dependence of Band-Edge Exciton Fine Structure in CdSe Nanocrystals. *Nano Lett.* **2007**, *7*, 3274-3280.
- (46) Efros, A. L.; Rosen, M.; Kuno, M.; Nirmal, M.; Norris, D. J.; Bawendi, M., Band-Edge Exciton in Quantum Dots of Semiconductors with a Degenerate Valence Band: Dark and Bright Exciton States. *Phys. Rev. B: Condens. Matter Mater. Phys* **1996**, *54*, 4843-4856.
- (47) Granados del Águila, A.; Pettinari, G.; Groeneveld, E.; de Mello Donegá, C.; Vanmaekelbergh, D.; Maan, J. C.; Christianen, P. C. M., Optical Spectroscopy of Dark and Bright Excitons in CdSe Nanocrystals in High Magnetic Fields. *J. Phys. Chem. C* **2017**, *121*, 23693-23704.
- (48) Kang, I.; Wise, F. W., Electronic Structure and Optical Properties of PbS and PbSe Quantum Dots. *J. Opt. Soc. Am. B* **1997**, *14*, 1632-1646.
- (49) Kim, S.; Fisher, B.; Eisler, H. J.; Bawendi, M., Type-II Quantum Dots: CdTe/CdSe(Core/Shell) and CdSe/ZnTe(Core/Shell) Heterostructures. *J. Am. Chem. Soc.* **2003**, *125*, 11466-11467.
- (50) Tyrakowski, C. M.; Shamirian, A.; Rowland, C. E.; Shen, H.; Das, A.; Schaller, R. D.; Snee, P. T., Bright Type II Quantum Dots. *Chem. Mater.* **2015**, *27*, 7276-7281.
- (51) Chen, C.-Y.; Cheng, C.-T.; Lai, C.-W.; Hu, Y.-H.; Chou, P.-T.; Chou, Y.-H.; Chiu, H.-T., Type-II CdSe/CdTe/ZnTe (Core–Shell–Shell) Quantum Dots with Cascade Band Edges: The

Separation of Electron (at CdSe) and Hole (at ZnTe) by the CdTe Layer. *Small* **2005**, *1*, 1215-1220.

(52) Balet, L. P.; Ivanov, S. A.; Piryatinski, A.; Achermann, M.; Klimov, V. I., Inverted Core/Shell Nanocrystals Continuously Tunable between Type-I and Type-II Localization Regimes. *Nano Lett.* **2004**, *4*, 1485-1488.

(53) Rabouw, F. T.; van der Bok, J. C.; Spinicelli, P.; Mahler, B.; Nasilowski, M.; Pedetti, S.; Dubertret, B.; Vanmaekelbergh, D., Temporary Charge Carrier Separation Dominates the Photoluminescence Decay Dynamics of Colloidal CdSe Nanoplatelets. *Nano Lett.* **2016**, *16*, 2047-2053.

(54) Marchioro, A.; Whitham, P. J.; Nelson, H. D.; De Siena, M. C.; Knowles, K. E.; Polinger, V. Z.; Reid, P. J.; Gamelin, D. R., Strong Dependence of Quantum-Dot Delayed Luminescence on Excitation Pulse Width. *J. Phys. Chem. Lett.* **2017**, *8*, 3997-4003.

(55) Li, B.; Brosseau, P. J.; Strandell, D. P.; Mack, T. G.; Kambhampati, P., Photophysical Action Spectra of Emission from Semiconductor Nanocrystals Reveal Violations to the Vavilov Rule Behavior from Hot Carrier Effects. *J. Phys. Chem. C* **2019**, *123*, 5092-5098.

(56) Hoy, J.; Morrison, P. J.; Steinberg, L. K.; Buhro, W. E.; Loomis, R. A., Excitation Energy Dependence of the Photoluminescence Quantum Yields of Core and Core/Shell Quantum Dots. *J. Phys. Chem. Lett.* **2013**, *4*, 2053-2060.

(57) Martynenko, I. V.; Baimuratov, A. S.; Osipova, V.; Kuznetsova, V. A.; Purcell-Milton, F.; Rukhlenko, I. D.; Fedorov, A. V.; Gun'ko, Y. K.; Resch-Genger, U.; Baranov, A. V., Excitation Energy Dependence of the Photoluminescence Quantum Yield of Core/Shell CdSe/CdS Quantum Dots and Correlation with Circular Dichroism. *Chem. Mater.* **2018**, *30*, 465-471.

(58) Aerts, M.; Bielewicz, T.; Klinke, C.; Grozema, F. C.; Houtepen, A. J.; Schins, J. M.; Siebbeles, L. D. A., Highly Efficient Carrier Multiplication in PbS Nanosheets. *Nat. Commun.* **2014**, *5*, 3789.

Chapter 5: Facet-Dependent Etching of CdSe Nanoplatelets by Lead Oleate

5.1 Introduction

The precise size and shape control of colloidal semiconducting nanomaterials is necessary for their use in a variety of optoelectronic applications.^{1,2} Significant effort has been spent to synthesize nanocrystals (NCs) in a controllable manner with predictable sizes and band gaps. In particular, zinc blende (ZB) CdSe nanoplatelets (NPLs) with large lateral sizes (lengths and widths) and very small thicknesses can be synthesized with thickness increments equal to a single CdSe monolayer (ML) with a total thickness of 3.5, 4.5, or 5.5 ML.^{3,4} These NPLs have large, atomically flat top and bottom cadmium facets terminated with carboxylate ligands.^{3,4} Size-selection through precipitation enables the preparation of samples of NPLs with a given thickness.⁵⁻⁷ Recently, the direct synthesis of CdSe NPLs up to 8.5 ML in thickness has been reported, expanding the range of thicknesses and optical band gaps accessible for this unique shape.^{8,9}

Post-synthetic processing can be utilized to expand the potential uses of the NPLs in optoelectronic devices. For instance, ligand exchange¹⁰⁻¹⁵ and heterostructure growth^{7,16-20} are both powerful methods for tuning the band edge energies, band gap, and wave functions in NCs (Chapters 3 & 4). Post synthetic modification can alter the size, shape, and composition of the NCs. In CdSe/CdSe_{1-x}Te_x core/crown NPLs, the emission energy was modulated by varying the alloy composition of a deposited NPL crown. A NPL crown extends the NPL length and width without changing the thickness.¹⁷ Since shape directly impacts the optoelectronic properties of

semiconducting NCs, it is important to understand what these changes are, why they occur, and how they impact the NC properties.

As shown in Chapter 3, PbS shells can be epitaxially grown on ZB CdSe quantum dots (QDs), uniformly covering all sides of the CdSe core.²¹ The growth of PbS shells on ZB CdSe nanoplatelets (NPLs) is not as uniform, as shown in Chapter 4. Simple PbS shell growth on CdSe NPLs should result in an increase in the dimensions of the NPLs in all directions (length, width, and thickness); instead, the thicknesses and widths of the NPLs increase while the lengths decrease. At the same time, the shapes of the large top and bottom faces change from rectangular faces, with sharp, 90° corners for the CdSe NPLs to oval shaped with the growth of the PbS shell on the NPLs.

The PbS shell growth involves a variety of chemical species that could be responsible for the observed shape changes. These chemical species can interact with the NPL surface in several different binding modes, including octylamine (neutral two-electron donor, L-type ligand), lead oleate ($\text{Pb}(\text{oleate})_2$, neutral two-electron acceptor, Z-type ligand), and oleate (one-electron anionic donor forming covalent bonds, X-type ligand).^{13,14,22} Similar chemical species have been observed to cause etching in a variety of NCs, producing different NC shapes dependent on the initial NC facets.²³⁻²⁶ The ratio of oleic acid to its conjugate base, oleate, promotes the growth on certain facets or etching of certain facets in NaYF_4 nanoparticles.²³ A higher concentration of oleic acid promotes growth on the (100) facets on the sides of hexagonal NaYF_4 NCs, producing relatively thin hexagonal disks with a large diameter. In contrast, a higher concentration of oleate promotes growth on the (001) top and bottom facets of the nanocrystal, leading to the formation of hexagonally shaped nanorods with a relatively small diameter. Combining this ratio with other synthetic parameters enables the production of a variety of complex shapes and heterostructures,

including rods with sections of alternating composition and hourglass-shaped heteronanocrystals from the same starting nanorod or hexagonal nanocrystal core.²³ At slightly elevated temperatures (80 °C), an amine (3-amino-1-propanol)/water solution in the presence of oxygen etches CdSe hexagonal prismatic NCs.²⁴ In this case, the Se atoms on the surface oxidize, and the basic solution dissolves the SeO₂, revealing a Cd-rich facet. As the NC etches, the hexagonal prismatic NCs form pyramidal shapes. The oxidation of the surface Cd to CdO temporarily hinders further etching, but the etching process can continue. Reactive facets are also important in the zinc oleate-induced etching of CdS nanorods.²⁵ In this case, zinc oleate etches the CdS nanorods from the end facets, reducing the length without changing the diameter of the rods.²⁵ Upon injection of a highly reactive selenium precursor, the solubilized Cd species, but not the zinc oleate, can react to form CdSe-on-CdS dot-on-rod NC heterostructures.

The expressed facets in PbTe QDs also play an important role in determining ligand exchange *versus* ion exchange in treatment with sodium sulfide.²⁶ While {100} facets are inert to ion exchange, {111} facets promote a rapid ion-exchange process. This difference in reactivity causes significant differences in cubic PbTe NCs, which merely undergo a ligand exchange when exposed to sulfide ions, in comparison to cuboctahedra PbTe NCs, which convert to PbS with exposure to sulfide ions. The same reactivity trend holds true when the PbTe NCs are treated with silver nitrate; the {100} facets of cubic NCs are unreactive while the {111} facets of cuboctahedra PbTe NCs allow the cation exchange to take place, converting the PbTe to Ag₂Te.

In the CdSe/PbS core/shell NPL synthesis described in Chapter 4, the NPLs were exposed to a variety of chemical species that have been the cause of etching or selective growth in similar NCs. A series of experiments were conducted to determine the likely cause of the unpredictable shape changes of the NPLs during the PbS shell synthesis. Specifically, CdSe

NPLs were treated with individual chemical precursors and the changes were monitored by transmission electron microscopy (TEM). Once the cause of the etching was determined, the role of etching-induced morphological changes on the energetics over time was further studied using absorption spectroscopy.

5.2 Results

In order to determine the source of the shape changes in the CdSe/PbS core/shell NPL synthesis, 4.5 ML (1.22 nm thick) CdSe NPLs were treated with each component of the PbS shell reaction. An aliquot of the CdSe NPL stock solution was treated with (1) sonication for 10 minutes, (2) octylamine, (3) oleic acid, (4) sodium oleate, (5) Pb(oleate)₂ in octadecene, and (6) Pb(oleate)₂ in octylamine. Sonication, octylamine, and Pb(oleate)₂ dissolved in octylamine are all directly used in the PbS shell synthesis and could be responsible for morphological changes to the CdSe NPLs. In order to eliminate the possibility of effects of the combination of Pb(oleate)₂ and octylamine, the CdSe NPLs were also treated with Pb(oleate)₂ dissolved in octadecene, a non-coordinating solvent. Oleic acid is not used in the PbS shell synthesis, but an excess of oleic acid is used in the synthesis of Pb(oleate)₂ (see preparation of Pb(oleate)₂ from Pb(Ac)₂, Chapter 2), and is therefore present in the PbS shell synthesis. Similarly, sodium oleate is not used directly in the PbS shell synthesis, but when the lead in Pb(oleate)₂ is deposited as PbS, a significant amount of oleate is generated in solution.

The ZB CdSe NPLs (4.5 ML) were synthesized and purified according to the procedure described in Chapter 2 and dispersed in methylcyclohexane as a stock solution (Chapter 2).^{5,7} The NPLs were an average of 30(3) (length) × 8(1) (width). See Figure A3-1 for full size statistics and histograms of the length and width. See Chapter 2 for full details of the etching procedure, but an abbreviated procedure follows here. In each case, the aliquot of NPLs was

diluted in 2 mL toluene, the treatment was applied (in the case of a control reaction, nothing was done), and the reaction (if any) proceeded for 3 hours. The resultant nanoparticles were purified from any molecular species in solution by adding 1 mL methanol, centrifuging at 4500 RPM (3260 g) for 5 minutes, decanting the supernatant, and redispersing the solid in toluene.

There were no visible changes to the transmission electron microscope (TEM) images of the CdSe NPLs after treatment with sonication, sodium oleate, oleic acid, or octylamine (Figure 5-1a). TEM images of the product NCs showed the presence of approximately spherical nanodots (NDs) after treatment with $\text{Pb}(\text{oleate})_2$ in either octylamine or octadecene (Figure 5-1a). $\text{Pb}(\text{oleate})_2$ is therefore concluded to be the primary cause of the etching process.

The etching product differs in the presence or absence of octylamine. Octadecene is assumed not to participate in the etching process since octadecene is a non-coordinating solvent. The average ND size is not statistically different when etching with $\text{Pb}(\text{oleate})_2$ dispersed in octylamine (diameter = 4.1(8) nm) *versus* octadecene (diameter = 4.3(7) nm). See Figure A3-2 in Appendix 3 for ND diameter distributions. Note that the etching of the CdSe NPLs with $\text{Pb}(\text{oleate})_2$ in octadecene produces NDs that are physically separated from the NPLs, while etching with $\text{Pb}(\text{oleate})_2$ in octylamine generates NDs attached to the NPLs.

The shape of the NPLs after etching is also significantly different depending on the $\text{Pb}(\text{oleate})_2$ solvent (see Figure A3-1 for statistics and size histograms of NPLs). After etching by $\text{Pb}(\text{oleate})_2$ in octadecene, the NPLs are 31(4) nm \times 8(1) nm and are still rectangular in shape, with an average corner angle of 91(6) $^\circ$ (33 measurements). In comparison to the initial CdSe NPLs, there is no statistically significant difference in the size of these NPLs.

The NPLs exposed to $\text{Pb}(\text{oleate})_2$ in octylamine remain similar in size to the initial NPLs when measured at the largest length and width of the NPL, 31(3) nm \times 8(1) nm, but they become

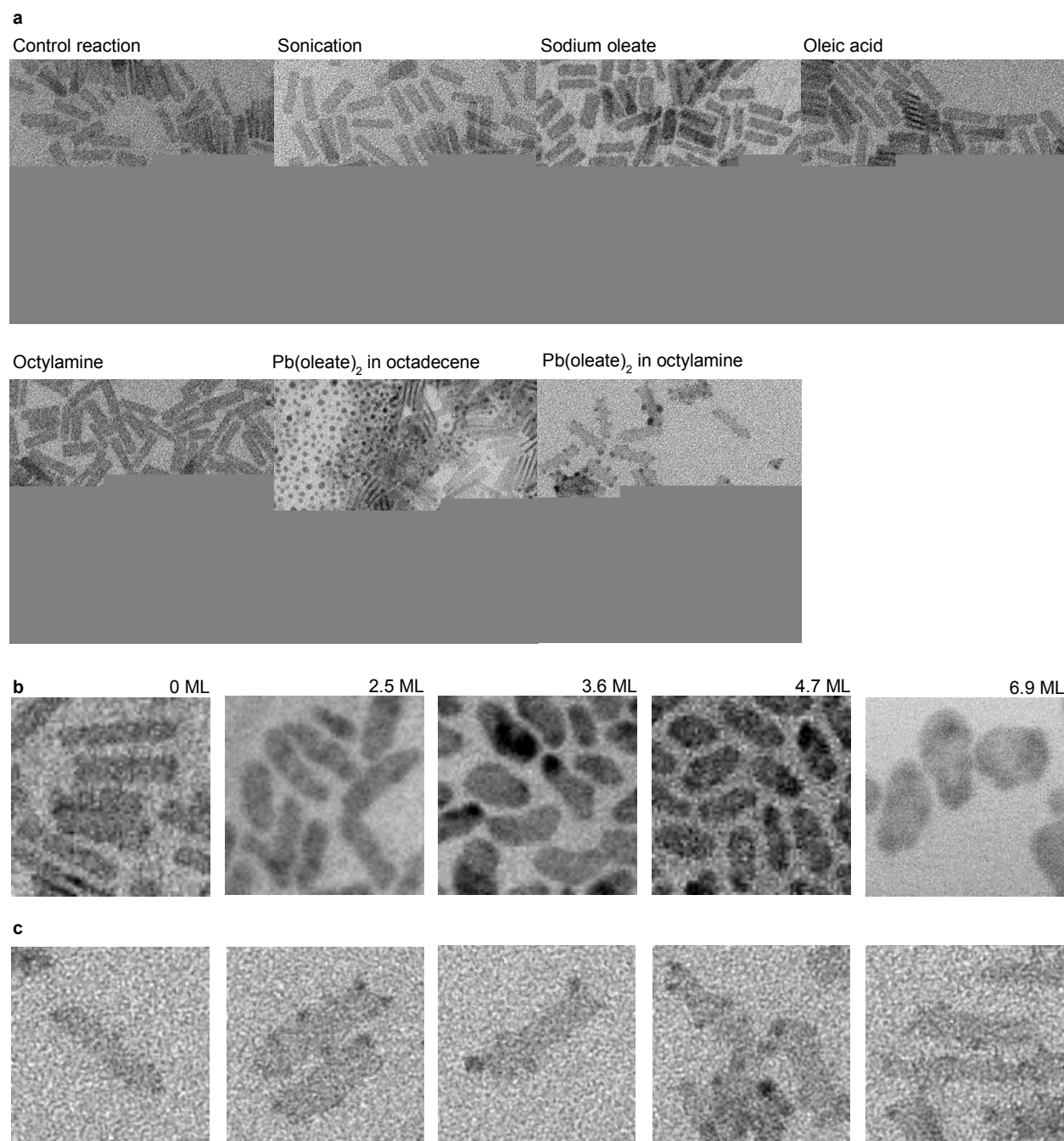


Figure 5-1. (a) TEM images of 4.5 ML CdSe NPLs treated with different chemical precursors (and physical processes) used in the PbS shell synthesis. Each image is 200 × 200 nm. (b) TEM images of CdSe/PbS core/shell NPLs labeled with number of PbS MLs in upper right of each image. Each image is 50 × 50 nm. (c) TEM images of CdSe NPLs etched with Pb(oleate)₂ in octylamine highlighting changes in shape of underlying NPL. Each image is 50 × 50 nm.

irregular in shape, with a mixture of obtuse and acute angles (Figure 5-1c). As a result, one or both of the long edges of the NPL are shorter than the longest measured dimension of the NPL. This difference is statistically significant and is highlighted in the histograms plotted in Figure 5-2. The longest dimension and width of the NPLs are not statistically different in comparison to the initial CdSe NPLs.

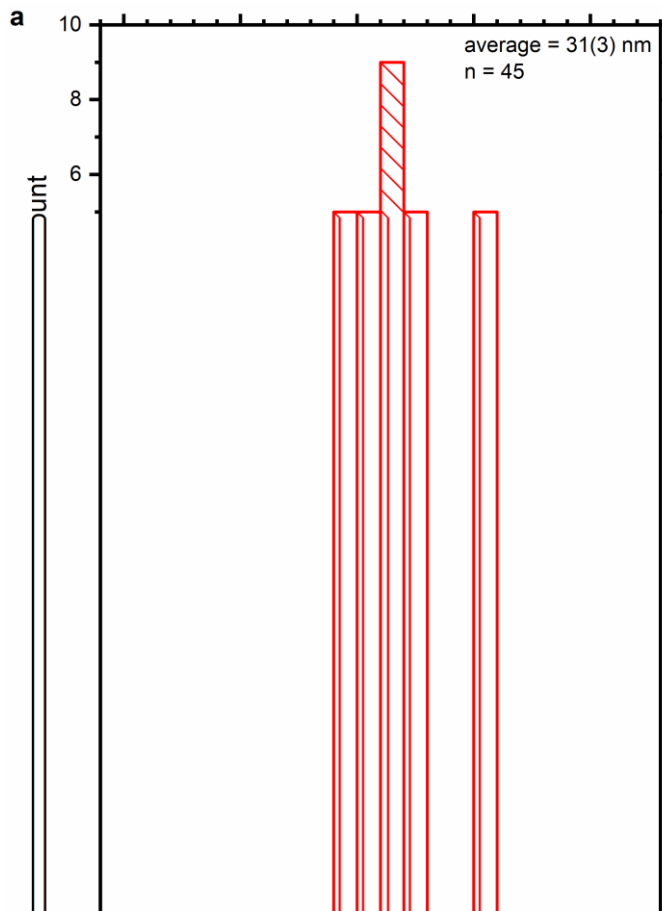


Figure 5-2. Distributions of the length of CdSe NPLs etched with $\text{Pb}(\text{oleate})_2$ in octylamine measured along (a) the longest dimension of the NPL and (b) along the shortest edge of the NPL along the length dimension. The average length and number of measurements, n , are noted in the upper right of each panel.

These changes to the CdSe NPLs are notably different than the morphological changes to the CdSe NPLs observed to occur during the PbS shell synthesis (Figure 5-1b). In the PbS shell

synthesis, no NDs were observed, and the NPLs become more oval shaped with increasing shell thickness.

To investigate this reaction further, the amount of time the CdSe NPLs were treated with Pb(oleate)₂ in octylamine was varied. Aliquots of CdSe NPLs were treated with Pb(oleate)₂, and the reaction was stopped at 3, 6, 9, and 12 hours by precipitating the product nanocrystals and separating them from the molecular precursors. The TEM images, Figure 5-3, indicate the CdSe NPLs continue to etch and reduce in size with etching time. Histograms and statistics of the dimensions of the as-synthesized NPLs and the NPLs after etching for 3 hours and 9 hours can be found in Figure A3-3. The NPL dimensions reduced from 31(4) by 8(1) nm (CdSe cores) to 29(3) by 7(2) nm after 3 hours to 21(3) by 3.4(7) nm after 9 hours. The change in length is not statistically significant after etching for 3 hours, but is statistically significant after etching for 9 hours. The changes in width are statistically significant after etching for 3 hours and after 9 hours. The formation of NDs on the NPLs after 3 and 6 hours was observed again. The aggregation and number of NDs on the NPLs after 6 hours was so severe that it was not possible to accurately measure the NPL size. After 9 hours, the NPLs appeared to be physically separated and fewer QDs were attached to the NPLs. In addition to these NPLs, some large particles were

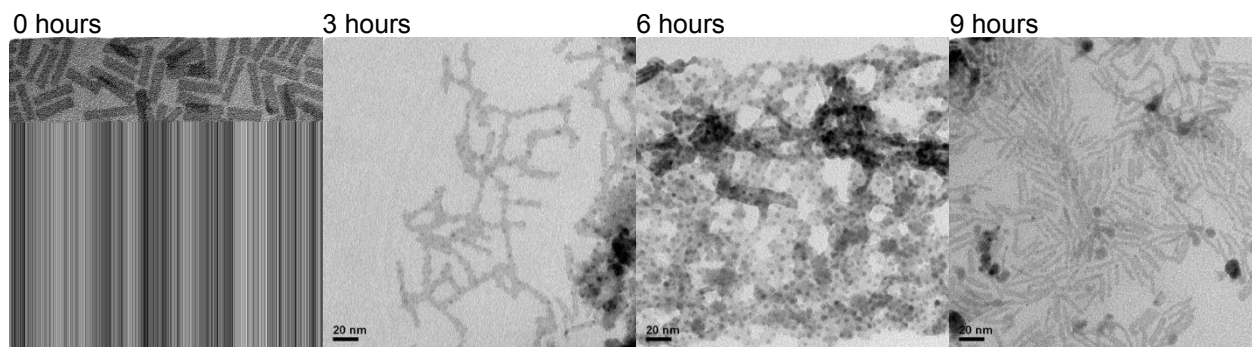


Figure 5-3. TEM images of CdSe NPLs treated with 0.01 M Pb(oleate)₂ in octylamine after different periods of time (labeled top left of each image).

observed. By 12 hours, the NPLs were completely absent in the TEM, replaced by large flakes, visible to the naked eye, that quickly settle out of the clear and colorless solution.

To further study the changes to the NPLs with etching, visible extinction spectra (Figure 5-4) were collected. The CdSe NPL absorption features shift to higher energy and a curved baseline grows in at low energy with Pb(oleate)₂-induced etching. This baseline offset could not be corrected using the wavelength dependence appropriate for scattering with a constant baseline offset ($y = b\lambda^{-4} + a$). The normalized extinction spectra are plotted in Figure 5-4a. Using the raw extinction data, the first absorption peak was identified using two different methods, by using the local maximum of each feature and by calculating the second derivative of the extinction spectrum (Figure A3-4). The local maximum of the band edge CdSe NPL absorption transition shifts to higher energy by 34 meV. This method for peak identification is expected to overestimate the shift to higher energy due to the sloping background signal. The peak identified by the second derivative first shifts to lower energy by 4 meV, but then shifts to higher energy by 9 meV, resulting in a total shift to higher energy by 5 meV. Peak identification using the second derivative of the extinction spectra is expected to underestimate the shift to higher energy. Therefore, the actual shift of the first feature is expected to be in the range 5-34 meV. In order to further probe the shift to higher energy, the baseline was fitted to $y = a + bE^c$, where E is the energy in eV. The corrected spectra are plotted in Figure 5-4b and the fitting parameters can be found in Table A3-1. This background correction, unlike the correction for the scattering (in which $c = 4$), has no physical significance, but it does appear to correct for the sloping extinction, allowing the CdSe peak energies to be identified using either the local maximum of the corrected extinction spectra or the local minimum of the second derivative of the extinction spectra (Figure A3-5). There is still a discrepancy in the peak energies measured using the two methods; the first

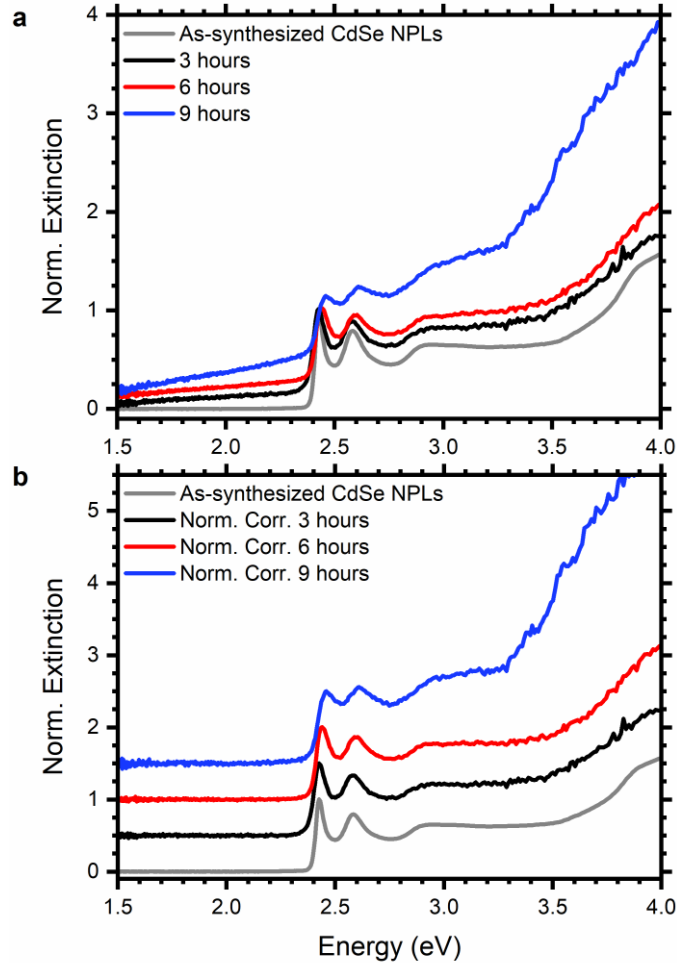


Figure 5-4. Extinction spectra normalized to the same value at the first absorption peak energy (identified by second derivative) of as-synthesized CdSe NPLs (gray) and CdSe NPLs etched with 0.01 M Pb(oleate)₂ in octylamine for 3 (black), 6 (red), or 9 hours (blue).

The raw extinction spectra (a) are plotted with the baseline corrected spectra (b).

CdSe absorption peak shifts to higher energy by 34 meV when identified by the local maximum of the extinction spectra and 19 meV when identified using the second derivative spectra.

Nevertheless, all these analyses indicate the first transition shifts to higher energies, consistent with increasing quantum confinement in CdSe NPLs.

The heavy hole and light hole transitions are distinct in the spectra of CdSe NPLs etched for different times, but the breadth of the features increases with etching time (Figure 5-4), which is consistent with reduced sample homogeneity. As the NPLs etch, quantum confinement

increases significantly in the lateral dimensions, particularly the width. As a result, the absorption features would be increasingly susceptible to inhomogeneity in NPL width.

These trends can be demonstrated with a simple 3D particle-in-a-box model using the CdSe effective masses of the electron ($m_e^* = 0.12m_e$) and hole ($m_{hh}^* = 2.14m_e$).²⁷ The contribution of quantum confinement in the NPL length to the energy of the first absorption transition is at most very minor (3.4-7.5 meV for 31-21 nm, respectively). The energetic shift resulting from quantum confinement in the width of the NPLs increases from 51.2 meV for the core (8(1) nm wide) to 286 meV for the NPLs etched for 9 hours (3.4(7) nm wide). Based on variations in the dimensionality, the contribution of quantum confinement from the width can vary and be estimated using the standard deviation of the width. The quantum confinement in the width ranges from 40.9-67.5 meV (a range of 26.6 meV) for the 8(1) nm wide as-synthesized CdSe NPLs, and increases to 197-454 meV (a range of 257 meV) for the 3.4(7) nm wide CdSe NPLs etched for 9 hours. Since the 3D particle-in-a-box model dramatically overestimates the first absorption transition energy (calculated energy of 3.96 eV for the as-synthesized NPLs compared to the observed transition energy of 2.426 eV), these calculated values should only be considered a guide to the expected trends and not a prediction of the transition energies. The spectroscopic features also indicate that the composition of the NPLs remains CdSe. After treatment with $Pb(oleate)_2$, the CdSe NPLs could conceivably convert to PbSe, though this is unlikely since direct Cd-for-Pb cation exchange typically requires elevated temperatures.²⁸ The heavy hole and light hole transitions are characteristic of the CdSe NPLs and would not be present in PbSe NPLs. Additionally, if the NPLs fully converted to PbSe NPLs, the band edge absorption transition is expected to shift to a significantly lower energy.¹⁹

The sloping background that increases with etching time could be the result of absorption of Pb-containing NDs, which will require further characterization by NIR absorption spectroscopy. PbSe has a much lower band gap of 0.28 eV, and so the band gap of these NDs is expected to be significantly smaller than the CdSe NPLs.²⁹ Williams *et. al.* recently reported the heterogeneous growth of PbSe QDs on CdSe NPLs. The absorption features of PbSe-on-CdSe QDs-on-NPLs resemble the combination of absorption from the original CdSe NPLs and a 1.18 eV absorption feature attributed to a PbSe excitonic transition.³⁰ If the sloping background observed in Figure 5-4 is the result of absorption into PbSe QDs on CdSe NPLs, etching and redeposition of PbSe could provide an alternative route to the synthesis of PbSe-on-CdSe QD-on-NPL heterostructures.

In order to identify the composition of the product semiconductor NPLs and NDs, the elemental composition was measured using ICP-MS. These data are summarized in Table 5-1. The Pb:Cd ratio generally increases with etching time (with the exception of the sample after 9 hours of etching). The lead measured in the samples could be present in two forms: (1) as an X-type ligand on the surface of CdSe NPLs (Pb(oleate)₂) and/or (2) as Pb-containing nanocrystals.

Table 5-1. ICP-MS data of CdSe NPLs treated with 0.01 M Pb(oleate)₂ in octylamine after different periods of time with standard deviations. The Pb:Cd ratio is calculated with its standard deviation determined from the propagation of error.

Reaction Time (hours)	Cd Concentration (ppb)	Pb Concentration (ppb)	Pb:Cd ratio
3	3.1(4)	22(3)	7(1)
6	4.4(6)	40(5)	9(2)
9	6.8(9)	44(6)	6(1)
12	3.5(5)	38(5)	11(2)

In order to test the possibility that lead is present exclusively as a Pb(oleate)₂ ligand, the ratio of surface to interior Cd sites in the CdSe NPLs was estimated. An example calculation can

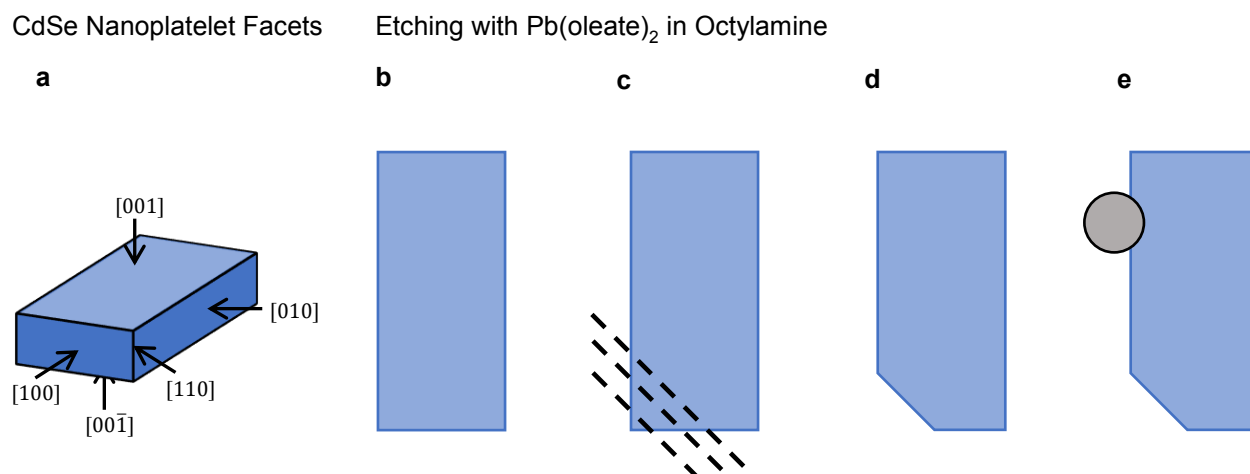
be found in Table A3-2. The surface area was first calculated from the average dimensions of the NPL. The CdSe NPLs are terminated by Cd-rich {100} facets on all sides. Using the lattice constant of ZB CdSe (6.050 Å) and the calculated surface density of 5.46 Cd atoms/nm² on the {100} facets, the total number of surface Cd atoms was calculated (3388 Cd atoms).^{31,32} Next, using the total volume of the CdSe NPL (319 nm³) and the number of Cd atoms per unit cell volume (18.06 Cd/nm³, calculated from 4 Cd atoms per 0.221 nm³), the total number of Cd atoms per NPL was calculated (5762 Cd atoms). This gave a ratio of 1.43 surface to interior Cd sites. This calculation is simplistic and should not be considered an indication of the precise number of Cd atoms per CdSe NPL, but it does serve as a qualitative guide for evaluating these Pb:Cd ratios.

If Pb is present only as an X-type ligand (Pb(oleate)₂), the Pb:Cd ratio should approach the calculated surface:interior Cd sites ratio of 1.43 since each surface Cd site would exchange for Pb (assuming 100% surface exchange). After just 3 hours, the Pb:Cd ratio of 7(1) is significantly higher than the calculated ratio of surface to interior Cd sites, indicating that the Pb cannot exclusively be present as a surface ligand. The Pb must be present either in the NPL crystal or in the NDs. Since the NPL composition remains constant on the basis of the extinction spectral features, the Pb cannot be present in the NPL crystal lattice. Therefore, the Pb must be present in the NDs as PbSe.

5.3 Discussion

These etching experiments indicate that the Pb(oleate)₂-induced etching of CdSe NPLs is a facet-dependent cation exchange process. ZB CdSe NPLs have six {100} facets, four horizontal {101} edges, four horizontal {011} edges, and four vertical {110} edges (Scheme 5-

1a).³² The observed changes suggest that the etching starts from the four vertical $\{110\}$ edges of the NPLs without significantly etching the broad top or bottom $\{100\}$ facets.



Scheme 5-1. CdSe nanoplatelet facets and proposed schematic of the etching process that occurs during treatment with Pb(oleate)_2 in octylamine for three hours. (a) Facets of as-synthesized CdSe core nanoplatelet with four vertical $\{110\}$ edges. (b-e) Cross section along width and length of (b) starting CdSe core nanoplatelet (blue) with high aspect ratio, (c) etching to expose the $\{110\}$ facet, (d) resulting etched CdSe nanoplatelet shape, and (e) nanodot (grey) grown on CdSe nanoplatelet.

Since the energies of the lowest-energy feature in the absorption spectra do not change significantly with etching, the thickness dimension, which dominates the quantum-confinement, must not change appreciably. It is possible that the thicknesses of the NPLs change non-uniformly, resulting in individual NPLs that are 4.5 MLs thick over the majority of the NPL area but have small sections that are 3.5 MLs thick. In this case, the absorption spectra could still be dominated by the first absorption transition corresponding to 4.5 ML NPLs (2.42 eV). This seems unlikely since the Cd atoms on the NPL edges have a higher number of dangling bonds than the large top and bottom facets. Instead, the small shift of these absorption features, <34 meV, is likely the result of additional quantum confinement in the lateral dimensions, as discussed previously.

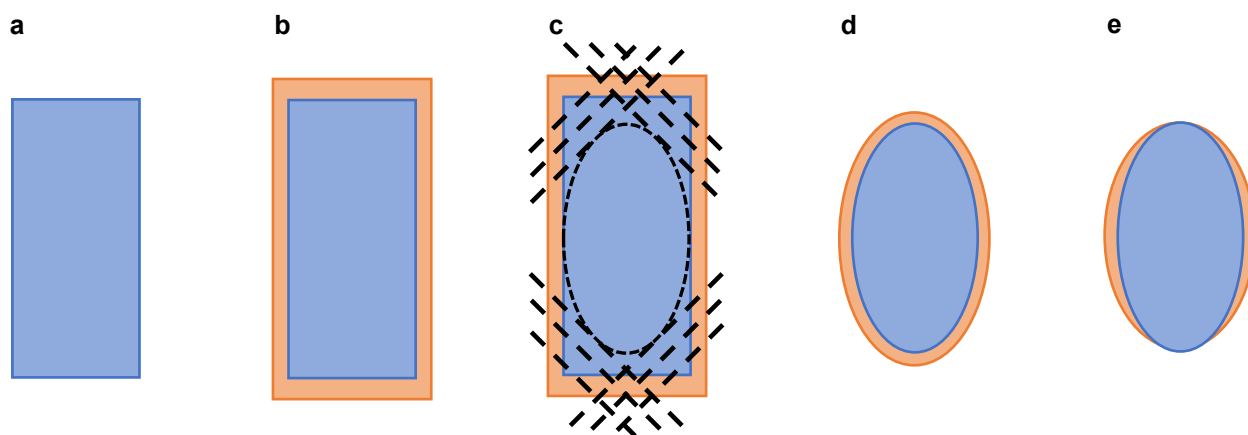
The morphological changes observed in the TEM images also support our conclusion that the NPLs are not etched from the broad top or bottom facets and that the etching is a facet-dependent process starting from the $\{100\}$ edges. The width and length of the NPLs decrease by 5(1) and 11(5) nm, respectively, after etching with Pb(oleate)_2 in octylamine for 9 hours, which is significantly greater than the thickness of the NPLs (1.22 nm). If etching proceeded along the thickness, the NPLs would dissolve completely during this time. See length and width histograms of NPLs in Figure A3-3.

Additionally, the shape of the etched NPLs indicate the etching proceeds from the $\{100\}$ edges rather than from the small sides of the NPLs. See Scheme 5-1 for the proposed etching process when CdSe NPLs are treated with Pb(oleate)_2 in octylamine for three hours. The cross section along the two longer dimensions (width and length) of the original CdSe core NPL in its original high aspect ratio geometry is shown in Scheme 5-1b. The NPLs are etched proceeding along the $\{110\}$ edge, shown as dashed lines in Scheme 5-1c, resulting in a CdSe NPL with at least one obtuse corner, Scheme 5-1d. For simplicity, this etching is only shown to proceed from a single $\{110\}$ edge, but in principle it could start from any or all of the $\{110\}$ edges. Etching to reveal the $\{110\}$ facet would result in a 135° angle between the newly revealed facet and the side of the NPL, which is consistent with the $130(10)^\circ$ angle observed in the CdSe NPLs etched with Pb(oleate)_2 in octylamine. Lastly, solvated selenide from the CdSe NPL can react with Pb(oleate)_2 in solution to form a PbSe ND on the NPL represented by a grey circle in Scheme 5-1e.

Etching from the $\{100\}$ edges also helps explain the morphological changes observed in the CdSe/PbS core/shell NPL synthesis. TEM images in Figure 5-1b indicate the lateral size and shape of the NPLs change dramatically with shell growth. Instead of isotropic growth in all

directions, as observed in the CdSe/PbS core/shell QDs,²¹ or in CdSe/CdS core/shell NPLs,^{20,34} the length decreases while the width increases. In addition, the shape changes dramatically, from the starting rectangular shape to more oval-type shapes (Figure 5-1b). The proposed etching process that occurs during shell growth is represented in Scheme 5-2. The cross section of the original CdSe core NPL in its original high aspect ratio geometry is shown in Scheme 5-2a. With an isotropically added PbS shell, the NPL cross section would increase in length and width (Scheme 5-2b). Etching along the {110} facets (Scheme 5-2c, dashed lines) results in an oval-shaped NC (representation of modified CdSe core is outlined as a dashed oval shape in Scheme 5-2c). The etching from these four vertical edges and simultaneous PbS shell growth would generate NPLs with reduced length and increased width as a result of the original large NPL aspect ratio (Scheme 5-2d and 5-2e). It is not clear whether the PbS covers the tips of the NPL (d) or not (e). The simultaneous PbS shell growth and NPL etching would therefore be a

Etching with Pb(oleate)_2 during PbS Shell Synthesis



Scheme 5-2. Proposed schematic of etching process during PbS shell growth. Cross section along width and length of (b) starting CdSe core nanoplacoid (blue) with high aspect ratio (c) CdSe/PbS core/shell nanoplacoid (blue/orange, respectively) without etching (d) CdSe/PbS core/shell nanoplacoid with etching to expose the {110} facets (diagonal dashed lines) with the resulting CdSe core shape (oval) and (e-f) resulting CdSe/PbS core/shell nanoplacoid with reduced length and increased width compared to CdSe core nanoplacoid with (e) and without (f) PbS surrounding the ends of the NPL.

{100} facets. These morphological changes also indicate that the etching does not start from the small side facets such as the {010} facet. Etching from the {010} facet would result in a CdSe/PbS core/shell NPL with a rectangular shape since the Pb(oleate)₂ would etch evenly along the length of the NPL facet, which is not observed.

Differences in the stable facets of ZB CdSe NPLs and rock salt PbS nanosheets could be the cause for etching during the PbS shell synthesis. PbS nanosheets have {110} facets on the thin sides of the nanocrystal while the side facets of the CdSe NPLs are {100} facets.^{32,35} As a result of these differences, the {100} facets of the deposited PbS shell may be unstable. Etching from the corners of the NPL would enable the expression of the more stable PbS {110} facet on the PbS shell surface. Concurrently, the PbS shell deposition apparently arrests the Pb(oleate)₂-induced etching, preventing the etching along the entire length of the NPL.

5.4 Conclusions

By treating ZB CdSe NPLs with a variety of chemical precursors used in the PbS shell synthesis, Pb(oleate)₂ is shown to etch CdSe NPLs starting from the smallest edges of the NPLs. The etching mechanism at the atomic level cannot be definitively determined without further experiments, such as *in-situ* TEM-imaging of the etching reaction, but several results suggest the Pb(oleate)₂ etches the CdSe NPLs starting from the four vertical {110} edges of the NPL. Specifically, the first absorption peak shifts only slightly with etching, ruling out the possibility of etching the broad top or bottom facets of the CdSe NPLs. Additionally, the changes to the lateral dimensions are larger than the thickness of the NPLs, further confirming the conclusion that the etching cannot occur layer by layer from the large, top facet, and must occur from one of the small side facets or edges. The final shape of the etched CdSe NPLs and the oval shape of the CdSe/PbS core/shell NPLs suggest that the etching starts from the four vertical {110} edges.

With improved control over the extent of this reaction, it could be possible to manipulate this etching mechanism to form ND-on-NPL structures, which could behave as a type-I heterostructure, funneling charges to the ND.³⁰

5.5 References

- (1) Buhro, W. E.; Colvin, V. L., Shape Matters. *Nat. Mater.* **2003**, *2*, 138.
- (2) Peng, X.; Manna, L.; Yang, W.; Wickham, J.; Scher, E.; Kadavanich, A.; Alivisatos, A. P., Shape Control of CdSe Nanocrystals. *Nature* **2000**, *404*, 59-61.
- (3) Riedinger, A.; Ott, F. D.; Mule, A.; Mazzotti, S.; Knüsel, P. N.; Kress, Stephan J. P.; Prins, F.; Erwin, S. C.; Norris, D. J., An Intrinsic Growth Instability in Isotropic Materials Leads to Quasi-Two-Dimensional Nanoplatelets. *Nat. Mater.* **2017**, *16*, 743.
- (4) Nasilowski, M.; Mahler, B.; Lhuillier, E.; Ithurria, S.; Dubertret, B., Two-Dimensional Colloidal Nanocrystals. *Chem. Rev.* **2016**, *116*, 10934-10982.
- (5) Abécassis, B.; Tessier, M. D.; Davidson, P.; Dubertret, B., Self-Assembly of CdSe Nanoplatelets into Giant Micrometer-Scale Needles Emitting Polarized Light. *Nano Lett.* **2014**, *14*, 710-715.
- (6) Jana, S.; Phan, T. N. T.; Bouet, C.; Tessier, M. D.; Davidson, P.; Dubertret, B.; Abécassis, B., Stacking and Colloidal Stability of CdSe Nanoplatelets. *Langmuir* **2015**, *31*, 10532-10539.
- (7) Pelton, M.; Andrews, J. J.; Fedin, I.; Talapin, D. V.; Leng, H.; O'Leary, S. K., Nonmonotonic Dependence of Auger Recombination Rate on Shell Thickness for CdSe/CdS Core/Shell Nanoplatelets. *Nano Lett.* **2017**, *17*, 6900-6906.
- (8) Christodoulou, S.; Climente, J. I.; Planelles, J.; Brescia, R.; Prato, M.; Martín-García, B.; Khan, A. H.; Moreels, I., Chloride-Induced Thickness Control in CdSe Nanoplatelets. *Nano Lett.* **2018**, *18*, 6248-6254.
- (9) Cho, W.; Kim, S.; Coropceanu, I.; Srivastava, V.; Diroll, B. T.; Hazarika, A.; Fedin, I.; Galli, G.; Schaller, R. D.; Talapin, D. V., Direct Synthesis of Six-Monolayer (1.9 nm) Thick Zinc-Blende CdSe Nanoplatelets Emitting at 585 nm. *Chem. Mater.* **2018**, *30*, 6957-6960.

- (10) Yao, Y.; Zhou, Y.; Sanderson, W. M.; Loomis, R. A.; Buhro, W. E., Metal-Halide-Ligated Cadmium Selenide Quantum Belts by Facile Surface Exchange. *Chem. Mater.* **2018**, *30*, 2848-2857.
- (11) Zhou, Y.; Buhro, W. E., Reversible Exchange of L-Type and Bound-Ion-Pair X-Type Ligation on Cadmium Selenide Quantum Belts. *J. Am. Chem. Soc.* **2017**, *139*, 12887-12890.
- (12) Zhou, Y.; Wang, F.; Buhro, W. E., Large Exciton Energy Shifts by Reversible Surface Exchange in 2D II-VI Nanocrystals. *J. Am. Chem. Soc.* **2015**, *137*, 15198-15208.
- (13) Anderson, N. C.; Hendricks, M. P.; Choi, J. J.; Owen, J. S., On the Dynamic Stoichiometry of Metal Chalcogenide Nanocrystals: Spectroscopic Studies of Metal Carboxylate Binding and Displacement. *J. Am. Chem. Soc.* **2013**, *2*, 11457-11471.
- (14) Anderson, N. C.; Hendricks, M. P.; Choi, J. J.; Owen, J. S., Ligand Exchange and the Stoichiometry of Metal Chalcogenide Nanocrystals: Spectroscopic Observation of Facile Metal-Carboxylate Displacement and Binding. *J. Am. Chem. Soc.* **2013**, *135*, 18536-18548.
- (15) Kroupa, D. M.; Vörös, M.; Brawand, N. P.; McNichols, B. W.; Miller, E. M.; Gu, J.; Nozik, A. J.; Sellinger, A.; Galli, G.; Beard, M. C., Tuning Colloidal Quantum Dot Band Edge Positions Through Solution-Phase Surface Chemistry Modification. *Nat. Commun.* **2017**, *8*, 15257.
- (16) Kelestemur, Y.; Guzelurk, B.; Erdem, O.; Olutas, M.; Gungor, K.; Demir, H. V., Platelet-in-Box Colloidal Quantum Wells: CdSe/CdS@CdS Core/Crown@Shell Heteronanoplatelets. *Adv. Func. Mat.* **2016**, *26*, 3570-3579.
- (17) Kelestemur, Y.; Guzelurk, B.; Erdem, O.; Olutas, M.; Erdem, T.; Usanmaz, C. F.; Gungor, K.; Demir, H. V., CdSe/CdSe_{1-x}Te_x Core/Crown Heteronanoplatelets: Tuning the Excitonic Properties without Changing the Thickness. *J. Phys. Chem. C* **2017**, *121*, 4650-4658.

- (18) Pedetti, S.; Ithurria, S.; Heuclin, H.; Patriarche, G.; Dubertret, B., Type-II CdSe/CdTe Core/Crown Semiconductor Nanoplatelets. *J. Am. Chem. Soc.* **2014**, *136*, 16430-16438.
- (19) Bouet, C.; Laufer, D.; Mahler, B.; Nadal, B.; Heuclin, H.; Pedetti, S.; Patriarche, G.; Dubertret, B., Synthesis of Zinc and Lead Chalcogenide Core and Core/Shell Nanoplatelets Using Sequential Cation Exchange Reactions. *Chem. Mater.* **2014**, *26*, 3002-3008.
- (20) Mahler, B.; Nadal, B.; Bouet, C.; Patriarche, G.; Dubertret, B., Core/Shell Colloidal Semiconductor Nanoplatelets. *J. Am. Chem. Soc.* **2012**, *134*, 18591-18598.
- (21) Wieliczka, B. M.; Kaledin, A. L.; Buhro, W. E.; Loomis, R. A., Wave Function Engineering in CdSe/PbS Core/Shell Quantum Dots. *ACS Nano* **2018**, *12*, 5539-5550.
- (22) Chen, P. E.; Anderson, N. C.; Norman, Z. M.; Owen, J. S., Tight Binding of Carboxylate, Phosphonate, and Carbamate Anions to Stoichiometric CdSe Nanocrystals. *J. Am. Chem. Soc.* **2017**, *139*, 3227-3236.
- (23) Liu, D.; Xu, X.; Du, Y.; Qin, X.; Zhang, Y.; Ma, C.; Wen, S.; Ren, W.; Goldys, E. M.; Piper, J. A.; Dou, S.; Liu, X.; Jin, D., Three-Dimensional Controlled Growth of Monodisperse Sub-50 nm Heterogeneous Nanocrystals. *Nat. Commun.* **2016**, *7*, 10254.
- (24) Li, R.; Lee, J.; Yang, B.; Horspool, D. N.; Aindow, M.; Papadimitrakopoulos, F., Amine-Assisted Faceted Etching of CdSe Nanocrystals. *J. Am. Chem. Soc.* **2005**, *127*, 2524-2532.
- (25) Oh, N.; Shim, M., Metal Oleate Induced Etching and Growth of Semiconductor Nanocrystals, Nanorods, and Their Heterostructures. *J. Am. Chem. Soc.* **2016**, *138*, 10444-10451.
- (26) Hewavitharana, I. K.; Brock, S. L., When Ligand Exchange Leads to Ion Exchange: Nanocrystal Facets Dictate the Outcome. *ACS Nano* **2017**, *11*, 11217-11224.

- (27) Cadmium Selenide (CdSe) Electronic Properties, Cubic Modification. In *Landolt-Börnstein - Group III Condensed Matter 41B (II-VI and I-VII Compounds; Semimagnetic Compounds)*, Madelung, O.; Rössler, U.; Schulz, M., Eds. Springer-Verlag: Berlin/Heidelberg, 1999; pp 1-6.
- (28) Lee, D.; Kim, W. D.; Lee, S.; Bae, W. K.; Lee, S.; Lee, D. C., Direct Cd-to-Pb Exchange of CdSe Nanorods into PbSe/CdSe Axial Heterojunction Nanorods. *Chem. Mater.* **2015**, *27*, 5295-5304.
- (29) Du, H.; Chen, C.; Krishnan, R.; Krauss, T. D.; Harbold, J. M.; Wise, F. W.; Thomas, M. G.; Silcox, J., Optical Properties of Colloidal PbSe Nanocrystals. *Nano Lett.* **2002**, *2*, 1321-1324.
- (30) Williams, K. R.; Diroll, B. T.; Watkins, N. E.; Rui, X.; Brumberg, A.; Klie, R. F.; Schaller, R. D., Synthesis of Type I PbSe/CdSe Dot-on-Plate Heterostructures with Near-Infrared Emission. *J. Am. Chem. Soc.* **2019**, *141*, 5092-5096.
- (31) Madelung, O., *Semiconductors - Basic Data*. Springer-Verlag: 1996.
- (32) Hutter, E. M.; Bladt, E.; Goris, B.; Pietra, F.; van der Bok, J. C.; Boneschanscher, M. P.; de Mello Donegá, C.; Bals, S.; Vanmaekelbergh, D., Conformal and Atomic Characterization of Ultrathin CdSe Platelets with a Helical Shape. *Nano Lett.* **2014**, *14*, 6257-6262.
- (33) Ithurria, S.; Tessier, M. D.; Mahler, B.; S M Lobo, R. P.; Dubertret, B.; Efros, A. L., Colloidal Nanoplatelets with Two-Dimensional Electronic Structure. *Nat. Mater.* **2011**, *10*, 936-941.
- (34) Ithurria, S.; Talapin, D. V., Colloidal Atomic Layer Deposition (c-ALD) using Self-Limiting Reactions at Nanocrystal Surface Coupled to Phase Transfer Between Polar and Nonpolar Media. *J. Am. Chem. Soc.* **2012**, *134*, 18585-18590.

(35) Zhang, H.; Savitzky, B. H.; Yang, J.; Newman, J. T.; Perez, K. A.; Hyun, B.-R.; Kourkoutis, L. F.; Hanrath, T.; Wise, F. W., Colloidal Synthesis of PbS and PbS/CdS Nanosheets Using Acetate-Free Precursors. *Chem. Mater.* **2016**, *28*, 127-134.

Chapter 6: Conclusions & Future Directions

6.1 Summary

This dissertation has focused on the synthesis and characterization of CdSe/PbS core/shell nanocrystal (NC) heterostructures. By using the heterostructure to control the charge carrier wave functions in the NC, the optoelectronic properties of these materials can be tailored for a variety of uses. In particular, multiexciton generation (MEG) has the potential to dramatically increase the efficiency of solar cells from the 33% single-junction Shockley-Queisser limit to 66%.^{1,2} Additionally, control of the absorption transition strengths at different energies could enable the use of CdSe/PbS core/shell NCs as luminescent solar concentrators (LSCs).³⁻⁷ Working towards these goals, the synthesis and characterization of CdSe/PbS core/shell quantum dots (QDs) and nanoplatelets (NPLs) were studied in Chapters 3 and 4. The chemical etching of CdSe NPLs by lead oleate ($\text{Pb}(\text{oleate})_2$) was also studied in Chapter 5 in order to understand the observed differences in the PbS shell synthesis on CdSe core QDs and NPLs.

The PbS shell synthesis was first conducted on CdSe QDs, which demonstrated the efficacy of a room-temperature shell synthesis reaction.⁸ The epitaxial core/shell QDs were synthesized with a range of shell thicknesses dependent on the quantities of lead and sulfur shell precursors used. X-ray diffraction data showed that the PbS shell grew in the rock salt crystal structure on top of the underlying zinc blende CdSe core. The PbS shell significantly impacted the spectroscopic properties of the CdSe/PbS core/shell QDs in comparison with the CdSe cores. The first absorption transition shifted to lower energies by up to 280 meV with increasing PbS

shell thickness, and the band gap absorption transition strengths decreased relative to the higher energy transitions.

The PbS shell synthesis was also applied to CdSe NPLs, demonstrating the versatility of this shell synthesis and the potential to grow PbS shells on NCs of varying size and dimensionality. Unlike the CdSe/PbS core/shell QD synthesis, in which the PbS shell grew isotropically on the underlying CdSe core, the shape of the product CdSe/PbS core/shell NPLs was significantly different than that of the starting CdSe NPLs. The CdSe NPLs were rectangular, with $91(6)^\circ$ corners, while the CdSe/PbS core/shell NPLs were more oval-shaped. Simultaneously, the average dimensions of the CdSe/PbS core/shell NPLs changed compared to the starting core NPLs; the NPL length decreased while the width and thickness increased relative to the CdSe core NPLs. Despite these more complicated changes to the NC morphology in the synthesis of CdSe/PbS core/shell NPLs *versus* QDs, transmission electron microscopy images and elemental analysis data confirmed the growth of a PbS shell. The changes to the optical properties of the CdSe/PbS core/shell NPLs were very similar to those of the CdSe/PbS core/shell QDs. The first absorption transition shifted to lower energies with increasing shell thickness by up to 480 meV, indicating a decrease in quantum confinement and the delocalization of the electron and/or hole wave functions over the core/shell NPL thickness. Also like the CdSe/PbS core/shell QDs, the absorption transition strength at the band gap decreased relative to the absorption transition strength at high energy.

These changes to the absorption transition strengths were interpreted based on the differences in the band structures of CdSe and PbS. The band gap of CdSe is at the Γ point where the gap between the valence band (VB) and conduction band (CB) of PbS is very large. The inverse is true at the L point; the band gap of PbS is at the L point, at which point the gap

between the VB and CB of CdSe is very large. As a result, the optical properties of CdSe/PbS core/shell NCs is likely to resemble the combination absorption transitions at the Γ and L points. Charge carriers excited at or close to the Γ point are strongly confined by the PbS. As a result, transitions involving charge carriers with these values of k are not expected to reach the bulk CdSe band gap transition energy. Transitions at or near the L point are strongly confined in the thin PbS shell. These transitions are expected to decrease in energy with increasing shell thickness, eventually reaching the bulk PbS band gap for a very thick PbS shell. Due to the changing volume of the PbS shell versus the CdSe core, the absorption transition strengths at these different points in k are expected to change dramatically with shell thickness, leading to the dramatic spectral changes observed in CdSe/PbS core/shell QDs and NPLs. The absorption transitions at or near the Γ point are dominated by the CdSe core, which does not change in volume with increasing shell thickness, resulting in a relatively constant transition strength. Absorption transitions at or near the L point are dominated by the PbS shell, which changes volume significantly. With the increasing PbS shell volume, the transition strength at or near the L point increases dramatically. Therefore, absorption at high energy was observed to be significantly stronger than absorption at the band gap in CdSe/PbS core/shell NCs.

Lastly, the unexpected changes in shape of the NPLs that occurred during the CdSe/PbS core/shell NPL synthesis were investigated by treating CdSe NPLs with chemical precursors used in the PbS shell synthesis. Pb(oleate)₂ was shown to chemically etch the CdSe NPLs. The available evidence indicates the etching proceeds from the four vertical $\{110\}$ edges of the NPL. As a result, the size of the NPLs decreased and the shape of the NPL face changed from the starting rectangular shape with $91(6)^\circ$ corners to a faceted shape with $130(10)^\circ$ corners. The changes in size were monitored with transmission electron microscopy and absorption spectra.

The modest shift of the absorption features to higher energies confirmed that the NPL thickness did not change significantly with Pb(oleate)_2 -induced etching. This etching was responsible for the unexpected shape changes in the CdSe/PbS core/shell NPL synthesis, in which the NPL face changed from the rectangular CdSe NPL shape to the oval shape.

6.2 Future Directions

6.2.1 Synthesis

In order to fulfill the promise of inexpensive, solution-processable solar cells that exceed the Shockley-Queisser limit through MEG in CdSe/PbS core/shell NCs, the NCs must have two interrelated primary attributes: first, the nanocrystals must behave as an inverse type-I heterostructure, and second, the band gap of the nanocrystals must be close to the optimal single junction band gap of 1.1 eV.¹ An inverse type-I heterostructure is necessary for charge funneling into the shell; without it, charge carriers are isolated in the interior of the core/shell heterostructure and are unavailable for extraction into the solar cell device. Since the band gaps of the NCs synthesized in this dissertation work have energies significantly greater than 1.1 eV, any gains in efficiency from MEG would be offset by reduced absorption at sub-band gap photon energies.

Even though the NCs synthesized in this dissertation work do not fulfill either of these attributes, it does lay the groundwork necessary for achieving this objective. Future research should build on this progress in order to synthesize thicker PbS shells, which should allow the synthesis of CdSe/PbS core/shell NCs with type-I heterostructure behavior and significantly smaller band gaps. With increasing PbS shell thickness, the degree of quantum confinement in the PbS shell is expected to decrease, and eventually the zero point energy of charge carriers in the PbS would be small enough that the charge carriers would be localized in the shell.

There are several methods building on the synthesis developed here that could achieve this result. First, the addition of shell precursors could be optimized for injection over time using a syringe pump. This method, if properly tailored to reduce homogeneous PbS nucleation, could allow for much thicker PbS shells. This method has previously been used for the synthesis of thick-shell CdSe/ZnSe and ZnSe/CdS core/shell QDs.⁹ Second, a successive PbS shell deposition method could be implemented. The colloidal alternating layer deposition method is a room-temperature shell synthesis that relies on successively depositing half monolayers of the desired shell.¹⁰ As a room-temperature shell synthesis, this would avoid Cd-for-Pb cation exchange in a similar manner as the PbS shell synthesis used here while allowing for a large number of PbS deposition cycles.

This research could also pursue the synthesis of CdSe/PbS core/crown NPLs. Like CdSe/PbS core/shell QDs, the charge carriers generated in CdSe/PbS core/crown NPLs would be available for extraction since they would be localized in the NPL crown. This could be an attractive morphology because of the enhanced MEG in nanosheets attributed to the higher density of states¹¹ The synthesis of CdSe/PbS core/crown NPLs could be targeted in one of two ways. Heterogeneous nucleation of PbSe on CdSe NPLs has already been demonstrated to form PbSe-on-CdSe QD-on-NPL heterostructures.¹² The reactivity of the lead and chalcogenide precursors could be tuned to form core/crown NPLs instead of QD-on-NPL structures. Another possible method of forming CdSe/PbS core/crown NPLs could be through a seeded growth method using pre-synthesized CdSe NPLs and PbS QDs. PbS nanosheets are commonly synthesized through the self-assembly of PbS QDs.^{11,13} It could be possible to initiate the assembly of PbS QDs onto the edges of CdSe NPLs by seeding the QD solution with NPLs. PbS nanosheet formation could be inhibited by conditions including growth temperature and

surfactants. This would be a new synthetic route to generating a CdSe/PbS core/crown NPL structure in which the PbS increases the lateral sizes of the NPLs. Furthermore, the PbS crown thickness could be modulated by varying the diameter of the starting PbS QDs.

Another important direction for future synthetic efforts is the formation of other CdE/PbE core/shell heterostructures ($E = S, Se, Te$). For example, CdS/PbS core/shell QDs could be a useful heterostructure since the bulk band gap of CdS is significantly larger (2.42 eV),¹⁴ allowing the formation of an inverse type-I heterostructure with a thinner PbS shell. By varying the core and shell composition, the differences resulting from different band gaps and band structures can be studied and optimized for use in optoelectronic devices.

6.2.2 Optical Characterization

Once the synthesis of inverse type-I CdSe/PbS core/shell NCs has been established, the material will be ripe for spectroscopic studies such as shape- and size-dependence of (1) MEG efficiency and (2) energy transfer from the CdSe to the PbS. Specifically, transient absorption studies of these NCs will be necessary to characterize the MEG. Here, the intensity of the first absorption feature in the transient absorption spectra would be monitored while varying the excitation energy without significantly changing the photon fluence.¹⁵ At energies just above the band gap (E_g), the first absorption feature bleach is not expected to change with varying excitation energy. Above $2E_g$, the relative amplitude of the first absorption feature bleach is expected to increase with increasing photon excitation energy but with constant photon fluence since the extra charge carriers generated by MEG will directly affect the strength of the bleach signal. Other optical spectroscopies could also be an important tool for probing the energy transfer between high energy CdSe-dominated states and the band gap PbS-dominated states. This includes measuring the photoluminescence lifetime, which could be an indicator for the

interaction required to change the charge carriers' momentum between the states at or near the Γ and L points. Since charge carriers excited at the Γ point must change their value of k by coupling to phonons in the crystal structure in order to relax to the L point, the photoluminescence lifetime would be expected to increase dramatically.

6.2.3 Calculations of Electronic Structure

High-level calculations in two main areas would further the understanding of the CdSe/PbS core/shell NC heterostructure. First, the effect of the differences in band structure of CdSe and PbS should be investigated. As proposed in Chapter 4, the spectral features of the CdSe/PbS core/shell NCs could be the direct result of the differing NC volume and absorption energies at the Γ and L points. Higher-level calculations are necessary to validate or disprove this model. Second, the effect of the angular momentum quantum numbers of the hole states in the CdSe and PbS should be investigated. This could change the absorption transition strength and the coupling of states significantly, directly affecting the optoelectronic properties near the band gap.

6.3 Conclusion

In conclusion, CdSe/PbS core/shell QDs and NPLs have been synthesized and characterized, laying the groundwork for future studies of this novel heterostructure. Taking advantage of the differences in band structure of CdSe and PbS is a particularly novel way to tailor the optoelectronic properties of this heterostructure. With further development, these new materials could improve solar cell efficiency through MEG or be used in a variety of other optoelectronic applications, including as LSCs, visible or NIR emitters, or for biological imaging.^{5,6,15-17} Furthermore, the proposed model addressing the differences in band structure could be vital to the fundamental understanding of semiconductor NC heterostructures.

6.4 References

- (1) Shockley, W.; Queisser, H. J., Detailed Balance Limit of Efficiency of p-n Junction Solar Cells. *J. Appl. Phys.* **1961**, *32*, 510-519.
- (2) Beard, M. C., Multiple Exciton Generation in Semiconductor Quantum Dots. *J. Phys. Chem. Lett.* **2011**, *2*, 1282-1288.
- (3) Coropceanu, I.; Bawendi, M. G., Core/shell Quantum Dot Based Luminescent Solar Concentrators with Reduced Reabsorption and Enhanced Efficiency. *Nano Lett.* **2014**, *14*, 4097-4101.
- (4) Guk Jeong, B.; Park, Y.-S.; Hyuk Chang, J.; Cho, I.; Kyeong Kim, J.; Kim, H.; Char, K.; Cho, J.; Klimov, V. I.; Park, P.; Lee, D. C.; Ki Bae, W., Colloidal Spherical Quantum Wells with Near-Unity Photoluminescence Quantum Yield and Suppressed Blinking. *ACS Nano* **2016**, *10*, 9297-9305.
- (5) Bradshaw, L. R.; Knowles, K. E.; McDowall, S.; Gamelin, D. R., Nanocrystals for Luminescent Solar Concentrators. *Nano Lett.* **2015**, *15*, 1315-1323.
- (6) Erickson, C. S.; Bradshaw, L. R.; McDowall, S.; Gilbertson, J. D.; Gamelin, D. R.; Patrick, D. L., Zero-Reabsorption Doped-Nanocrystal Luminescent Solar Concentrators. *ACS Nano* **2014**, *8*, 3461-3467.
- (7) Meinardi, F.; Colombo, A.; Velizhanin, K. A.; Simonutti, R.; Lorenzon, M.; Beverina, L.; Viswanatha, R.; Klimov, V. I.; Brovelli, S., Large-Area Luminescent Solar Concentrators Based on 'Stokes-Shift-Engineered' Nanocrystals in a Mass-Polymerized PMMA Matrix. *Nat. Photonics* **2014**, *8*, 392-399.
- (8) Wieliczka, B. M.; Kaledin, A. L.; Buhro, W. E.; Loomis, R. A., Wave Function Engineering in CdSe/PbS Core/Shell Quantum Dots. *ACS Nano* **2018**, *12*, 5539-5550.

- (9) Acharya, K. P.; Nguyen, H. M.; Paulite, M.; Piryatinski, A.; Zhang, J.; Casson, J. L.; Xu, H.; Htoon, H.; Hollingsworth, J. A., Elucidation of Two Giants: Challenges to Thick-Shell Synthesis in CdSe/ZnSe and ZnSe/CdS Core/Shell Quantum Dots. *J. Am. Chem. Soc.* **2015**, *137*, 3755-3758.
- (10) Ithurria, S.; Talapin, D. V., Colloidal Atomic Layer Deposition (c-ALD) using Self-Limiting Reactions at Nanocrystal Surface Coupled to Phase Transfer Between Polar and Nonpolar Media. *J. Am. Chem. Soc.* **2012**, *134*, 18585-18590.
- (11) Aerts, M.; Bielewicz, T.; Klinke, C.; Grozema, F. C.; Houtepen, A. J.; Schins, J. M.; Siebbeles, L. D. A., Highly Efficient Carrier Multiplication in PbS Nanosheets. *Nat. Commun.* **2014**, *5*, 3789.
- (12) Williams, K. R.; Diroll, B. T.; Watkins, N. E.; Rui, X.; Brumberg, A.; Klie, R. F.; Schaller, R. D., Synthesis of Type I PbSe/CdSe Dot-on-Plate Heterostructures with Near-Infrared Emission. *J. Am. Chem. Soc.* **2019**, *141*, 5092-5096.
- (13) Schliehe, C.; Juarez, B. H.; Pelletier, M.; Jander, S.; Greshnykh, D.; Nagel, M.; Meyer, A.; Foerster, S.; Kornowski, A.; Klinke, C.; Weller, H., Ultrathin PbS Sheets by Two-Dimensional Oriented Attachment. *Science* **2010**, *329*, 550.
- (14) Madelung, O., *Semiconductors - Basic Data*. Springer-Verlag: 1996.
- (15) Kroupa, D. M.; Pach, G. F.; Vörös, M.; Giberti, F.; Chernomordik, B. D.; Crisp, R. W.; Nozik, A. J.; Johnson, J. C.; Singh, R.; Klimov, V. I.; Galli, G.; Beard, M. C., Enhanced Multiple Exciton Generation in PbS|CdS Janus-like Heterostructured Nanocrystals. *ACS Nano* **2018**, *12*, 10084-10094.
- (16) Kovalenko, M. V.; Manna, L.; Cabot, A.; Hens, Z.; Talapin, D. V.; Kagan, C. R.; Klimov, V. I.; Rogach, A. L.; Reiss, P.; Milliron, D. J.; Guyot-Sionnest, P.; Konstantatos, G.; Parak, W.

J.; Hyeon, T.; Korgel, B. A.; Murray, C. B.; Heiss, W., Prospects of Nanoscience with Nanocrystals. *ACS Nano* **2015**, *9*, 1012-1057.

(17) Derfus, A. M.; Chan, W. C. W.; Bhatia, S. N., Probing the Cytotoxicity of Semiconductor Quantum Dots. *Nano Lett.* **2004**, *4*, 11-18.

Appendix 1: Wave Function Engineering in CdSe/PbS Core/Shell Quantum Dots

Reproduced with permission from: Wieliczka, B. M.; Kaledin, A. L.; Buhro, W. E.; Loomis, R. A., Wave Function Engineering in CdSe/PbS Core/Shell Quantum Dots. *ACS Nano*. **2018**, *12*, 5539-5550. Copyright 2018 by the American Chemical Society.

Table A1-1. Calculation of shell precursor quantities

Table A1-1. Example calculations of desired quantities of lead and sulfur precursors, Pb(oleate)₂ and TAA, to add for the synthesis of a desired PbS shell thickness in #ML using a single step starting from CdSe cores. The difference in volume, number of S atoms, and number of Pb atoms between the targeted CdSe/PbS core/shell QD compared to the core QD are listed as Δ volume vs. core, Δ S atoms/QD vs. core, and Δ Pb atoms/QD vs. core, respectively.

Desired #ML	Δ radius (nm)	Radius (nm)	Volume (nm ³)	Δ volume vs. core (nm ³)	Δ S atoms/QD vs. core	Δ Pb atoms/QD vs. core	Moles of each atom added as shell	Pb(oleate) ₂ solution (μ L)	TAA (mg)
0	0.000	1.450	12.77	0.00	0	0	0.000E+00	0.00	0.00
1	0.343	1.793	24.13	11.36	217	217	3.361E-07	33.61	3.36
2	0.685	2.135	40.79	28.02	536	536	8.287E-07	82.87	8.29
3	1.028	2.478	63.75	50.98	975	975	1.508E-06	150.77	15.08
4	1.371	2.821	94.03	81.26	1554	1554	2.403E-06	240.30	24.03
5	1.714	3.164	132.63	119.86	2292	2292	3.545E-06	354.47	35.45
6	2.056	3.506	180.58	167.81	3209	3209	4.963E-06	496.26	49.63
7	2.399	3.849	238.87	226.10	4324	4324	6.687E-06	668.65	66.87
8	2.742	4.192	308.53	295.76	5656	5656	8.747E-06	874.66	87.47
9	3.085	4.535	390.57	377.80	7225	7225	1.117E-05	1117.25	111.73
10	3.427	4.877	485.99	473.22	9050	9050	1.399E-05	1399.44	139.94

Figure A1-1. Size histograms of CdSe and CdSe/PbS QDs

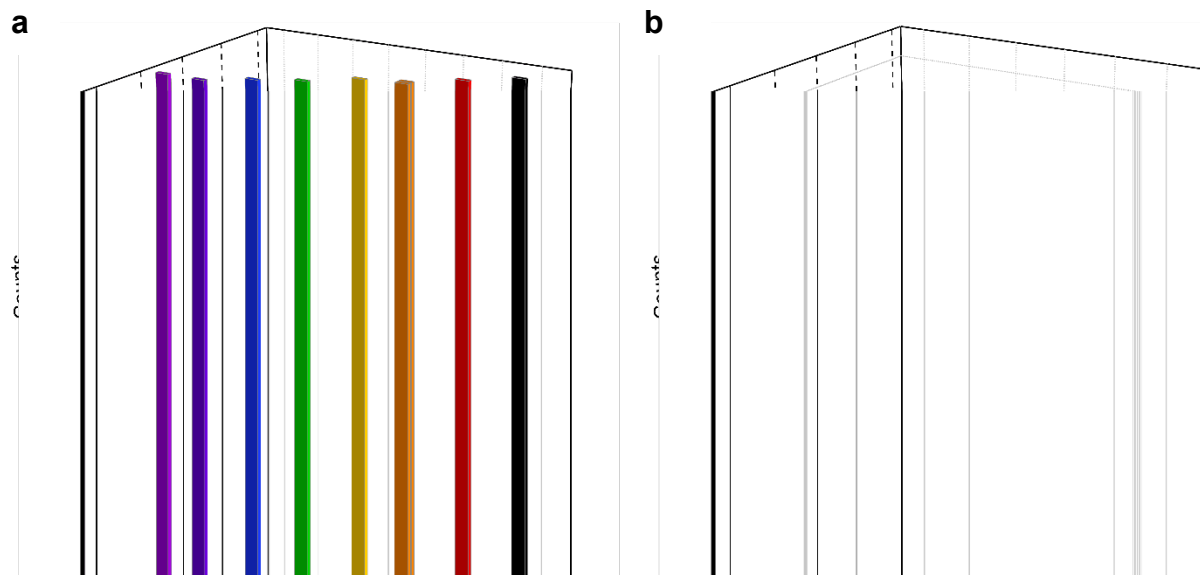


Figure A1-1. Normalized diameter histograms of CdSe/PbS QDs with 3.0 nm diameter CdSe cores (a) and 4.2 nm diameter CdSe cores (b). Arrows along the diameter axes indicate the average diameter of each sample.

Table A1-2. Diameter statistics of CdSe and CdSe/PbS QDs

Table A1-2. Diameter statistics of CdSe/PbS QDs measured by measuring across the middle of the QDs in TEM images. The number of QD diameters measured is indicated by n.

#ML	Core Diameter (nm)	n	Mean diameter (nm)	SD (%)	Mean radius (nm)
0.0	3.0(3)	323	3.0(3)	10	1.5
1.5	3.0(3)	329	4.0(4)	10	2.0
2.9	3.0(3)	313	5.0(5)	10	2.5
4.0	3.0(3)	336	5.7(5)	8.8	2.8
4.9	3.0(3)	348	6.3(5)	7.9	3.1
6.4	3.0(3)	247	7.3(7)	9.6	3.7
7.1	3.0(3)	316	7.9(7)	8.9	3.9
8.1	3.0(3)	392	8.5(9)	10.5	4.2
0.0	4.2(4)	200	4.2(4)	9.5	2.1
0.6	4.2(4)	251	4.6(4)	8.7	2.3
1.8	4.2(4)	301	5.4(6)	11	2.7
2.5	4.2(4)	245	5.9(7)	12	3.0
4.3	4.2(4)	303	7.1(9)	13	3.6
7.3	4.2(4)	218	9.0(8)	8.9	4.5

Table A1-3. List of other CdSe/PbS QD synthetic attempts

Table A1-3. List of experimental attempts to grow CdSe/PbS core/shell QDs by method using c-ALD method published by Ithurria *et al.*¹ and continuous growth method published by Mahler *et al.*²

Expt. Index	Literature Method	CdSe Core Crystal Structure	Sulfur Precursor	Pb Precursor	Solvent	Co-Solvent	Notes	Result
1	c-ALD	WZ	(NH ₄) ₂ S	Pb(Ac) ₂ •2H ₂ O	FA/toluene	None		Aggregation of QDs and homogeneous nucleation of PbS
2	c-ALD	WZ	(NH ₄) ₂ S	Pb(Ac) ₂ •2H ₂ O	FA/toluene	None	End with Sulfur/DDAB termination	Aggregation of QDs and homogeneous nucleation of PbS
3	c-ALD	ZB	(NH ₄) ₂ S	Pb(Ac) ₂ •2H ₂ O	FA/toluene	None		Aggregation of QDs and homogeneous nucleation of PbS
4	c-ALD	ZB	(NH ₄) ₂ S	Pb(Ac) ₂ •2H ₂ O	FA/toluene	None	Without washing CdSe cores	Aggregation of QDs and homogeneous nucleation of PbS
5	c-ALD	ZB	(NH ₄) ₂ S	Pb(Ac) ₂ •2H ₂ O	FA/toluene	None	1/10 th DDAB and Et ₄ NBr used in phase transfer	Aggregation of QDs and homogeneous nucleation of PbS
6	Continuous Growth	ZB	Thioacetamide	Pb(oleate) ₂	Chloroform	Octylamine		Significant homogeneous nucleation of PbS
7	Continuous Growth	ZB	Thiourea	Pb(oleate) ₂	Chloroform	Octylamine		Very slow or no reaction
8	Continuous Growth	ZB	Thioacetamide	Pb(oleate) ₂	Chloroform	Octylamine	Slow addition of Pb precursor	Least quantity of black precipitate (PbS nucleation and aggregate of QDs) observed
9	Continuous Growth	ZB	(NH ₄) ₂ S	Pb(oleate) ₂	Chloroform	Octylamine	Slow addition of Pb precursor	Significant homogeneous nucleation of PbS
10	Continuous Growth	ZB	Thiourea	Pb(oleate) ₂	DCM	Octylamine		Very slow or no reaction

11	Continuous Growth	ZB	Thiourea	Pb(oleate) ₂	Chloroform	Octylamine	Increased quantity of octylamine	Very slow or no reaction
12	Continuous Growth	ZB	Thiourea	Pb(oleate) ₂	Octylamine	None		Very slow or no reaction
13	Continuous Growth	ZB	Thioacetamide	Pb(Ac) ₂ •2H ₂ O	Chloroform	Octylamine		Aggregation of QDs
14	Continuous Growth	ZB	Thioacetamide	Pb(oleate) ₂	Chloroform	Octylamine	Added oleic acid	No observable difference in synthesis compared to expt 6
15	Continuous Growth	ZB	Thioacetamide	Pb(oleate) ₂	Chloroform	Octylamine	Air-free synthesis	No observable difference in synthesis compared to expt 6
16	Continuous Growth	ZB	Thioacetamide	Pb(oleate) ₂	Chloroform	Octylamine	Pb(oleate) ₂ as limiting reagent	Significant homogeneous nucleation of PbS

Abbreviations

c-ALD – Colloidal Alternating Layer Deposition

DDAB – Didodecyldimethylammonium Bromide

Et₄NBr – Tetraethylammonium Bromide

FA – Formamide

DCM – Dichloromethane

(NH₄)₂S – Solution of 40% by weight (NH₄)₂S in water

Pb(oleate)₂ – 0.1 M solution of lead oleate in octylamine

WZ – Wurtzite crystal structure

ZB – Zinc Blende crystal structure

Figure A1-2. Identification of first absorption peak of CdSe core and CdSe/PbS core/shell QDs by second derivative

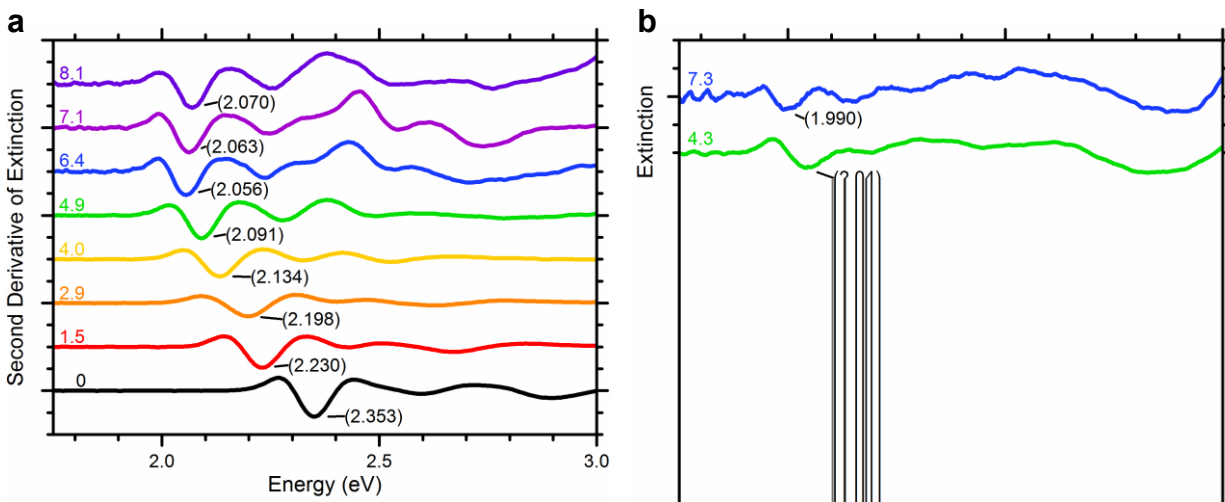


Figure A1-2. Second derivative of extinction spectra of CdSe core and CdSe/PbS core/shell QDs with 3 nm diameter cores (left) and 4 nm diameter cores (right) labeled with #ML PbS on left of each spectrum. The first absorption peak energy is labeled for each spectrum. The derivative spectra are offset for clarity.

Table A1-4. First absorption peak, PL peak, and Stokes shift for CdSe and CdSe/PbS QDs

Table A1-4. Spectroscopic data for the energies of the first absorption peak (ABS Peak), PL peak, and Stokes shift between the first absorption peak and the PL peak for CdSe and CdSe/PbS QDs by #ML. Errors for peak identification were based on noise of the spectra and curvature of the features.

#ML	diameter (nm)	ABS Peak (eV)	PL Peak (eV)	Stokes Shift (meV)
0.0	3.0(3)	2.353(5)	2.283(4)	70(6)
1.5	4.0(4)	2.230(4)	2.201(4)	29(6)
2.9	5.0(5)	2.198(4)	2.168(4)	30(6)
4.0	5.7(5)	2.134(7)	2.073(4)	61(8)
4.9	6.3(5)	2.091(4)	2.011(6)	80(7)
6.4	7.3(7)	2.056(7)	1.997(6)	59(9)
7.1	7.9(7)	2.063(7)	2.006(3)	57(8)
8.1	8.5(9)	2.070(7)	1.996(7)	70(10)
0.0	4.2(4)	2.160(4)	2.118(2)	42(4)
0.6	4.6(4)	2.149(4)	2.112(4)	37(6)
1.8	5.4(6)	2.084(7)	2.041(7)	40(10)
2.5	5.9(7)	2.127(7)	2.075(4)	52(8)
4.3	7.1(9)	2.04(1)	1.994(6)	50(10)
7.3	9.0(8)	1.990(3)	1.970(2)	20(4)

Table A1-5. PLQY values for CdSe and CdSe/PbS QDs

Table A1-5. Dependence of PLQY (in %) measured for each CdSe core and CdSe/PbS core/shell QD sample (identified by #ML, diameter of the CdSe core, and total diameter of the CdSe/PbS QD) on excitation energy.

CdSe/PbS QD Sample			Excitation Energy (eV)								
#ML	Core diameter (nm)	QD diameter (nm)	2.25	2.36	2.48	2.61	2.76	2.92	3.10	3.31	3.54
0.0	3.0(3)	3.0(3)			3.43(9)	3.50(9)	3.18(8)	2.8(1)	2.4(1)	2.4(1)	2.4(1)
1.5	3.0(3)	4.0(4)			0.80(7)				0.72(7)		
2.9	3.0(3)	5.0(5)		0.22(2)					0.10(1)		
4.0	3.0(3)	5.7(5)		0.15(1)					0.09(1)		
4.9	3.0(3)	6.3(5)		0.18(1)					0.20(2)		
6.4	3.0(3)	7.3(7)		1.37(7)					1.2(1)		
7.1	3.0(3)	7.9(7)		0.67(6)					0.79(7)		
8.1	3.0(3)	8.5(9)		0.71(6)					0.91(8)		
0.0	4.2(4)	4.2(4)	10.5(3)		12.5(4)		12.9(4)		11.8(6)		11.7(6)
0.6	4.2(4)	4.6(4)			3.26(9)				2.32(6)		
1.8	4.2(4)	5.4(6)			10.2(3)				2.23(6)		
2.5	4.2(4)	5.9(7)			0.10(1)						
4.3	4.2(4)	7.1(9)			0.10(1)						
7.3	4.2(4)	9.0(8)	0.21(2)						0.76(6)		

Figure A1-3. Integrated absorption spectra of 4 nm CdSe core and CdSe/PbS core/shell QDs

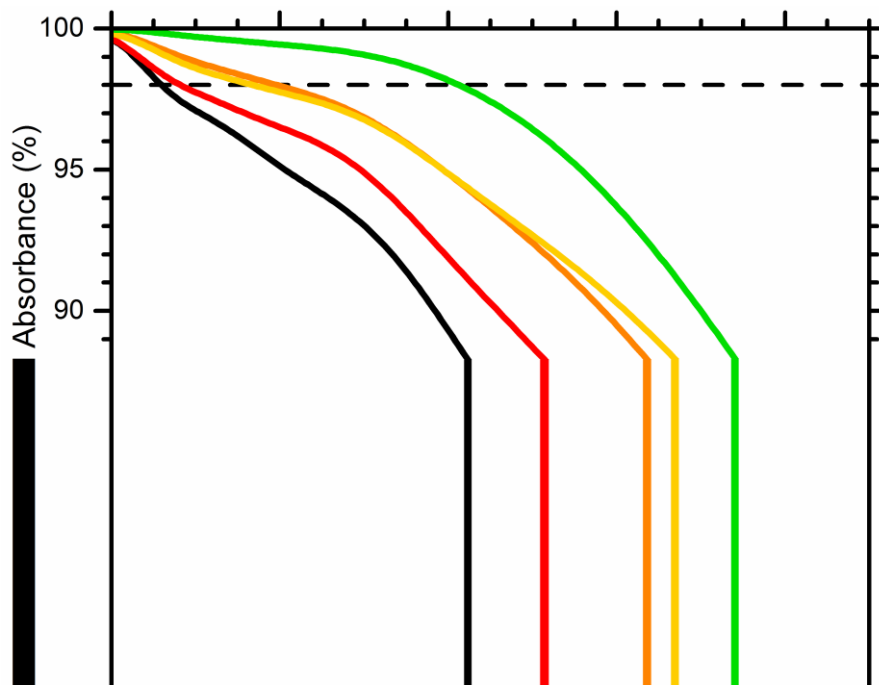


Figure A1-3. Integrated absorption spectra for CdSe core and CdSe/PbS core/shell QDs with 4 nm cores. These spectra were obtained by integrating from 4.2 eV down through the entire absorption spectra. The spectra are labeled by the #ML of the PbS shell. The spectra are normalized to a total of 100%, and the 98% level is indicated with a dashed line.

Figures A1-4 to A1-11. Radial probability density (RPD) functions

Haus *et al.* Method, $1S_e$ and $1S_h$:

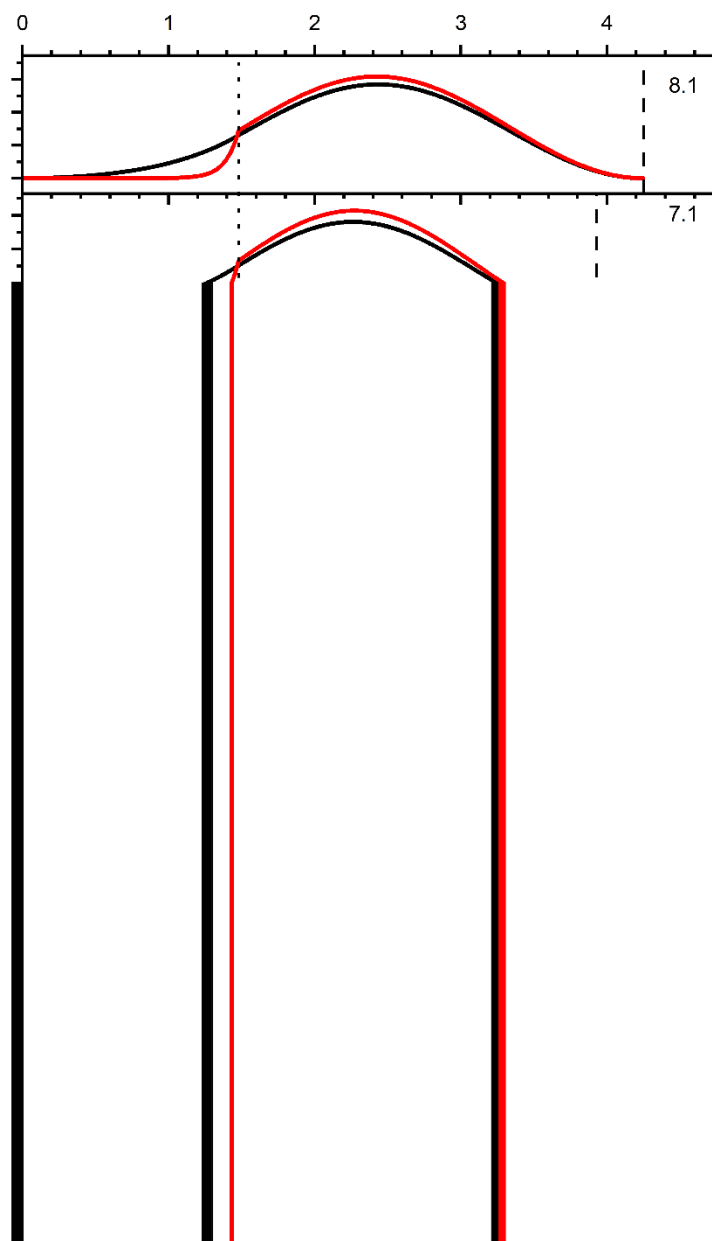


Figure A1-4. RPD functions calculated using the method published by Haus *et al.*^{3,4} plotted as a function of radius of the $1S_e$ (black) and $1S_h$ (red) states for CdSe and CdSe/PbS QDs with 3 nm diameter cores. Each panel is labeled with the #ML in the upper right corner. The effective masses utilized in the calculations are $m_e^*(\text{CdSe}) = 0.12m_e$, $m_e^*(\text{PbS}) = 0.105m_e$, $m_{hh}^*(\text{CdSe}) = 2.14m_e$, and $m_h^*(\text{PbS}) = 0.108m_e$.⁵⁻⁷ The radii of the core and the core/shell QDs are labeled with dotted and dashed vertical lines, respectively.

Haus *et al.* Method, $2S_e$ and $2S_h$:

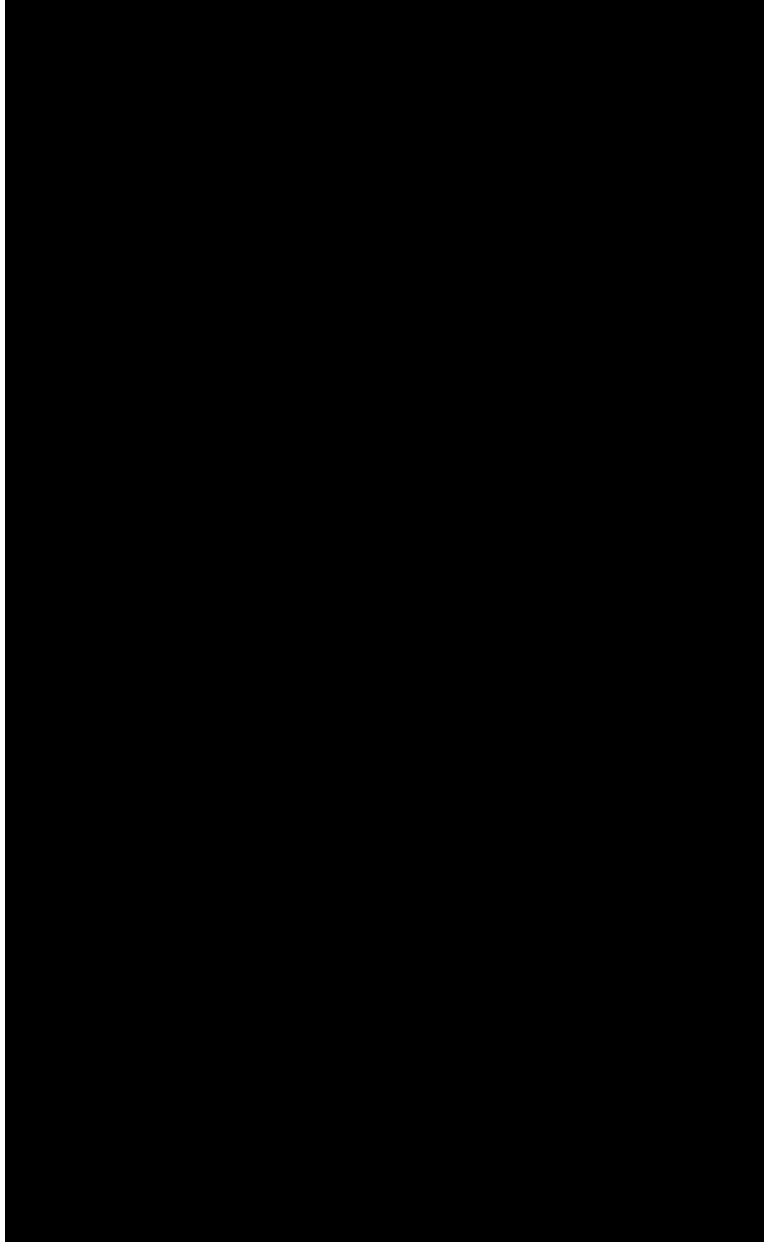


Figure A1-5. RPD functions calculated using the method published by **Haus *et al.***^{3,4} plotted as a function of radius of the $2S_e$ (black) and $2S_h$ (red) states for CdSe and CdSe/PbS QDs with 3 nm diameter cores. Each panel is labeled with the #ML in the upper right corner. The effective masses utilized in the calculations are $m_e^*(\text{CdSe}) = 0.12m_e$, $m_e^*(\text{PbS}) = 0.105m_e$, $m_{hh}^*(\text{CdSe}) = 2.14m_e$, and $m_h^*(\text{PbS}) = 0.108m_e$.⁵⁻⁷ The radii of the core and the core/shell QDs are labeled with dotted and dashed vertical lines, respectively.

Haus *et al.* Method, $3S_e$ and $3S_h$:

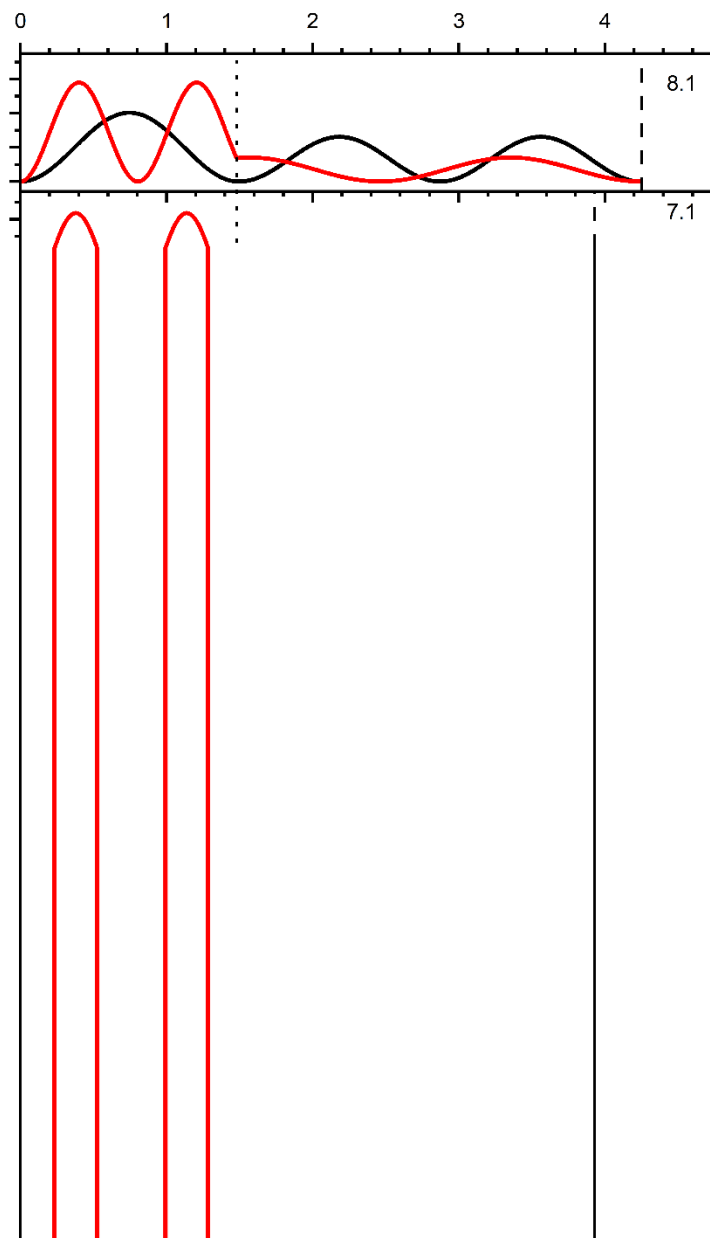


Figure A1-6. RPD functions calculated using the method published by Haus *et al.*^{3,4} plotted as a function of radius of the $3S_e$ (black) and $3S_h$ (red) states for CdSe and CdSe/PbS QDs with 3 nm diameter cores. Each panel is labeled with the #ML in the upper right corner. The effective masses utilized in the calculations are $m_e^*(\text{CdSe}) = 0.12m_e$, $m_e^*(\text{PbS}) = 0.105m_e$, $m_{hh}^*(\text{CdSe}) = 2.14m_e$, and $m_h^*(\text{PbS}) = 0.108m_e$.⁵⁻⁷ The radii of the core and the core/shell QDs are labeled with dotted and dashed vertical lines, respectively.

Kaledin *et al.* Method, $1S_e$ and $1S_h$ (heavy hole)

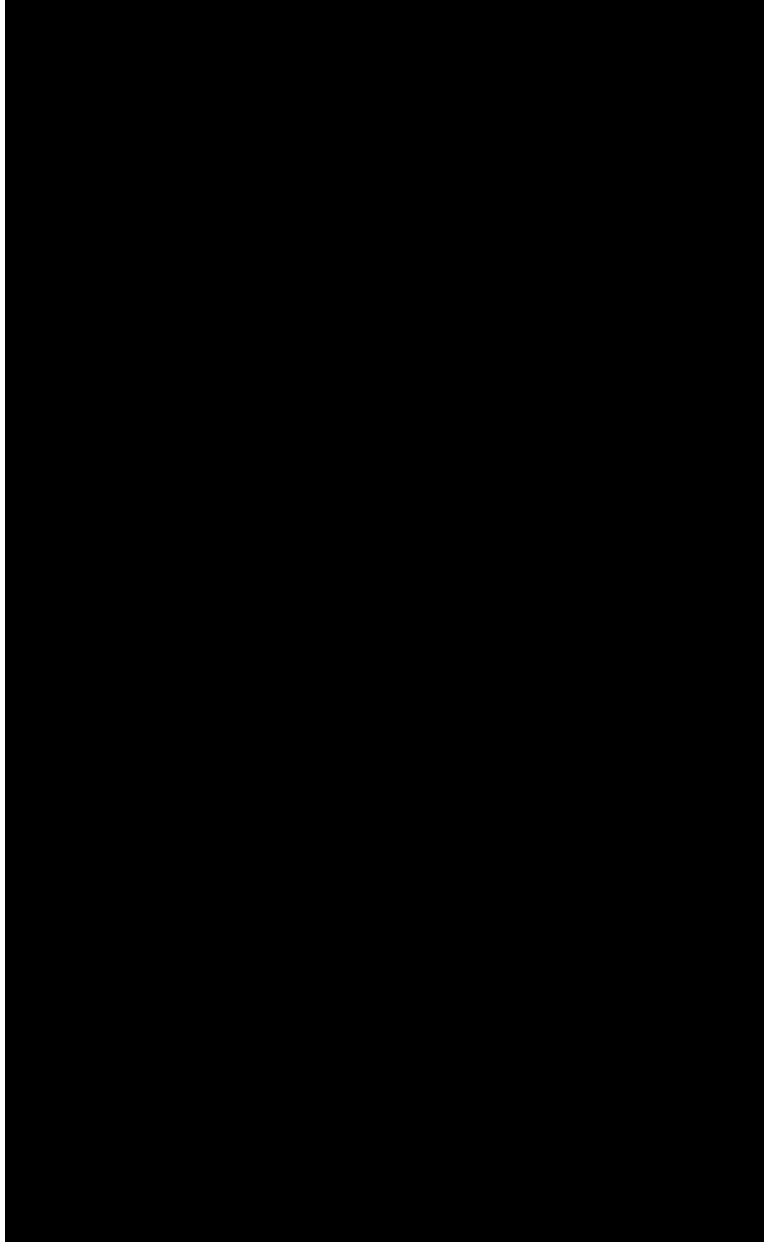


Figure A1-7. RPD functions calculated using the method published by **Kaledin *et al.***⁸ plotted as a function of radius of the $1S_e$ (black) and $1S_h$ (red) states for CdSe and CdSe/PbS QDs with 3 nm diameter cores. Each panel is labeled with the #ML in the upper right corner. The effective masses utilized in the calculations are $m_e^*(\text{CdSe}) = 0.12m_e$, $m_e^*(\text{PbS}) = 0.105m_e$, $m_{hh}^*(\text{CdSe}) = 2.14m_e$, and $m_h^*(\text{PbS}) = 0.108m_e$.⁵⁻⁷ The bare electron mass was used outside the QD. The radii of the core and the core/shell QDs are labeled with dotted and dashed vertical lines, respectively.

Kaledin *et al.* Method, $1S_e$ and $1S_h$ (light hole)

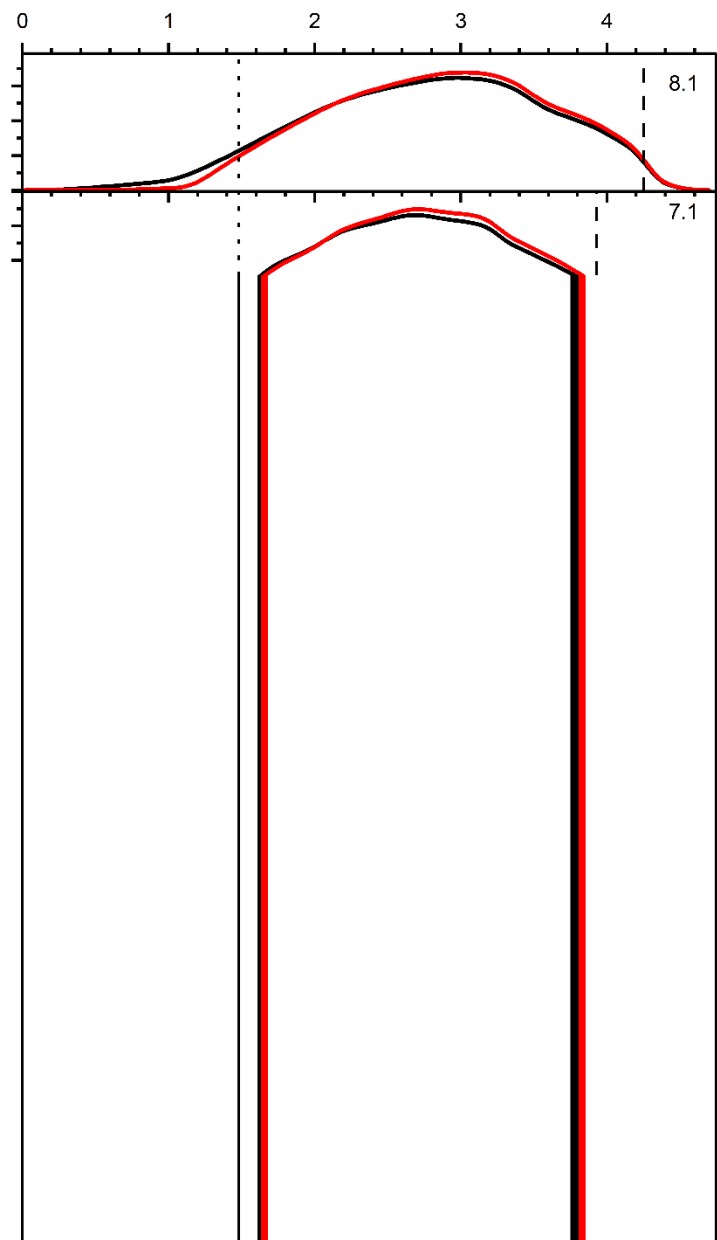


Figure A1-8. RPD functions calculated using the method published by **Kaledin *et al.***⁸ plotted as a function of radius of the $1S_e$ (black) and $1S_h$ (red) states for CdSe and CdSe/PbS QDs with 3 nm diameter cores. Each panel is labeled with the #ML in the upper right corner. The effective masses utilized in the calculations are $m_e^*(\text{CdSe}) = 0.12m_e$, $m_e^*(\text{PbS}) = 0.105m_e$, $m_{lh}^*(\text{CdSe}) = 0.16m_e$, and $m_{lh}^*(\text{PbS}) = 0.108m_e$.⁵⁻⁷ The bare electron mass was used outside the QD. The radii of the core and the core/shell QDs are labeled with dotted and dashed vertical lines, respectively.

Poulsen *et al.* Method, $1S_e$ and $1S_h$

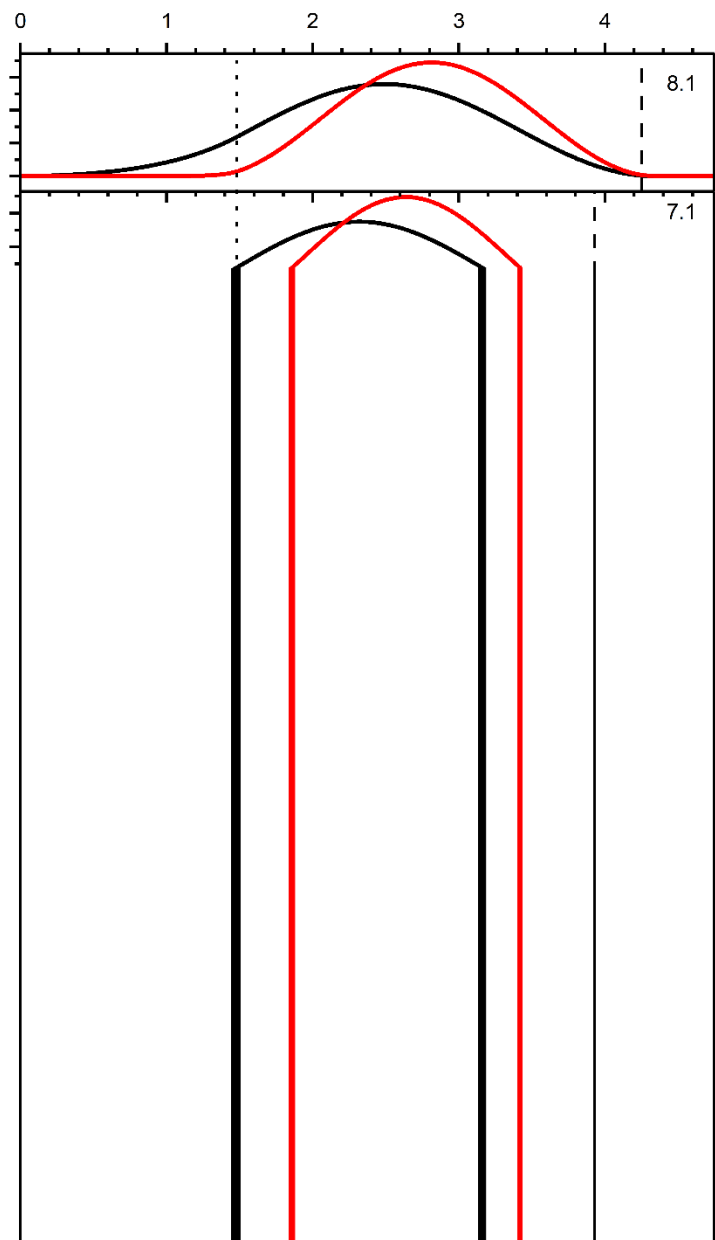


Figure A1-9. RPD functions calculated using the method published by **Poulsen *et al.***⁹ plotted as a function of radius of the $1S_e$ (black) and $1S_h$ (red) states for CdSe and CdSe/PbS QDs with 3 nm diameter cores. Each panel is labeled with the #ML in the upper right corner. The effective masses utilized in the calculations are $m_e^*(\text{CdSe}) = 0.12m_e$, $m_e^*(\text{PbS}) = 0.105m_e$, $m_{hh}^*(\text{CdSe}) = 2.14m_e$, and $m_h^*(\text{PbS}) = 0.108m_e$.⁵⁻⁷ The bare electron mass was used outside the QD. The radii of the core and the core/shell QDs are labeled with dotted and dashed vertical lines, respectively.

Poulsen *et al.* Method, $2S_e$ and $2S_h$

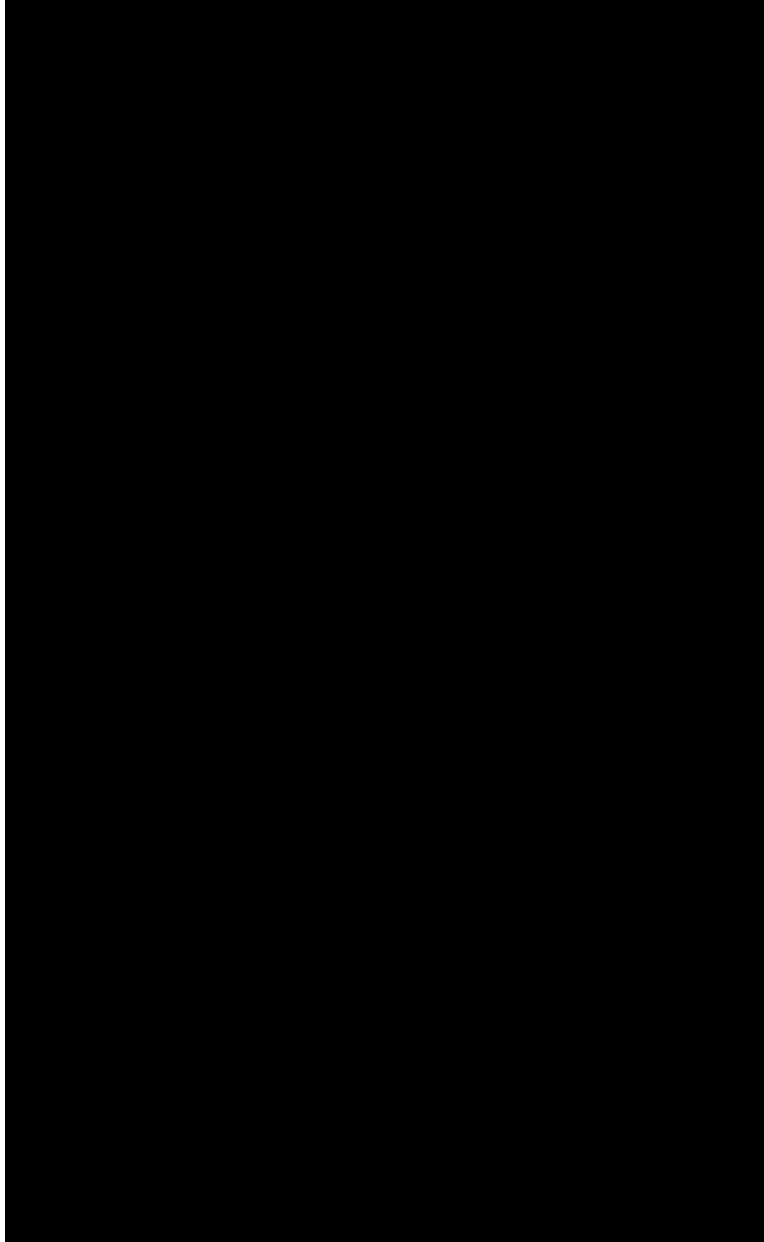


Figure A1-10. RPD functions calculated using the method published by **Poulsen *et al.***⁹ plotted as a function of radius of the $2S_e$ (black) and $2S_h$ (red) states for CdSe and CdSe/PbS QDs with 3 nm diameter cores. Each panel is labeled with the #ML in the upper right corner. The effective masses utilized in the calculations are $m_e^*(\text{CdSe}) = 0.12m_e$, $m_e^*(\text{PbS}) = 0.105m_e$, $m_{hh}^*(\text{CdSe}) = 2.14m_e$, and $m_h^*(\text{PbS}) = 0.108m_e$.⁵⁻⁷ The bare electron mass was used outside the QD. The radii of the core and the core/shell QDs are labeled with dotted and dashed vertical lines, respectively.

Poulsen *et al.* Method, $3S_e$ and $3S_h$

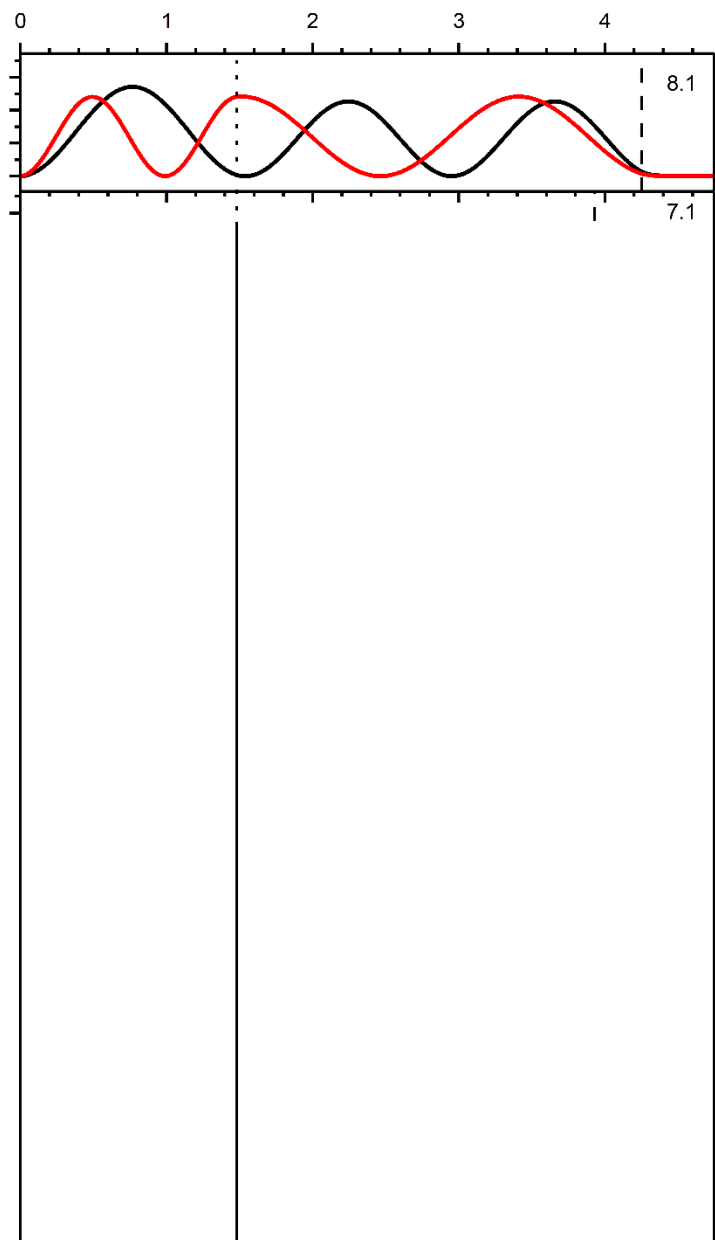


Figure A1-11. RPD functions calculated using the method published by **Poulsen *et al.***⁹ plotted as a function of radius of the $3S_e$ (black) and $3S_h$ (red) states for CdSe and CdSe/PbS QDs with 3 nm diameter cores. Each panel is labeled with the #ML in the upper right corner. The effective masses utilized in the calculations are $m_e^*(\text{CdSe}) = 0.12m_e$, $m_e^*(\text{PbS}) = 0.105m_e$, $m_{hh}^*(\text{CdSe}) = 2.14m_e$, and $m_h^*(\text{PbS}) = 0.108m_e$.⁵⁻⁷ The bare electron mass was used outside the QD. The radii of the core and the core/shell QDs are labeled with dotted and dashed vertical lines, respectively.

Figure A1-12. Calculated eigenstate energies plotted *versus* radius for CdSe core and CdSe/PbS core/shell QDs

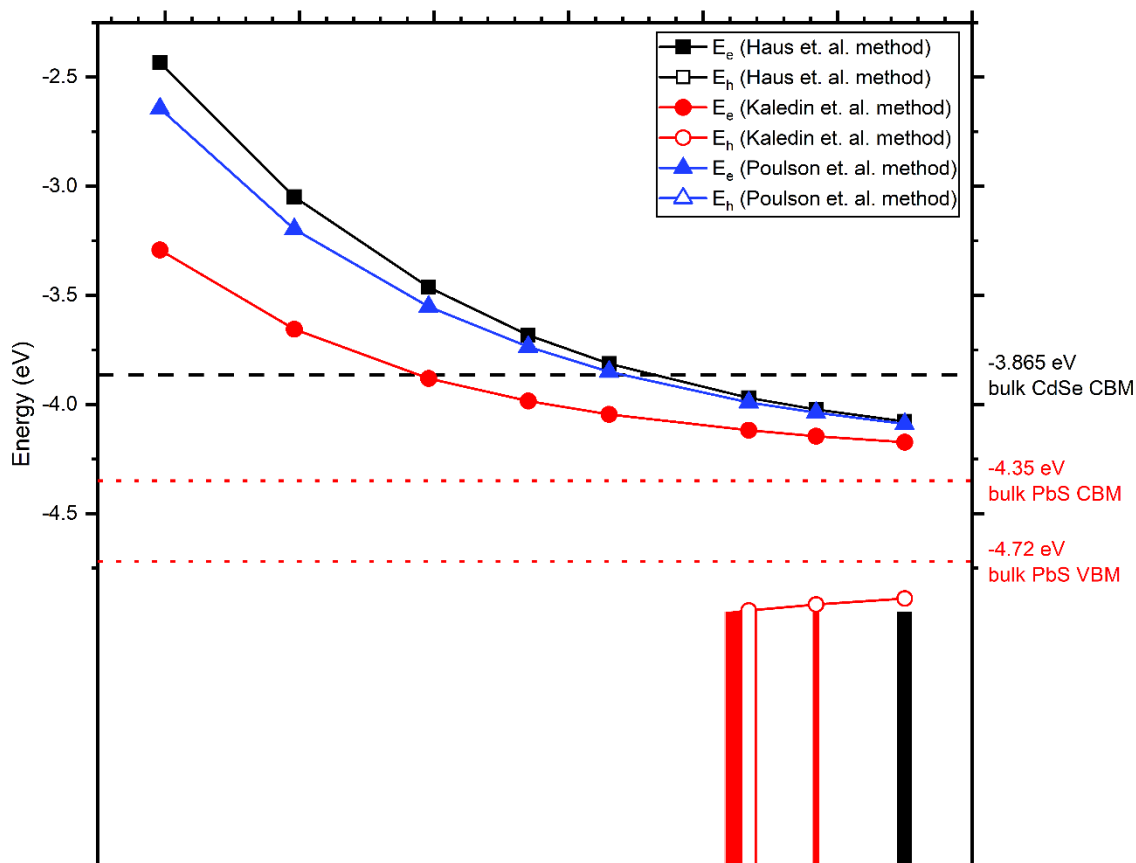


Figure A1-12. Energies relative to vacuum of the $1S_e$ electron (filled) and $1S_h$ heavy hole (open) states of CdSe/PbS QDs calculated using the method by Haus *et al.*^{3,4} (black squares), Kaledin *et al.*⁸ (red circles), and Poulson *et al.*⁹ (blue triangles) plotted as a function of QD radius. The bulk conduction band minima (CBM) and valence band maxima (VBM) of CdSe and PbS are plotted as dashed and dotted lines, respectively.^{10,11}

Figure A1-13. Calculated band gap energies plotted *versus* d^{-2}

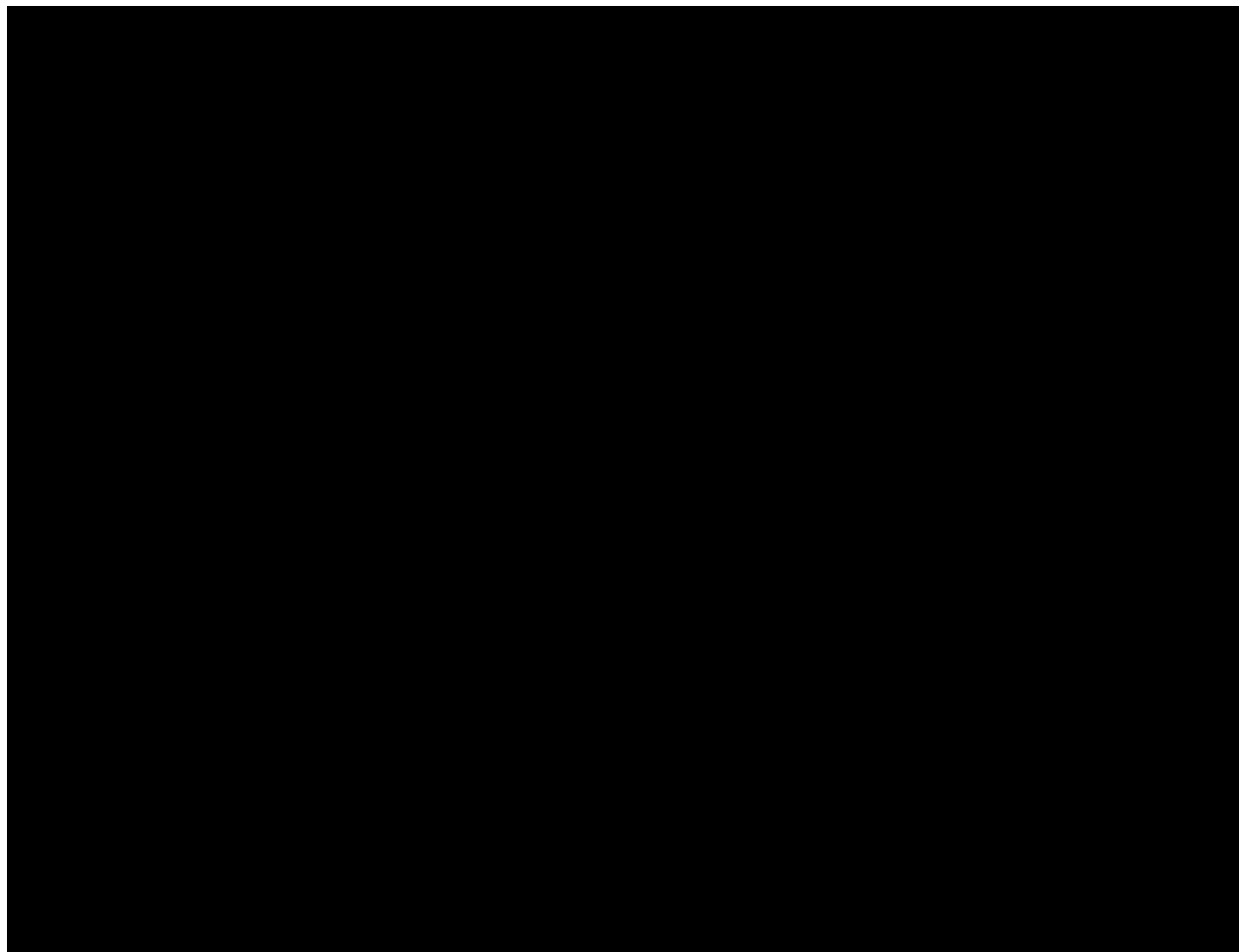


Figure A1-13. Difference in energy of the calculated $1S_e-1S_h$ absorption transition from the bulk CdSe ZB band gap (1.74 eV) for 3 nm core CdSe and CdSe/PbS core/shell QDs *versus* d^{-2} , where d is the total diameter of the QD. The calculations were performed using the methods of Haus *et al.*^{3,4} (black squares), Kaledin *et al.*⁸ (red circles), and Poulsen *et al.*⁹ (blue triangles) and using effective masses of $m_e^*(\text{CdSe}) = 0.12m_e$, $m_e^*(\text{PbS}) = 0.105m_e$, $m_{hh}^*(\text{CdSe}) = 2.14m_e$, and $m_h^*(\text{PbS}) = 0.108m_e$.⁵⁻⁷

Table A1-6. Calculated eigenstate and transition energies for CdSe and CdSe/PbS QDs

Table A1-6. Calculated eigenstate energies (in eV relative to vacuum) of the 1S electron state (1S_e) and 1S heavy hole state (1S_h) and the 1S_e–1S_h transition energies of the 3 nm core CdSe/PbS QDs listed by method.^{3,4,8,9}

Diameter (nm)	Haus			Kaledin			Poulsen		
	1S _e	1S _h	1S _e –1S _h	1S _e	1S _h	1S _e –1S _h	1S _e	1S _h	1S _e –1S _h
3.0(3)	-2.434	-5.621	3.187	-3.292	-5.619	2.327	-2.643	-5.610	2.967
4.0(4)	-3.049	-5.619	2.570	-3.655	-5.549	1.894	-3.197	-5.581	2.384
5.0(5)	-3.462	-5.613	2.151	-3.880	-5.215	1.335	-3.551	-5.556	2.005
5.7(5)	-3.682	-5.492	1.810	-3.983	-5.089	1.106	-3.736	-5.524	1.788
6.3(5)	-3.813	-5.301	1.488	-4.045	-5.020	0.975	-3.850	-5.462	1.612
7.3(7)	-3.970	-5.102	1.132	-4.118	-4.943	0.825	-3.990	-5.271	1.281
7.9(7)	-4.023	-5.042	1.019	-4.145	-4.917	0.772	-4.037	-5.189	1.152
8.5(9)	-4.078	-4.983	0.905	-4.173	-4.889	0.716	-4.088	-5.099	1.011

Strain-Induced Band Gap Modification. The strain-induced band gap modification can be calculated using the calculated Young's modulus (49.8 GPa/unit strain) and band gap pressure coefficient (43.1 meV/GPa).¹²⁻¹⁶ Based on the 1.9% strain between the bulk lattice constants of CdSe and PbS, the band gap change is ~41 meV. Using the strain between the measured CdSe QD lattice parameter and the bulk PbS lattice constant (3.5%), the strain-induced band gap change is ~75 meV. These calculations assume that the CdSe lattice parameter is compressed to the same lattice constant as the bulk PbS.

References

- (1) Ithurria, S.; Talapin, D. V., Colloidal Atomic Layer Deposition (c-ALD) using Self-Limiting Reactions at Nanocrystal Surface Coupled to Phase Transfer Between Polar and Nonpolar Media. *J. Am. Chem. Soc.* **2012**, *134*, 18585-18590.
- (2) Mahler, B.; Nadal, B.; Bouet, C.; Patriarche, G.; Dubertret, B., Core/Shell Colloidal Semiconductor Nanoplatelets. *J. Am. Chem. Soc.* **2012**, *134*, 18591-18598.
- (3) Haus, J. W.; Zhou, H. S.; Honma, I.; Komiyama, H., Quantum Confinement in Semiconductor Heterostructure Nanometer-Size Particles. *Phys. Rev. B: Condens. Matter Mater. Phys* **1993**, *47*, 1359-1365.
- (4) Vlaskin, V. A.; Beaulac, R.; Gamelin, D. R., Dopant—Carrier Magnetic Exchange Coupling in Colloidal Inverted Core/Shell Semiconductor Nanocrystals. *Nano Lett.* **2009**, *9*, 4376-4382.
- (5) Cadmium Selenide (CdSe) Electronic Properties, Cubic Modification. In *Landolt-Börnstein - Group III Condensed Matter 41B (II-VI and I-VII Compounds; Semimagnetic Compounds)*, Madelung, O.; Rössler, U.; Schulz, M., Eds. Springer-Verlag: Berlin/Heidelberg, 1999; pp 1-6.
- (6) Springholz, G.; Bauer, G., 9.1 IV-VI Semiconductors: General Properties. In *Landolt-Börnstein - Group III Condensed Matter 34A*, Springer-Verlag Berlin Heidelberg: Berlin, Heidelberg, 2013; Vol. 16, pp 415-421.
- (7) Kim, Y. D.; Klein, M. V.; Ren, S. F.; Chang, Y. C.; Luo, H.; Samarth, N.; Furdyna, J. K., Optical Properties of Zinc-Blende CdSe and $Zn_xCd_{1-x}Se$ Films Grown on GaAs. *Phys. Rev. B: Condens. Matter Mater. Phys* **1994**, *49*, 7262-7270.
- (8) Kaledin, A. L.; Lian, T.; Hill, C. L.; Musaev, D. G., An Infinite Order Discrete Variable Representation of an Effective Mass Hamiltonian: Application to Exciton Wave Functions in Quantum Confined Nanostructures. *J. Chem. Theory Comput.* **2014**, *10*, 3409-3416.

- (9) Poulsen, F.; Hansen, T., Band Gap Energy of Gradient Core—Shell Quantum Dots. *J. Phys. Chem. C* **2017**, *121*, 13655-13659.
- (10) Reiss, P.; Couderc, E.; De Girolamo, J.; Pron, A., Conjugated Polymers/Semiconductor Nanocrystals Hybrid Materials—Preparation, Electrical Transport Properties and Applications. *Nanoscale* **2011**, *3*, 446-489.
- (11) Li, J.; Wang, Shape Effects on Electronic States of Nanocrystals. *Nano Lett.* **2003**, *3*, 1357-1363.
- (12) Zhou, Y.; Wang, F.; Buhro, W. E., Large Exciton Energy Shifts by Reversible Surface Exchange in 2D II-VI Nanocrystals. *J. Am. Chem. Soc.* **2015**, *137*, 15198-15208.
- (13) Shan, W.; Walukiewicz, W.; Ager, J. W.; Yu, K. M.; Wu, J.; Haller, E. E., Pressure Dependence of the Fundamental Band-Gap Energy of CdSe. *Appl. Phys. Lett.* **2004**, *84*, 67-69.
- (14) Yang, J. W.; Hou, H. J., A First-Principles Study on the Structural and Elastic Properties and the Equation of State of Wurtzite-Type Cadmium Selenide under Pressure. *High Pressure Res.* **2012**, *32*, 376-384.
- (15) Jastrzebski, Z. D., In *The Nature and Properties of Engineering Materials*, 2nd ed.; Jon Wiley & Sons: New York, 1977; pp 202-203.
- (16) Deligoz, E.; Colakoglu, K.; Ciftci, Y., Elastic, Electronic, and Lattice Dynamical Properties of CdS, CdSe, and CdTe. *Phys. B.* **2006**, *373*, 124-130.

Appendix 2: Spectroscopy of CdSe/PbS Core/Shell Nanoplatelets

Table A2-1. Calculation of shell precursor quantities

Table A2-1. Example calculations of lead and sulfur precursor quantities, Pb(oleate)₂ and TAA, to add for the synthesis of a desired PbS shell thickness in #ML using a single step starting from CdSe core NPLs. The difference in volume and number of Pb atoms between the targeted CdSe/PbS core/shell NPL compared to the core NPL are listed as Δvolume vs. core and ΔPb atoms per NPL vs. core, respectively.

Calculation for CdSe/PbS Core/Shell NPLs using CdSe NPLs batch 181127b												
lateral size (nm ²):		261.45		Absorption details								
molar extinction coeff:	3290041	stock soln (mL)	0.06									
concentration (M)	2.7235E-07	solvent (mL)	3.5									
volume used in shell synthesis (uL)	200	total soln (mL)	3.56									
mols CdSe NPLs in shell synthesis	5.4471E-11	1st peak absorbance - absorption soln	0.15102									

#ML	Length (nm)	Width (nm)	Thickness (nm)	Volume (nm ³)	Δvolume vs core (nm ³)	ΔPb atoms per NPL vs. core	mols Pb atoms added total	vol. 0.01M Pb Oleate soln (uL)	TAA (mg)	Cd:Pb	Pb:Cd
0	31.5	8.3	1.22	318.97	0.0	0	0	0	0.0	N/A	N/A
1	31.843	8.643	1.563	430.17	111.2	2127	1.158E-07	12	1.2	2.868	0.349
2	32.186	8.986	1.906	551.26	232.3	4442	2.420E-07	24	2.4	1.373	0.728
3	32.529	9.329	2.249	682.49	363.5	6952	3.787E-07	38	3.8	0.877	1.140
4	32.872	9.672	2.592	824.10	505.1	9660	5.262E-07	53	5.3	0.631	1.584
5	33.215	10.015	2.935	976.32	657.4	12571	6.848E-07	68	6.8	0.485	2.061
6	33.558	10.358	3.278	1139.41	820.4	15690	8.547E-07	85	8.5	0.389	2.572
7	33.901	10.701	3.621	1313.61	994.6	19021	1.036E-06	104	10.4	0.321	3.118
8	34.244	11.044	3.964	1499.15	1180.2	22570	1.229E-06	123	12.3	0.270	3.700

Table A2-2. NPL Size Statistics

Table A2-2. Size statistics of the length, width, and thickness of CdSe core and CdSe/PbS core/shell NPLs with the number of measurements (n). The CdSe NPLs labeled CdSe #1 were used for the synthesis of 2.5, 3.4, and 4.7 ML CdSe/PbS core/shell NPLs. CdSe #2 was used for the synthesis of 6.9 ML CdSe/PbS core/shell NPLs.

Sample	Length		Width		Thickness		#ML
	Mean (nm)	n	Mean (nm)	n	Mean (nm)	n	
CdSe #1	30(3)	85	8(1)	60	2.0(3)	60	0
CdSe/PbS	23(4)	106	8(1)	106	2.8(3)	11	2.5
CdSe/PbS	21(4)	114	9(2)	114	3.55	1	3.4
CdSe/PbS	20(3)	141	9(1)	141	4.5(4)	5	4.7
CdSe #2	23(3)	120	10(1)	120			
CdSe/PbS	22(4)	70	14(3)	70	6.0(2)	10	6.9

Figure A2-1. Size histograms of CdSe core and CdSe/PbS core/shell NPLs

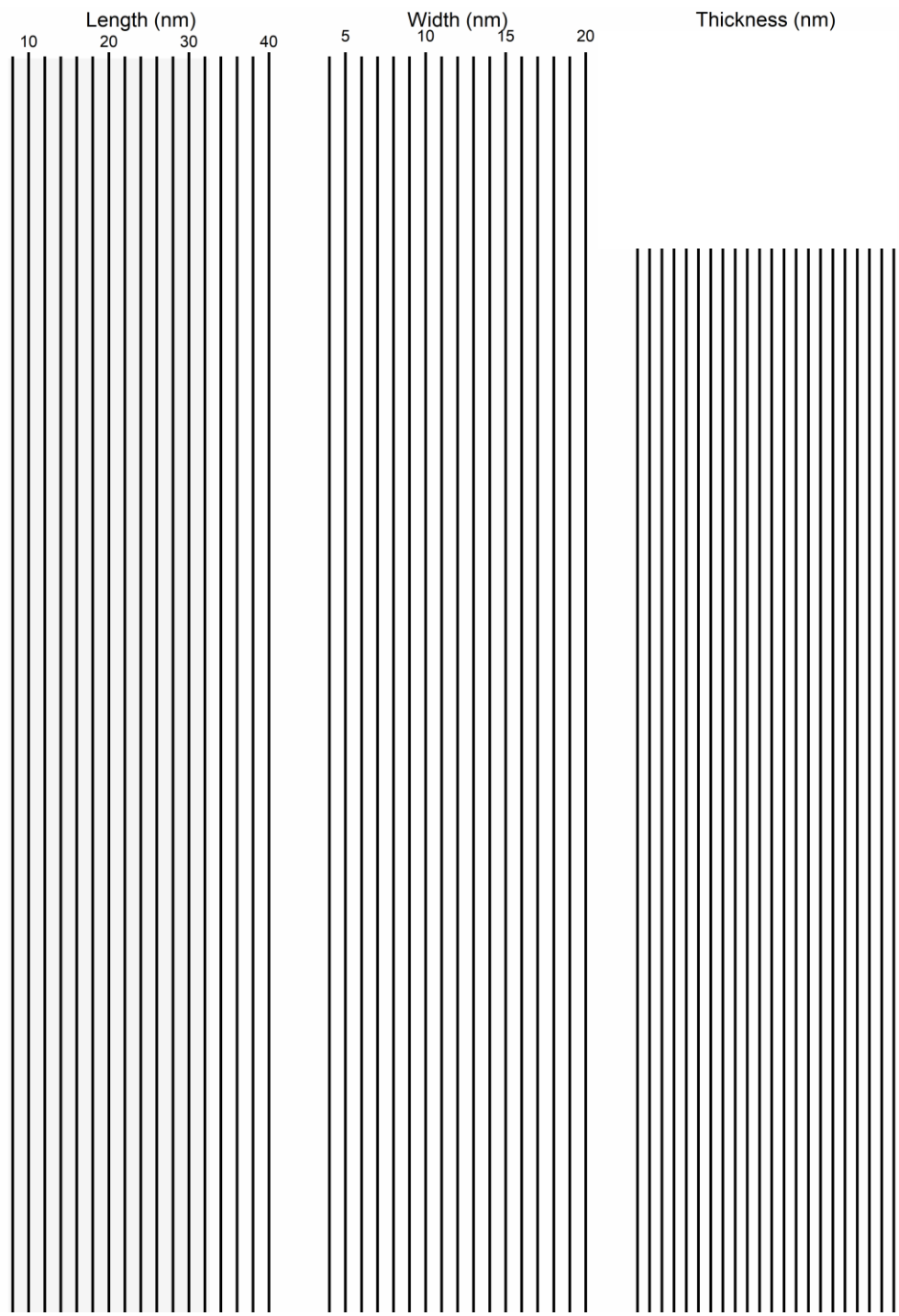


Figure A2-1. Length, width, and thickness histograms of CdSe core and CdSe/PbS core/shell NPLs labeled with the average thickness in # PbS ML, the average dimension, and the number of measurements (n). The 0 ML NPLs at top were used for the 3.5, 3.4, and 4.7 ML CdSe/PbS NPLs while the 0 ML NPLs in the fifth row were used for the synthesis of the 6.9 ML NPLs

Figure A2-2. CdSe core NPLs standing on edge.

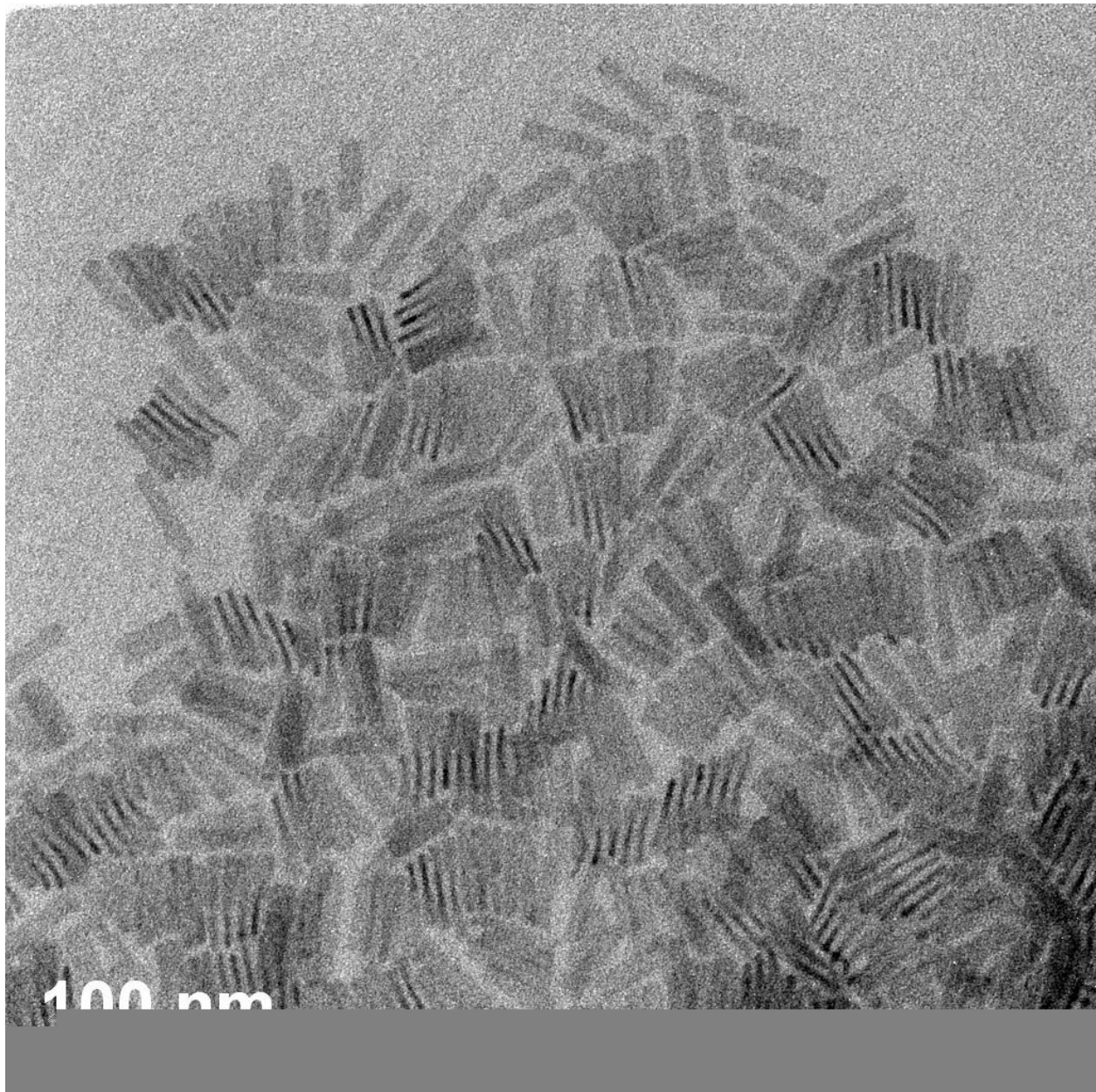


Figure A2-2. Representative TEM image of as-synthesized CdSe core NPLs. The core NPLs readily cluster and stand on end. The differences in contrast along the length of the NPLs can also be observed, resulting from differences in the crystallographic alignment of the NPL with the electron beam.

Table A2-3. NPL Size Statistics for samples used in ICP-MS experiments

Table A2-3. Size statistics of the length, width, and thickness of CdSe core and CdSe/PbS core/shell NPLs used in ICP-MS experiments. The number of measurements (n) and standard deviation (SD) are noted for each measurement.

Sample	Length			Width			Thickness			#ML
	Mean (nm)	SD (nm)	n	Mean (nm)	SD (nm)	n	Mean (nm)	SD (nm)	n	
CdSe	30	3	85	7	1	85	1.22	0.3	60	
CdSe/PbS	23	4	106	8	1	106	3.1	0.4	7	2.7
CdSe/PbS	20	3	141	9	1	141	4.5	0.4	5	4.8
CdSe	32	4	92	8	1	92	1.22			
CdSe/PbS	34	4	105	8	1	105	2.2	0.2	8	1.4
CdSe/PbS	24	5	40	8	1	39	3.1	0.3	7	2.7

Table A2-4. ICP-MS data of CdSe/PbS core/shell NPLs

Table A2-4. Volume calculations and Pb:Cd ratios from ICP-MS data for a variety of CdSe core and CdSe/PbS core/shell samples. The sizes were used to calculate the volume of the CdSe core and the PbS shell assuming a perfectly cuboid shape and an elliptical prism to provide a range of Pb:Cd ratios expected for a given sample. The ratio of Pb:Cd derived from ICP-MS data, with its standard deviation, is given at far right.

Sample	#ML	Volume - assuming cuboid (nm ³)	V _{shell} :V _{core} assuming cuboid	Volume - assuming ellipse (nm ³)	V _{core} remaining	V _{shell} :V _{core} assuming ellipse	Pb:Cd	SD
CdSe		256		201				
CdSe/PbS	2.7	570	1.23	448	154	1.90	1.5	0.2
CdSe/PbS	4.8	810	2.16	636	134	3.74	3.9	0.5
CdSe		312		245				
CdSe/PbS	1.4	598	0.92	470	261	0.80	0.7	0.1
CdSe/PbS	2.7	595	0.91	467	184	1.54	1.2	0.2

Figure A2-3. Peak identification in extinction spectra

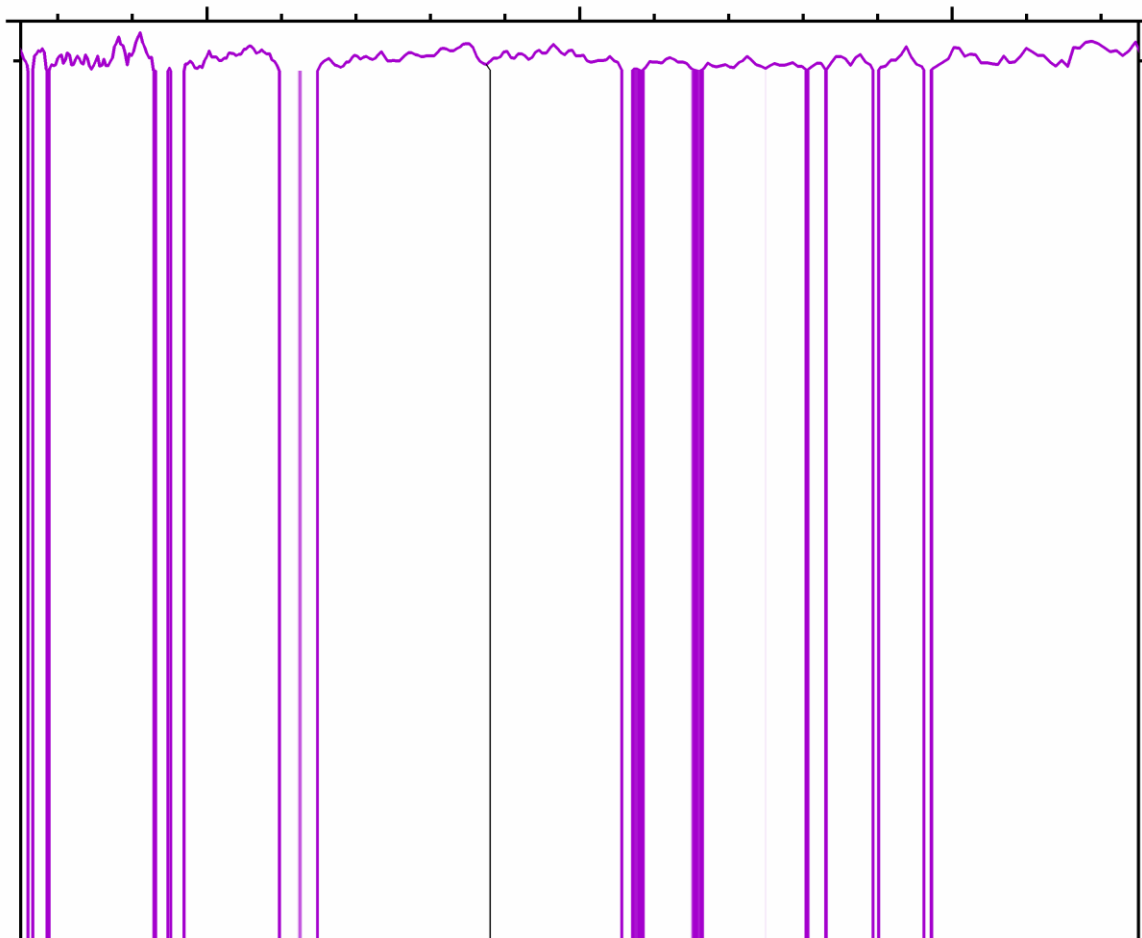


Figure A2-3. Second derivative of extinction spectra of CdSe core and CdSe/PbS core/shell NPLs with the number of PbS monolayers labeled at the right of each spectrum. The peaks are labeled and identified at the local minima for the $1e-1_{hh}$, $1e-1_{lh}$, and $1e-1_{so}$ transitions from lowest to highest energy, respectively. The derivative spectra are offset for clarity.

Table A2-5. First absorption peak, PL peak, and Stokes shift for CdSe and CdSe/PbS NPLs

Table A2-5. Spectroscopic data for the energies of the first absorption peak (Abs Peak), PL peak, and Stokes shift between the first absorption peak and the PL peak for CdSe and CdSe/PbS NPLs by #ML. Errors for peak identification were based on noise of the spectra and curvature of the features.

#ML	Abs Peak (eV)	PL Peak (eV)	Stokes Shift (meV)
0.0	2.426(5)	2.417(5)	9(7)
0 ML with S	2.31(1)	2.28(2)	30(20)
2.5	2.105(5)	2.072(5)	33(7)
3.4	2.049(7)	2.019(7)	30(10)
4.7	1.993(6)	1.975(6)	18(8)
6.9	1.943(7)	1.933(8)	10(11)

Table A2-6. PLQY values for CdSe and CdSe/PbS NPLs

Table A2-6. Dependence of PLQY (in %) for each CdSe core and CdSe/PbS core/shell NPL sample (identified by # PbS ML) on excitation energy. Two batches of CdSe core NPLs were used; one batch, with 4.8% PLQY at 3.1 eV excitation energy, was used for the preparation of the samples: 0 with S, 2.5, 3.4, and 4.7 ML. The batch with PLQY of 7.9% was used for the preparation of 6.9 ML CdSe/PbS core/shell NPLs.

#ML	Excitation Energy (eV)				
	3.54	3.10	2.76	2.48	2.25
0		4.8(3)			
0 with S		<0.01			
2.5	21.9(9)	21.4(9)	22.4(9)	22.6(9)	22.3(9)
3.4	13.9(8)	16.6(9)	19.1(9)	18.7(9)	17.5(9)
4.7	18.7(9)	19.5(9)	21.8(9)	24.4(9)	24.4(9)
0		7.9(5)			
6.9		<0.01			

Figure A2-4. Trap Emission from CdSe NPLs

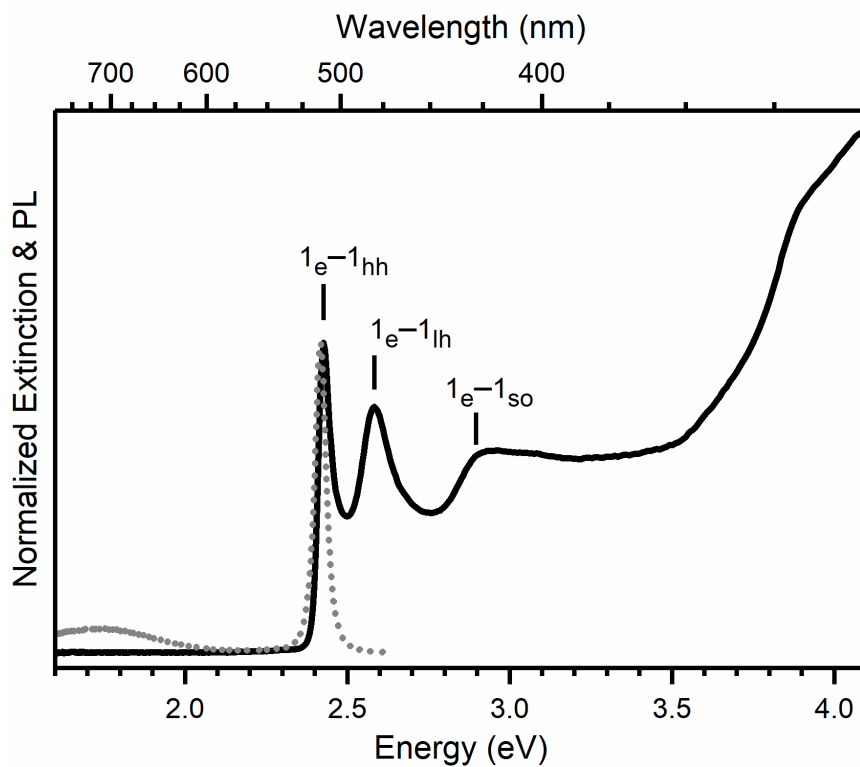


Figure A2-4. Extinction (black dotted line) and photoluminescence (gray dotted line) of CdSe core NPLs. Trap emission from the CdSe core NPLs is at low energy, centered at approximately 1.75 eV.

Figure A2-5. Fitting of first two absorption transitions

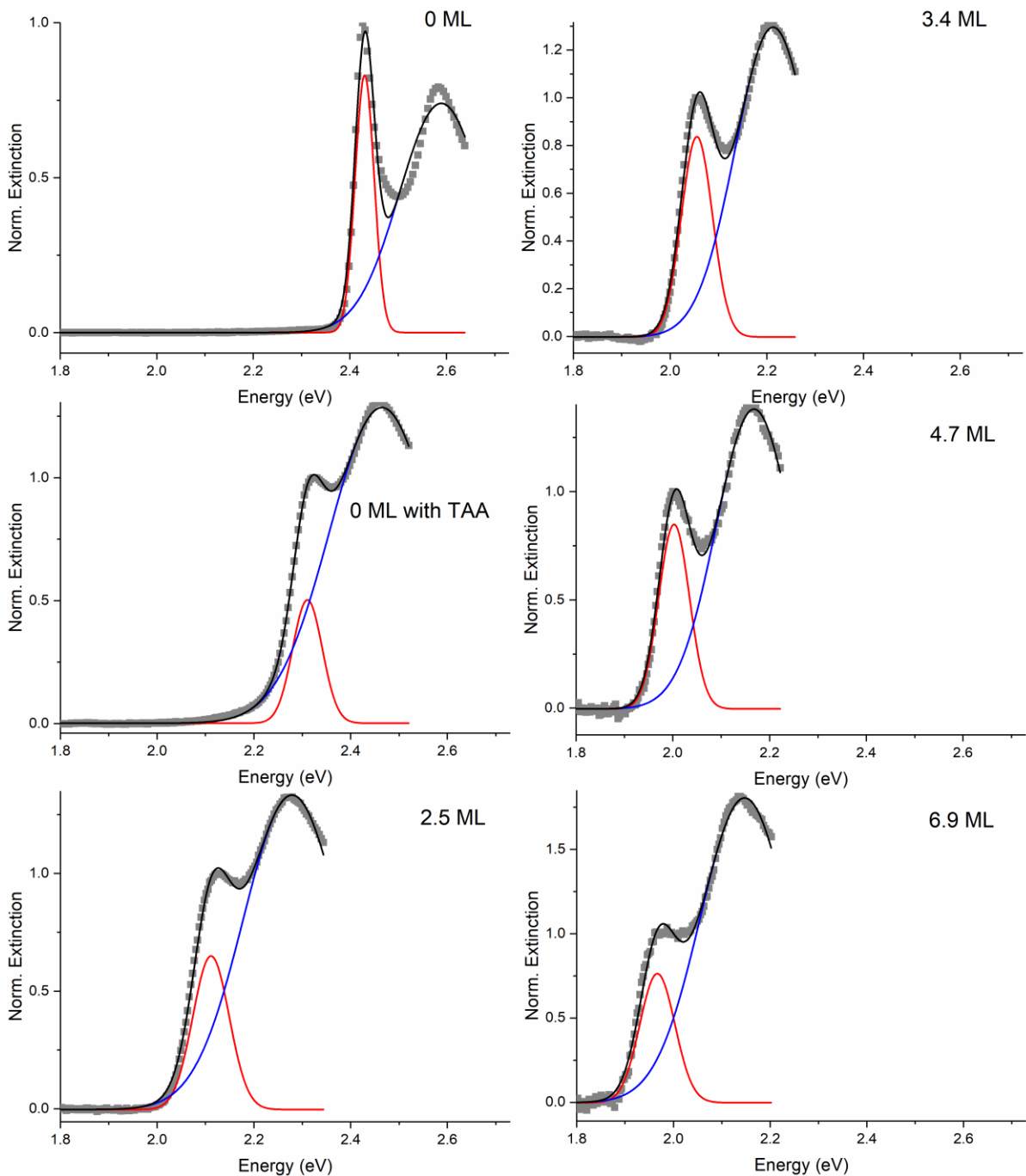


Figure A2-5. Results of fitting the first two absorption transitions (gray squares) to the sum of two Gaussian peaks (red and blue lines) with the total fit (black line). The thickness of the sample is labeled in the upper right of each panel.

Table A2-7. Calculated difference between light hole and heavy hole effective mass

Table A2-7. Calculation of difference in heavy hole and light hole effective masses ($\Delta\text{mass}_{\text{hh-lh}}$) in units of the bare electron mass from the $1_{e-1_{\text{hh}}}$ and $1_{e-1_{\text{lh}}}$ transition energies assuming a 1D particle in a box model. $\Delta_{\text{hh-lh}}$ is the difference in energy between the two transitions and L is the thickness of the box.

#ML	$1_{e-1_{\text{hh}}}$ (eV)	$1_{e-1_{\text{lh}}}$ (eV)	$\Delta_{\text{hh-lh}}$ (eV)	L (m)	$\Delta\text{mass}_{\text{hh-lh}}$ (m_e)
0 ML	2.426	2.583	-0.157	1.2E-09	-1.6
0 ML with S	2.309	2.455	-0.146	1.6E-09	-1.1
2.5 ML	2.105	2.267	-0.162	2.9E-09	-0.27
3.4 ML	2.049	2.202	-0.153	3.6E-09	-0.19
4.7 ML	1.993	2.149	-0.156	4.4E-09	-0.12
6.9 ML	1.943	2.112	-0.169	6.0E-09	-0.063

Figure A2-6. Extinction and PL spectra of CdSe core and CdSe/PbS core/shell NPLs used in PL lifetime study.

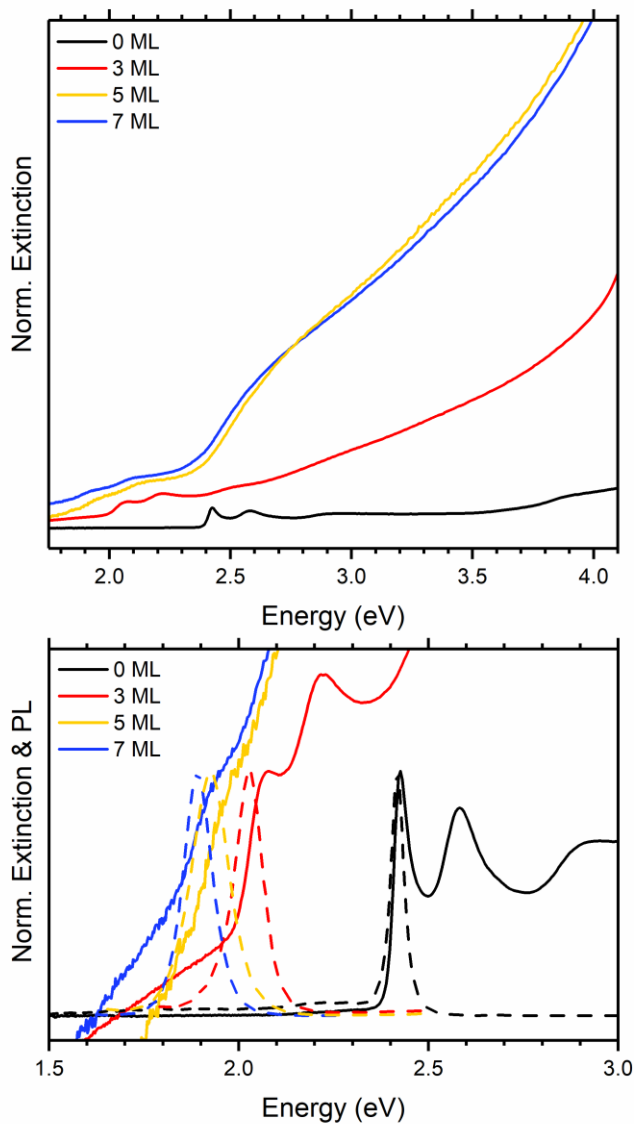


Figure A2-6. Extinction spectra (solid lines) and PL spectra (dashed lines) of CdSe NPLs and CdSe/PbS core/shell NPLs showing full UV-Vis absorption (a) and band edge region (b). Extinction spectra in (a) are offset for clarity. Scattering could not be corrected for the CdSe/PbS core/shell NPL extinction spectra.

Figure A2-7. Instrument response function for photoluminescence lifetimes

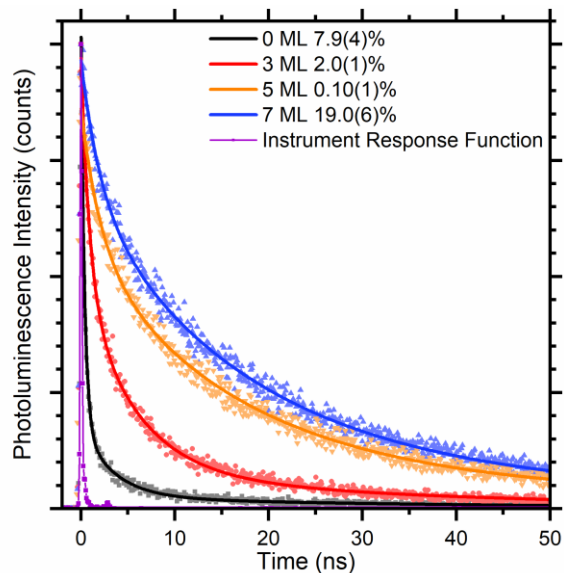


Figure A2-7. Measured photoluminescence lifetimes of CdSe core NPLs and CdSe/PbS core/shell NPLs (data points) with fitted exponential decay (line) labeled with photoluminescence quantum yield. The instrument response function (data points connected by straight line) is plotted in purple.

Table A2-8. Fitting parameters for time-resolved photoluminescence

Table A2-8. Results of fitting time-resolved PL decay of CdSe/PbS core/shell NPLs by monolayer (ML) with the photoluminescence quantum yield (PLQY). The fitting parameters are organized by lifetime, ranging from the shortest to longest lifetime for each sample.

#ML	PLQY (%)	Short		Medium		Long	
		Amplitude	Lifetime (ns)	Amplitude	Lifetime (ns)	Amplitude	Lifetime (ns)
0	7.9(4)	0.834(3)	0.384(2)	0.157(2)	3.36(5)	0.0249(5)	37.1(7)
3	2.0(1)	0.478(6)	0.90(1)	0.414(4)	5.55(7)	0.078(2)	35.5(6)
5	0.10(1)	0.289(4)	2.08(6)	0.476(3)	15.5(2)	0.096(4)	64(1)
7	19.0(6)	0.281(4)	2.05(6)	0.564(4)	16.6(2)	0.121(5)	61(1)

Appendix 3: Facet-Dependent Etching of CdSe Nanoplatelets by Lead Oleate

Figure A3-1. Size histograms of starting CdSe NPLs (black) and after etching with Pb(oleate)_2 in octadecene (red) or octylamine (blue).

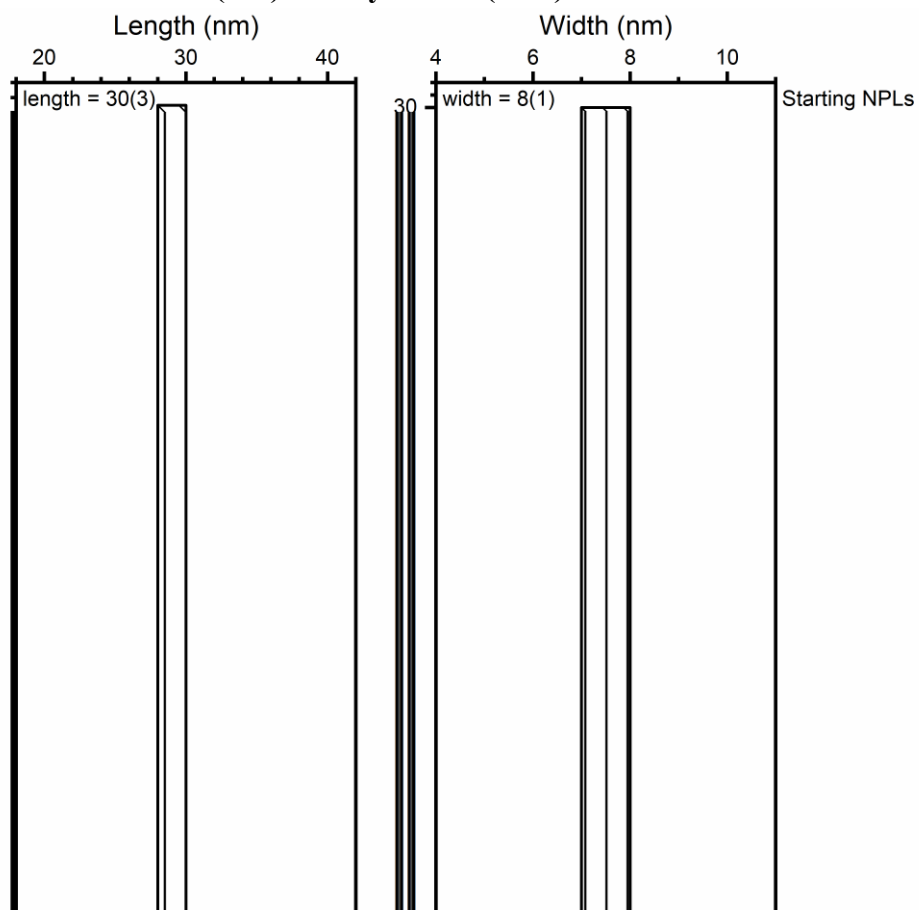


Figure A3-1. Histograms of length and width of nanoplatelets of starting CdSe NPLs (black), after etching with Pb(oleate)_2 in octadecene (red), and after etching with Pb(oleate)_2 in octylamine (blue). Each panel is labeled with the average size, the standard deviation in parentheses, and the number of measurements (n).

Figure A3-2. Size histograms of NDs produced by etching CdSe NPLs.

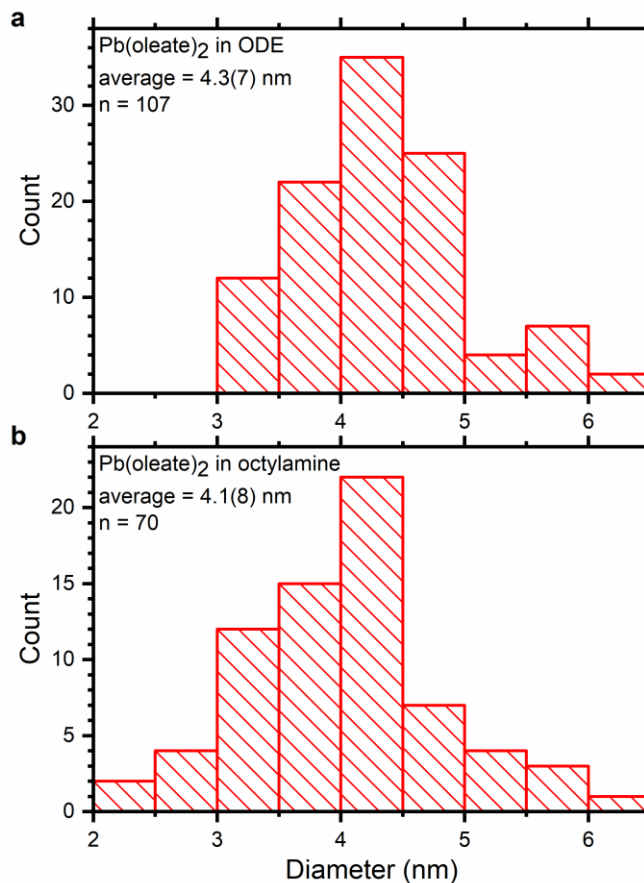


Figure A3-2. Distribution of diameter of nanodots produced by etching CdSe NPLs with (a) Pb(oleate)₂ in octadecene and (b) Pb(oleate)₂ in octylamine. Each panel is labeled with the average size, the standard deviation in parentheses, and the number of measurements (n).

Figure A3-3. Size histograms of NPLs with varying etching times.

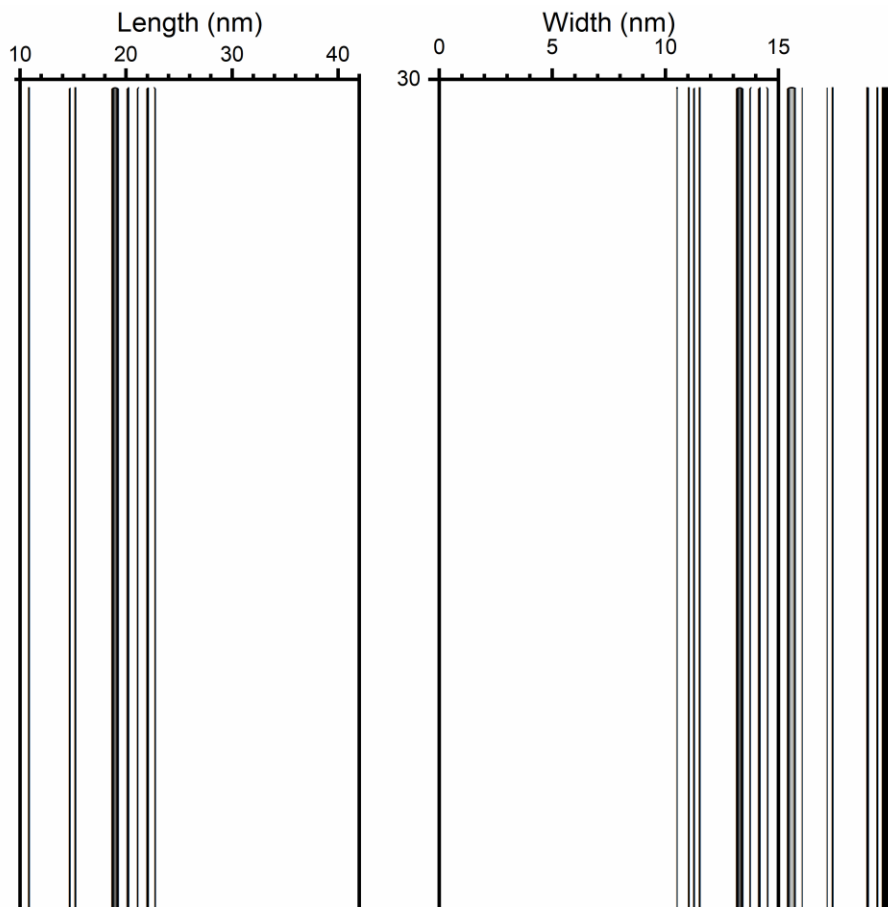


Figure A3-3. Distribution of length and width of NPLs after etching for varying amounts of time. The average value, with the standard deviation in parentheses, and the number of measurements (n) are noted in each panel.

Figure A3-4. Identification of first absorption feature by second derivative without baseline subtraction.

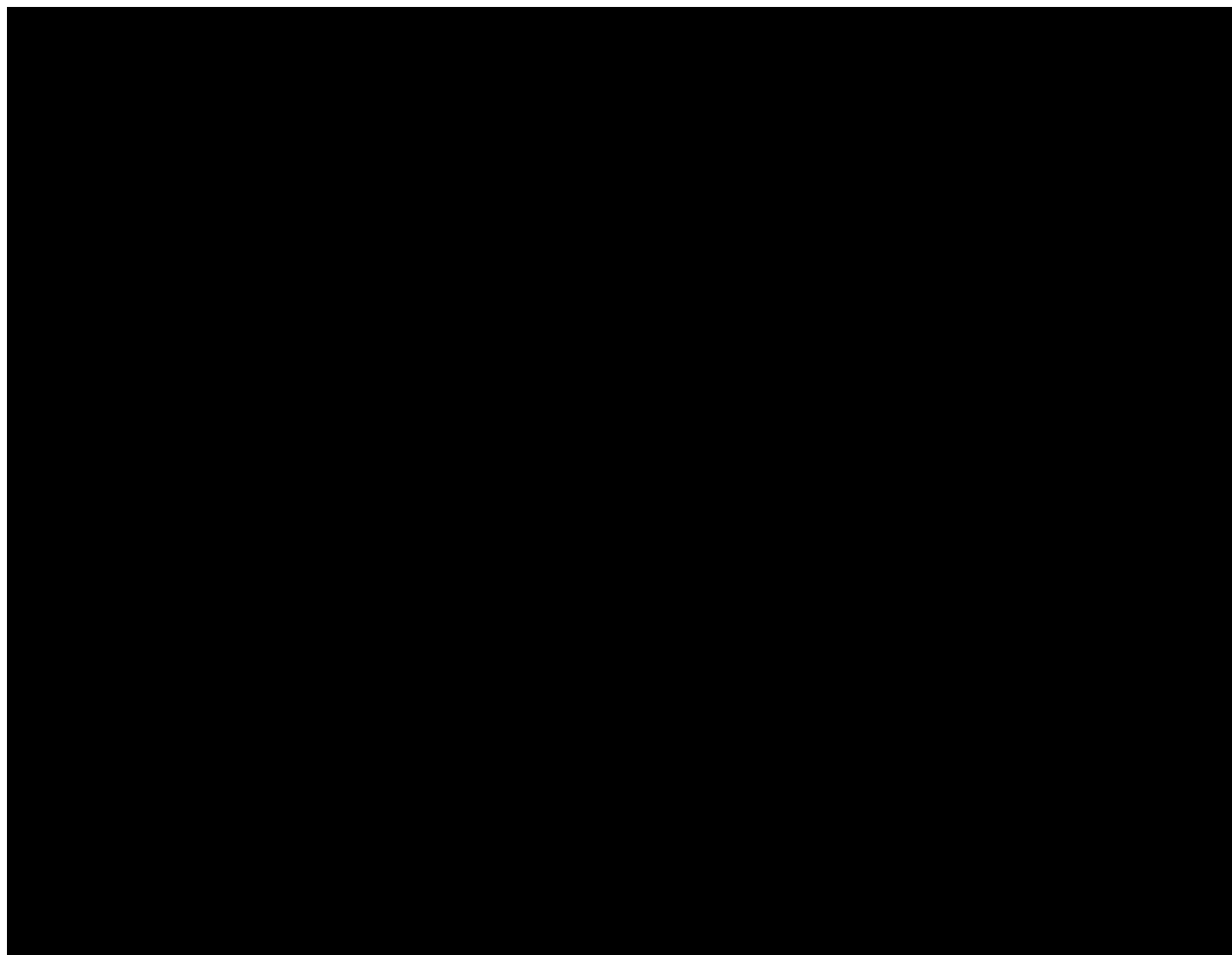


Figure A3-4. Band edge extinction spectra (black) and second derivative of extinction spectra (red) of CdSe NPLs etched with 0.01 M Pb(oleate)₂ in octylamine for 3, 6, or 9 hours, labeled in upper left of each panel. The energies of the local maximum of the extinction spectrum and the local minimum of the second derivative of the extinction spectra are labeled.

Table A3-1. Fitting parameters of curved extinction spectra baseline.

Table A3-1. Fitting parameters of extinction spectra baseline of etched NPLs etched with CdSe NPLs used in Figure A3-5, where the formula is $y = a + bE^c$ and E is the energy in eV.

Sample	a	b	c
3 hours	-47.38079	47.32944	0.00536
6 hours	-0.35055	0.3763	0.61183
9 hours	-0.29266	0.30103	1.14757

Figure A3-5. Identification of first absorption feature by second derivative with curved baseline subtraction.

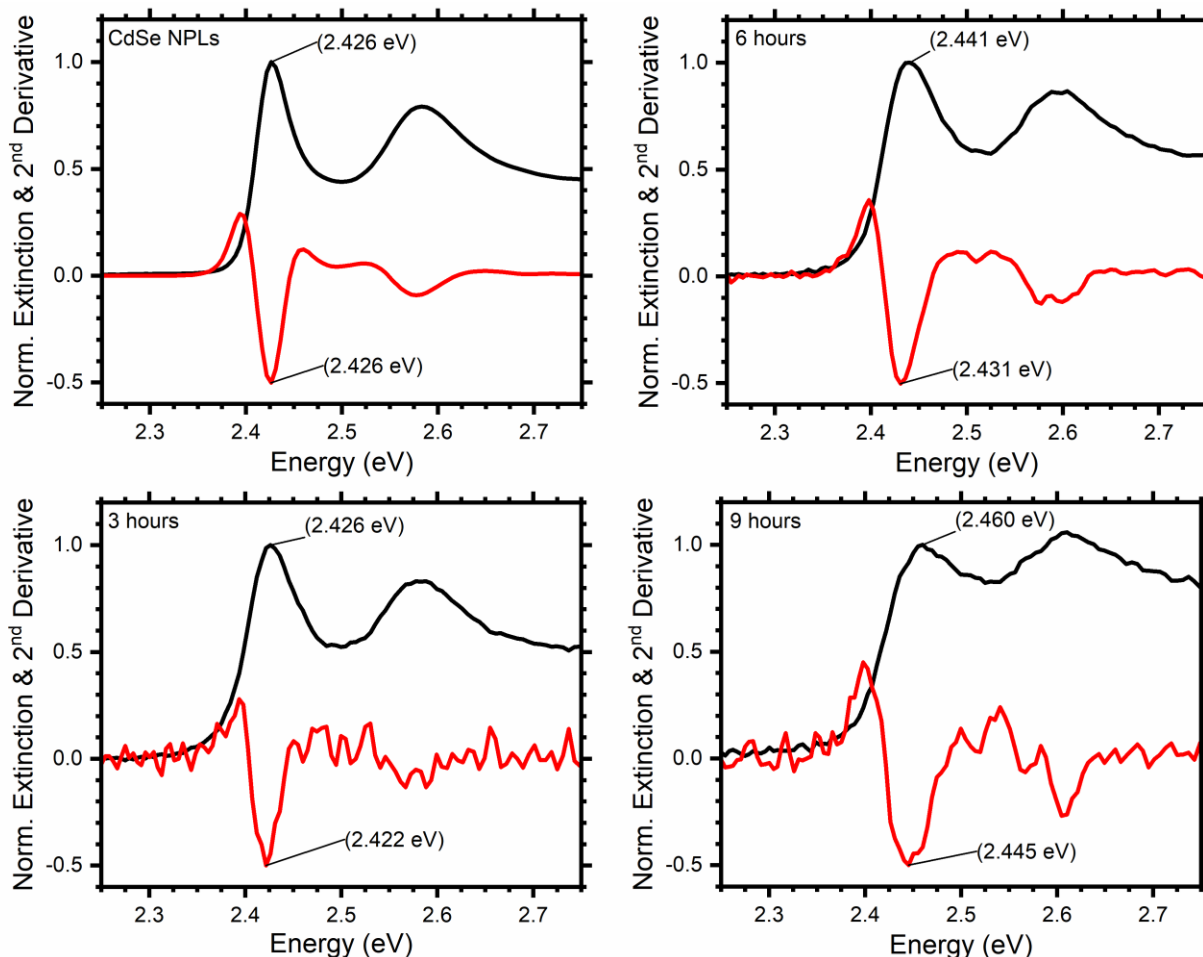


Figure A3-5. Band edge extinction spectra (black) and second derivative of extinction spectra (red) of CdSe NPLs etched with 0.01 M Pb(oleate)₂ in octylamine for 3, 6, or 9 hours, labeled in upper left of each panel. The baseline of the extinction spectra were fit to the formula $y = a + b\lambda^c$. The energies of the local maximum of the extinction spectrum and the local minimum of the second derivative of the extinction spectra are labeled.

Table A3-2. Example calculation of surface and interior Cd atoms in CdSe NPL.

Table A3-2. Example calculation of the ratio of Pb:Cd ratio if all surface Cd sites (and no interior Cd sites) were exchanged for Pb.

Length (nm)	31.5
Width (nm)	8.3
Thickness (nm)	1.22
Surface Area per NPL (nm ²)	620
Facet Density of Atoms (per nm ²)	5.46
Surface Cd atoms per NPL	3388
Volume per NPL (nm ³)	319
Density of atoms per unit cell (Cd atoms/nm ³)	18.06
Number of Cd atoms per NPL	5762
Number of interior Cd atoms per NPL	2374
Ratio of surface to total	0.588
Pb:Cd Ratio if all surface atoms were exchanged	1.427

Appendix 4: Maple 2017 Code for Solving 1D Double-Well Particle in a Box Model

```
[> restart;
[> digits:=100:
[>
[> ML := 4;
  t[c] := 1.22e-9;
  t[tot] := 1.22e-9 + (2·ML·0.343e-9);
                                ML := 4
                                tc := 1.22 10-9
                                ttot := 3.964 10-9
[>
```

(1)

```
> psi[e,I] := x -> A * sin(k[e,s] * x) :
psi[e,II] := x -> B * cosh(k[e,c] * (x - t[e,tot] / 2)) :
> psi[e,III] := x -> A * sin(k[e,s] * (t[e,tot] - x)) :
```

```
>
> E[e,I] := x -> \frac{-\frac{0.5}{m[e,s]} \cdot \text{diff}(\text{diff}(\text{psi}[e,I](x), x), x)}{\text{psi}[e,I](x)} :
E[e,II] := x -> \frac{-\frac{0.5}{m[e,c]} \cdot \text{diff}(\text{diff}(\text{psi}[e,II](x), x), x) + V[e,c] \cdot \text{psi}[e,II](x)}{\text{psi}[e,II](x)} :
E[e,III] := x -> \frac{-\frac{0.5}{m[e,s]} \cdot \text{diff}(\text{diff}(\text{psi}[e,III](x), x), x)}{\text{psi}[e,III](x)} :
```

```
>
> Kappa[e] := solve(E[e,I](x) = E[e,II](x), k[e,c]) :
> Gamma[e] := Kappa[e][1];
```

$$\Gamma_e := \frac{\sqrt{m_{e,s} m_{e,c} (2 \cdot V_{e,c} m_{e,s} - 1 \cdot k_{e,s}^2)}}{m_{e,s}} \quad (2)$$

```
> k[e,c] := sqrt(2 * m[e,c] * (E[e] - V[e,c])) / hbar :
> k[e,s] := sqrt(2 * m[e,s] * (E[e] - V[e,s])) / hbar :
```

```
>
> TransEq := \frac{\left( k[e,s] \cdot \cot\left( k[e,s] \cdot \left( -\frac{t[e,c]}{2} + \frac{t[e,tot]}{2} \right) \right) \right)}{m[e,s]}
- \frac{\left( -\text{Gamma}[e] \cdot \tanh\left( \text{Gamma}[e] \cdot \left( \frac{t[e,c]}{2} \right) \right) \right)}{m[e,c]} :
```

```
>
> V[e,c] := \frac{0.485}{27.2107}; #0.821 for hole, #0.485 for electron
V[e,s] := \frac{0}{27.2107};
t[e,c] := \frac{t[c]}{5.292e-11};
#t[e,s] := \frac{t[s]}{5.292e-11};
t[e,tot] := \frac{t[tot]}{5.292e-11};
m[e,c] := 0.12;
```

```
#2.14 for CdSe heavy hole; #0.16 for CdSe light hole; #0.12 for CdSe electron;  
m[e, s] := 0.105; #0.108 for PbS hole; #0.105 for PbS electron;  
hbar := 1;
```

$$V_{e,c} := 0.01782387076$$

$$V_{e,s} := 0.$$

$$t_{e,c} := 23.05366591$$

$$t_{e,tot} := 74.90551777$$

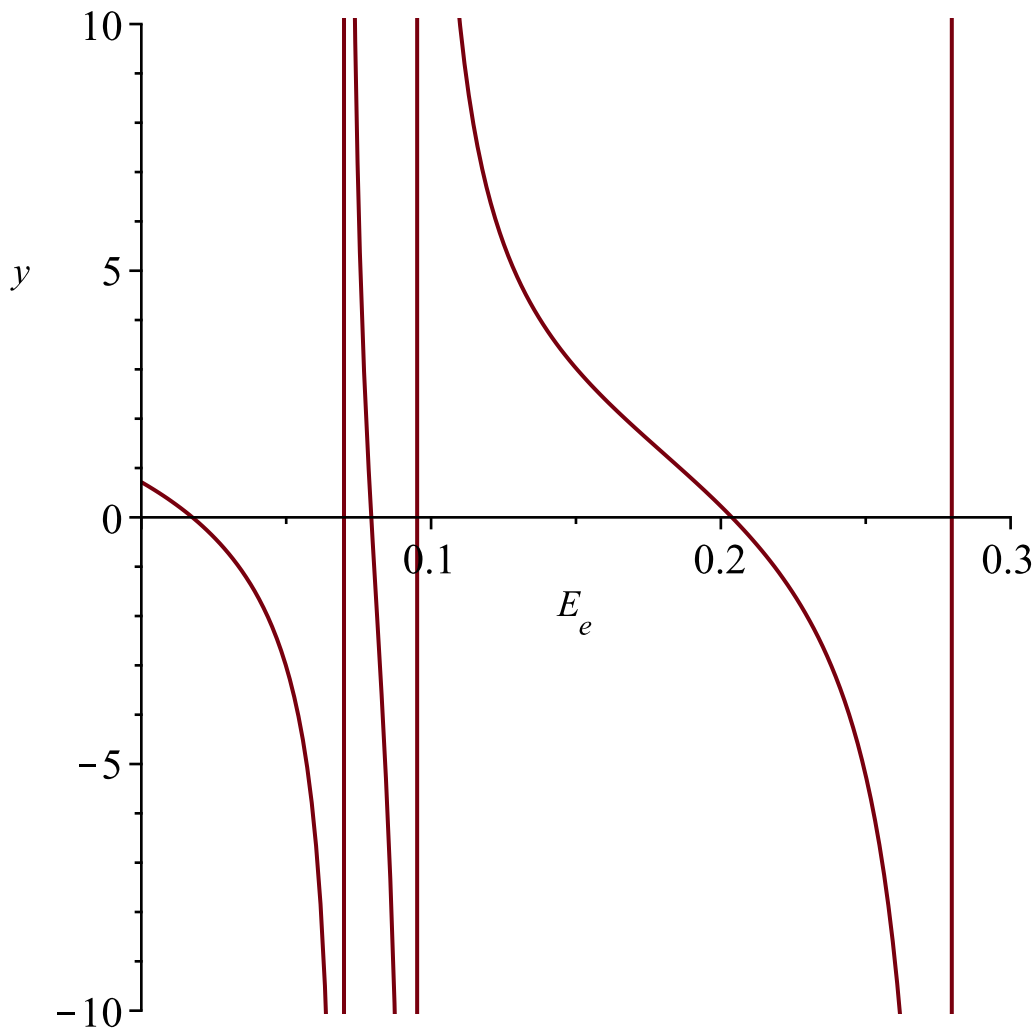
$$m_{e,c} := 0.12$$

$$m_{e,s} := 0.105$$

$$\hbar := 1$$

(3)

```
>  
> plot(TransEq, E[e]=0..0.3, y=-10..10);
```



> Calculates the numerical solution to the spherical Bessel function. Adjust the E[e] range in order to select which solution is used (1st, 2nd, 3rd, etc.) for different n quantum numbers.

```
fsolve(TransEq=0, E[e]=0.0..0.05);  
0.01764171287
```

(4)

```
> E[e] := %:
```

```
>
```

```
> Valuek[e, s] := sqrt(2 * m[e, s] * (E[e] - V[e, s])) / hbar :  
Valuek[e, c] := k[e, c] :
```

```
>
```

```
> psi[e, I] := x → sin(k[e, s] · x) :
```

```
psi[e, II] := x → 1 · cosh( Gamma[e] · ( x -  $\frac{t[e, tot]}{2}$  ) ) :
```

```
psi[e, III] := x → sin(k[e, s] · ( t[e, tot] - x ) ) :
```

```
>
```

```
> alpha[e] := psi[e, I]  $\left( \frac{t[e, tot]}{2} - \frac{t[e, c]}{2} \right)$  :
```

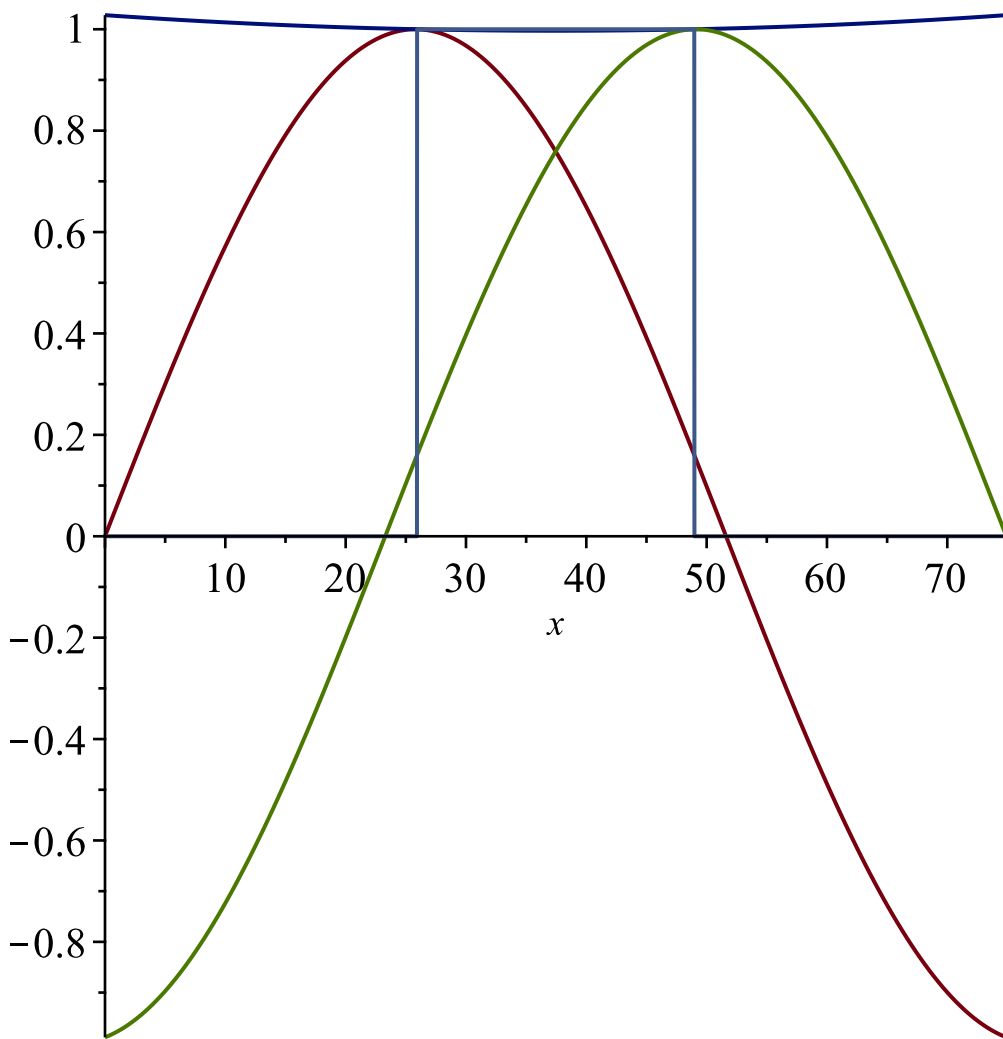
```
> beta[e] := psi[e, II]  $\left( \frac{t[e, tot]}{2} - \frac{t[e, c]}{2} \right)$  :
```

```
> B[e] :=  $\frac{\text{alpha}[e]}{\text{beta}[e]}$  :
```

```
>
```

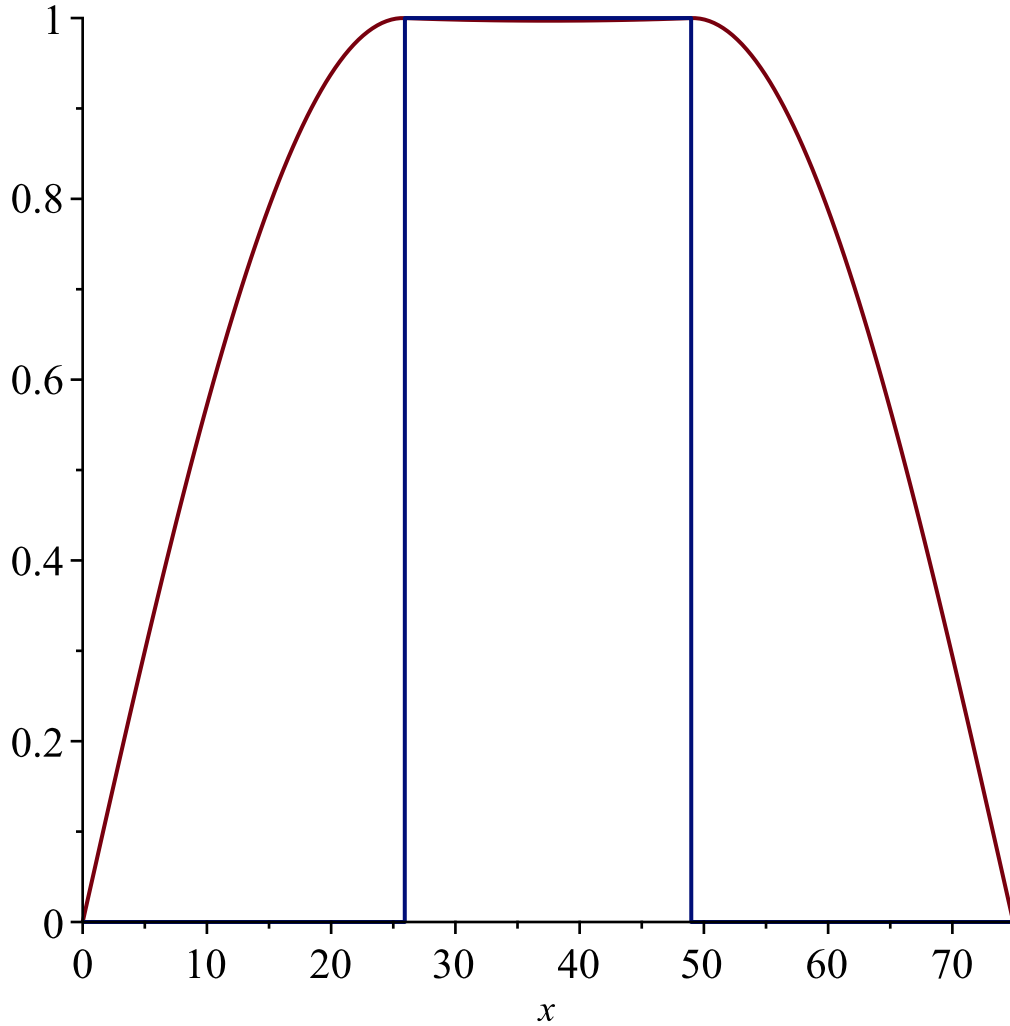
```
>
```

```
> plot  $\left( \left[ \text{psi}[e, I](x), B[e] \cdot \text{psi}[e, II](x), \text{psi}[e, III](x), \text{piecewise} \left( x \geq \left( \frac{t[e, tot]}{2} - \frac{t[e, c]}{2} \right) \text{ and } x \leq \left( \frac{t[e, tot]}{2} + \frac{t[e, c]}{2} \right), 1 \right) \right], x=0..t[e, tot] \right)$ ;
```



```
> plot  $\left( \left[ \text{piecewise} \left( x \geq 0 \text{ and } x \leq \left( \frac{t[e, tot]}{2} - \frac{t[e, c]}{2} \right), \Psi[e, I](x), x > \left( \frac{t[e, tot]}{2} \right) \right) \right] \right)$ ;
```

$$-\frac{t[e, c]}{2}) \text{ and } x < \left(\frac{t[e, tot]}{2} + \frac{t[e, c]}{2}\right), B[e] \cdot \psi[e, II](x), x \geq \left(\frac{t[e, tot]}{2} + \frac{t[e, c]}{2}\right) \text{ and } x \leq t[e, tot], \psi[e, III](x), \text{ piecewise} \left(x \geq \left(\frac{t[e, tot]}{2} - \frac{t[e, c]}{2}\right) \text{ and } x \leq \left(\frac{t[e, tot]}{2} + \frac{t[e, c]}{2}\right), 1\right), x = 0 .. t[e, tot];$$



> #Normalization of electron wave function over shell region (X) and core region (Y)

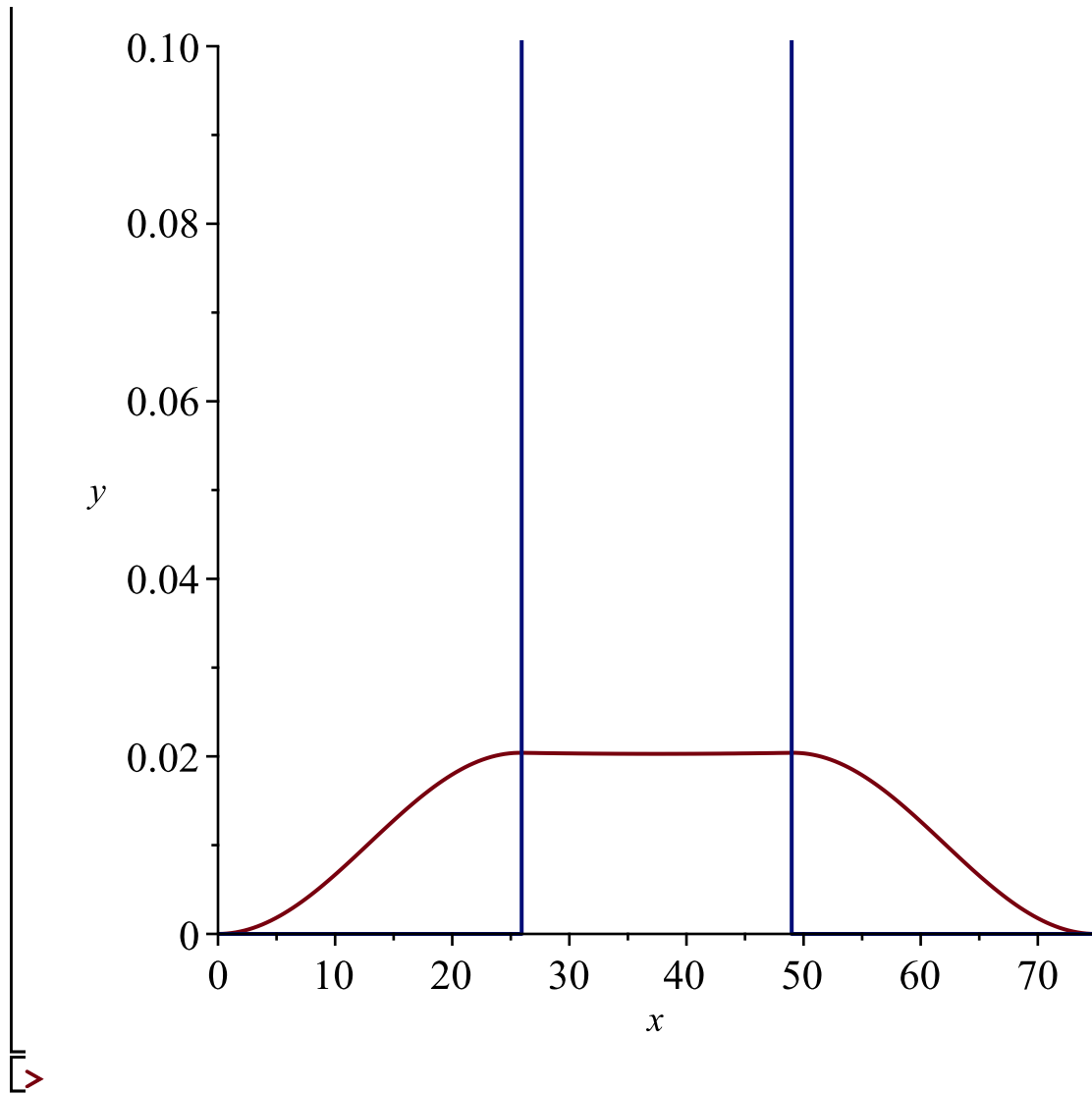
$$X[e] := \text{int} \left((\psi[e, I](x))^2, x = 0 .. \left(\frac{t[e, tot]}{2} - \frac{t[e, c]}{2}\right) \right) + \text{int} \left((\psi[e, III](x))^2, x = \left(\frac{t[e, tot]}{2} + \frac{t[e, c]}{2}\right) .. t[e, tot] \right);$$

$$Y[e] := \text{int} \left((B[e] \cdot \psi[e, II](x))^2, x = \left(\frac{t[e, tot]}{2} - \frac{t[e, c]}{2}\right) .. \left(\frac{t[e, tot]}{2} + \frac{t[e, c]}{2}\right) \right);$$

$$\begin{aligned}
& + \frac{t[e, c]}{2} \Big) \Big); \\
N[e] & := \frac{1}{\text{sqrt}(X[e] + Y[e])}; \\
& X_e := 26.04470907 \\
& Y_e := 22.96350101 \\
& N_e := 0.1428451763
\end{aligned} \tag{5}$$

>

$$\begin{aligned}
> \text{plot} \Big(& \left[\text{piecewise} \left(x \geq 0 \text{ and } x \leq \left(\frac{t[e, tot]}{2} - \frac{t[e, c]}{2} \right), (N[e] \cdot \Psi[e, I](x))^2, x \right. \right. \\
& > \left(\frac{t[e, tot]}{2} - \frac{t[e, c]}{2} \right) \text{ and } x < \left(\frac{t[e, tot]}{2} + \frac{t[e, c]}{2} \right), (N[e] \cdot B[e] \cdot \Psi[e, \\
& II](x))^2, x \geq \left(\frac{t[e, tot]}{2} + \frac{t[e, c]}{2} \right) \text{ and } x \leq t[e, tot], (N[e] \cdot \Psi[e, III](x))^2 \Big), \\
& \left. \text{piecewise} \left(x \geq \left(\frac{t[e, tot]}{2} - \frac{t[e, c]}{2} \right) \text{ and } x \leq \left(\frac{t[e, tot]}{2} + \frac{t[e, c]}{2} \right), 1 \right) \right], x=0 \\
& ..t[e, tot], y=0..0.1 \Big);
\end{aligned}$$



```

> psi[lh, I] := x -> A * sin(k[lh, s] * x) :
psi[lh, II] := x -> B * cosh(k[lh, c] * (x - t[lh, tot] / 2)) :
psi[lh, III] := x -> A * sin(k[lh, s] * (t[lh, tot] - x)) :

```

$$E[lh, I] := x \rightarrow \frac{-\frac{0.5}{m[lh, s]} \cdot \text{diff}(\text{diff}(\text{psi}[lh, I](x), x), x)}{\text{psi}[lh, I](x)} :$$

$$E[lh, II] := x \rightarrow \frac{-\frac{0.5}{m[lh, c]} \cdot \text{diff}(\text{diff}(\text{psi}[lh, II](x), x), x) + V[lh, c] \cdot \text{psi}[lh, II](x)}{\text{psi}[lh, II](x)} :$$

$$E[lh, III] := x \rightarrow \frac{-\frac{0.5}{m[lh, s]} \cdot \text{diff}(\text{diff}(\text{psi}[lh, III](x), x), x)}{\text{psi}[lh, III](x)} :$$

```

> Kappa[lh] := solve(E[lh, I](x) = E[lh, II](x), k[lh, c]) :
> Gamma[lh] := Kappa[lh][1] :
>
> k[lh, c] := sqrt(2 * m[lh, c] * (E[lh] - V[lh, c])) / hbar :
> k[lh, s] := sqrt(2 * m[lh, s] * (E[lh] - V[lh, s])) / hbar :
>
> TransEq := \frac{\left(k[lh, s] \cdot \cot\left(k[lh, s] \cdot \left(-\frac{t[lh, c]}{2} + \frac{t[lh, tot]}{2}\right)\right)\right)}{m[lh, s]}
- \frac{\left(-\text{Gamma}[lh] \cdot \tanh\left(\text{Gamma}[lh] \cdot \left(\frac{t[lh, c]}{2}\right)\right)\right)}{m[lh, c]} :
>
> V[lh, c] := \frac{0.821}{27.2107}; #0.821 for hole, #0.485 for electron
V[lh, s] := \frac{0}{27.2107};
t[lh, c] := \frac{t[c]}{5.292e-11};
#t[lh, s] := \frac{t[s]}{5.292e-11};
t[lh, tot] := \frac{t[tot]}{5.292e-11};
m[lh, c] := 0.16;
#2.14 for CdSe heavy hole; #0.16 for CdSe light hole; #0.12 for CdSe electron;
m[lh, s] := 0.108; #0.108 for PbS hole; #0.105 for PbS electron;
hbar := 1;

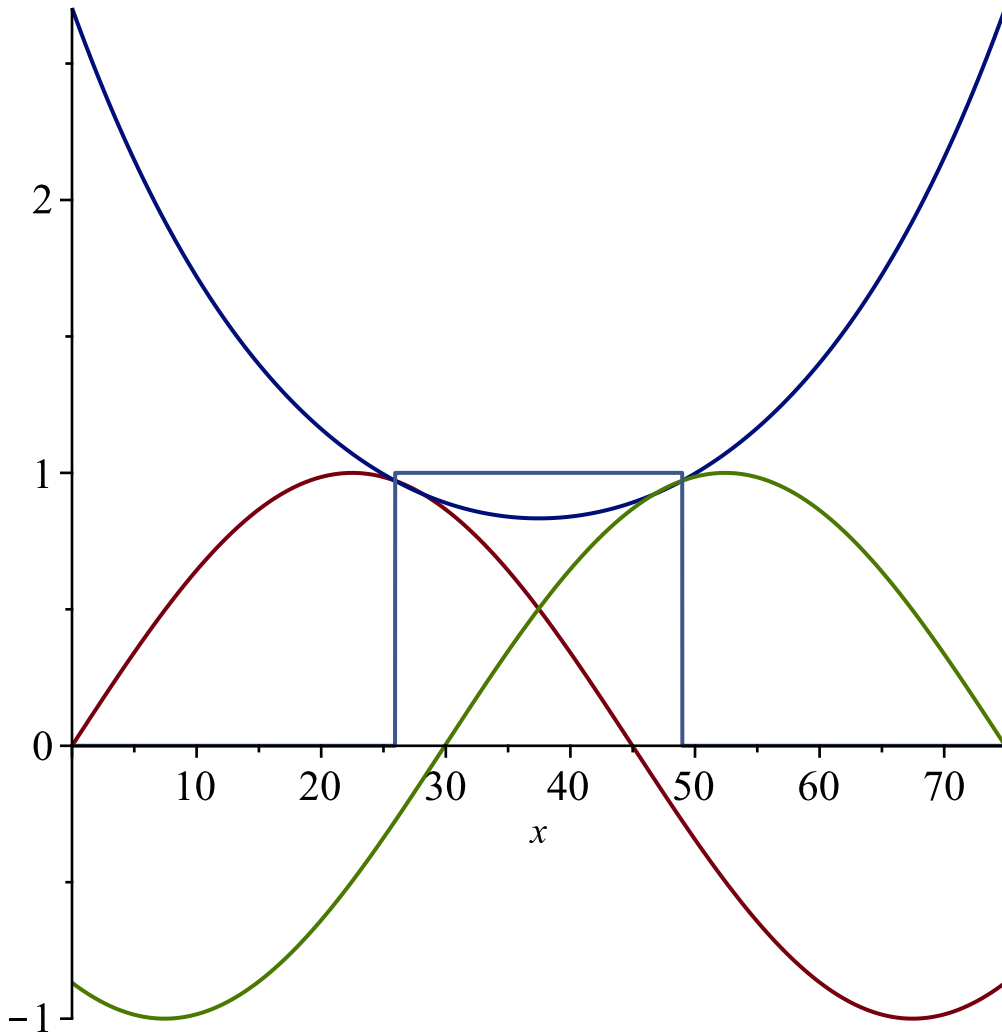
```



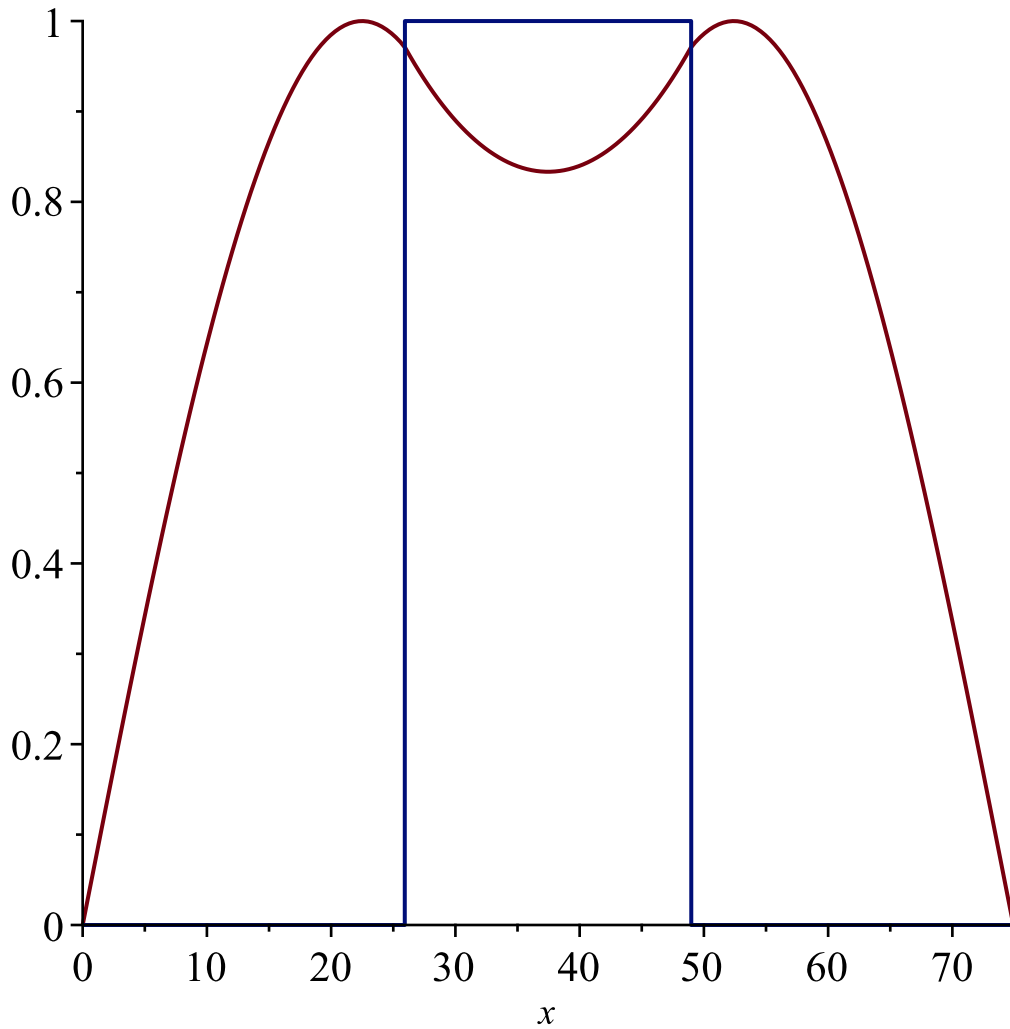
```

> E[lh] := %:
>
> Valuek[lh, s] := sqrt(2 * m[lh, s] * (E[lh] - V[lh, s])) / hbar :
Valuek[lh, c] := k[lh, c] :
>
> psi[lh, I] := x → sin(k[lh, s] · x) :
psi[lh, II] := x → 1 · cosh(Gamma[lh] · (x - t[lh, tot] / 2)) :
psi[lh, III] := x → sin(k[lh, s] · (t[lh, tot] - x)) :
>
> alpha[lh] := psi[lh, I] ( t[lh, tot] / 2 - t[lh, c] / 2 ) :
> beta[lh] := psi[lh, II] ( t[lh, tot] / 2 - t[lh, c] / 2 ) :
> B[lh] := alpha[lh] / beta[lh] :
>
>
> plot( [ psi[lh, I](x), B[lh] · psi[lh, II](x), psi[lh, III](x), piecewise( x ≥ ( t[lh, tot] / 2 - t[lh, c] / 2 ) and x ≤ ( t[lh, tot] / 2 + t[lh, c] / 2 ), 1 ) ], x = 0 .. t[lh, tot] );

```



$\triangleright \text{plot}\left(\left[\text{piecewise}\left(x \geq 0 \text{ and } x \leq \left(\frac{t[lh, tot]}{2} - \frac{t[lh, c]}{2}\right), \psi[lh, I](x), x > \left(\frac{t[lh, tot]}{2} - \frac{t[lh, c]}{2}\right) \text{ and } x < \left(\frac{t[lh, tot]}{2} + \frac{t[lh, c]}{2}\right), B[lh] \cdot \psi[lh, II](x), x \geq \left(\frac{t[lh, tot]}{2} + \frac{t[lh, c]}{2}\right) \text{ and } x \leq t[lh, tot], \psi[lh, III](x)\right], \text{piecewise}\left(x \geq \left(\frac{t[lh, tot]}{2} - \frac{t[lh, c]}{2}\right) \text{ and } x \leq \left(\frac{t[lh, tot]}{2} + \frac{t[lh, c]}{2}\right), 1\right), x = 0 .. t[lh, tot]\right);$



```

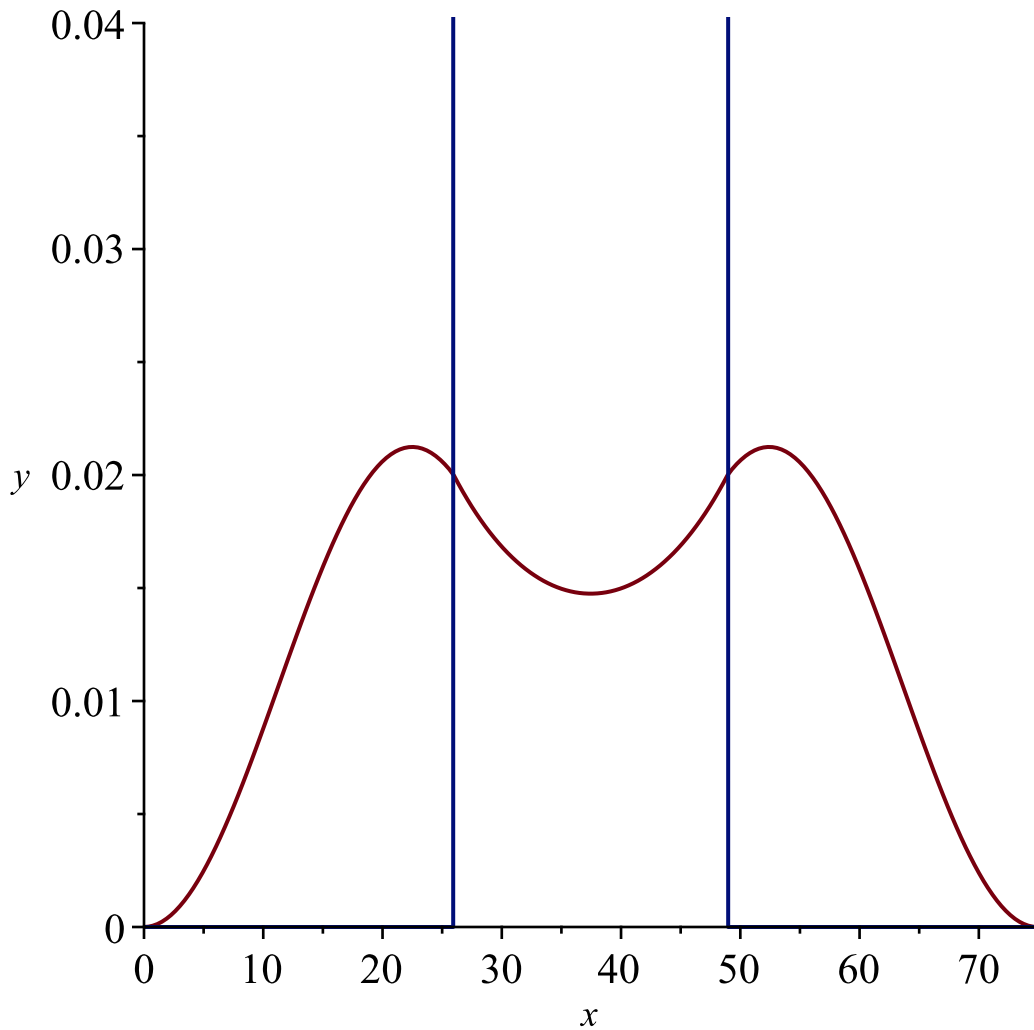
>
> #Normalization of electron wave function over shell region (X) and core region (Y)
X[lh] := int( (psi[lh, I](x))^2, x=0..( (t[lh, tot] - t[lh, c]) / 2 ) ) + int( (psi[lh,
    III](x))^2, x = ( (t[lh, tot] + t[lh, c]) / 2 ) ..t[lh, tot] );
Y[lh] := int( (B[lh]·psi[lh, II](x))^2, x = ( (t[lh, tot] - t[lh, c]) / 2 ) ..( (t[lh, tot]
    + t[lh, c]) / 2 ) );
N[lh] := 1 / sqrt(X[lh] + Y[lh]);
Xlh := 29.23156450
Ylh := 17.84332877

```

$$N_{lh} := 0.1457489142$$

(8)

```
> plot([piecewise(x ≥ 0 and x ≤ (t[lh, tot] - t[lh, c]) / 2, (N[lh] · ψ[lh, I](x))2, x
> (t[lh, tot] - t[lh, c]) / 2 and x < (t[lh, tot] + t[lh, c]) / 2, (N[lh] · B[lh]
· ψ[lh, II](x))2, x ≥ (t[lh, tot] + t[lh, c]) / 2 and x ≤ t[lh, tot], (N[lh] · ψ[lh,
III](x))2), piecewise(x ≥ (t[lh, tot] - t[lh, c]) / 2 and x ≤ (t[lh, tot]
+ t[lh, c]) / 2, 1)], x = 0 .. t[lh, tot], y = 0 .. 0.04);
```



```

> psi[hh, I] := x -> A * sin(k[hh, s] * x) :
psi[hh, II] := x -> B * cosh(k[hh, c] * (x - t[hh, tot] / 2)) :
> psi[hh, III] := x -> A * sin(k[hh, s] * (t[hh, tot] - x)) :
>
>
E[hh, I] := x -> 
$$\frac{-\frac{0.5}{m[hh, s]} \cdot \text{diff}(\text{diff}(\text{psi}[hh, I](x), x), x)}{\text{psi}[hh, I](x)} :$$

E[hh, II] := x
- 
$$\frac{0.5}{m[hh, c]} \cdot \text{diff}(\text{diff}(\text{psi}[hh, II](x), x), x) + V[hh, c] \cdot \text{psi}[hh, II](x)$$

- 
$$\rightarrow \frac{\text{psi}[hh, II](x)}{\text{psi}[hh, II](x)} :$$

E[hh, III] := x -> 
$$\frac{-\frac{0.5}{m[hh, s]} \cdot \text{diff}(\text{diff}(\text{psi}[hh, III](x), x), x)}{\text{psi}[hh, III](x)} :$$

>
> Kappa[hh] := solve(E[hh, I](x) = E[hh, II](x), k[hh, c]) :
> Gamma[hh] := Kappa[hh][1] :
>
> k[hh, c] := sqrt(2 * m[hh, c] * (E[hh] - V[hh, c])) / hbar :
> k[hh, s] := sqrt(2 * m[hh, s] * (E[hh] - V[hh, s])) / hbar :
>
> TransEq := 
$$\frac{\left( k[hh, s] \cdot \cot\left( k[hh, s] \cdot \left( -\frac{t[hh, c]}{2} + \frac{t[hh, tot]}{2} \right) \right) \right)}{m[hh, s]}$$

- 
$$\frac{\left( -\text{Gamma}[hh] \cdot \tanh\left( \text{Gamma}[hh] \cdot \left( \frac{t[hh, c]}{2} \right) \right) \right)}{m[hh, c]} :$$

>
> V[hh, c] :=  $\frac{0.821}{27.2107}$ ; #0.821 for hole, #0.485 for electron
V[hh, s] :=  $\frac{0}{27.2107}$ ;
t[hh, c] :=  $\frac{t[c]}{5.292e-11}$ ;
#t[hh, s] :=  $\frac{t[s]}{5.292e-11}$ ;
t[hh, tot] :=  $\frac{t[tot]}{5.292e-11}$ ;
m[hh, c] := 2.14;
#2.14 for CdSe heavy hole; #0.16 for CdSe light hole; #0.12 for CdSe electron;
m[hh, s] := 0.108; #0.108 for PbS hole; #0.105 for PbS electron;
hbar := 1;

```

$$V_{hh,c} := 0.03017195441$$

$$V_{hh,s} := 0.$$

$$t_{hh,c} := 23.05366591$$

$$t_{hh,tot} := 74.90551777$$

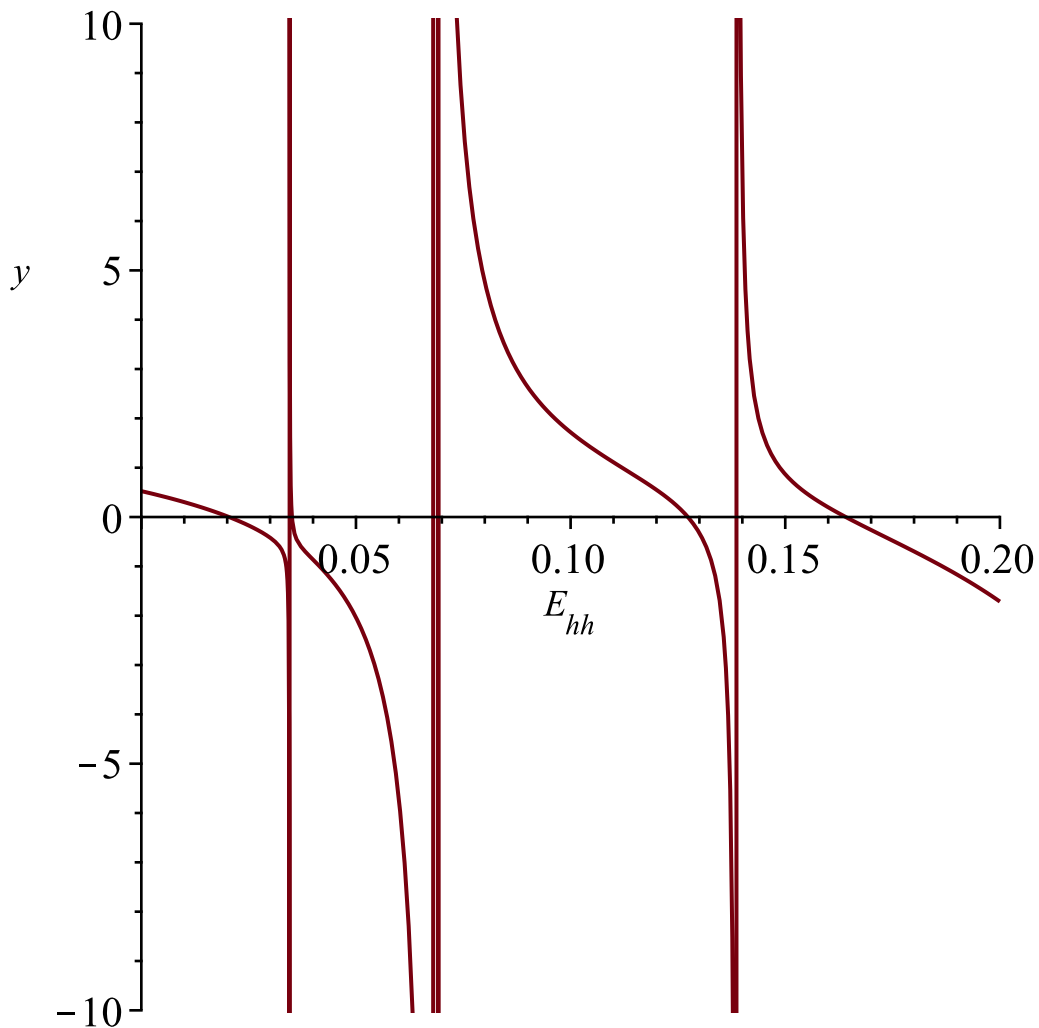
$$m_{hh,c} := 2.14$$

$$m_{hh,s} := 0.108$$

$$\hbar := 1$$

(9)

```
>  
> plot(TransEq, E[hh]=0..0.2, y=-10..10);
```

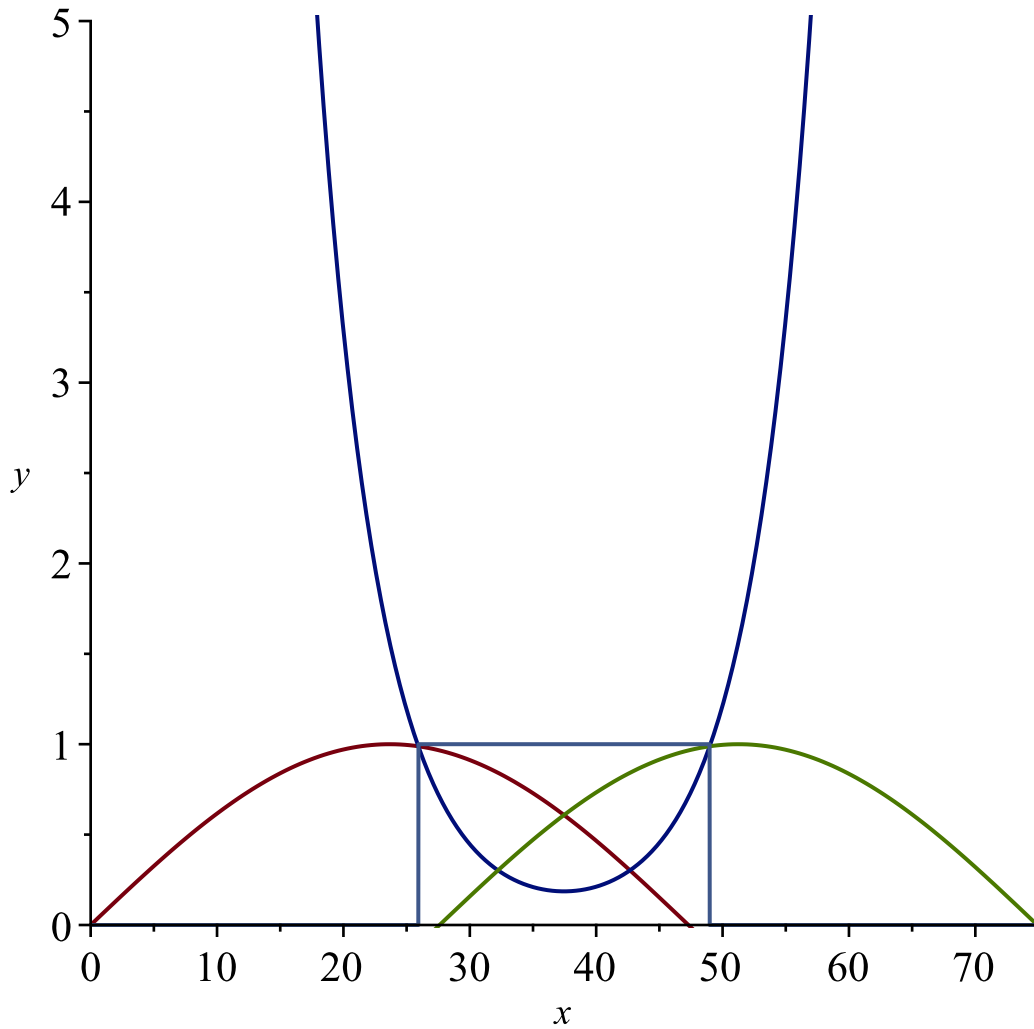


```
> Calculates the numerical solution to the spherical bessel function. Adjust the E[e] range in  
order to select which solution is used (1st, 2nd, 3rd, etc.) for different n quantum numbers.  
fsolve(TransEq=0, E[hh]=0.0..0.03);
```

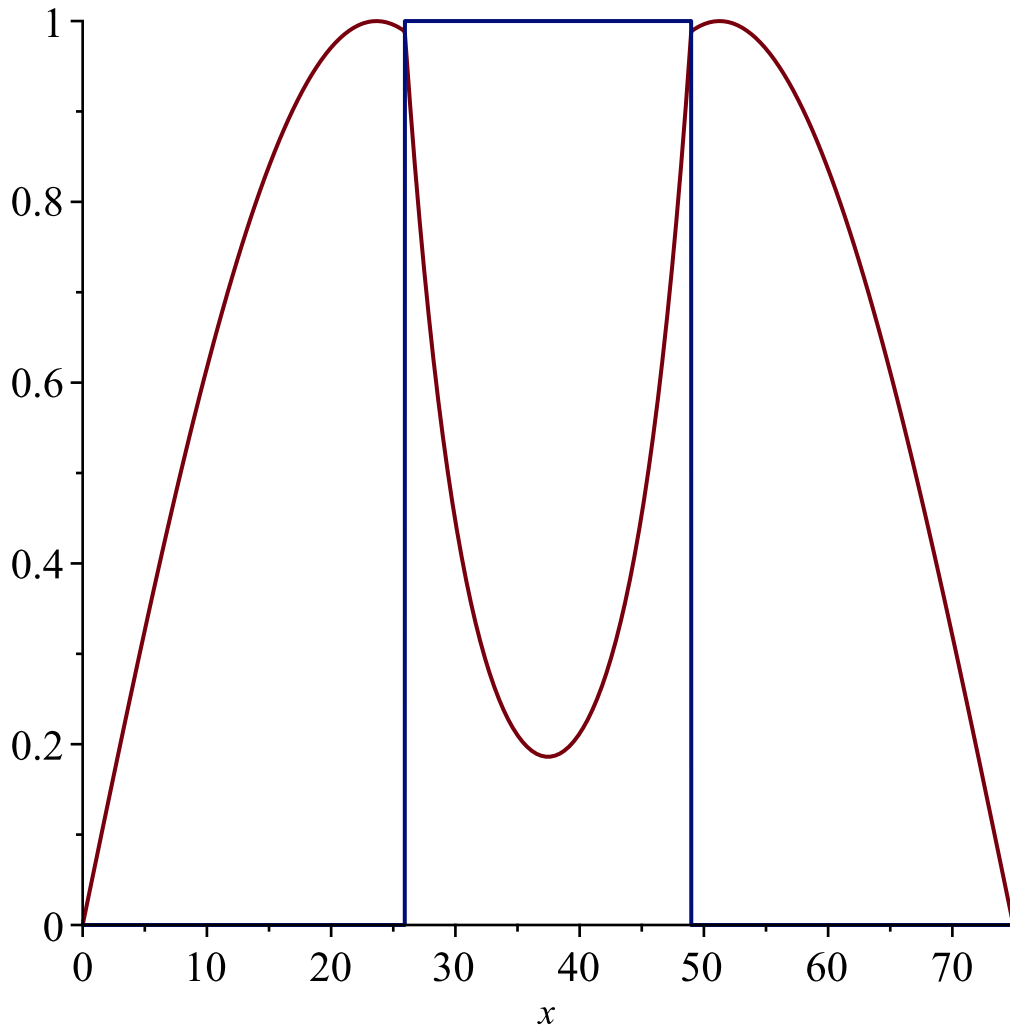
```

> E[hh] :=% :
>
> Valuek[hh, s] := sqrt(2 * m[hh, s] * (E[hh] - V[hh, s])) / hbar :
Valuek[hh, c] := k[hh, c] :
>
> psi[hh, I] := x → sin(k[hh, s] · x) :
psi[hh, II] := x → 1 · cosh(Gamma[hh] · (x -  $\frac{t[hh, tot]}{2}$ )) :
psi[hh, III] := x → sin(k[hh, s] · (t[hh, tot] - x)) :
>
> alpha[hh] := psi[hh, I]( $\frac{t[hh, tot]}{2} - \frac{t[hh, c]}{2}$ ) :
> beta[hh] := psi[hh, II]( $\frac{t[hh, tot]}{2} - \frac{t[hh, c]}{2}$ ) :
> B[hh] :=  $\frac{\text{alpha[hh]}}{\text{beta[hh]}}$  :
>
>
> plot( $\left[ \text{psi[hh, I]}(x), B[hh] \cdot \text{psi[hh, II]}(x), \text{psi[hh, III]}(x), \text{piecewise}\left(x \geq \left(\frac{t[hh, tot]}{2} - \frac{t[hh, c]}{2}\right) \text{ and } x \leq \left(\frac{t[hh, tot]}{2} + \frac{t[hh, c]}{2}\right), 1\right) \right], x=0..t[hh, tot], y=0..5$ );

```



$$\begin{aligned}
 &> \text{plot}\left(\left[\text{piecewise}\left(x \geq 0 \text{ and } x \leq \left(\frac{t[hh, tot]}{2} - \frac{t[hh, c]}{2}\right), \psi[hh, I](x), x\right.\right.\right. \\
 &\quad \left.\left.\left. > \left(\frac{t[hh, tot]}{2} - \frac{t[hh, c]}{2}\right) \text{ and } x < \left(\frac{t[hh, tot]}{2} + \frac{t[hh, c]}{2}\right), B[hh] \cdot \psi[hh, \right.\right.\right. \\
 &\quad \left.\left.\left. II\right](x), x \geq \left(\frac{t[hh, tot]}{2} + \frac{t[hh, c]}{2}\right) \text{ and } x \leq t[hh, tot], \psi[hh, III\right](x)\right), \\
 &\quad \left.\text{piecewise}\left(x \geq \left(\frac{t[hh, tot]}{2} - \frac{t[hh, c]}{2}\right) \text{ and } x \leq \left(\frac{t[hh, tot]}{2} + \frac{t[hh, c]}{2}\right), 1\right), x\right. \\
 &\quad \left.= 0 \dots t[hh, tot]\right);
 \end{aligned}$$



```

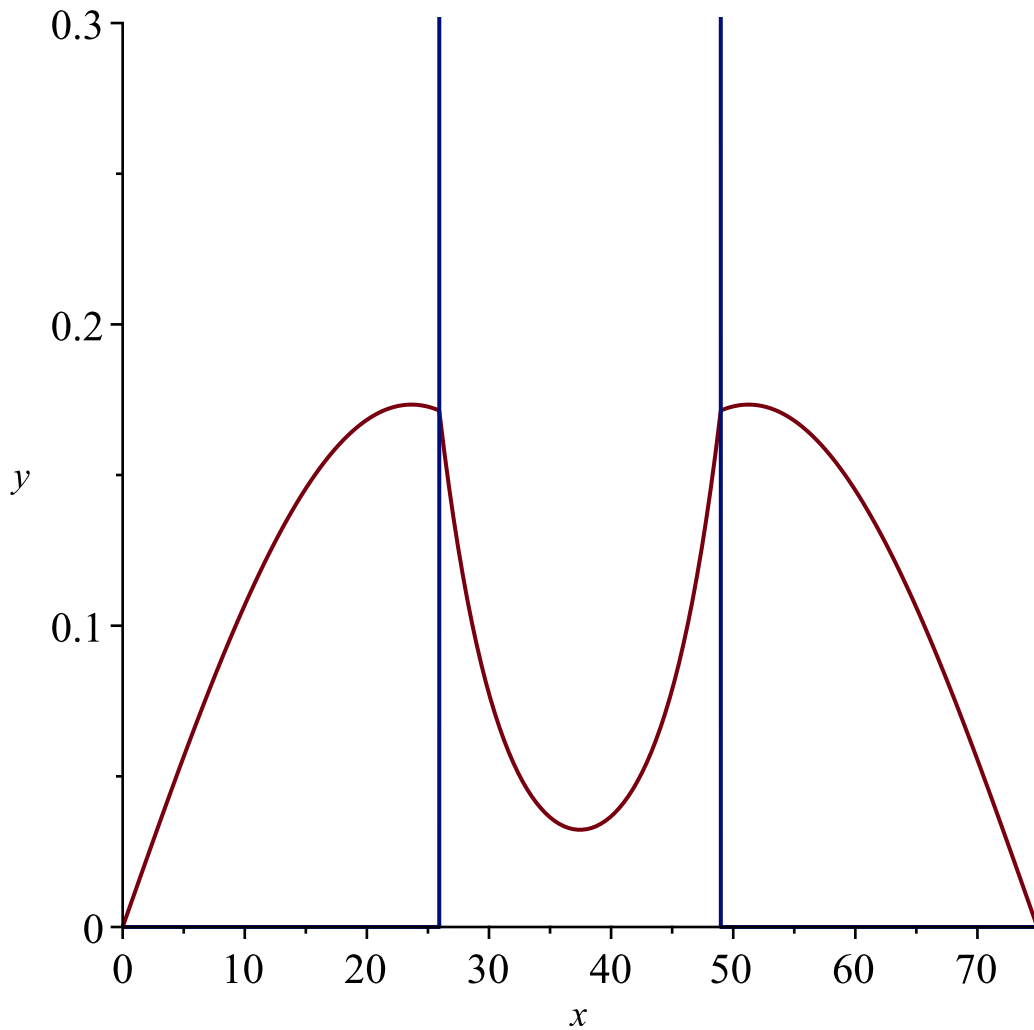
>
> #Normalization of electron wave function over shell region (X) and core region (Y)
X[hh] := int((psi[hh, I](x))^2, x=0..(t[hh, tot]/2 - t[hh, c]/2)) + int((psi[hh,
    III](x))^2, x=(t[hh, tot]/2 + t[hh, c]/2)..t[hh, tot]);
Y[hh] := int((B[hh]*psi[hh, II](x))^2, x=(t[hh, tot]/2 - t[hh, c]/2)..(t[hh, tot]/
    + t[hh, c]/2));
N[hh] := 1/sqrt(X[hh] + Y[hh]);
X_hh := 28.16844465
Y_hh := 5.098500010

```

$$N_{hh} := 0.1733778216$$

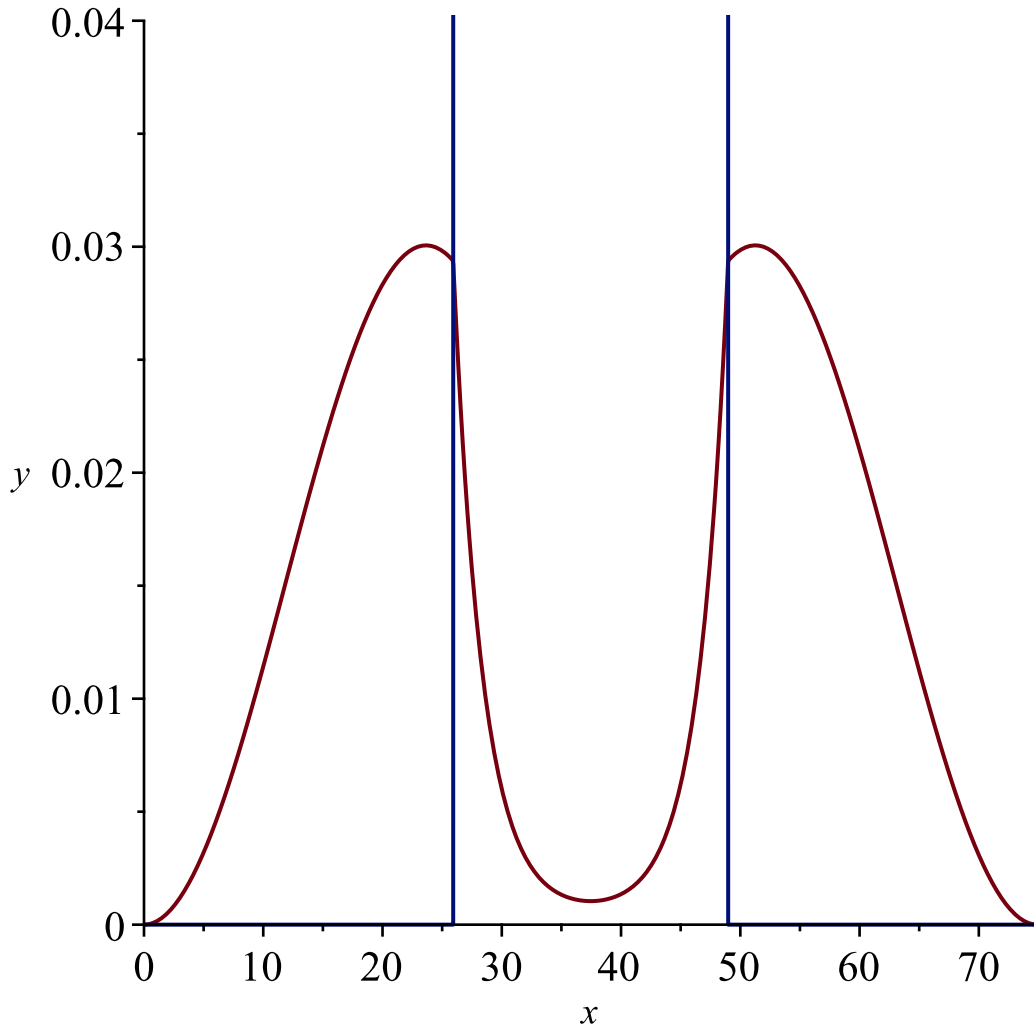
(11)

```
> plot([piecewise(x ≥ 0 and x ≤ (t[hh, tot] - t[hh, c]) / 2), N[hh] · ψ[hh, I](x), x
> (t[hh, tot] - t[hh, c]) / 2 and x < (t[hh, tot] + t[hh, c]) / 2, N[hh] · B[hh]
· ψ[hh, II](x), x ≥ (t[hh, tot] + t[hh, c]) / 2 and x ≤ t[hh, tot], N[hh] · ψ[hh,
III](x), piecewise(x ≥ (t[hh, tot] - t[hh, c]) / 2 and x ≤ (t[hh, tot]
+ t[hh, c]) / 2, 1)], x=0..t[hh, tot], y=0..0.3);
```



```
> plot([piecewise(x ≥ 0 and x ≤ (t[hh, tot] - t[hh, c]) / 2), (N[hh] · ψ[hh, I](x))2, x
```

$$\begin{aligned}
 &> \left(\frac{t[hh, tot]}{2} - \frac{t[hh, c]}{2} \right) \text{ and } x < \left(\frac{t[hh, tot]}{2} + \frac{t[hh, c]}{2} \right), (N[hh] \\
 &\cdot B[hh] \cdot \psi[hh, II](x))^2, x \geq \left(\frac{t[hh, tot]}{2} + \frac{t[hh, c]}{2} \right) \text{ and } x \leq t[hh, tot], \\
 &(N[hh] \cdot \psi[hh, III](x))^2, \text{ piecewise} \left(x \geq \left(\frac{t[hh, tot]}{2} - \frac{t[hh, c]}{2} \right) \text{ and } x \right. \\
 &\left. \leq \left(\frac{t[hh, tot]}{2} + \frac{t[hh, c]}{2} \right), 1 \right), x = 0 .. t[hh, tot], y = 0 .. 0.04);
 \end{aligned}$$



$$\begin{aligned}
> \text{Overlap}[e, lh] &:= \text{int}\left(N[e] \cdot \text{psi}[e, I](x) \cdot N[lh] \cdot \text{psi}[lh, I](x), x=0 \dots \left(\frac{t[e, tot]}{2}\right.\right. \\
&\quad \left.\left. - \frac{t[e, tot]}{2}\right)\right) + \text{int}\left(N[e] \cdot B[e] \cdot \text{psi}[e, II](x) \cdot N[lh] \cdot B[lh] \cdot \text{psi}[lh, II](x), x \right. \\
&= \left(\frac{t[e, tot]}{2} - \frac{t[e, tot]}{2}\right) \cdot \left(\frac{t[e, tot]}{2} + \frac{t[e, tot]}{2}\right) + \text{int}\left(N[e] \cdot \text{psi}[e, III](x) \right. \\
&\quad \left. \cdot N[lh] \cdot \text{psi}[lh, III](x), x = \left(\frac{t[e, tot]}{2} + \frac{t[e, tot]}{2}\right) \dots t[e, tot]\right); \\
&\qquad \text{Overlap}_{e, lh} := 2.196927795 \tag{12}
\end{aligned}$$

$$\begin{aligned}
> \text{Overlap}[e, hh] &:= \text{int}\left(N[e] \cdot \text{psi}[e, I](x) \cdot N[hh] \cdot \text{psi}[hh, I](x), x=0 \dots \left(\frac{t[e, tot]}{2}\right.\right. \\
&\quad \left.\left. - \frac{t[e, tot]}{2}\right)\right) + \text{int}\left(N[e] \cdot B[e] \cdot \text{psi}[e, II](x) \cdot N[hh] \cdot B[hh] \cdot \text{psi}[hh, II](x), x \right. \\
&= \left(\frac{t[e, tot]}{2} - \frac{t[e, tot]}{2}\right) \cdot \left(\frac{t[e, tot]}{2} + \frac{t[e, tot]}{2}\right) + \text{int}\left(N[e] \cdot \text{psi}[e, III](x) \right. \\
&\quad \left. \cdot N[hh] \cdot \text{psi}[hh, III](x), x = \left(\frac{t[e, tot]}{2} + \frac{t[e, tot]}{2}\right) \dots t[e, tot]\right); \\
&\qquad \text{Overlap}_{e, hh} := 48.36026323 \tag{13}
\end{aligned}$$

$$\begin{aligned} &> E[e] \cdot 27.2107; \\ & \qquad \qquad \qquad 0.4800433564 \end{aligned} \tag{14}$$

$$\begin{aligned} &> E[lh] \cdot 27.2107; \\ & \qquad \qquad \qquad 0.6145426620 \end{aligned} \tag{15}$$

$$\begin{aligned} &> E[hh] \cdot 27.2107; \\ & \qquad \qquad \qquad 0.5557840503 \end{aligned} \tag{16}$$

$$\begin{aligned} &> \text{unprotect}(\Psi); \\ &> \Psi[e, I] := \text{factor}(N[e] \cdot \text{psi}[e, I](\text{Col}(A))); \\ &> \Psi[e, II] := \text{factor}(N[e] \cdot B[e] \cdot \text{psi}[e, II](\text{Col}(A))); \\ &> \Psi[e, III] := \text{factor}(N[e] \cdot \text{psi}[e, III](\text{Col}(A))); \\ & \qquad \qquad \Psi_{e, I} := 0.1428451763 \sin(0.06086673722 \text{Col}(A)) \\ & \qquad \qquad \Psi_{e, II} := 0.1424275826 \cosh(0.006611950912 \text{Col}(A) - 0.2476358032) \\ & \qquad \qquad \Psi_{e, III} := 0.1428451763 \sin(4.559254467 - 0.06086673722 \text{Col}(A)) \end{aligned} \tag{17}$$

$$\begin{aligned} &> \Psi[lh, I] := \text{factor}(N[lh] \cdot \text{psi}[lh, I](\text{Col}(A))); \\ &> \Psi[lh, II] := \text{factor}(N[lh] \cdot B[lh] \cdot \text{psi}[lh, II](\text{Col}(A))); \\ &> \Psi[lh, III] := \text{factor}(N[lh] \cdot \text{psi}[lh, III](\text{Col}(A))); \\ & \qquad \qquad \Psi_{lh, I} := 0.1457489142 \sin(0.06984463258 \text{Col}(A)) \\ & \qquad \qquad \Psi_{lh, II} := 0.1214497801 \cosh(0.04927428072 \text{Col}(A) - 1.845457755) \\ & \qquad \qquad \Psi_{lh, III} := 0.1457489142 \sin(5.231748367 - 0.06984463258 \text{Col}(A)) \end{aligned} \tag{18}$$

$$\begin{aligned} &> \Psi[hh, I] := \text{factor}(N[hh] \cdot \text{psi}[hh, I](\text{Col}(A))); \\ &> \Psi[hh, II] := \text{factor}(N[hh] \cdot B[hh] \cdot \text{psi}[hh, II](\text{Col}(A))); \\ &> \Psi[hh, III] := \text{factor}(N[hh] \cdot \text{psi}[hh, III](\text{Col}(A))); \\ & \qquad \qquad \Psi_{hh, I} := 0.1733778216 \sin(0.06642171090 \text{Col}(A)) \\ & \qquad \qquad \Psi_{hh, II} := 0.03226107075 \cosh(0.2042451941 \text{Col}(A) - 7.649546007) \\ & \qquad \qquad \Psi_{hh, III} := 0.1733778216 \sin(4.975352646 - 0.06642171090 \text{Col}(A)) \end{aligned} \tag{19}$$

$$\begin{aligned} &> \frac{t[e, \text{tot}]}{2} - \frac{t[e, c]}{2}; \\ & \qquad \qquad \qquad 25.92592592 \end{aligned} \tag{20}$$

$$\begin{aligned} &> \frac{t[e, \text{tot}]}{2} + \frac{t[e, c]}{2}; \\ & \qquad \qquad \qquad 48.97959184 \end{aligned} \tag{21}$$

$$\left[\begin{array}{l} > t[e, tot]; \\ > \frac{t[e, tot]}{2}; \end{array} \right. \begin{array}{l} 74.90551777 \\ 37.45275888 \end{array} \quad \begin{array}{l} (22) \\ (23) \end{array}$$